Alma Mater Studiorum · Università di Bologna

DOTTORATO DI RICERCA IN
MECCANICA E SCIENZE AVANZATE
DELL'INGEGNERIA (DIMSAI)

CICLO 32

Settore Concorsuale: 09/C2
Settore Scientifico Disciplinare: ING-IND/10

Experimental and Numerical Analysis of Gas Flows in Microchannels and Micro Heat Exchanger

Presentata da: Danish Rehman

Coordinatore Dottorato

Prof. Ing. Marco Carricato

Supervisore

Prof. Ing. Gian Luca Morini

Esame finale anno 2020

Abstract

Due to increased interest in miniaturization, great attention has been given in the recent decade to the micro heat exchanging systems as well. Considerable experimental, as well as numerical literature, exist for the liquid flows inside micro geometries however, there is still a limited understanding of gas flows in micro heat exchanging systems. The aim of the current thesis is to further the understanding of fluid flow and heat transfer phenomenon inside such geometries when a compressible working fluid is utilized. A combined experimental and numerical approach has been utilized in order to overcome the lack of employable sensors for micro dimensional channels. Due to various data reduction methodologies employed in the literature for the gas microflows, a detailed comparison of the existing methodologies has been conducted and the best suited methodology for gas microflow experimentalists is proposed. This data reduction methodology ensured that the physics of the microflows is conserved even during the flow choking. A transitional $\gamma - Re_\theta$ turbulence model proposed by Abraham et al. [1] is extensively validated for the first time against the experimental results of the microtubes and microchannels under adiabatic wall conditions. After validation, this model is used for the prediction of heat transfer inside microchannels and heat exchangers. Heat transfer analysis of single microtubes showed that when the compressible working fluid is used, Nusselt number results are in partial disagreement with the conventional theory at highly turbulent flow regime for microtubes having a hydraulic diameter less than 250 μm. An emphasis on the conventional definition of the Nusselt number for gas microflows has also been done to highlight the role of compressibility and subsequent decrease of gas static temperature towards the establishment of heat transfer characteristics of micro gas flows. Experimental and numerical analysis on a prototype double layer microchannel heat exchanger showed that compressibility is detrimental to the thermal performance. Furthermore, it has been found out that compressibility effects for such heat exchangers are significant when the average Mach number at the outlet of the microchannel is greater than 0.1 compared to the adiabatic limit of 0.3. These findings suggest that for a microchannel heat exchanger where gas is to be used as the working fluid, low values of the mass flow should be employed in order to avoid Mach numbers greater than 0.1 at the outlet of the channel. Depending

on the mass flow ratio of cold and hot sides, experimental results of unbalanced flows showed deviation from the conventional ε-NTU theory again suggesting that conventional design rules need to be revisited as soon as compressibility becomes dominant. Furthermore, to avoid a staggering amount of the computational power needed to simulate the micro heat exchanging systems with hundreds of microchannels, a reduced order model based on the porous medium has been developed that takes into account the compressibility of the gas inside microchannels. The validation of the proposed model against experimental results of average thermal effectiveness and the pressure drop showed an excellent match between the two. This provides a basis to carry out further investigations on the role of manifold (maldistribution, the thickness of partition foil, wall conductivity, etc.) on the hydraulic thermal performance of such devices in detail at a considerably less computational cost.

Acknowledgements

I would like to express the deepest gratitude to my supervisor Prof. Gian Luca Morini for his mentoring and for the opportunity he offered to start this work. He believed in me and instilled the skills that were missing in my career and provided me with his constant support throughout the development of this work. I would also like to thank Dr. Michel Delanaye and Mr. Joseph Jojomon who supervised and guided me during my secondment at MITIS, Belgium. My thanks also go to Prof. Juergen Brandner and Prof. Lucien Baldas for the fruitful discussions towards the development of this work and also for being part of my thesis review committee.

I greatly acknowledge the financial support that was received during these three years from the European Union's Framework Programme for Research and Innovation Horizon 2020 (2014–2020) under the Marie Sklodowska-Curie Grant Agreement No. 643095 (MIGRATE Project).

I would extend my thanks to the alumni of the lab Dr. Behnam Rostami and Ing. Stefano Cancellara for their support and discussions. My thanks also go to Dr. Matteo Dongellini, Dr. Jean Pierre Campana and Dr. Usman Hadi, Mrs. Natasa Djordjevic and Ms. Sofia Toto for their friendly discussions around the lunch table and coffee breaks. I would thank Ing. Davide Barattini for assisting me in the development of this work.

My special thanks to Dr. Francesco Vai from the Mechanical Lab, who helped me realizing the experimental devices that are used throughout this work. Without his kind support, this work would never have been possible. I would also extend my gratitude to the lab technicians Mr. Maurizio Chendi, Mr. Fabrizio Casarini, Mr. Franco Ferri and Mr. Stefano Monti a.k.a Maestro, who have been of constant help throughout my stay. A big thanks to Dr. Adrian H. Lutey from the University of Parma, Italy for his help in characterizing the fabricated microchannels with laser profilometer. I am also in debt to Dr. Ing. Stefania Falcioni for managing the lab and for her assistance in all the administrative work during these three years.

I would like to acknowledge the constant emotional and moral support of my wife Mrs.

Reema Fayyaz. I cannot thank her enough for the time that she has allowed me to finish this work while taking care of my parenting responsibilities as well. I would also like to thank my parents and siblings for their constant love, prayers, and support to embark on this journey.

Finally, I pray to Almighty Allah, who bestowed upon me all these blessings, to give me strength and wisdom to use the learnt knowledge the way He wants.

Nomenclature

Nu	Nusselt number
Ma	Mach number
τ_w	Wall shear stress
τ	Shear stress
ρ	Density
T	Temperature
$\overline{T}$	Average temperature along the length of the microchannel
ΔT	Temperature difference
p	Pressure
R	Gas constant
Re	Reynolds Number
D_h	Hydraulic diameter
A	Cross section area of the microchannel/microtube
A_{ht}	Heat transfer area for the heat exchanger
Per	Perimeter of the flow cross section
$\dot{G}$	ratio of mass flow rate and area
$\dot{m}$	Mass flow rate
μ	Dynamic viscosity of the fluid
μ_t	Turbulent/eddy viscosity
ν	Kinematic viscosity of the fluid
u	Velocity in the streamwise direction
$\overline{u}$	Mean velocity

u'	Fluctuating component of the velocity
Δp	Pressure drop
K	Minor loss coefficient
h	Convective heat transfer coefficient
q	Heat flux
f_f	Fanning friction factor
$f_{c,lam}$	Laminar friction factor for circular cross section
$f_{R,lam}$	Laminar friction factor for rectangular cross section
f_B	Blasius friction factor
h	Height of the microchannel
w	Width of the microchannel
α	Aspect ratio of the microchannel
Ł	Length of the the microchannel/microtube
L_h	Heated length of the microtube
ϵ	Surface roughness of the microchannel/microtube
k	Turbulent kinetic energy
ω	Specific rate of turbulent destruction
P_k	Rate of kinetic energy production
F_1, F_2	Blending functions in SST-k-ω turbulence model
γ	Intermittency factor
$c_{\gamma,2}$	Transitional model constant
$c_{\theta,t}$	Transitional model constant
E_1, E_2	Intermittency destruction terms
$P_{\gamma,1}, P_{\gamma,2}$	Intermittency production terms
$P_{\theta,t}$	Production term for the transition onset Reynolds number
$Re_{\theta,t}$	Transition momentum thickness Reynolds number
S	Absolute value of the shear strain
χ	SST model constant
β_1, β_2	SST model constants

Ω	Magnitude of the absolute vorticity rate
$y+$	Non-dimensional distance between the wall and first node element
H_{man}	Height of the manifold
H_{in}	Height of the reducer
Pr	Prandlt number
α_{th}	Thermal diffusivity of the fluid
C_p	Specific heat of the gas at constant pressure
k_f	Thermal conductivity of the gas
ψ	Kinetic energy recovery coefficient
$\dot{Q}$	Heat exchange power
$\dot{q}$	Heat exchange power per unit area A_{ht}
n	Number of channels
U	Overall heat transfer coefficient for the heat exchanger
ε_{th}	Thermal efficiency of the heat exchanger
λ	Heat conduction parameter
C^*	Ratio of the mass flows in the hot and cold fluid streams for the heat exchanger
δ	Thickness of the partition foil
t_w	Thickness of the microchannel wall
$\frac{1}{\alpha}$	Viscous coefficient of the porous model
Γ	Inertial coefficient of the porous model
D_p	Effective particle diameter in porous model
κ	Fractional void volume in porous model

Subscripts

in	at the inlet of the microtube/microchannel
out	at the outlet of the microtube/microchannel
1	at the entrance of the inlet manifold
2	at the exit of the outlet manifold
b	Bulk value of the fluid
f	material property of the fluid
$w/wall$	wall of the microtube
tot	Total (static and dynamic) part of the flow quantity
$stag$	Stagnation flow quantity
$static$	Static flow quantity
x	Flow quantity at cross section located at distance 'x' from the inlet
av	Averaged over the whole length of the microtube/microchannel
$w-f$	Wall to fluid
cr	Critical
t	Turbulent
c	cold side of the heat exchanger
h	hot side of the heat exchanger
h,in	Flow quantity at the inlet of the hot fluid side of heat exchanger
h,out	Flow quantity at the outlet of the hot fluid side of heat exchanger
c,in	Flow quantity at the inlet of the cold fluid side of heat exchanger
c,out	Flow quantity at the outlet of the cold fluid side of heat exchanger
KE	Flow quantity due to kinetic energy
f,h	Flow quantity expressed for the hot side of the heat exchanger
f,c	Flow quantity expressed for the cold side of the heat exchanger
$h-w$	Hot fluid to the wall
$w-c$	Wall to the cold side of the fluid
$loss$	Loss of the fluid quantity
$exit$	Exit of the microchannel

Abbreviations

PCHE	Printed circuit heat exchanger
RANS	Reynolds-averaged Navier–Stokes equations
PMMA	Poly methyl methacrylate (acrylic)
PEEK	Polyether ether ketone
MT	Microtube
MC	Microchannel
HPC	High performance computing
μHx	Micro heat exchangers
CFD	Computational fluid dynamics
2D/3D	Two dimensional and three dimensional
LMTD	Logarithmic mean temperature difference
DMM	Digital multimeter
NI	National Instruments
NTU	Number of transfer units
MEMS	Micro electro mechanical systems
CHT	Conjugate heat transfer
LES	Large eddy simulation
DES	Detached eddy simulation
DNS	Direct numerical simulation
M1	First data reduction methodology
M2	Second data reduction methodology
RE	Rounded entrance
SC	Sudden contraction
VS	V-shaped
BM	Bellmouth
S&L	Shah and London
PF	Parallel flow

CF Counter flow

lam Laminar

BL Blasius

Contents

List of Tables

List of Figures

Chapter 1

Introduction

Miniaturization of the heat transfer devices has promised increased heat transfer coefficients with the reduced or comparable pressure drops to that of their macro sized counterparts. Much of the present literature deals with the liquid flows and limited understanding of the gas flows inside these micro heat exchanging systems that exist in the open literature. The objective of the current research thesis is, therefore to further the understanding of flow and heat transfer in micro heat exchanging systems in the continuum flow regime with the use of a compressible gas as the working medium. This main objective has been achieved in four steps that are enumerated as follows:

1. A Reynolds-averaged Navier–Stokes equations (RANS) based transitional turbulence model, capable of predicting the transitional flow characteristics, has been validated using the experimental pressure drop analysis of commercial stainless steel microtubes with the isothermal/adiabatic wall boundary condition. The fluid flow characteristics have been studied experimentally for commercial microtubes where the effect of minor losses on the experimental evaluation of friction factor has been explained using the validated transitional turbulence model. An experimental campaign to compare micro convection with conventional correlations has been carried out and discrepancies have been explained. In order to

understand the behavior of local heat transfer of gas flow, numerical parametric analysis has been performed to elaborate on the role of compressibility on the heat transfer characteristics.

2. Detailed experimental studies have been conducted using a series of microchannels that were fabricated by performing micromilling in PMMA. Milling parameters were chosen such that the resulting surface roughness of the microchannels was less than 1 μm. A new modular test assembly for a single microchannel was fabricated and leak tightness has been achieved. This assembly allowed to experiment with the adiabatic flows by varying different geometric parameters of the rectangular microchannels. Pressure taps for the local pressure measurements were also incorporated in the assembly to establish the local frictional characteristics of the gas microflows. Using this assembly the effect of aspect ratio and inlet manifold shape of the microchannels on the laminar to turbulent flow transition has been investigated.

3. Fluid flow and heat transfer investigations on the double layer micro heat exchangers are performed in the next step. An experimental assembly of a double layer micro heat exchanger has been manufactured. Individual layers containing dividing and collecting manifolds along with 51 parallel microchannels were realized using the micromilling within PMMA plastic sheets. A new test bench was developed with two equally sized volume flow controllers for the hot and cold fluids. Experimental investigations in both parallel and counterflow configurations have been performed. To have a better understanding of the flow and heat transfer physics inside the parallel microchannels, computational modeling is also employed in parallel.

4. A hybrid CFD methodology for the thermal performance analysis of micro heat exchangers has been developed where parallel microchannels are modeled as a porous medium. This allowed to correctly estimate the heat exchanger effectiveness of a double layer microchannel heat exchanger with much less computational

cost.

1.1 Contributions

The main contributions of the Ph.D. thesis can be summarized as follows:

1. An experimental validation of the transitional turbulence model proposed by Abraham et al. [1] was performed for the first time for internal gas microflows.

2. The role of minor losses towards the evaluation of experimental frictional characteristics has been critically discussed for both microtubes and microchannels in the presence of compressible gas flows.

3. Effect of aspect ratio and inlet manifold shape on the laminar to turbulent transition in adiabatic rectangular microchannels is investigated both experimentally and numerically for a compressible fluid.

4. A new prototype of a double layer microchannel heat exchanger assembly has been fabricated. The effects of compressibility on the heat transfer between hot and cold fluids are highlighted using both experimental and numerical methods.

5. A novel computational methodology based on the modified Darcy-Forschiemmer law was developed for the thermal performance analysis of micro heat exchangers. It reduces the significant computational cost associated with modeling a large number of parallel microchannels typically employed in microchannel heat exchangers and micro heat sinks. The method has been validated against the experimental results obtained for a double layer microchannel heat exchanger.

1.2 Outline of the Dissertation

The current thesis has been divided into two parts. The first part deals with the fluid flow and heat transfer in single micro geometries with circular and rectangular cross sections. Experimental data reduction methodology and numerical model pertinent to single channel studies are first introduced in this part and later experimental and numerical investigations are reported.

Later in Part II of the thesis, experimental as well as numerical methodologies developed in Part I are further expanded to understand the hydro-thermal behavior of gas flows inside microchannel heat exchangers. A prototype double layer micro heat exchanger is built and experimentally investigated in different flow configurations. In parallel, local heat transfer within the fabricated micro heat exchanger is elaborated using a numerical model. Lastly, a hybrid computational methodology based on CFD and the porous medium is developed for the gas micro heat exchangers. The developed methodology is validated using the experimental results of a double layer micro heat exchanger available in the open literature.

Further outline of the chapters contained within these two parts are given as follows:

1. In Chapter 2, the state of the art in the gas microflows within the continuum regime is presented. Gas flow frictional characteristics from experimental and numerical studies have been presented in detail. Moreover, a summary of experimental and numerical results of forced convection using gas flow inside microchannels and microtubes available in the open literature has also been presented. Later a detailed review of most relevant experimental results obtained with double layer micro heat exchangers has been made.

2. In Chapter 3, an introduction to the experimental test rig used for the fluid flow and heat transfer experimental campaigns for single microtubes and microchannels is presented. A brief introduction of the used instrumentation is given to

the reader and experimental data reduction is outlined for the calculation of experimental friction factor and Nusselt number. Fabrication methodology of the rectangular microchannels and their surface roughness measurements are described. Furthermore, typical measuring uncertainties are also presented.

3. In Chapter 4, governing equations, computational domain and meshing strategy of the employed numerical model are explained. The solution procedure along with the boundary conditions are also presented in detail for both microtubes and microchannels. Validation studies against the experimental pressure drop in the case of adiabatic walls for both tested cross sections (circular and rectangular) are also discussed.

4. In Chapter 5, experimental as well as numerical fluid flow and heat transfer analyses of the microtubes are presented. The role of minor losses and their relative contribution to the total pressure drop for the microtubes is discussed in detail. Experimental results of forced convection in a microtube are further presented and challenges in correctly establishing the value of Nusselt number for compressible flow are described. A numerical parametric study is further carried out to see the effect of hydraulic diameter on the heat transfer characteristics of the gas microflows.

5. In Chapter 6, a combined experimental and numerical analysis on the frictional characteristics of the microchannel gas flow is conducted. Various data reduction methodologies available in the open literature for the establishment of the friction factor from pressure drop analysis of adiabatic gas microflows are compared and the best experimental strategy has been outlined. The role of the average gas temperature estimation between two axial pressure measurement taps is explained. A new equation for the estimation of friction factor for adiabatic gas microflows considering the integral average of temperature is presented.

6. In Chapter 7, laminar to turbulent flow transition in rectangular microchannels with gas flows is investigated. To this end, two campaigns where the effects of

aspect ratio and inlet manifold shape on the critical Reynolds number are experimentally pursued. Moreover, the capability of the previously used transitional turbulence RANS model was explored against the aforementioned experimental results. After validation with experimental results, a parametric study was carried out to decouple the effect of hydraulic diameter and aspect ratio on the laminar to turbulent flow transition.

7. In Chapter 8, an analysis of the thermal performance of a double layer micro heat exchanger is presented. The newly developed experimental test rig is described in detail. Experimental and numerical insights on the thermal performance of the double layer micro heat exchanger in both parallel flow and counterflow configurations are discussed.

8. In Chapter 9, a new methodology for the thermal performance evaluation based on the porous model approximation for a microchannel heat exchanger is proposed. The validation of the proposed methodology is performed using the experimental results of a double layer micro heat exchanger available in the open literature. The effect of manifolds' presence on thermal performance has been highlighted.

9. In Chapter 10, important findings from all the previous chapters have been presented. Limitations of the current work, as well as the future work recommendations, have also been highlighted.

Chapter 2

Literature Review

2.1 Fluid Flow and Heat Transfer of Gas Flows in Single Microchannels and Microtubes

A great interest in the investigations of gas flows inside very narrow channels is due to pioneering studies of Wu and Little. In their first study [4], they presented the frictional characteristics of a gas flow inside channels having width of 130 to 200 μm with heights of 30 to 60 μm made from lithographic techniques. Their results suggested that frictional characteristics of these gas flows inside microchannels (MCs) are very different than the conventional sized channels where they noted a significant increase in the friction factor for small sized MCs. They later conducted a thermal analysis to predict the heat transfer characteristics in the laminar as well as turbulent flow regimes [5]. Evaluated Nusselt number (Nu) in the transitional and turbulent flow regimes was slightly higher than the conventional sized channels for which they presented a correlation.

These investigation were followed by the gas flow analysis of Choi et al. [6] who tested gas flow inside circular microtubes (MTs) and found out that Nu in the laminar regime instead of being a constant value is a function of Re and also in the turbulent regime

is significantly higher than in conventional sized tubes/ducts.

Yu et al. [7] also studied the water and nitrogen gas flow inside MTs of 19, 52 and 102 μm for a Re in the range of 250 to almost 20,000. Frictional characteristics of water flow were lower than the conventional Poiseuille's law and Blasius law throughout the laminar and turbulent flow regimes, respectively but Nu followed a completely different trend. Based on their experimental results with water and nitrogen, they suggested correlations for Nu which again was increasing linearly in the laminar regime unlike macro channels. Correlation proposed by the Yu et al. [7] and Choi et al. [6] were in contrast with each other as highlighted by Rosa et al. [8], therefore have been under constant scrutiny since then.

A later investigation by Guo et al.[9, 10] revealed that compressibility effects induce an acceleration along the length of the microtube and therefore cause much distortion to the velocity profile. In summarizing the effects of compressibility Guo et al. [11] highlighted that additional pressure drop due to acceleration along the length of the MT does not only increases the magnitude of the velocity downstream but also the shape of the velocity profile which in turn does not let temperature profile to be developed as well. Due to increased velocity along the length, the heat produced due to viscous dissipation also starts becoming significant close to the walls which influences the heat transfer whereas due to the overall increase in the bulk velocity, the temperature of the gas also decreases significantly. They presented the ratio of radial viscous diffusion of momentum and axial acceleration in terms of their characteristic time which showed a dependence on the square of Mach number (Ma). They concluded that if $Ma << 1$, then this ratio is also close to zero signifying that the diffusion process is much faster than the acceleration and in that case, the velocity profile along the length stays parabolic just like incompressible fluids. And in the cases where this ratio is close to unity, acceleration process becomes the dominant process and axial velocity keeps changing magnitude and profile shape resulting in a never developing velocity and temperature profiles for the accelerating gas.

Numerical simulations were also performed by Du [12] where he found out that local Eckert number, which is defined as the ratio of advective mass transport and heat dissipation, just like local friction factor increases along the length of the tube when compressibility is significant. This causes therefore, a decrease in static temperature of the gas along the channel and at times may result in negative values of Nu if the compressibility effects become strong.

Asako et al. [13] performed numerical computation using Arbitrary Lagrangian Eulerian (ALE) code for the solution of compressible NS equations in parallel plates. The height between two parallel plates was varied between 10 μm to 100 μm for a wide range of inlet pressures to achieve low to high Mach numbers at the outlet of the parallel plate channels. Both adiabatic and isothermal wall conditions were simulated and the results showed that for Poiseuille's number Po (product of Fanning friction factor and Re) value differs from the theoretical value of 96 for the cases where Ma at the channel outlet is higher than 0.4. The difference between two different wall boundary conditions was within 2%. They calculated Darcy and Fanning friction factor in all the simulated cases and showed that both of these differ when compared to incompressible flows and recommended the correlation for the prediction of Fanning friction factor (f_f) as follows:

$$f_f = \frac{96}{Re} + \frac{1}{Re}\left(8.17Ma + 59.57Ma^2\right) \tag{2.1}$$

Kohl et al. [14] later investigated in detail the difference between the possible discrepancies that existed in the experimental evaluation of the friction factor using liquid and gas flows. They fabricated 5 MCs with a hydraulic diameter in the range of 25 to 100 μm with integrated pressure measuring ports. They used water and air as the working fluids in all of these channels where maximum Re for air was in between $\sim$5300 to $\sim$18000 whereas it was $\sim$114 to $\sim$2000 for water flows. Concerning the friction factor of the liquid flows, they found out that experimental results follow the classical Poiseuille's law in the laminar regime but start deviating due to developing flow length. If the effects of increased pressure due to developing flow are catered for, the results did

not show any significant variation from their macro counterparts. For the experiments with air as the working fluid, friction factor in the laminar regime was compared with numerically evaluated friction factor which catered for the increased acceleration due to density variation. The experimental friction factor for all the channels in the laminar regime was within the experimental uncertainty when compared against the numerical results but showed deviation from Blasius law for Re >2300. Surprisingly, MTs with hydraulic diameter less than 50μm showed compliance to the Blasius correlation in turbulent/transitional regime whereas MTs with a hydraulic diameter greater than 60μm were significantly lower than Blasius. They also noted that for gas flows, the transition to turbulent flow was delayed to higher values with respect to $Re = 2300$. Moreover, they also stated that critical Re increases with the decreasing length to diameter ratio of the MT. Moreover, for compressible flows, their measured local pressure readings showed a good match with numerically estimated values.

Hong et al. [15] further conducted the numerical simulations of compressible microflows using ALE code as proposed by Asako et al. [13]. As for their earlier study height of the channels was varied from 10 μm to 100 μm with both cooling and heating wall boundary conditions. Inlet stagnation pressure was varied such that Re stayed lower than 2300 i.e. in the laminar regime whereas rarefaction and compressibility effects were encountered through the range of pressure simulated. Due to a broader range of boundary conditions considered in this study, authors updated the previously proposed correlation [13] for the f_f as follows:

$$f_f = \frac{96}{Re} + \frac{1}{Re}\left(7.09Ma - 0.27Ma^2 + 94.02Ma^3\right) \tag{2.2}$$

The difference between the correlation rose from the numerical data processing for the calculation of Fanning friction factor f_f. In this study, it was calculated using the velocity gradients close to the wall whereas in [13] it was evaluated using the average cross sectional results at the inlet and outlet of flow field variables. The difference between the relations, however, was less than 4%.

Hong and Asako [16] also estimated the heat transfer for gas microflows with constant wall temperature boundary condition inside parallel plates for the same geometries considered in [15]. Under both cooling and heating boundary conditions, identical heat transfer coefficients were obtained for incompressible working fluids whereas they differed when the compressible gas was used as a working medium. They proposed a correlation to predict the heat transfer rate using the static temperature, dynamic temperature and a temperature ratio that they defined from their numerical data. The same authors also reported heat transfer characteristics of the micro gas flows under constant wall heat flux boundary condition in [17]. They concluded that for low speed gas flows heat transfer coefficients coincide with that of an incompressible fluid but as the gas speed increases and compressibility effects become significant, heat transfer coefficients varied depending upon the heating and cooling boundary condition. They also presented a correlation to predict the wall temperature of the channel carrying compressible gas flow based upon the incompressible wall temperature and fluid temperature ratio. Compressibility effects were found to be dominating than slip effects under the simulated conditions.

Morini et al. [18] performed pressure drop experiments in commercial stainless steel long microtubes with the hydraulic diameter ranging from 762 to 127 μm. Three different methods were employed to calculate the friction factor with varying Re and recommended that for the long microtubes the friction factor can better be calculated using isothermal flow assumption [19]. It was found that compressibility effects become quite significant for higher Re or smaller hydraulic diameters due to increased pressure drop which causes strong density variations of the gas along the length of the microtube. Using SEM imaging of the tested MTs, they recommended that for commercial microtubes the hydraulic diameter must be verified which may be different than the nominal value mentioned by the manufacturer. Their results of the friction factor in the laminar regime for all the tested microtubes followed the theoretical predictions in the laminar regime. Their results also showed no dependency of the varying length to diameter ratio on the laminar to turbulent transition.

A detailed experimental campaign to understand the effects of compressibility, surface roughness and rarefaction on the friction factor of gas flow was later conducted by Tang et al. [20]. They used both microtubes (circular) and microchannels (rectangular) geometries made from different materials and processes in order to obtain different values of surface roughness. The hydraulic diameter of the fused silica microtubes, fused silica microchannels, and stainless steel microtubes ranged from 50 to 201 μm, 52 to 100 μm and 119 to 300 μm, respectively. Using a wide range of hydraulic diameter and inlet mass flow conditions, they were able to decouple various scaling effects. For smooth microtubes and microchannels made of the fused silica MT having a relative surface roughness of less than 1%, the laminar friction factor was in close agreement with the conventional theory. For microtubes made from stainless steel, laminar as well as transitional friction factors were higher than Poiseuille's law and Blasius equation respectively. They attributed this increase to the increased surface roughness of the tubes which was measured to be 7 μm giving relative surface roughness in the range of 2.3 to 5.9 % for stainless steel microtubes. Therefore they recommended that for all the microtubes having relative surface roughness greater than 1% friction factor can not be estimated by conventional correlation. They also observed that by increasing Re, Po showed a positive increase due to compressibility. A trend of their experimental data matched well with the analytical correlation proposed by Guo et al. [11]. For the smooth tubes at lower Re they also observed a decrease in the values of Po lower than conventional values due to flow slip effects.

Celata et al. [21] performed pressure drop experiments using helium gas in fused silica microtubes having a hydraulic diameter of 30 - 254 μm. The experimental range of Re was concentrated on the lower laminar regime (Re <600). The absolute surface roughness was less than 0.05 μm for the tested microtubes. Authors showed that for the range of mass flows considered in their study, friction factor values were remarkably close to the theoretical predictions and hence no effect of compressibility and rarefaction could be observed if the experimental uncertainty is catered for. This was followed by an experimental study conducted by Celata et al. [22] in the laminar, transitional and

turbulent flow regimes for the fused silica microtubes considered in [21]. By increasing the tested Re compared to [21] for the small diameters microtubes, an increase in friction factor above the Poiseuille's law is noticed for Re >1000 due to compressibility effects and the associated increased speed of gas flow. The authors also compared the experimental results for the same microtubes at another experimental facility [18] using nitrogen gas flow. Results from two different test rigs showed an excellent agreement where both showed compliance of friction factor with the conventional law for the lower laminar regime. Due to an increased Ma of the flow at the exit of the microtubes, there was an increase in the friction factor above the macro scale towards the higher end of the laminar flow regime. Authors concluded that for the rough microtubes, the Colebrook-White equation can not predict the transitional friction factor as their experimental data did not show any variation with increasing Re and rather stayed constant.

An experimental campaign to investigate the compressibility effects and flow transition was also conducted by Vijaylakshmi et al. [23] inside trapezoidal microchannels with a hydraulic diameter of 60.5 to 211 μm. They investigated nitrogen gas flow inside smooth channels that were etched in silicon with surface roughness from 75 to 109 nm. Local pressure readings were also taken at 3 axial locations along the length of the microchannel. They deduced the experimental friction factors using the equation employed by Kohl et al. [14]. With their experimental and numerical results, the authors highlighted that if significant compressibility effects are correctly catered for, the laminar friction factor follows the macro law until $Ma \leq$0.3 at the outlet of the channel. As soon as it is higher than this value, an increase in friction factor is observed which should not be confused with laminar to turbulent transition. Values of friction factor in the turbulent regime for all the microchannels that they tested were lower than Blasius law, however. The decrease below the Blasius correlation was significant with the decrease in the hydraulic diameter of the trapezoidal microchannels investigated.

Lorenzini et al. [24] conducted a comparison of experimental isothermal friction factor for smooth and rough microtubes in the laminar, transitional and turbulent flow regi-

mes. Commercial microtubes manufactured using fused silica and stainless steel were used having hydraulic diameters in the ranges of 20 to 100 μm and 250 to 500 μm respectively. SEM images revealed that fused silica microtubes were smooth whereas stainless steel ones had a roughness of 3-4 μm. They again noticed that friction factor results were in accordance with the conventional macro law for both smooth and rough walled microtubes in the laminar regime deviating only when the flow compressibility becomes dominant i.e Ma >0.3 at the outlet.

Murakami et al. [25] performed numerical computations using ALE solver [13] to estimate the friction factor of compressible gas flows in laminar as well as turbulent regimes. The focus was given to the turbulent regime which had not been computationally investigated much until this point. By extending the outlet domain further downstream the exit of the microtube they were able to simulate the flow choking where flow stagnates at a maximum value of Ma. Their analysis showed that the Fanning friction factor matches with Blasius correlation for fully turbulent flow regimes and does not depend on the Ma as was the case with the laminar flow regime.

Hong et al. [26] performed experimental investigations on the heat transfer characteristics of three microtubes in laminar and transitional flow regimes. Hydraulic diameters of the tubes were 123 μm, 163 μm and 243 μm with a constant length of 50 mm. Nitrogen gas flow was used and the temperature of the microtube wall was maintained at the desired value using a custom made water jacket mounted around the microtube. The outlet temperature of the gas exiting from the microtube was measured after letting it pass through a sponge to recover the kinetic energy into thermal energy. By varying the inlet stagnation pressure and wall temperature they measured the total temperature of the gas due to effects of additional acceleration and compared it against the numerical simulation performed earlier [15]. For high speed flows (Ma >0.3) the total temperature of the gas is higher than the stagnation temperature considering the incompressible flow due to additional heat exchange between the wall and fluid linked to an increase in flow kinetic energy close to the outlet of the microtube. They validated

their proposed correlation [15] for the prediction of gas total temperature at the outlet of microtube using the bulk temperature of incompressible flow, recovery ratio and the dynamic temperature. However, no comparison of the evaluated Nu was provided with conventional correlations.

Hong et al. [27] also experimentally investigated the fluid flow behavior inside rectangular microchannels by measuring the local pressure of the gas flow inside the channels in the axial direction. By using the measured pressure at the local ports along the length of the microchannel, they established the Fanning friction factor between two consecutive pressure ports and referred it as semi local friction factor. Hydraulic diameters ranged from 69-148 μm whereas the aspect ratio of the microchannels was in the range of 0.036 to 0.078. Inlet stagnation pressure was varied such that gas flow experienced laminar, transitional and turbulent flow regimes in all the microchannels tested. For the calculation of the semi local friction factors, an isothermal behavior of the gas was assumed inside the microchannels. Values of semi-local Fanning friction factor in the laminar regime were slightly higher than macro scale prediction as the flow velocity (Re) increased due to the flow compressibility whereas in the turbulent regime they coincided with the Blasius correlation given the measurement uncertainty. They were able to validate the correlation proposed by their group earlier [15] based on the numerical study which showed that Po in the laminar regime for compressible flows was not constant and varied with the outlet Ma.

Yang et al. [28] performed the pressure drop and forced convection in microtubes with air as a working medium. Hydraulic diameters of the microtubes were from 86- 920 μm. Considering the compressibility effects and utilizing the correlation of friction factor proposed by Shapiro [19] they showed that experimental frictional characteristics follow the conventional laws in the laminar as well as in the turbulent regimes. They further heated up the microtube wall using DC power and measured the surface temperature of the microtube by coating the wall with thermographic liquid crystals (TLCs). In this way, they were able to reconstruct the local variation of the wall temperature along

the length of the microtube. They further estimated the heat losses for each microtube and considered these in the data reduction. Heat convection results with air showed that for all the microtubes tested, Nu follows the conventional correlations and no new micro effects were observed in laminar, transitional and turbulent flow regimes. Due to ongoing flow development (acceleration), Nu was higher in transitional regimes but matched well within experimental uncertainty with the Gnielinski's correlation [29].

Yang et al. [30] conducted experiments using nitrogen gas in three microtubes with hydraulic diameters of 750 μm, 510 μm and 170 μm. They used Joule's heating effect and applied a wall heat flux at the wall of the stainless steel microtube. Temperatures at the outlet were measured in an expansion chamber attached after the outlet of the microtube in order to recover the kinetic energy of fast exiting gas from the microtube outlet. Thermocouples were attached to the external wall of the microtube and gas temperature near the wall was estimated to be almost equal to this measured temperature. A numerical model was also utilized in order to extract the correct distribution of the axial bulk temperature of the gas which was found to be non-linear in the laminar regime due to the axial wall conduction for their specific experimental conditions. It was shown that if nonlinear bulk temperature estimated from the numerical model was considered for the experimental data reduction, Nu of gas flows in the laminar regime becomes close to theoretical predictions of a constant Nu in the laminar regime. On the other hand, if the variation of axial bulk temperature of the gas is considered to be linear as for the incompressible flows, a linear trend and lower values of the Nu were obtained in the lower laminar regime pointing out the wrong conclusions drawn in the previous investigations [6].

Yang et al. [31] also conducted coupled experimental and numerical investigations on the evaluation of Nu with nitrogen in the turbulent flow regime for the same microtubes that were used earlier in [30]. Due to an increased Ma of the gas at the outlet of microtube, total temperature, and recovery coefficients were used to estimate the Nu. They found out that for the microtubes of 750 μm and 510 μm, evaluated Nu coincided

well with the Gnielinski's correlation but it was significantly higher for the smallest microtube (170 μm) tested. Moreover Nu for the smallest tube followed the correlation of Choi et al. [6] in the turbulent regime.

Kawashima and Asako [32] later proposed a new equation to predict the axial temperature of the gas along the microtube length for adiabatic gas flows. Until this point in the literature, experimental friction factor evaluation for the gas flows in the microtubes/ microchannels had been done using an isothermal gas assumption. Using the total temperature definition they derived a quadratic equation that can be used to estimate the gas temperature at any cross section given that there is no heat transfer from the walls. It was validated using a 2D numerical simulation of the NS equations. This further updated the data reduction for the friction factor evaluation of adiabatic gas flows from the experimental results considering a temperature decrease from the inlet to the outlet.

Hong et al. [33] then experimentally investigated the frictional characteristics of the nitrogen gas flow inside rectangular microchannels made in silicon by etching. The tested microchannels had a hydraulic diameter of 146 μm and 203 μm. Similar experimental setup and measurements were used as of their earlier study of the microchannels [27]. Using the new data reduction methodology proposed by Kawashima et al. [32], they found out that when the temperature decrease of the gas from one axial cross section to the other due to flow acceleration is catered, and the resulting friction factor in highly turbulent regime coincides better with the Blasius law. On the contrary, it is lower than the Blasius law if the isothermal gas temperature assumption is pursued.

Kawashima and Asako [34] also conducted experimental investigations on the semi local friction factors in a PEEK microtube with a hydraulic diameter of 512 μm. They used nitrogen gas as the working fluid and found out that experimental semi local friction factors are 15-20 %higher than Blasius correlation in the turbulent flow regime. They also performed numerical simulations using the experimental boundary conditions and tube diameter where the friction factor was found to be in accordance with the Blasius

relation. They associated the increased pressure drop to the roughness and burrs caused by the drilling of static pressure holes which was not the case of EDM machined microtube tested by Hong et al. [35].

Kawashima et al. [36] performed numerical investigations for the laminar and turbulent nitrogen gas flows inside microtubes in order to investigate the choked gas flows. The tube diameter was varied in the range of 50-500 μm and the outlet of the computational domain was extended to allow for any underexpansion at the microtube outlet. It was noted that Ma at the outlet of the microtube was higher than 1 (in the range of 1.16 to 1.25) depending on the microtube diameter. They also proposed a correlation to estimate the choked Ma of gas flow based on the hydraulic diameter of the microtube. Flow choking and associated Ma was later experimentally analyzed by Hong et al. [37]. They placed a needle close to the exit of the microtube to visualize shock waves by using Shadowgraph and Schlieren methods. Pressure and Ma of the underexpanded jet at the microtube outlet were calculated based on the angle formed by the shock wave. The numerical results and experimental results were in an excellent agreement where choking Ma increased with a decrease in hydraulic diameter as it was concluded in [36].

Recently, numerical investigations were further conducted by Hong et al. [38] for microtubes having hydraulic diameters of 10-500 μm having two different length to diameter ratios of 100 and 200. They validated their numerical model with the experimental results of 397 μm smooth glass tube where local pressure, temperature and Ma measurements were in excellent agreement with the numerical model predictions. Their numerical parametric study showed that even in the choked flow regime, the local Fanning friction factor evaluated from wall shear stress followed the Blasius correlation in the turbulent regime as well as in the choked flow regime. Similar to the previous studies it was noted that choked Ma increases with the decrease of the hydraulic diameter. For the same Re, the choked and unchoked Ma at the outlet of the tube stay are identical for microtubes having the same hydraulic diameter but different lengths. In

other words, the length to diameter ratio did not affect the outlet Ma of the microtube if the mass flow at the inlet is the same.

Experimental as well as numerical gas flow studies in microchannels and microtubes that are available in the open literature are summarized above. It can be said that if compressibility is correctly catered for in the experimental results, frictional characteristics of the gas flows inside microtubes/microchannels can be described well by the macro laws in both laminar as well as turbulent flow regimes. Local pressure measurements and new data reduction methodologies have helped to attain the uniformity in the experimental as well as numerical results of gas microflows that appeared in the current decade. Heat transfer characteristics, on the other hand, are still not fully explored. Experimental results of a few studies predict significantly higher Nu for smaller diameter microtubes (e.g. [6, 31]) whereas it is found to be following the conventional correlations as in [28]. Therefore further research in the field of forced convection in microtubes when gas flows are used is needed using both experimental as well as numerical methods. Flow choking is another phenomenon that has been quite recently established in underexpanded microjets where only a few experimental studies have tackled this problem. However, there are a good number of numerical investigations that have appeared in this regard. Effect of the choking on the frictional as well as heat transfer characteristics is still not fully explored and therefore should also be pursued by the scientific community.

2.2 Laminar to Turbulent Flow Transition

Laminar to turbulent flow transition inside microchannels has been debated since earlier studies of Wu et al. [4, 5, 6, 39] which reported an anticipated transition to the turbulent regime at critical Reynolds (Re_c) of 900. In the same period, few groups [40, 41] reported the conformance to the macro scale theory. Recent reviews [42, 43] however conclude that experimental data obtained in the recent decade establishes

that single phase fluids in microchannels and microtubes follow conventional macro laws. A comprehensive review outlining possible reasons for deviations from macro theory in earlier reported experiments is due to Morini et al. [44], according to which macro theory is applicable to MC flows if scaling effects are negligible. It also details various scaling effects that need to be ascertained before interpreting experimental results which may cause deviation from conventional correlations. In another work Morini [3] gathered previously published experimental data for laminar to turbulent flow transition in MCs and compared it with macro laws. The analysis showed that various published results for critical Reynolds number (Re_c) are in accordance with Obot-Jones model developed for conventional sized channels.

Starting with Osborne Reynolds [45] more than a century ago, turbulent transition within wall bounded flows has been investigated mainly through experimental observations. Similarly, flow visualization, as well as pressure drop studies, have been utilized to observe Re_c of microflows. For liquid flows, μPIV studies were conducted by Li and Olsen [46]. They tested four MCs with the almost same hydraulic diameter (D_h) with aspect ratios (α), which is the ratio of MC height and width, between $0.2 - 1$. They found that Re_c increased from 1715 to 2315 by decreasing the aspect ratio from 1 to 0.2. Similar experimentation was also performed by Wibel and Ehrhard [47] where they reported that an increase in Re_c from 1600 to 2200 is observed for a decrease in the aspect ratio from 1 to 0.2. Both studies showed conformance with macro scale results. More recently Kim [48] presented experimental results of fluid flow and heat transfer for 10 chips containing 10 parallel microchannels each. The critical Reynolds number increased from 1700 to 2400 with a decrease in the aspect ratio from 1 to 0.25. Unlike the previous μPIV studies, microchannel dimensions are changed such that the aspect ratio and hydraulic diameter varied simultaneously. Due to a relatively higher density of seeding particles, μPIV cannot be applied to gas flows in MCs and therefore a pressure drop study (Moody chart) remains the only dispensable tool to observe turbulent transition. Such analysis for gas flows in 11 different microtubes with a diameter of 125-180 μm has been presented by Morini et al. [49]. By comparing their results

with previously published gas flow pressure drop studies, it was shown that if friction factor is calculated by taking into account compressibility effects and minor losses, Re_c was in between 1800-2000, contrary to anticipated transitions reported by other groups [4, 50]. An analytical study based on energy gradient that deals with the current subject, is reported by Chang at al. [51]. Based on their analysis it was shown that in a rectangular channel the shorter side dictates the transition. Moreover, a correlation was also provided to predict Re_c as a function of aspect ratio for rectangular MCs.

Although there had been a debate in the open literature about the anticipated transition in the earlier studies, the most recent experimental investigations appearing in the literature by vast majority confirm that transition to turbulent flow happens in between Re of 1800-3000 [14, 20, 18, 52, 21, 22, 23, 24, 27, 33]. For microchannels, it is dependent on the geometry of the channel where aspect ratio affects the transition. No systematic investigations for laminar to turbulent transition in rectangular microchannels with gas microflows exist in the literature and therefore should be pursued further to contribute to this field.

2.3 Micro Heat Exchangers

Energy dissipation has a significant potential for the innovation including microelectronics and High Performance Computing (HPC) systems and to meet the requirements of the electronic industry, compact and micro heat exchangers (μHxs) have been of interest due to their potential high volumetric heat transfer rates and compactness. Due to the extensive nature of the subject matter, only the most relevant studies pertinent to micro heat exchangers are reviewed here.

Bier et al. [53] tested with a cross flow μHx with N_2 He and Ar as working fluids at constant solid wall temperature. They reported a volumetric thermal power of 18,000 MW/m^3 can be achieved with an overall heat transfer coefficient of 20 kW/m^2K.

Three liquid to gas cross flow heat exchangers made in PMMA, ceramic and aluminum were fabricated using LIGA manufacturing methodology by Harris et al. [54]. The initial goal was to design a μHx for the replacement of a conventional car radiator. Under the given design constraints, the manufactured cross flow μHxs did not match with the comparative conventional car radiator in terms of heat transfer per frontal area. However, it was shown that the heat transfer rate per unit volume of the cooling fluid is much higher for μHxs than the existing radiator. Values of volumetric heat transfer using PMMA and aluminum μHx were 3.7 and 6.6 times higher when compared to the conventional radiator value (33.3W/cm^3). Harris et al. [55] also fabricated nickel cross flow μHx by embossing a sacrificial polymer using LIGA fabricated inserts. Nickel was coated on the mandrel and later this sacrificial layer of the mandrel was dissolved. Experiments were conducted using water (hot fluid) towards one side and air on the other side as a coolant. Results in terms of pressure drop and temperature differences on the hot and cold sides were measured and compared against the empirical model developed using the results of the previous study [54]. They obtained similar findings where volumetric heat transfer rates of the tested μHxs were significantly higher than the conventional radiator.

Fabrication and performance evaluation of various microstructured devices fabricated at KIT were also presented by Schubert et al. [56]. Amongst these devices were cross-flow and counterflow μHxs that were fabricated by micromachining the metallic foils with microchannels or microcolumns. These foils were then stacked together and joined using diffusion bonding and furthermore welded to the housing. Using water as the test fluid, overall heat transfer coefficients of 54 kW/m^2 were measured with a 7t/hour throughput. Performance evaluation and geometric characteristics of these heat exchangers were further presented by Brandner et al. [57]. Microchannels with three different hydraulic diameters of 70, 133 and 144 μm were realized to see the effect of reducing hydraulic diameter on the thermal performance. They showed that by reducing the diameter of the channels, a substantial gain in the heat transfer rates have been attained when deionized water was used as the test fluid. By reducing the hydraulic

diameter from 170 μm to 140 μm, an increase of $\sim$60% was observed in the values of heat transfer rate (thermal power). Pressure drop and heat transfer characteristics were in line with the conventional theory due to lower Re investigated in the study when conventional MCs were employed. However, to disturb the thermal boundary layer in the lower Re regime, MCs were replaced by microcolumns (80 μm$\times$150 μ) in both aligned and staggered configurations. Thermal power achieved from the staggered arrangement was the highest followed by the aligned microcolumns layout, however, both of them showed superior heat transfer performance than straight MCs. Nonetheless, an increase in thermal power in these μHxs also resulted in an increased pressure drop compared to straight MCs layout and therefore it was recommended to find a tradeoff based on the application objectives. Authors also presented an industrial application where the manufactured heat exchangers were utilized and pointed out that further understanding of the process and design parameters needs to be made for scaling of this technology.

Just what has been investigated by Brandner et al. [57], multitudes of passive heat transfer augmentation techniques can be found in the open literature. Detailed reviews about the active, as well as passive heat transfer enhancement at the microscale, can be found in [58, 59]. An interesting design where instead of simple microcolumns, S-shape pertubators were employed in a layered compact heat exchanger, was presented by Nikitin et al. [60]. Experimental results where supercritical CO_2 is used as working fluid, S-shape printed circuit heat exchanger (PCHE) showed better performance than usual plate heat exchanger with volumetric thermal power of 4.4 MW/m^3. Alongside the experimental loop, simple 2D numerical calculations using a commercial CFD solver were also performed in order to estimate the heat losses from hot and cold loops of the device. Heat losses from experiments and numerical results were found to be in agreement where these losses were compensated by adding strap heaters over the surface of insulation material. Using the compensated outlet temperatures they found the overall heat transfer coefficient to be varying from 300 W/m^2K to 600 W/m^2K by changing the mass flow from 42 kg/h to 85 kg/h. A detailed 3D CFD study of

these PCHE with S-shaped pertubators used on the water side instead of CO_2 loop was presented by Ngo et al. [61]. PCHE was tested in the heat recovery experimental setup where water was heated up from 7 ^oC to 90 ^oC by exchanging heat from supercritical CO_2 at 118 ^oC. In comparison with the conventional residential hot water supplier in use, the volumetric thermal power of PCHE was 3.3 times higher. It also resulted in a ten times smaller pressure drop. A numerical study was later conducted by Utamura [62] to compare the experimental and numerical results from the printed circuit S-shaped μHx and found a good agreement between numerical and experimental results (within 5%).

Tsuzuki et al. [63] later performed numerical investigations on the optimum size and angle of these S-shaped pertubators to be used in the recuperators of CO_2 gas turbine cycles. In the conventional PCHE zigzag shaped channels enhance the heat transfer due to flow separation and eddies at the corners while adding discontinuous S-shaped pertubators reduced the pressure drop to 1/5 of the value with respect to the conventional PCHE. This reduction of pressure was attributed to the optimum incidence angle (52^o) which did not exhibit any eddies and guaranteed the same thermal performance with much less pressure drop. Implementation of these pertubators in a μHx was later done by Tsuzuki et al. [64] by chemically etching these patterns on the metallic sheets. Again utilizing 3D CFD studies they developed the correlations for the prediction of Nu for these μHxs. Experimental testing with water as working fluid in counterflow configuration showed only 5% deviation from the correlations developed using numerical analysis. Turbulent structures were found to be present even at Re of 1500 which generally is in the laminar flow regime. The authors concluded that the performance of μHxs with complex geometries can be estimated well with the CFD.

Three prototype μHxs made from a ceramic material (alumina) were fabricated and tested by Alm et al. [65]. Experimental studies of heat transfer and pressure drop were performed on the two counterflow and one crossflow μHxs. Each μHx had 17 MCs per alumina plate with length and width of MCs to be 12.5 mm and 250 μm respectively.

The height of the MCs varied from one μHx to the other but was in between 320 μm to 420 μm giving the average hydraulic diameter to be in the range of 280 μm to 313 μm for all the tested μHxs. Except for one counterflow μHx which had 3 layers of each hot and cold fluid, the other two had two layers per side. Deionized water was used as a working fluid on both hot and cold sides. For the maximum water flow rate of 120kg/h tested under balanced flow conditions, the counterflow μHx with 3 layers per side resulted in the highest thermal efficiency, which is the ratio of actual heat power transferred to the maximum possible, of 0.22 compared to 0.18 and 0.19 for the other two. Theoretical calculation where only a single channel was considered resulted in lower estimations than the experimental results of heat exchange thermal efficiency. They associated this increase in pressure drop and thermal performance of the complete μHx to the channel blockage effect encountered due to imperfect manufacturing of the device. They further compared their experimental results with the porous body detailed numerical simulations and found out that the heat transfer estimated by the porous model is lower than the experimental results using ceramic μHxs due to the same channel blockage effects that are nearly impossible to cater in the numerical model.

Two double layer (one for each fluid side) μHxs were also experimentally analyzed by Garcia et al. [66] with water as testing fluid. The hydraulic diameters of the square MCs were 100 μm and 200 μm and they were machined in 4mm thick stainless steel plates. Based on the available pressure, water mass flow was varied such that Re was in the range of 20 to 1600 in the hot fluid side and 20 to 1200 on the cold fluid side. Both devices were tested under balanced conditions and counterflow configuration. They achieved heat transfer coefficients of $\sim$5 kW/m^2K in the μHx with 100 μm MCs and sightly higher values for the 200 μm MCs prototype. On comparison of the average heat exchanger effectiveness with the conventional ε-NTU theory, no deviations were found and it was concluded that conventional correlations developed for macro heat exchangers shall be valid on the μHxs without any surprising scaling effects. They further highlighted that plate conduction is a major restriction for μHxs performance

and plate thickness and material are critical for the design of such devices.

The effect of multiple fluid layers on the heat exchange effectiveness for μHxs was experimentally investigated by Cao at al. [67]. They fabricated μHxs with three different MC dimensions where the first μHx was just two stainless steel plates separated with a gap of 197 μm giving a single channel with the width of 45 mm and hydraulic diameter of 392 μm. Two other μHxs where the number of MCs was 19 and 49 with hydraulic diameters of 360 μm (2122 μm$\times$197 μm) and 301 μm (639 μm$\times$197 μm) respectively, were also fabricated. The length of the MCs was kept fixed at 30 mm. Moreover, to check the performance variation with the number of plates or layers, they also fabricated the previously described μHxs with 10 layers in each case. MCs were chemically etched on the stainless steel plates and layers were subsequently joined by diffusion bonding technique. Experiments were performed with water as the working fluid in counterflow configurations in all six manufactured μHxs. Balanced conditions on both hot and cold sides were maintained where the volume flow rate was varied from 20 mL/vmin to 80mL/min in the steps of 10mL/min. Corresponding Re varied in the range of 15 to 65 and volumetric thermal power of 2-5 kW/m^{2}K was observed. While comparing heat exchanger effectiveness between μHxs with different hydraulic diameters, almost similar values were found out for all three sizes of MCs with no significant variation. This meant that heat transfer achieved using one single MC (360μm) has a similar performance than the other two designs with 19 and 49 MCs in each layer. Since they measured water temperatures at the inlet and outlet of the whole device, therefore an estimation of the heat exchange only inside MCs was not possible. They associated the effectiveness independence between tested μHxs to the presence of manifolds. Using the results of double layered (1 layer for hot and cold flows each) μHxs, they developed correlations for the estimation of pressure drop and thermal performance of multilayered μHxs. They further conducted experiments with 10 layered μHxs and compared their results with previously developed correlations from 2 layer models. At the maximum mass flow of 4.8 t/hr, the pressure drop of 10 layer μHx estimated from the correlations was lower than the experimental results. To understand

the ambiguity they conducted an experimental pressure drop study on a single layer made from PMMA and found out that pressure drop of a single layer was 3.5 times less than the double layer μHx. They associated these discrepancies with inefficient fabrication processes and estimated that 64-72% of total pressure drop is associated to the combining and dividing manifolds.

The same authors of the above mentioned study also conducted the thermal hydraulic performance evaluation of four different cross flow μHxs having different hydraulic diameters and number of layers [68]. In comparison to the study conducted in counterflow configurations [67], they changed the manifold design and adopted a rectangular manifold design instead of trapezoidal in their previous study. In addition to the dimensions already discussed in their previous study [67], they also manufactured μHx having a hydraulic diameter of 342 μm (1194 μm$\times$200 μm) for both 2 layers and 10 layers models. Performance investigations for these μHxs were made using water and air as working fluids. At the maximum Re of 65 with water as the working fluid, the maximum pressure drop was lower than 6kPa which is much less compared to the values reported for the counterflow configuration in [67]. They developed correlations for Nu for both fluids where there has been a linear increasing trend of Nu with Re for both fluids. Using the experimental results of 2 layers model they further predicted the performance of hot air to cold water μHx by fixing the hot air volume flow rate to 20 L/min and varying the cold water volume flow rate in the range of 30-80 mL/min. Heat exchanger effectiveness greater than 0.9 was estimated which were later confirmed by the experiments at the same flow conditions. Furthermore, they also predicted the performance of 10 layered μHx using the developed correlations from 2 layer experimental data, for water as working fluid on both sides. The difference between the predicted and experimental temperature difference was less than 1.8 K and therefore they concluded that correlations for Nu developed from the 2 layers model can be safely used in order to predict the performance of multi layered cross flow μHxs.

Experimental as well as a numerical study of another double layer μHx made from

Aluminium was performed by Dang et al. [69]. They made two layers having 10 MCs each with a hydraulic diameter of 375 μm with a constant channel length of 32 mm. Hot and cold water entered perpendicularly into rectangular manifolds in counterflow configuration. Under the unbalanced mass flow conditions from hot and cold sides, they achieved the highest performance. In parallel, they also setup a complete 3D model for the μHx to estimate the losses to the surroundings as well as the fluid flow behavior inside the MCs. Experimental and numerical results showed a good agreement where the maximum error was less than 9%. Moreover, the conventional ε-NTU method has been found applicable in their μHx. To compare the performance of plate thickness (wall conjugate effects) and the flow configuration Dang & Ten [70] also undertook an experimental campaign. They changed the thickness of the layer on which MCs were micromachined and found no influence on the heat exchanger effectiveness in the counterflow configuration. In another study, Dang & Ten [71] compared the thermal hydraulic performance of a μHx with a mini channel heat exchanger. Under the same average velocities used for the two heat exchangers, the effectiveness of μHx was 1.2–1.53 times of that measured for the mini channel heat exchanger, however again with higher pressure drops in case of μHx.

An attempt to study numerically the heat transfer characteristics of gas to gas double layer μHxs was performed by Miwa et al. [72]. As it is the norm in macroscale heat exchangers heat transfer contribution due to the partition wall were neglected and consequently, the two fluid streams were not separated by any solid wall. The height of the MC was varied within 10–100μm with two different lengths of 12.7 mm and 25.4 mm. Performance analysis was evaluated for the four different mass flow cases which signified low speed flows in both hot and cold sides, high speed flows in both sides, high speed on the cold side and slow speed on the hot side as well as high speed flow on the hot side and slow moving flow on the cold side. For all four mass flow cases, both parallel flow and counterflow configurations were studied. For all the heights considered except for 100 μm, a temperature inversion at the outlet of the MC was observed when Re from the hot side was very high as compared to the cold side. Temperature inversion

where outlet temperature of the hot side decreases the outlet temperature of the cold side was observed due to kinetic energy of the gas which becomes significant at high values of the exit Mach number which in their case was 0.622 and 0.08 at the exits of hot and cold gas sides respectively. Similarly, temperature inversions were also observed in the case of counterflow configurations where the total bulk temperature of the gas at the cold outlet became greater than total inlet temperature at the hot inlet and vice versa, Effectiveness becomes greater than unity when such inversion occurs. For unbalanced flow conditions, average thermal conductivity evaluated using the total temperatures instead of the static ones can be predicted using conventional theory.

Another μHx with gas as working fluid on both hot and cold sides was tested by Koyama & Asako [73] in a counterflow configuration. A single layer contained 34 MCs with hydraulic diameter of 240 μm ((300 μm$\times$200 μm)) and the length of 35 mm. A total of 20 layers (10 for each of the hot and cold sides) were stacked together and bolted to make a counterflow μHx. Air was used as the working fluid and due to limited pressure of the source, their investigations were limited to volume flow rates of 5-15L/min that translate into a Re range of 63.5–191. Therefore gas flow can be considered to be in the pure laminar regime. Experimental results showed that the pressure drop estimated using the theoretical framework that included minor losses in the manifolds and bends was 10 times less than the experimental values. The reasons were associated with the pressure drops in pressure ports, manifolds as well as flow maldistribution between and within the layers. Heat transfer rate estimations performed assuming the conventional LMTD method and laminar Nu from the literature were lower than the experimentally measured values. They further associated this additional heat transfer with the thickness of the wall and proposed a model that assumes a constant wall temperature boundary condition at the thick partition foil. Using this method, the estimated heat rates were in good agreement with the experimental results. A volumetric heat rate of 10.4 MW/m^3 was measured for their counterflow μHx.

Koyama and Asako [74] also conducted experimental investigations for thermal per-

formance evaluation of a parallel flow μHx. Geometry and design of μHx were similar to the one in [73]. Again they used air as the working fluid and the obtained pressure drops were 10 times higher than the theoretical prediction. They applied the constant wall temperature model developed in their previous study of counterflow configuration [73] and found out that the conventional Logarithmic mean temperature difference (LMTD) method predicts the heat transfer better than their proposed model of the previous study. They concluded that heat transfer performance in the range of evaluated Re was highly dependent on the flow configuration where it can be employed in the parallel flow configuration but cannot be applied in the counterflow configuration in which case constant wall temperature model will predict better.

In order to see the effect of thermal conductivity and thickness of the partition foil on the thermal performance evaluation of a μHx, Koyama et al. [75] performed numerical simulations using ALE simulation code previously utilized by Miwa et al. [72]. The thickness of the foil that was assumed to be made of the stainless steel was varied from 200 μm to 6μm where channel height was fixed at 100μm. Due to 2D nature of the solver width of the MC was not considered in the study. Air flow was assumed to vary in the laminar and turbulent regimes although the same laminar solver was utilized for all the calculations. Numerical simulations revealed that by increasing the thickness of the partition foil, the effectiveness of the μHx decreases. Moreover by adopting the geometry of the MCs encountered in their earlier experimental study [73], numerical simulations of a single channel and a thick partition foil showed that indeed partition wall assumes a constant wall temperature and hence authors justified their assumption in the experimental analysis of [73].

A CFD model based experimental design of a ceramic (94% alumina) μHx was presented by Kee et al. [76]. The heat exchanger was realized using 4 layers, 2 for each hot and cold fluids having 10 MCs with a hydraulic diameter of 919 μm. In order to enhance the convective mixing, MCs were truncated at three locations along the axial length. Channels were made in an alumina ceramic sheet having a thickness of

approximately 600 μm. Air was used as the working medium on both sides of the μHx with inlet temperatures of 700 ^oC and the room temperature for hot and cold sides respectively. They used the CFD model in order to tune the design parameters and estimate the pressure drop using the laminar flow solver. Experimental results showed some losses between hot and cold sides of the μHx however they were always less than 5% than the total heat transferred from the hot fluid to the cold fluid. For their results presentation, they always used the heat transfer as evaluated from the cold side. Effect of thermal conductivity of the separation foil was also conducted using the estimation model and they concluded that for their design point which refers to a small NTU value of 0.96, axial wall conduction did not have a strong influence on the effectiveness. The pressure drop of the μHx was measured for the air at the room temperature and was found to be in agreement with the CFD model except at the higher end of the mass flows tested. This discrepancy was associated to the laminar to turbulent transition. In the experimental campaign with hot gases, the pressure drop was not measured. Thermal effectiveness was investigated for balanced and unbalanced flows. Although the conducted study was a great attempt in demonstrating the feasibility and performance evaluation of the ceramic μHx, however no comparisons with the theory were made in particular. Due to the industrial nature of the work presented, no comparisons in terms of non dimensional numbers were made which makes it difficult to be compared against the performance of another μHx.

The analytical design and testing of another water to air crossflow μHx was presented by Nacke et al. [77]. They fabricated the MCs on a stainless steel plate using a SAW blade that was 254 μm thick giving the width of the MC. The cut was made 762 μm deep giving the MCs a hydraulic diameter of 381 μm. Water was used as the hot fluid inside these MCs where the air was flown over the fins attached to the external surface metallic sheet containing MCs. There were a total of 65 rows of external fins each containing 7 fins. Fin height varied from 635μm at the high side to 127μm on the lower side giving the forming angle of 2.29^o with respect to the surface of the plate containing MCs. In parallel, an analytical model based on the conventional heat ex-

changer design, thermal resistance design, and fin efficiencies, was pursued to compare the experimental prototype results with this model. Experiments were performed for the range of unbalanced flow conditions and various water inlet temperatures. The comparison showed that the analytical model can predict the behavior of such micro sized plate fin heat exchanger in the crossflow configurations and hence showed a good match between outlet temperatures and heat transfer on both water and air sides.

Yang et al. [78] numerically investigated the effect of flow configuration that guaranteed the lowest mass flow maldistribution. Using CFD they modeled a complete layer of a double layer μHx containing 133 parallel square MCs having a hydraulic diameter of 200 μm. With different feeding pressures at the inlet of distributing manifold, they found out that designed μHx showed minimum maldistribution above feeding pressure of 250kPa. They also investigated the effect of thermal conductivity on the thermal performance of the μHx by comparing the existing literature in terms of the axial conduction parameter as defined by Maranzana et al. [79]. They found out that most of the experimental studies used the MC material such that the axial conduction parameter was significantly high affecting the experimental results. They recommended that for gas flows thermal conductivity of the solid material is important to be considered because, with the high thermally conductive material, heat transfer effectiveness becomes independent of the flow configuration.

A similar study on the manifold design optimization using the CFD for a crossflow μHx was also conducted by Alvarez et al. [80]. They conducted computational comparison at Re of 44 and out of four candidate manifold design configurations they selected the configuration that ensured the minimum maldistribution for the given inlet direction which was perpendicular to the flow inside the manifolds and the MCs. 4 plate cross flow μHx were then machined using micromilling, each plate containing 20 MCs having hydraulic diameter of $\sim$ 411 each. Leak tests were performed but the thermal performance was not reported.

Yang et al. [81] presented the experimental results highlighting the role of axial wall

conduction on the performance of the double layer μHx for the design that was reported in [78]. The tested μHx was tested under parallel, counterflow and crossflow configurations with various partition foils of different materials for the separation of hot and cold fluid streams. The materials considered for the separation foil were PEEK, stainless steel, aluminum and copper whose thermal conductivity varied between 0.25 W/mK to 400 W/mK. These materials allowed to test the μHx such that the effects of axial wall conduction, that have been the point of discussion in all the earlier results reported in this field, could be distinguished. Unlike all the previous studies summarized above, pressure and temperature sensors were integrated within the manifold to individuate the effects of manifolds and the MCs. Two thermocouples were placed in both manifolds and one pressure tap was in the centre of the manifolds. A novel methodology was presented to compare the experimental results of effectiveness that already had the axial wall conduction effects against the effectiveness if the wall axial conduction was not present. Experimental results of counterflow μHx showed that for the PEEK separation foil, effectiveness did not show any variation due to the very low thermal conductivity of the PEEK. Whereas it showed the maximum depreciation of effectiveness when copper (highly conductive) thick foil (500μm) was used. While comparing the experimental effectiveness of counterflow μHx it has been found out that PEEK material which ensured minimal axial heat conduction did not exhibit the best effectiveness because it hindered the conjugate heat transfer between the hot and cold fluids as well. A thin metallic foil made of an intermediate thermal conductive material, stainless steel, in this case, showed the highest thermal effectiveness at the lower Re. When the μHx was tested in the parallel flow arrangement the effectiveness was highest with the most conductive material of the foil in the lower Re range. Towards the higher end of Re investigated, the effectiveness values from all the partition foils became similar except PEEK foil which showed significantly lower values of effectiveness. Just like the case of counterflow μHx effectiveness was also highest with medium conductive material for the crossflow μHx whereas the difference was minimal for higher Re investigated. When results from all the configurations were compared

amongst each other for the same material of the partition foil, the effectiveness with the counterflow configuration was higher as compared to a parallel configuration where crossflow configuration effectiveness was in between these two extremes. The difference between a counter and crossflow configurations became minimal at the higher Re. The authors concluded with the recommendation that axial wall conduction depreciates the performance as soon as the axial wall conduction parameter, defined by Maranzana et al. [79] is higher than 0.01 in counterflow configuration whereas this limit is slightly lower in crossflow configuration.

Hydraulic and thermal performance of the double layer μHx in counterflow configuration was also reported by Yang et al. [82]. Tested μHx with a hydraulic diameter of 200μm showed volumetric thermal power of 100 MW/m^3 to 400 MW/m^3 compared to an average of 10 MW/m^3 for gas as the working fluid. Thanks to the presence of pressure taps inside manifolds, they noticed that pressure drop in the MCs core consisted of merely 10% of the total pressure drop and the maximum pressure drop of 60-70% occurred in the outlet manifold for the higher Re range. They pointed out that for the optimum performance of the μHx therefore manifold design should be studied with care.

The same device was later analysed by Gerken et al. [83] where authors presented the exergetic analysis combining heat transfer and associated pressure penalty of μHxs. They found that by changing the partition foils material and thickness the total pressure drop of the μHx was varying considerably. Up to the range of mass flows investigated, corresponding to maximum Re of $\sim$1200, the pressure drop varied linearly for all the foils but two thin separation foils made of the relatively higher conductive materials (aluminum and copper) with 100 μm thickness showed a square dependence with an increase in the mass flow. They calculated the effective temperature jump efficiency of the tested μHx with various partition foils and found that stainless steel partition foil with 100 μm thickness performs the best. On the other hand, when compared with reference to exergetic power loss due to the pressure drop aluminum foil with 100 μm

thickness was found to be the best. Authors concluded that due to different inlet pressures (total pressure drop) with different materials, identical conditions could not be achieved amongst the different test devices and therefore no unique solution as to the best performing material could be individuated. They pointed out that given a fixed geometry of the device for the incoming mass flow, pressure drop should be independent of the partition foil material but the measured differences were associated with possible bending of the partition foil amongst various materials. Or it might have been that changing the thermal conductivity, due to varying axial conduction the temperature of the gas in the distributing manifolds gets changed in a way that it ultimately changes the pressure drop as for the gas pressure is a strong function of the temperature. No solid conclusion on this matter could be withdrawn due to nonidentical inlet conditions. They emphasized however that pressure drop of compressible gas flows inside such microdevices affects the exergetic power loss predominantly and therefore should be of important design concern.

Experimental and numerical study of a double layer μHx that is operated with water as working fluid in counterflow configuration is reported by Zhuo et al. [84]. They developed a complete 3D model of the investigated μHx with all the manifolds and MCs. They validated their numerical model with the experimental results of temperature drop, friction factor and Nu evaluated from a prototype device. The hydraulic diameter of MCs in experimental μHx was 667 μm where 20 channels were milled into a copper plate of 2 mm thickness. Mass flows of the hot and cold sides were increased in the balanced flow conditions such that the resulting Re varied from 50–600. Temperatures at the device inlet and outlet were measured along with the pressure drops. These were further utilized to calculate the average Nu and friction factor of the μHx. The numerical model showed an excellent agreement with the experimentally observed values and then it was used to perform a parametric analysis to find the optimum geometry that results in the highest performance index for the given design conditions. They varied the height (0.5 mm–2 mm), width (0.2 mm–0.8 mm) and MC wall thickness/ channel spacing (0.4 mm–1 mm). Results showed that Nu increases with

an increase in the width of the MC for the constant height whereas it decreases if, for a constant width, height is increased. By observing the detailed velocity profiles along the axial direction of the MCs, they concluded that hydrodynamic entry length is not affected by the geometry of the MCs. Considering the best performance index they recommended the MC size of 1–1.5 mm in height and 0.4–0.6 mm in width. Based on their numerical results, they also developed the correlations for the prediction of the Nu which as expected increases with increasing Re.

Zhuo et al. [85] then fabricated various copper based double layer counterflow μHxs with the design that was explored in detail from their above mentioned study [84]. They used a multiblade cutting methodology to fabricate the MCs in a copper sheet. They again augmented their experimental results with numerical CFD study and found similar conclusions that were derived in the previous extensive parametric study [84].

A simulation based design of a novel μHx was more recently reported by Deng et al. [86]. The initial goal was to cool the natural gas onboard the vehicle using two available coolants namely air engine coolant (EC) and refrigerant (R134a). To cool the incoming natural gas, two different regions with their own pin fins and MCs (hydraulic diameter of 800 μm) were accommodated in a single layer of the μHx made out of stainless steel sheet. The other layer for the natural gas had continuous long MCs having a smaller hydraulic diameter of 521 μm. A total of 32 pairs (hot and cold) were assembled using diffusion bonding to make a counterflow μHx. The testing was performed by using air instead of EC and NG whereas R134a was replaced by water. Due to complex pin fins and novel design that incorporated a two stage heat sink in one plate (EC and R134a) with individual inlet/outlet vents for two fluids, a 3D CFD model was also prepared to understand the flow behavior. Pressure drop comparison from this CFD model and experimental results showed somewhat good agreement. From their numerical results, they found out that MCs only account for 7-18% pressure drop compared to the total pressure drop of the layer. Interestingly, CFD model of the complete domain also showed that maximum heat transfer occurred in the distribution and mixing zones

instead of the MCs. They concluded that it suggests that μHx is not operating at its designed conditions.

Summarizing the results of the recent literature for μHxs and heat sinks, Morini and Brandner [87] pointed out that μHx design follows the conventional rules and theories given that scaling effects are negligible. For single phase applications, deionized water has been the most employed heat exchanging fluid and there exists ample literature [55, 66, 67, 68, 69, 71, 70, 80] whereas for the gases as working medium limited literature can be found out. Following problems can be expected by reducing the dimensions and parallelizing the channels:

- Manufacturing problems
- Large pressure losses
- Maldistibution/ Fouling

Depending upon the application, maldistribution may become a big concern such as in condensers and evaporators. Maldistribution for two phase flows may lead to hydraulic instabilities and therefore must be minimized. In such reduced dimensions of the fluid transporting channels, the presence of the scaling effects will deviate for the conventional design rules but at the same time may represent an opportunity to yield unique performances from μHxs and heat sinks. Conjugate heat transfer becomes important where separation foil thickness becomes of a similar magnitude to the hydraulic diameter of MCs. Strong conjugate effects tend to reduce the overall performance (effectiveness) for larger values of the NTU which signifies higher values of heat transfer coefficients and smaller mass flows, which are amongst the peculiar characteristics of μHxs. Viscous dissipation may also become relevant at higher velocities of the fluid which again is common to experience in such devices. Authors also proposed a general labeling scheme to organize the available literature depending on the flow orientation inside μHxs and heat sinks, the shape of manifold and position of the inlet/outlet ports.

It was emphasized that to achieve optimum performance, the design of the manifolds should be such that it results in the minimum flow maldistribution. Moreover commenting on the role of axial wall conduction it was shown that it only degrades the average thermal performance of the μHx in the counter flow configuration and does not have any impact on the performance when parallel flow arrangement is considered.

Sing et al. [88] in their recent review have presented a detailed quantitative and qualitative analysis for the thermal performance and frictional characteristics of the compact and μHxs. Heat exchangers of the automotive industry have been completely replaced by compact heat exchangers with channels hydraulic diameter of 1 mm. Reduction of the hydraulic diameter of μHxs forces designers to operate in the laminar regime to avoid associated larger pressure drops with increasing flow speeds. In the laminar regime, typical thermal profile causes the Nu to be a constant value of 4.36 for uniform heat flux at the wall and 3.66 for constant temperature boundary condition at the wall. In order to then enhance the heat transfer active as well as passive methodologies should be sought after. Pressure drop data and hence frictional characteristics are not unequivocal for the gas flows in microtubes and microchannels where higher/lower values are in general associated with the compressibility and rarefaction effects or both. On commenting on the laminar to turbulent flow transition, they pointed out that transition is seen to occur in the range of Re 1400 to 1800 for gas flows which may be associated with the uncertainty of the hydraulic diameter and inconsideration of minor losses. Surface roughness, on the other hand, affects the critical Re. Several phenomena such as two and three dimensional transport effects may exist at the micro scale which are completely ignored while making analytical analogies. There are still unsettled questions related to the scaling effects in the micro flows which need to be addressed. Authors observe that a great disparity in Nu exists for gas flows in the turbulent as well as in some cases laminar regimes. Discrepancies are associated to inaccurate microfabrication and lack of understanding for the underlying physics of heat transfer. In an experimental campaign, it is both expensive and challenging to evaluate the degree of maldistribution and hence CFD has emerged as a potential tool

to replace the sensors. Their analysis confirmed that the understanding of fluid flow and convective heat transfer at the microscale must be considered an open scientific problem and more experimental data are needed to have possible explanations of observed behavior. The authors concluded that for the gas flows inside small channels, the friction factor in the turbulent regime was significantly lower than the conventional correlations. For the laminar flow regime, Nusselt number correlations from different authors are not in agreement with each other as well as with the conventional macroscale correlation.

Given that from 2000 onwards, more than 6000 papers have been published in the topic of microchannel heat transfer [89], it is beyond scope of this work to serve as an exhaustive review of the fluid flow and heat transfer in μHxs. However, an attempt has been made to summarize the most relevant studies which dealt with experimental as well as numerical investigations pertinent mostly to double or multilayered plate type μHxs. This is due to the fundamental nature of the work that is planned to be conducted during this Ph.D. thesis to further the understanding of the compressible continuum flows in micro heat exchanging systems.

2.4 Objectives of the Work

The detailed literature review carried above highlighted that the understanding of the fluid flow and heat transfer in MCs and μHxs, is still an open field of investigation when a compressible gas is used as the working fluid. In this regard, various open questions have been highlighted during the aforementioned review. Amongst these, the following are treated as the main objectives of the current thesis:

1. Role of the minor losses on experimental evaluation of the frictional characteristics using compressible fluid inside MCs/MTs

2. Effect of the flow choking on the evaluation of the Fanning friction factor and

heat transfer inside MCs/MTs

3. Effect of the aspect ratio and the inlet manifold shape on the laminar to turbulent transition in MCs

4. Heat transfer characteristics of the gas microflows using experimental and numerical approaches

5. Role of the compressibility in the thermal performance of gas to gas micro heat exchangers with balanced and unbalanced flows

6. Development of a computational methodology for the thermal performance evaluation of the micro heat exchangers with a large number of parallel MCs

Part I

Analysis of Fluid Flow in Single Microchannels

Chapter 3

Experimental Methodology and Data Reduction

3.1 Introduction

This chapter outlines the workflow and instrumentation used for experimental analysis of gas flow through commercial microtubes (MT) and in-house fabricated rectangular microchannels (MC). It also discusses the data reduction for the evaluation of friction factor from pressure drop analyses in these geometries. Due to ease of thermal boundary condition application, heat transfer analysis is performed only for MT and therefore evaluation of Nusselt's number is also detailed.

3.2 Experimental Setup

The experimental tests have been carried out at Microfluidics Laboratory of the University of Bologna. The testing apparatus with relevant instruments used to test the MC is shown in Fig. 3.1. Nitrogen gas is stored in a high pressure flask (200 bar). Before entering in the test section, its pressure is reduced to approximately 10 bar at

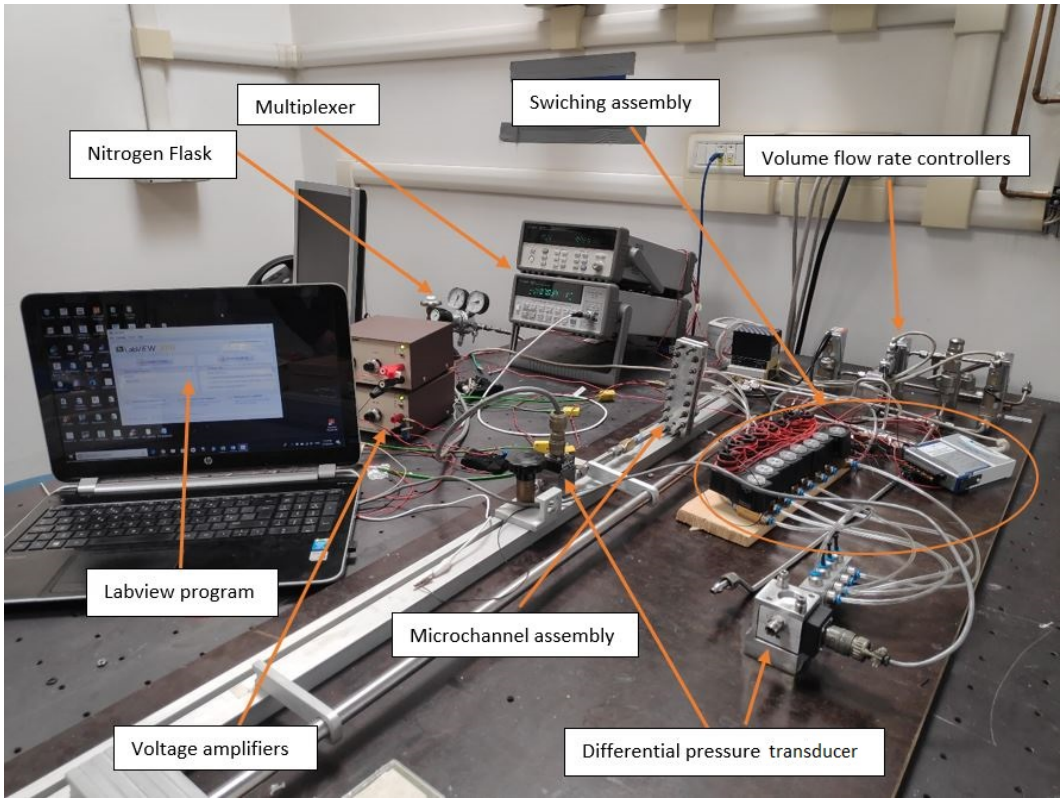

Figure 3.1: Experimental Setup.

room temperature (293 K). Working fluid then passes through a 7 μm particle filter, used to block impurities, in order to avoid clogging of mass flow controllers. The desired volume flow of the gas is imposed using the flow controller. Gas is then allowed to enter the test section where after passing through the MC/MT, it is vented into the atmosphere through outlet manifold.

3.3 Instrumentation

Instrumentation used for experimental campaigns is highlighted in Fig. 3.1. A description of each of these instruments is as follows:

3.3.1 Mass Flow Controllers

In order to impose the desired Reynolds number at the inlet of test section, it is essential to be able to control the volume flow rate (or mass flow rate) through the test section. The facility is equipped with three mass flow controllers (Bronkhorst® EL-Flow E700) having a different operative range as shown in 3.2. The smallest one is able to impose volume flow rate of $0 - 50\,\mathrm{Nml/min}$, the intermediate one $0 - 500\,\mathrm{Nml/min}$ and the largest one $0 - 5000\,\mathrm{Nml/min}$. Flow controllers are switched by means of a three way valve in order to obtain the desired Reynolds number (mass flow rate) with the best possible precision. These flow controllers are also capable of measuring the instantaneous mass flow rate that is allowed through the assembly which fluctuates a little (less than typical uncertainty of the instrument) above or below the imposed value. Therefore, instantaneous values measured by the flow controllers are further utilized for an accurate evaluation of imposed Reynolds number.

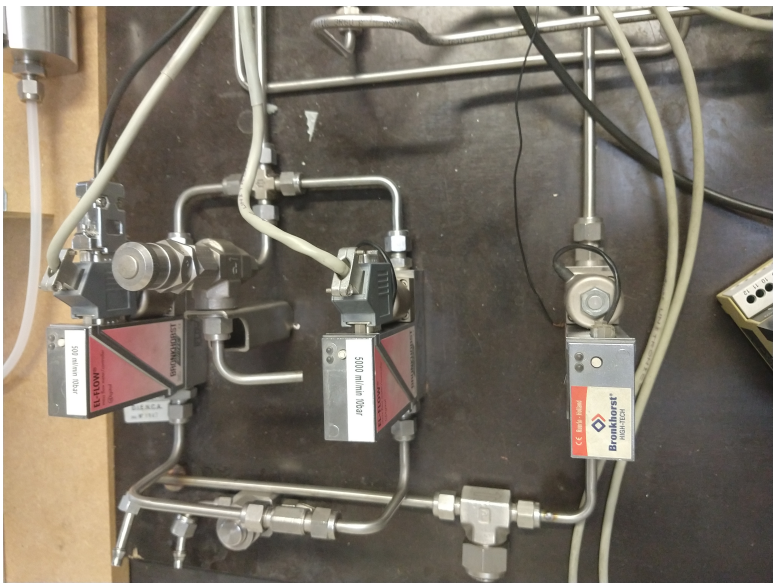

Figure 3.2: Bronkhorst mass flow controllers.

3.3.2 Pressure Transducers

Accurate pressure measurement results in accurate evaluation of frictional characteristics of fluid flows and therefore a pressure transducer is the most important sensor of the experimental setup. A differential pressure gauge (Validyne® DP15) is used to measure the relative pressure at the desired cross section of the MC/MT. The differential gauge has interchangeable membranes capable of measuring pressure drop of 86 kPa to 3500 kPa. Based upon the channel diameter, an estimate of the total pressure drop is made using analytical correlation and accordingly a suitable membrane is used. Due to the opening and closing of the instrument casing, it needs to be calibrated every time a new membrane is used. To begin with calibration, pressure transducer with appropriate membrane inserted, is mounted on a BT400 Comparison test pump as shown in Fig. 3.3a. This test pump is provided with a digital gauge to measure the applied hydrostatic pressure where output voltage signal after passing though the amplifier is fed to a digital multimeter (DMM). Initially, the pressure is reduced to zero and the output voltage signal from pressure transducer is checked which ideally should be 0 V. There are two knobs available on the amplifier (see Fig. 3.3b) for setting zero and span of the output voltage signal. If output at no applied pressure (0 kPa) is not equal to 0, Zero knob at amplifier is adjusted such that value read by DMM is close to zero. For practical purposes, this value is never exactly zero however, a value in a few microvolts is usually considered as zero. Applied hydrostatic pressure is then increased by revolving a metallic slider inside the comparator chamber. A gradual increase is made so that there are at least four data points to be noted from going to zero to full scale value of the employed membrane. If output at full scale (FS) does not correspond to 10 V, then signal conditioning is performed using the Span knob on the amplifier such that output is 10 V at FS. This procedure is repeated and a linear curve fit is made onto the measured data of output voltage against applied pressure. If the $R^2 = 0.999$ or greater, the pressure sensor is considered as calibrated. Calibration procedure also provides signal conditioning coefficients to calculate any unknown

pressure within 0-FS range that are to be used later in data acquisition program. To

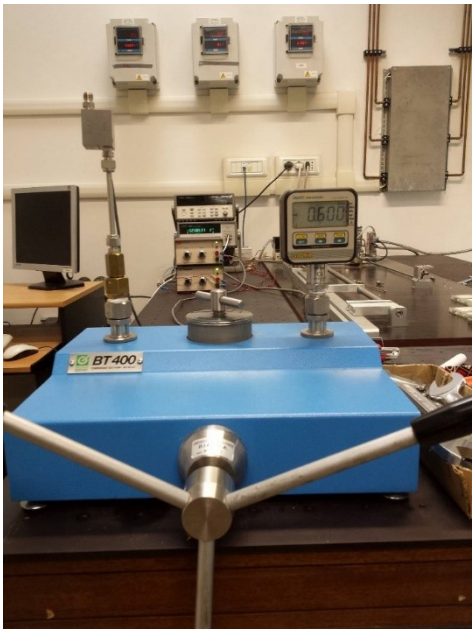

(a)

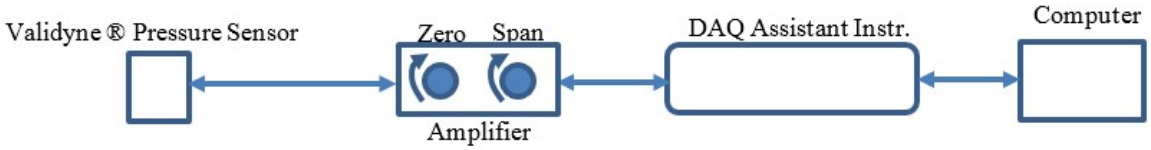

(b)

Figure 3.3: Experimental setup (**a**), and an exploded view of MC assembly (**b**).

measure the atmospheric pressure of the experimental laboratory, an absolute pressure gauge (Validyne® AP42) is used. This sensor does not require any calibration and is used with signal conditioning parameters as provided from the supplier.

3.3.3 Digital Multimeter

Output voltage signals of pressure and temperature sensors are read into the computer using a digital multimeter (DMM) (Agilent® 34970A). A prime subject of consideration in an experimental campaign is the resolution and accuracy of measuring instruments. Agilent 34970A has a built in DMM having $6-1/2$ digits resolution. Agilent 34420A on the other hand, has internal DMM with $7-1/2$ digits resolution and better accuracy than Agilent 34970A. However, it only has 2 input channels and hence all

the sensors cannot be directly fed into the DMM. Therefore Agilent 34970A is used as a switch unit and 34420A as DMM. Switch unit with a capability of 16 channels (sensors) is connected to 34420A using HP10833B cable and ultimately both of them are connected to a computer using GPIB-USB-HS cable by National Instruments®. In this way, both switch unit, as well as DMM, can be controlled and read through one connection to the computer.

3.3.4 Solenoid Valve Switching Assembly

In order to measure the pressure at various cross sections of the test assembly using a single pressure sensor, Validyne DP-15 in this case, a pressure switch is made using solenoid valves. A total of eight solenoid valves from FESTO® are used to make a switching assembly as shown in Figure 3.4a where each valve represents a pressure port. When electrically activated using a voltage of 24 V, the solenoid valve switches to the OPEN state and lets the gas pass through whereas it does not let any gas flow through when it is OFF (0 V). For the actuation of these solenoid valves and their subsequent control from the computer, an 8 channel digital output module NI 9472 from National Instruments® is used. This module is further connected to the computer using a Hi-Speed USB Carrier NI USB-9162.

Circuit diagram for the operation of the solenoid valve switch assembly using NI 9472 is shown in Fig.3.4b. When connected with external power supply, each port can provide 0.75 A current at applied voltage. Employed solenoid valves require and therefore this module suffices the requirement. An individual channel from 0 to 7 can be made ON and OFF using a computer data acquisition system to control the pressure ports as desired.

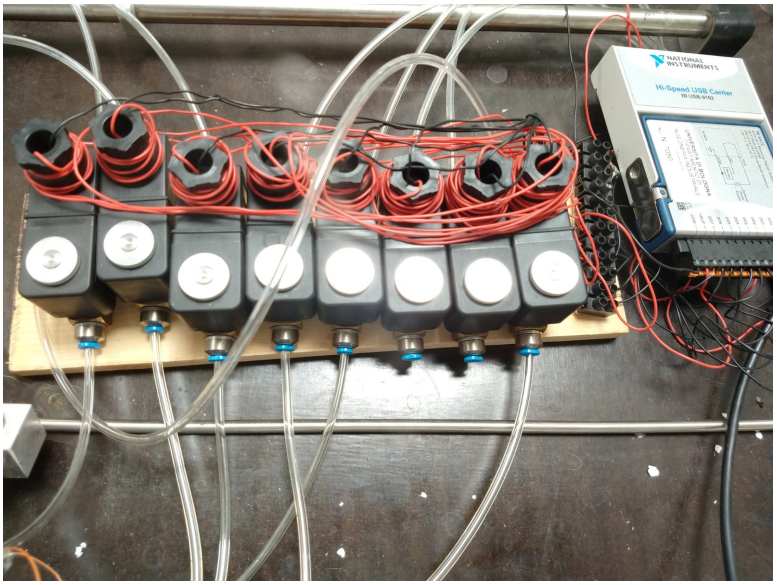

(a)

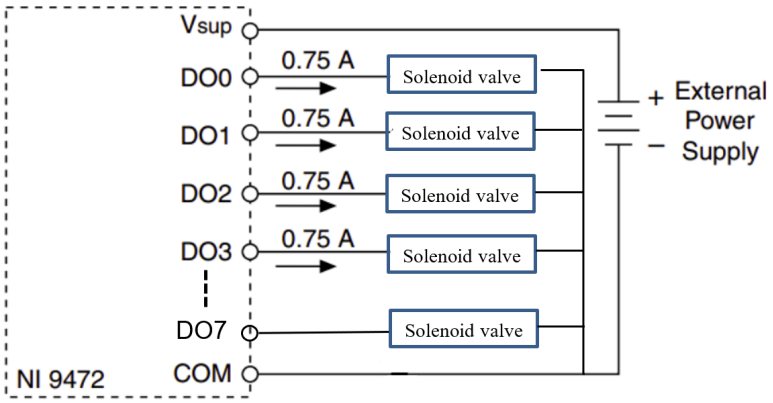

(b)

Figure 3.4: Solenoid switch assembly (**a**), and circuit diagram of NI 9472 (**b**).

3.3.5 Thermocouples

To measure the temperature of the gas and the room, K-type thermocouples are used in the experimental testing. These thermocouples are first calibrated using a calibration bath (Heto) and employing the temperature measured by a platinum resistance thermometer as temperature reference (Fluke Hart Scientific 5626) having a declared accuracy of $\pm 0.006\,^{\circ}C$ at $0\,^{\circ}C$ and $\pm 0.015\,^{\circ}C$ at $420\,^{\circ}C$. Thermocouple calibration setup is shown in Fig.3.5.

Figure 3.5: Thermocouple calibration setup.

3.4 Test Sections

For the pressure drop analysis, two test sections namely MT (circular) and MC (rectangular) are tested. A brief description of the test sections is given below:

3.4.1 Circular MT

Commercial stainless steel MT from Upchurch® were used in the current experimental campaign for the evaluation of frictional and thermal behavior of gas flows through such geometries. A range of MT hydraulic diameters were tested experimentally however, the external diameter of the tube remained 1.58 mm. Due to the accumulated experience of the Microfluidics laboratory, it is known that the real inner diameter of the MT can be different than the nominal values generally quoted by the manufacturer. Scanning Electron Microscope (SEM) imaging has been used in the past by the laboratory where diameters are extracted by an image fitting technique. However, in this study, an alternate indirect method is used to estimate the nominal hydraulic diameter of the MT. Experimental results on friction factor of MT in the recent decade confirm that Poiseuille's law is valid in almost all cases in the lower laminar regime. Although gas compressibility may cause deviation towards the higher end of the laminar regime friction factor follows the Poiseuille's law for smaller Reynolds number where the gas flow can be considered as incompressible. As friction factor for incompressible gas flow is inversely proportional to the fifth power of hydraulic diameter which makes the friction factor highly sensitive to small changes in hydraulic diameter. Due to such sensitivity, the hydraulic diameter of experimented MT was fine tuned from the manufacturer's quoted value using experimental pressure drop results. The hydraulic diameter was changed such that the resulting experimental friction factor follows the Poiseuille's law in the lower laminar regime. This method can be reliable if experiments are carefully carried out and in turn, it provides the value of hydraulic diameter which is averaged across the whole length of the MT. It automatically averages out any cross sectional changes along the length of MT as well. Moreover in the past, comparison of SEM images with the currently employed technique have yielded good agreements and therefore it has been utilized with confidence in present investigations.

3.4.2 Rectangular MC

A considerable amount of time has been spent in the first year of the current Ph.D. in order to fabricate in house MC at Microfluidics laboratory of the University of Bologna. This was achieved using a micromilling CNC machine (Roland®MDX40-A) which has a 100 W spindle motor. The only limitation has been that it cannot work with metals. Therefore, in this work, MCs are fabricated in PMMA plastic. The design of the whole MC assembly is performed using Fusion®360 CAD software. CAM codes are also generated within the same software. MC is realized in a 5 mm thick PMMA plate in the following steps:

- Plastic is cut into an appropriate size ($150mm \times 50mm$) and mounted on the working table of the CNC machine.
- Surfacing is performed using a maximum possible size cutter i.e. 6 mm for the machine. By removing $0.3 - 0.4$ mm of the plastic layer, it is ensured that stock is flat with respect to milling blade. It is performed in two to three steps by setting a maximum depth of cut equals to 0.2 mm and one final step of removing 100 μm. Although the acquired PMMA was extruded and had a good thickness tolerance but this step is essential to have an even surface. Alternatively, the realized MC depth may vary more than 100 μm along the length which will result in complete disagreement with the conventional theory. Therefore machine zero (when blade touches the stock) is checked before and after the surfacing operation at 6 different places on the stock. The surfacing is repeated in case the difference of height between different parts of the stock was more than 10 μm which is the sensitivity of the CNC machine.
- Tool paths generated through FUSION360 are loaded on the CNC machine to make manifolds, MC, O-ring groove and peripheral holes for the bolts respectively. Based upon the size of the feature milling blades are changed in between different operations. MCs are realized by straight endmills whereas a drill suitable

to plastic materials is used for the holes.

- Resulting plastic chip containing MC was exposed to cleaning alcohol for less than a minute and finally dried using Nitrogen gas. This step ensures that there are no plastic particles left on the chip that may clog MC or disturb the flow while experimental testing.

An exploded view of MC assembly is shown in Fig. 6.1. The chip containing MC (lower plastic) is covered by another chip of the same material (upper plastic) which acts as the top wall for the MC. Both plastics are sandwiched between two 5 mm thick Aluminium plates. An O-ring is placed between upper and lower plastic to prevent gas leakage. Finally, the whole assembly is compressed using 16 peripheral M6 bolts. Reducers (connectors) are used to connect inlet and outlet manifolds to the gas supply piping. To measure the local pressure along the length of the MC, 5 linearly distributed holes of 200 μm are drilled in the top plastic. Festo piping and connectors are used to read the pressure from these ports using the differential pressure gauge and solenoid switch assembly. Dimensions of the MC are determined using two methodologies. At

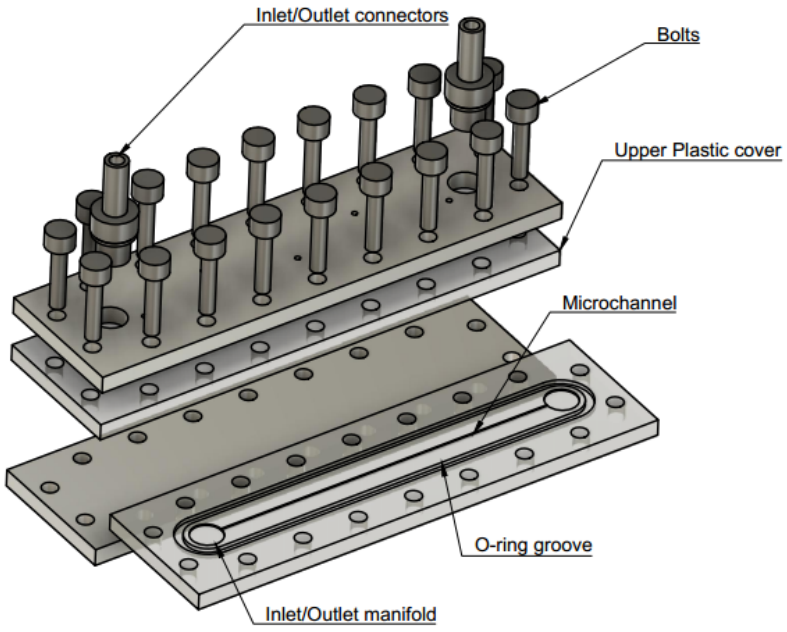

Figure 3.6: MC assembly

first, realized MCs are observed under an inverted microscope (Nikon Eclipse TE 2000-U). Due to the open channel, it is possible to mark the top surface of the chip and then focusing it using the microscope. Depth of channel cross section is then found out by measuring the total distance traveled by the lens (in 1 μm steps) in order to focus the bottom face of the channel that can be observed with ease due to milling signature of the blade as shown in Fig. 3.7. On the other hand, the width of the MC is measured using pixel counts for images of bottom and top surfaces. The length of one pixel is ascertained by comparing a known fixed length (width of a commercial etched MC) against the total number of pixels in the image. The width and depth of the MC are finally measured using this methodology at five locations along the length of the MC. These values are finally averaged to find out the mean width and height of the realized MC to calculate the average hydraulic diameter.

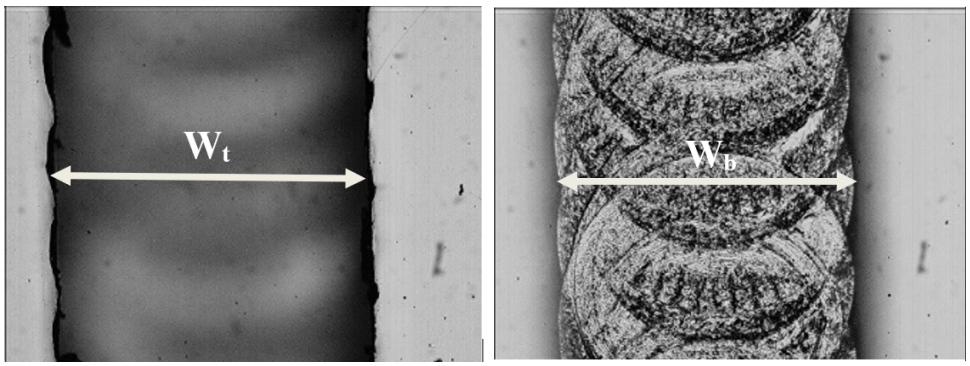

(a) (b)

Figure 3.7: Microscopic view of the top (**a**), and bottom (**b**) surfaces of realized MC.

To validate the dimensions of the MC evaluated using a microscope, five MCs are also observed using optical profilometer at the University of Parma, Italy. Another reason to use optical profilometer was to estimate the average surface roughness of the MC bottom wall with the used machining parameters. Surface roughness, width, and height of the channels are measured similarly at five axial locations and an average of three readings is taken at each location. A sample of images and extracted data at one specific cross section for a representative MC is shown in Fig.3.8. Finally, representative values for each individual location are averaged to find out the mean

height and width. The maximum difference between the calculated hydraulic diameter

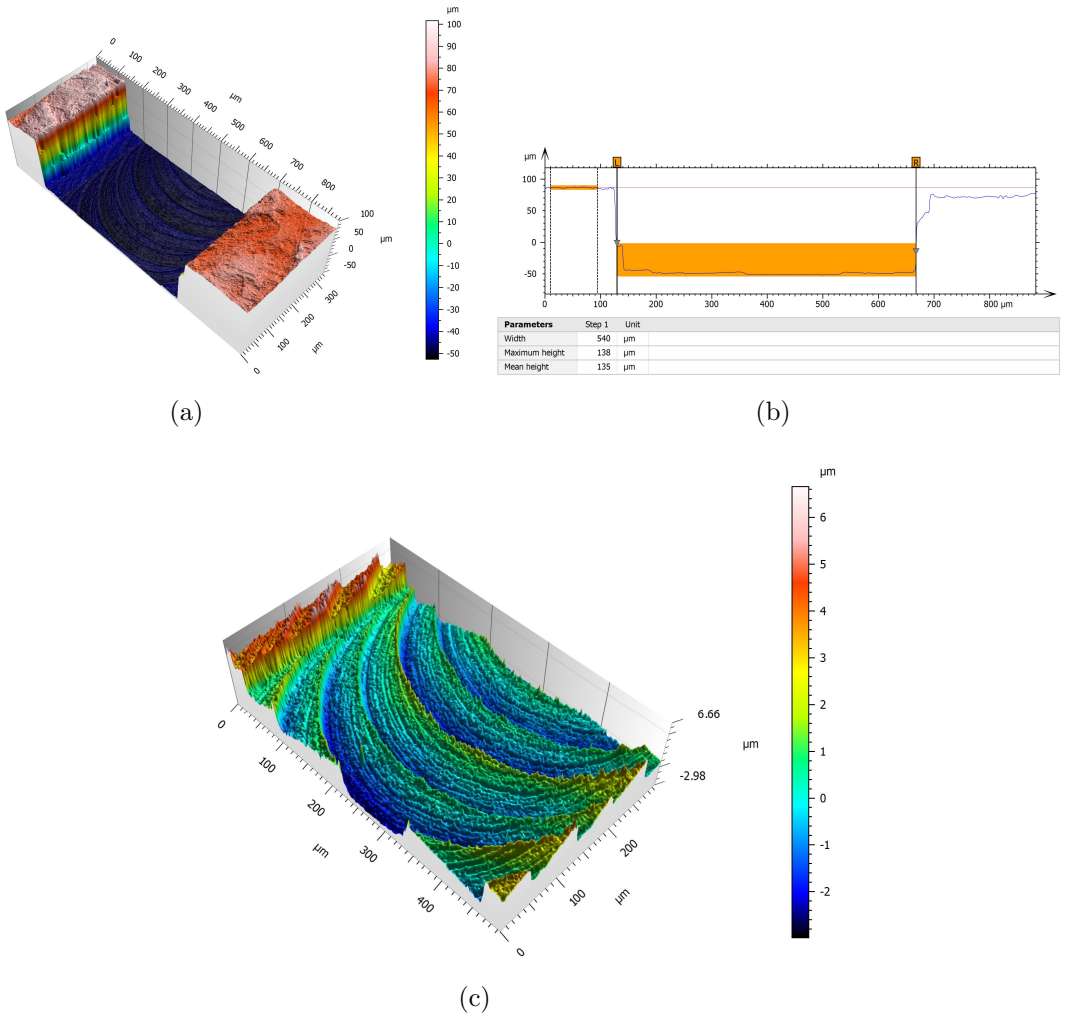

(a) (b)

(c)

Figure 3.8: 3D reconstruction of the MC (**a**), average dimensions (**b**), and surface roughness (**c**) of a representative MC using optical profilometer.

using the microscope and profilometer for all the six microchannels was less than 10%. Therefore due to the ready availability of microscope, dimensions were estimated using an inverted microscope for all the MCs that were realized afterward in this work.

3.5 Labview Interface for Data Acquisition

A graphical schematic of LABVIEW code is elaborated in Fig. 3.9. User is required to input a range of *Re* with initial value, increment and final value format. This input is then translated into the required volume flow rate to be set by mass flow controller.

For each fixed value of volume flow rate (Re) data acquisition through all sensors is performed until a specified relative error condition is met. Once the error condition is satisfied, a steady state of the system is considered to be achieved and all the sensor values are stored into a text file to be used later for post processing. In the case where solenoid switch assembly is used, the above mentioned procedure is repeated for every pressure port. All the signal conditioning to transform voltage outputs of pressure and temperature sensors have been incorporated in LABVIEW code and results stored in text files are in terms of direct physical quantities rather than voltages.

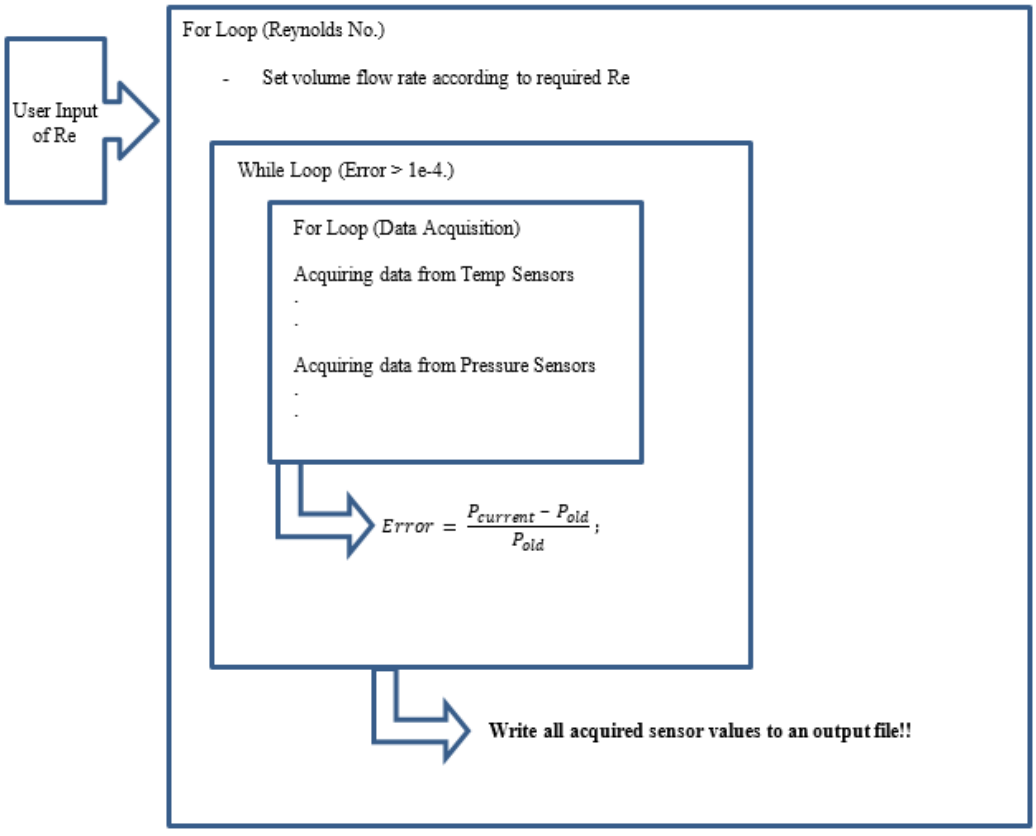

Figure 3.9: Labview schematic for data acquisition

3.6 Experimental Data Reduction

3.6.1 Friction Factor

Local Fanning friction factor can be defined by the following expression for a compressible flow [32]:

$$f_{f,local} = \frac{4\tau_w}{\frac{1}{2}\rho u^2} = \frac{2D_h}{p} - \frac{2D_h p}{\rho^2 u^2 RT}\frac{dp}{dx} - \frac{2D_h}{T}\frac{dT}{dx} \tag{3.1}$$

where p and T denote the pressure and temperature of the gas, R is the specific gas constant and 'x' represents the streamwise direction of the gas flow. Hydraulic diameter is defined as:

$$D_h = \frac{4A}{Per} \tag{3.2}$$

where Per and A are the wetted perimeter and average cross sectional area for the gas flow, respectively. Reynolds number at the inlet of MC/MT can then be calculated using ratio of measured mass flow rate to the area ($\dot{G} = \dot{m}/A$) and calculated viscosity (μ) at inlet temperature with the following equation:

$$Re = \frac{\dot{G}D_h}{\mu} \tag{3.3}$$

Considering one dimensional flow of ideal gas, Equation (3.1) can be integrated between two points a and b along the length (L), to calculate average friction factor between those points as follows:

$$f_f = \frac{D_h}{x_b - x_a}\left[\frac{p_a^2 - p_b^2}{RT_{av}\dot{G}^2} - 2\ln\left(\frac{p_a}{p_b}\right) + 2\ln\left(\frac{T_a}{T_b}\right)\right] \tag{3.4}$$

As mentioned previously, local pressure is measured in case of MC whereas for the MT only total pressure drop across the whole test section is measured. In the case of MC, when Equation (3.4) is applied between two closely spaced pressure ports (e.g., between p_4–p_5 in Fig. 3.10 for $\Delta x = x_5 - x_4$), resulting friction factor will be referred to as semi-

local friction factor ($\tilde{f}_f$) while when it is applied between inlet and outlet of MC/MT ($\Delta x = L$), it will be called as average adiabatic friction factor (f_f). In addition, under the hypothesis of adiabatic compressible flow, the energy balance for one dimensional Fanno flow, between inlet '*in*' and any other cross section at a distance 'x' from the inlet of the MC/MT yields the following quadratic equation for the estimation of average cross-sectional temperature [32]:

$$\left(\frac{\rho_{in}^2 u_{in}^2 R^2}{2c_p p_x^2}\right) T_x^2 + T_x - \left(T_{in} + \frac{u_{in}^2}{2c_p}\right) = 0 \tag{3.5}$$

Finally, knowing the average pressure and temperature of a specific cross section, average density and velocity of compressible gas can be obtained using ideal gas and continuity equations, respectively. The local value assumed by Mach number, defined as the ratio of velocity and the local speed of sound, can be calculated as follows:

$$Ma_x = \frac{u_x}{\sqrt{\gamma R T_x}} \tag{3.6}$$

In all the published experimental results, MC/MT is attached to a conventional piping system using an entrance manifold. The geometry of the manifold may vary case by case but a pressure drop between the manifold and MC/MT inlet exists there. Similarly, when gas exits the MC/MT, the expansion of the gas to the exit manifold or atmosphere causes an additional pressure drop. This is shown schematically in Fig. 3.10. The current experimental assemblies for MC/MT have a reducer that connects the entrance manifold to the gas supply piping. Similarly, another reducer towards the exit of assembly vents the gas to the atmosphere coming from exit manifold. Therefore, minor losses ($\Delta P_{in/out}$) in reducers and manifolds need to be accounted for to estimate the pressure drop of the MC/MT, alone (ΔP_{ch} see Figure 3.10) from the total measured pressure drop. The most used method for estimating these minor losses is to use loss coefficients ($K_{in/out}$) available in fluid mechanics texts, which are generally validated

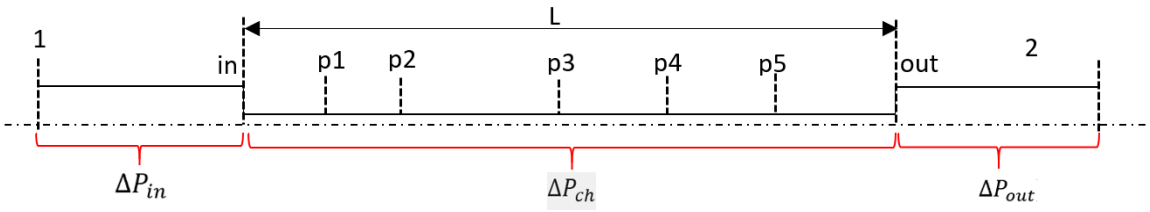

Figure 3.10: Schematic of minor losses.

for liquids and weakly compressible gases. Minor pressure losses are defined as [90]:

$$\Delta P_{in/out} = K_{in/out} \frac{1}{2} \rho u_{in/out}^2 \tag{3.7}$$

For the cases where average friction factor between inlet and outlet is of interest, an appropriate estimation of minor losses is therefore essential. Assuming the outlet pressure to be equal to atmospheric pressure ($p_{out} = p_{atm}$) and using the estimated p_{in} after employing minor losses, the average Fanning friction factor can then be calculated using Eq. (3.4). A detailed discussion on minor losses estimation and atmospheric pressure assumption at the outlet will be carried out in the subsequent chapters.

3.6.2 Nusselt Number

As microchannel fabrication material was limited to engineering plastics and metals could not be utilized with the present milling machine, thermal boundary application at the MC walls was not feasible. Therefore forced convection is only experimentally studied in stainless steel MT. A constant heat flux was applied at the wall of the MT using Joule's heating effect. Current was passed through the tube wall using a power supply (HP6032A) being controlled by Labview interface. Under the applied H-boundary condition (constant wall flux) the mean Nusselt number can be calculated from the experimental parameters as follows:

$$Nu_{av} = \frac{hD_h}{k_f} = \frac{D_h q_w}{k_f(\overline{T}_w - \overline{T}_b)} \tag{3.8}$$

where h is convective heat transfer coefficient, $\overline{T}_w$ is the average wall temperature along the length of the MT, $\overline{T}_b$ is the average bulk temperature of the gas between inlet and outlet, k_f is the fluid thermal conductivity calculated at average bulk temperature and q_w is the heat flux at the inner wall of the MT. Heat flux can be calculated by making energy balance between inlet and outlet of the MT as follows:

$$\Delta q_w = \frac{\dot{m} c_p \left(T_{out} - T_{in}\right)}{\pi D_h L_h} \tag{3.9}$$

where c_p is the gas specific heat at $\overline{T}_b$, T_{in} and T_{out} are the gas temperature at the inlet and outlet of the MT measured using thermocouples, and L_h represents the heated length of the tube.

3.7 Measurement Uncertainties

In order to assess the accuracy of the experimental measurements, the uncertainty associated to each instrument used in the experimental campaigns is reported in Table 3.1.

Table 3.1: Typical uncertainties of instruments used.

Instrument	**Range (0–Full Scale (FS))**	**Uncertainty**
Volume flow rate controllers	0–500 & 0–5000 nmL/min	± 0.5% FS
Pressure sensors	0–22, 0–86, 0–256, 0–860 & 0–1460 kPa	± 0.5% FS
K-type thermocouple	0–100 °C	± 0.25% FS

In a detailed study [2], Yang carried out the uncertainty analysis for friction factor and Nusselt number based on the theory of error propagation. It was highlighted that uncertainty in the evaluation friction factor is highly influenced by the uncertainty of hydraulic diameter. On the other hand, Nusselt number evaluation is affected the most by uncertainty in outlet temperature measurement of the gas flow. In the present case, the uncertainty of the hydraulic diameter, evaluated by using an optical profilometer

to measure both height (H_{ch}) and width (W_{ch}) of the MC, is of the order of 1.5%. The uncertainty associated to the measurement of L is around the 0.4%. Therefore the uncertainty in measuring f_f (with Eq. 3.4) and Re (with Eq. 3.3) is estimated to be equal to ±10% and ±3%, respectively. Moreover uncertainty in Nusselt number is evaluated to be between −33% and 13%. All these uncertainties are summarized in Table 3.2.

Table 3.2: Typical uncertainties of experimentally deduced parameters based on theory of propagation.

Calculated Parameter	**Uncertainty**
D_h	±5%
Re	±3%
f_f	±10%
Nu_{av}	$-33\% - +10\%$

3.8 Summary

Introduction to the experimental setup and employed instrumentation for the measurement of physical quantities of interest has been described. Firstly, a detailed description of the MC/MT characterization is provided and then an introduction to data acquisition using Labview is explained. Experimental procedure to calculate the f_f and Nu_{av} is outlined using all the measured quantities. Finally, uncertainties associated with data reduction methodology are presented. Presented methodology and uncertainties will be used for the experimental evaluation of friction factor and Nusselt number which are the topics of discussion in Part I of the thesis.

Chapter 4

CFD Modeling of Gas Microflows

In most experimental campaigns, global parameters such as total pressure drop along with inlet temperature of the gas are measured for internal microflows. Such pressure drop analysis is then used to understand the average frictional characteristics over the total length of MC/MT. For the gas as working fluid, compressibility has shown to influence the frictional factor even in the laminar regime [44, 42]. This effect gains the significance as the dimensions are reduced below 1000 μm. Due to change in density of the gas there exists an additional acceleration as the gas flows through the MC/MT. Consequently thermal energy is converted into kinetic energy and Mach number at the outlet is higher compared to inlet. Such continuous acceleration of gas particles along the length of the channel prohibits the development of fully developed velocity and temperature profiles. This causes the velocity gradient to change and hence friction factor does not stay constant along the length of MC/MT as it is the case with liquid flows. Due to small dimensions experimental investigations on the fluid flow through MC/MT can employ limited number of pressure and temperature sensors, therefore local flow physics can't be understood well enough. This lack of instrumentation in the internal microflows can be overcome by having a validated numerical model which can help to elaborate the local flow physics.

This chapter is focused on the development of numerical model for internal flows.

Mathematical modelling of compressible laminar, transitional and turbulent flows is presented. Implementation of the numerical model in a commercial CFD software is discussed. Finally validation of the proposed model and boundary conditions for both cross sectional geometries (circular and rectangular) is performed.

4.1 Mathematical Model

Flow physics is governed by conventional conservation equations i.e. mass, momentum and energy. For a steady state compressible flow they can be represented as follows:

Continuity Equation

$$\frac{\partial \rho u_i}{\partial x_i} = 0, \tag{4.1}$$

Momentum Equation

$$\frac{\partial \rho u_i}{\partial t} + \frac{\partial}{\partial x_j}\rho(u_j u_i) = -\frac{\partial p}{\partial x_i} + (\mu + \mu_t)\frac{\partial^2 u_i}{\partial x_j \partial x_j}, \tag{4.2}$$

Energy Equation

$$\rho C_\mu u_i \frac{\partial T}{\partial x_i} = -p\frac{\partial u_i}{\partial x_i} + \lambda \frac{\partial^2 T}{\partial {x_i}^2} - \tau_{ij}\frac{\partial u_j}{\partial x_i}, \tag{4.3}$$

where i,j=1,2,3; the u_i represents the Cartesian velocity components (u,v,w) in longitudinal, lateral and normal directions respectively; p is the pressure; ρ is the fluid density; T is the average fluid cross sectional temperature, μ is the fluid dynamic viscosity and μ_t is turbulent viscosity. For a laminar compressible fluid flow, there are 6 unknowns (u, v, w, p, ρ, T) for aforementioned set of 5 equations from Eqs. (4.1)-(4.3). An additional constitutive law must be added and gas equation is therefore used to complete the solution procedure for the complete set of Navier Stokes (NS) equations, as follows:

Ideal Gas Equation

$$p = \rho R T, \tag{4.4}$$

where R is the universal gas constant. When the flow becomes turbulent, additional viscosity offered by resulting flow patterns is modelled using an artificial turbulent viscosity term μ_t in the diffusive part of three momentum equations represented by Eq. (4.2). Flow variables consist of a mean and a fluctuating part in case of turbulent flow e.g an instantaneous streamwise velocity can be represented as:

$$u = \overline{u} + u' \tag{4.5}$$

where $\overline{u}$ represents the mean part and u' denotes the fluctuating part. For a steady state solution, NS equations are averaged and are known as Reynold average NS (RANS) equations. However when averaging is performed, fluctuations still appear as $-\overline{\rho u_i' u_j'}$ in the non linear acceleration part of the momentum equations. In order to proceed for a steady state solution of turbulent NS equations, an approximation of these fluctuating terms known as Reynold stresses as a function of mean flow velocities is needed. This closure problem has been addressed in the literature by various models such as Spallart Almaras $k-\omega$, and $k-\epsilon$ to name a few. In the current work a shear stress transport (SST) model presented by Menter [91] is used. This model uses $k-\omega$ approximation close to the walls and switches to $k-\epsilon$ far from the wall. In this model, closure problem is dealt with the following two transport equations for modelling turbulent kinetic energy (k) and specific rate of turbulent destruction (ω):

Transport Equations:

$$\frac{\partial(\rho u_i k)}{\partial x_i} = P_k - \beta_1 \rho k\omega + \frac{\partial\left(\left(\mu + \frac{\mu_t}{\sigma_k}\right)\frac{\partial k}{\partial x_i}\right)}{\partial x_i}, \tag{4.6}$$

$$\frac{\partial(\rho u_i \omega)}{\partial x_i} = \chi\rho S^2 - \beta_2 \rho k\omega^2 + \frac{\partial\left(\left(\mu + \frac{\mu_t}{\sigma_\omega}\right)\frac{\partial \omega}{\partial x_i}\right)}{\partial x_i} + 2(1-F_1)\rho\frac{1}{\sigma_{\omega 2}\omega}\frac{\partial k}{\partial x_i}\frac{\partial \omega}{\partial x_i}, \tag{4.7}$$

where P_k is the rate of kinetic energy production, σ_k and σ_ω are the equivalents of Prandtl number for the transport of turbulent kinetic energy and specific rate of tur-

bulent destruction respectively. Moreover subscripts 1 and 2 for these σ_k and σ_ω represent different constants assumed for original $k-\omega$ model close to the wall and $k-\epsilon$ far from the wall, respectively. S is the absolute value of shear strain rate and χ, β_1 & β_2 are SST model constants. F_1 is a blending function that allows to switch from standard $k-\epsilon$ model to $k-\omega$ in order to better simulate the low Reynolds number region.

For the solution of most industrial problems laminar flows are solved by NS equations whereas turbulent flows are dealt with RANS equations as described above. In the transitional flow regime between laminar and turbulent, computationally expensive models such as Large Eddy Simulations (LES), Detached Eddy Simulations (DES) and Direct Numerical Simulations (DNS) are applied where the transient evolution of the turbulence scales is modelled in the computational domain. Although accurate in predictions of flow characteristics, computational cost associated to these modelling techniques is enormous as compared to RANS and therefore are limited to academic evaluations. A revolution in transitional flow modeling with two equation transport model (RANS) is due to Menter et al. [92] where they coupled their previously presented SST model with two additional transport equations used to evaluate a so called intermittency factor (γ). Its role is to diminish turbulence production for flow conditions that are not fully turbulent and its value is between 0 and 1. Evaluation of γ however depends on another local flow property that is referred to as momentum thickness Re ($\tilde{Re_{\theta t}}$) which describes the local stability status of the flow in the near wall region. These two additional transport equations are as follows:

$$\frac{\partial(\rho\gamma)}{\partial t}+\frac{\partial(\rho u_i\gamma)}{\partial x_i}=P_{\gamma1}-E_{\gamma1}+P_{\gamma2}-E_{\gamma2}+\frac{\partial\left(\left(\mu+\frac{\mu_t}{\sigma_f}\right)\frac{\partial\gamma}{\partial x_i}\right)}{\partial x_i} \tag{4.8}$$

$$\frac{\partial(\rho\tilde{Re}_{\theta t})}{\partial t}+\frac{\partial(\rho u_i\tilde{Re}_{\theta t})}{\partial x_i}=P_{\theta t}+\frac{\partial\left(\sigma_{\theta t}(\mu+\mu_t)\frac{\partial\tilde{Re}_{\theta t}}{\partial x_i}\right)}{\partial x_i} \tag{4.9}$$

A detailed explanation of all the terms of Eqs. (4.8) and (4.9) can be found in [92, 93]. Here only the most relevant terms are presented. The transition source in the Eq. (4.8)

for intermittency:

$$P_{\gamma 1} = F_{length}\rho S(\gamma F_{onset})^{c_{a1}} \tag{4.10}$$

$$E_{\gamma 1} = c_{e1}P_{\gamma 1}\gamma \tag{4.11}$$

where F_{onset} is used to trigger the intermittency γ production and its formulation is a function of vorticity Reynolds number $Re_\nu = \frac{\rho y^2 S}{\mu}$ [93]. F_{length} is obtained from correlations and it is dependent on $\overline{Re}_{\theta t}$; the detail of formulas for these two terms can be found in [94]. The destruction/relaminarization sources that are defined as follows:

$$P_{\gamma 2} = c_{a2}\rho\Omega\gamma F_{turb} \tag{4.12}$$

$$E_{\gamma 2} = c_{e2}P_{\gamma 2}\gamma \tag{4.13}$$

where Ω denotes the magnitude of the absolute vorticity rate, $F_{turb} = e^{-(\frac{R_t}{4})^4}$ and $R_t = \frac{\rho k}{\mu\omega}$. Another important term is the production of $\tilde{Re}_{\theta t}$, defined as follows:

$$P_{\theta t} = c_{\theta t}\frac{\rho}{t}(Re_{\theta t} - \tilde{Re}_{\theta t})(1 - F_{\theta t}) \tag{4.14}$$

where the t is a time scale that is present for dimensional reason and $F_{\theta t}$ is a blending function that allows to turn off the source terms in the boundary layer where the scalar quantity $\tilde{Re}_{\theta t}$ is only diffusing.

Coupling between the intermittency equations and standar SST model can be done by multiplying γ with kinetic energy production term P_k and a modified form of the Eq. (4.6) can be written as:

$$\frac{\partial(\rho u_i k)}{\partial x_i} = \gamma P_k - \beta_1\rho k\omega + \frac{\partial\left(\left(\mu + \frac{\mu_t}{\sigma_k}\right)\frac{\partial k}{\partial x_i}\right)}{\partial x_i}, \tag{4.15}$$

As mentioned, γ is solved using Eqs. (4.8) & (4.9). A solution of Eq. (4.15) & (4.7)

would result in k and ω which can be then utilized to solve for turbulent viscosity μ_t as follows:

$$\mu_t = \frac{a\rho k}{max(a\omega, SF_2)} \tag{4.16}$$

where a is a constant and F_2 is another blending function that limits the value of turbulent viscosity inside the boundary layer.

Presented model is a great breakthrough in transition prediction because it is formulated taking into account only local variables which makes it compatible with modern CFD codes that are 3D and parallel. It was developed and then implemented in CFX, a CFD program distributed by ANSYS. However it is worthy to mention at this point that model constants in various utilized correlations are based on the experimental results for external flows. Hence in its original form, this SST transitional turbulence model is not suitable for modelling internal flows. However model constants can be modified based on the available experimental set of data for internal flows. Model constants for the original Menter's $\gamma - Re_\theta$ SST transitional turbulence model, in order of appearance in eqs. (4.10) - (4.14), are:

$$c_{a1} = 0.5;\ c_{e1} = 1.0;\ c_{a2} = 0.03;\ c_{e2} = 50;\ \sigma_f = 1.0;$$
$$c_{\theta t} = 0.03;\ \sigma_{\theta t} = 10;$$

Abraham et. al [1] later modified the constants of the Eqs. (4.13) & (4.14) using an iterative method such that transition in pipe flows was in between a generally accepted range of $2300 < Re < 4000$. Coefficients which predicted the transition at a Re lower than 2300 were not considered. The intermittency coefficient c_{e2} was increased from 50.0 to 70.0, and $c_{\theta t}$ was decreased from 0.03 to 0.015. Authors show that using these modified values of two coefficients of Menter's original $\gamma - Re_\theta$ SST model [92], transitional flow characteristics of pipe flows can be predicted. In the current work similar values of these coefficients as proposed by Abraham et. al [1, 95] are used unless explicitly mentioned otherwise in a specific section.

4.2 Numerical Implementation

The first step in the numerical implementation of the model is choosing the domain that allows the correct representation of the real experimental test assembly. As it has been explained in Ch. 3 that two different test sections are used in current work, therefore a brief discretion of both geometries and associated mesh is given in the following section:

4.2.1 Microtube

Test section schematic representing a MT is shown in Fig 4.1. A commercial reducer is also modelled in the computational domain that connects the gas piping to the MT inlet. Due to axisymmetric nature of the gas flow in MT, only a 10^o slice is modelled as the computational domain with rotational periodicity boundary condition on the side walls. This allows to save considerable computational time by using a smaller number of mesh elements.

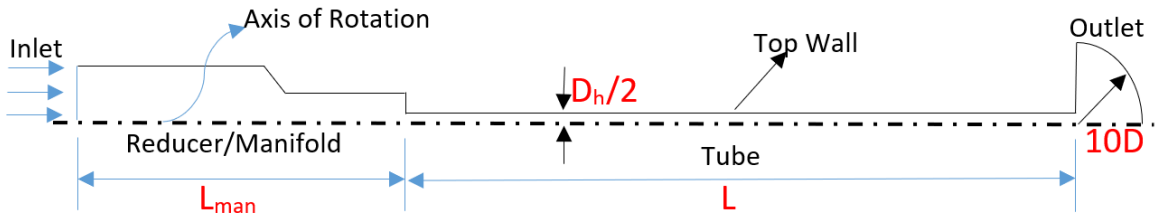

Figure 4.1: Computational domain for MT cross section.

Dimensions of the reducer are also shown in Fig. 4.2. Hydraulic diameter (D_h) of the MT varies in different set of numerical simulation and experimental runs however, dimensions of the reducer are the same for all cases.

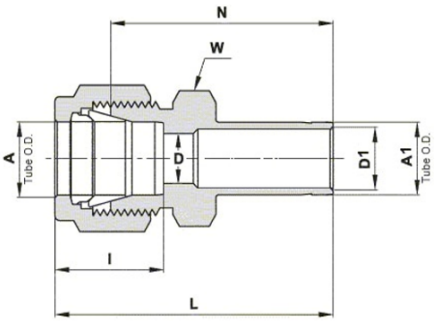

Label	Dimension (mm)	Label	Dimension (mm)
A	1.58	I	0.34
A1	6.35	N	27.68
D	1.27	L	31.5

Figure 4.2: Reducer and associated dimensions.

MT geometric model is designed in Workbench Design Modeler and is meshed using ANSYS meshing software. A structured mesh of 40×200 is used in the MT as shown in Fig. 4.3. Number of divisions along the radial direction are the same for inlet reducer/manifold and outlet whereas 15 meshing nodes are used along the length of reducer and outlet respectively.

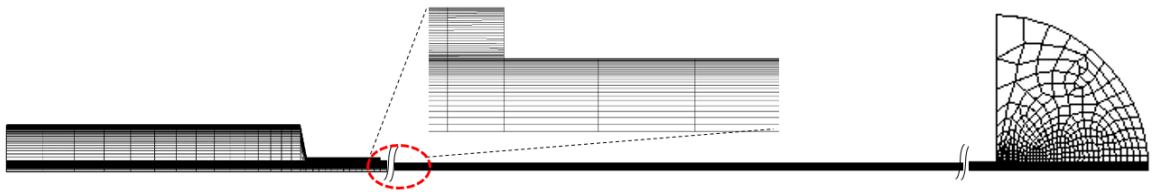

Figure 4.3: Mesh of the MT geometry.

4.2.2 Microchannel

To have a better understanding of the flow physics, symmetry boundary condition are not applied in case of rectangular cross section and therefore a complete 3D geometry as shown in Fig. 4.4 is used as computational domain. A mesh of $45 \times 30 \times 200$ is used in the MCs. Number of node points in the height direction of the MC are reduced accordingly if the height is reduced in simulation model in order to maintain better element quality. A structured mesh locally refined at the walls of the MC and

manifolds is employed. The mesh expansion factor is kept as 1.1 and first node point is placed such that $y+$, which is non-dimensional distance between first mesh node and MC wall, is in between 1 and 4 for the highest Re simulated. Orthogonality of mesh elements inside MC is between 0.95–1 in all the simulated cases. Reducers and manifolds are also simulated along with the MCs. Height of the reducer (H_{in}, see Figure 4.4) is 30 mm with an internal diameter of 4 mm. Whereas diameter of the circular manifolds is 9 mm and height (H_{man}) is kept same as the height of the simulated MC ($H_{man} = h$). Dimensions of these parts are chosen based upon the experimentally tested MC assembly. The outlet is perfectly symmetric to the inlet manifold and therefore two 90 degrees bends are present in the flow domain as they may influence the total pressure drop and hence friction factor evaluation.

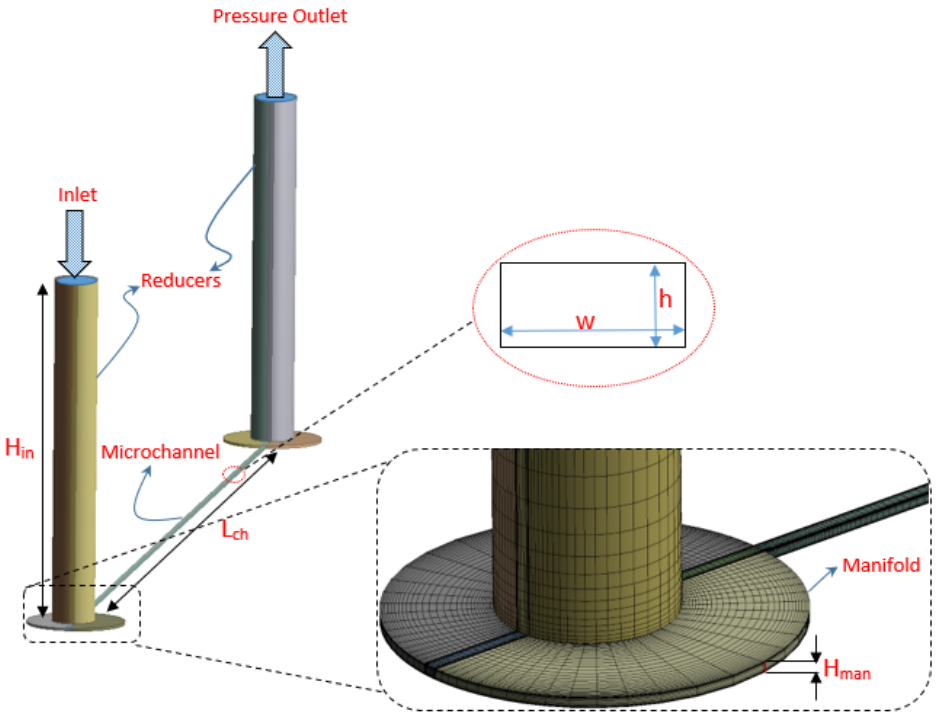

Figure 4.4: Geometry of the computational domain

4.2.3 Solution Procedure

In order to obtain the desired Re, mass flow calculated using Eq. (3.3) is imposed at the inlet of MT/MC. Ideal nitrogen gas enters the reducer/manifold for both considered geometries and is vented to the atmosphere using a orthogonal outlet reducer in case of MC and outlet extended domain in MT geometry. The value of turbulence intensity (TI) at the inlet is 5% for all considered Re, same as adopted by [1]. However, in current work the inlet boundary condition is set at the entrance of the domain and not at the MC/MT inlet as it was the case with [1] and [95]. Hence in laminar regime, due to the fact that reducer section is much longer than manifold, turbulence intensity gets dissipated in the first part of the manifold to a smaller value i.e. close to 1%.
Steady state RANS simulations are performed for all turbulent cases. Laminar flow solver is used for the cases where $Re \leq 1000$ and for $Re > 1000$, SST k-ω transitional turbulence model is used. A modified formulation of γ-Re_θ transition turbulence model for internal flows is applied as discussed in Sec. 4.1. High-resolution turbulence numerics are employed with a higher order advection scheme available in CFX. Pseudo time marching is done using a physical timestep of 0.01s. A convergence criteria of 10^{-6} for RMS residuals of governing equations is chosen while monitor points for pressure and velocity at the MC/MT inlet and outlet are also observed during successive iterations. In case where residuals stayed higher than supplied criteria, the solution is deemed converged if monitor points did not show any variation for 200 consecutive iterations. Reference pressure of 101 kPa was used for the simulation and all the other pressures are defined with respect to this reference pressure. Due to small measured surface roughness, walls of the MT/MC are treated as smooth in numerical model. A no slip boundary condition is applied at the walls which essentially means that fluid particles move with the velocity of the wall which in current case is zero. Energy equation was activated using total energy option available in CFX which adopts energy equation without any simplifications in governing equations solution. Kinematic viscosity

dependence on gas temperature is defined using Sutherland's law.

$$\mu = \mu_{ref} \left(\frac{T}{T_{ref}}\right)^{\frac{3}{2}} \left(\frac{T_{ref} + S}{T + S}\right), \tag{4.17}$$

where constants for Nitrogen gas are:

$$\mu_{ref} = 1.7812 \times 10^{-5}\,\text{Pa s}$$
$$T_{ref} = 298.15\,\text{K}$$
$$S = 111\,\text{K}$$

4.3 Validation

To validate the numerical settings and boundary conditions described earlier, it is essential to compare numerical predictions against the experimental results. In this section a comparison is made for the global parameters such as total pressure drop and average friction factor between inlet and outlet for both cross sectional geometries (MC/MT). Dimensions of both test sections considered for the validation study are shown in Table 4.3. MC has an aspect ratio (α) of 0.7 whereas it is 1 for MT. Surface roughness of the MC is measured using optical profilometer as explained in Ch. 3 whereas for MT a value reported by Yang [2], extracted from SEM imaging of stainless microtubes from the same manufacturer, is used. This yields the relative surface roughness (ϵ/D_h) of MC and MT to be 0.46% and 0.3% respectively. It has been proposed in the literature [44] that channel walls can be considered smooth if $\epsilon/D_h \leq 5\%$, hence considered test sections for the validation can safely be assumed as having smooth walls.

Table 4.1: Dimensions of the test sections used for validation study

Cross Section	h (μm)	w (μm)	L (mm)	α	D_h (μm)	ϵ (μm)
MC	250	360	100	0.7	295	1
MT	-	-	100	1	1000	3

Evaluation of fluid flow characteristics using adopted numerical model can be compared against experimental results with the help of average friction factor (f_f) between inlet and outlet of the considered test section. Theoretical values of friction factor in the laminar regime for considered test sections can be defined as follows:

MT: Circular

$$f_{c,lam} = \frac{64}{Re} \tag{4.18}$$

MC: Rectangular

$$f_{R,lam} = \frac{96}{Re}\left(1 - 1.3553\alpha + 1.9467\alpha^2 - 1.7012\alpha^3 + 0.9564\alpha^4 - 0.2537\alpha^5\right) \tag{4.19}$$

For the turbulent regime, Blasius law can be used to compare the frictional factor results from experimental and numerical analysis:

$$f_B = 0.3164 Re^{-0.25} \tag{4.20}$$

Experiments are performed for both geometries and total pressure drop with inlet static temperature is recorded for various mass flow rates. Data reduction for evaluation of friction factor is further performed as outlined in Ch. 3 using MATLAB for desired flow quantities. Resulting comparison is shown in Fig. 4.5. There is an excellent match between numerical and experimental values in laminar regime, although both experimental and numerical results are higher than conventional fully developed laminar flow friction factor given by Eqs. (4.18 and 4.19). Starting from transitional regime, experimental results in both cases stay higher than numerical ones. For fully developed turbulent flow, numerical results of average f_f follow the Blasius law whereas experimental results are significantly higher for both test sections.

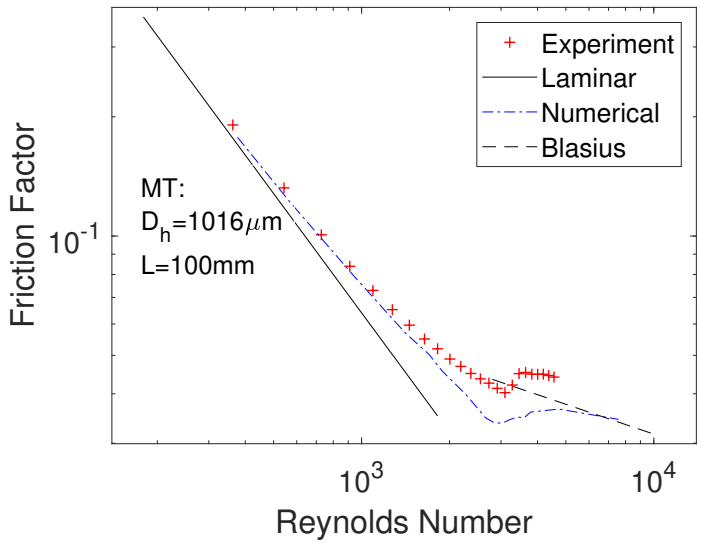

(a)

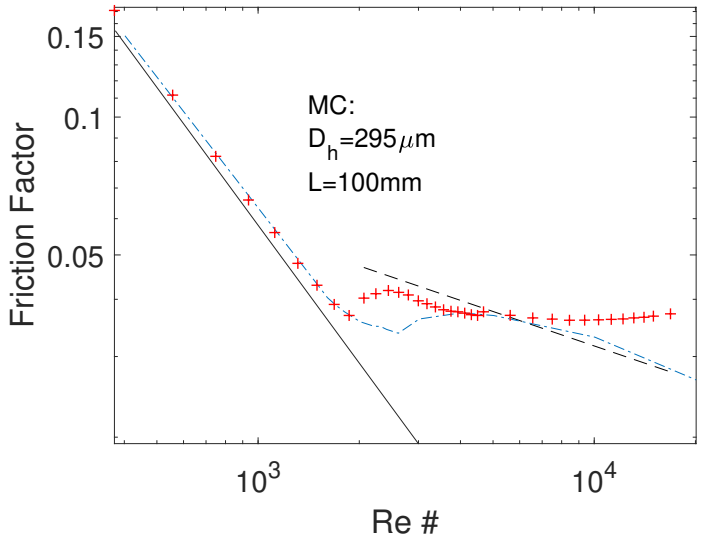

(b)

Figure 4.5: Friction factor comparison between experiment and numerical model for MT assembly (**a**), and MC assembly (**b**).

From the comparison made in Fig. 4.5, it appears that gas flow frictional characteristics in transitional regime, estimated using the adopted numerical model do not match with the experimental results. In order to clarify this ambiguity, total pressure drop for both test sections is also compared and is shown in Fig. 4.6. Focus has been paid to compare the predictions of the numerical model to the experimental pressure drop

in transitional and early turbulent regime. It can be seen that pressure drop for both MT and MC is predicted with excellent accuracy in the laminar regime as well as in the turbulent regime. In transitional regime, numerical results of MC are slightly lower than experiments whereas they are predicted quite well in case of MT.

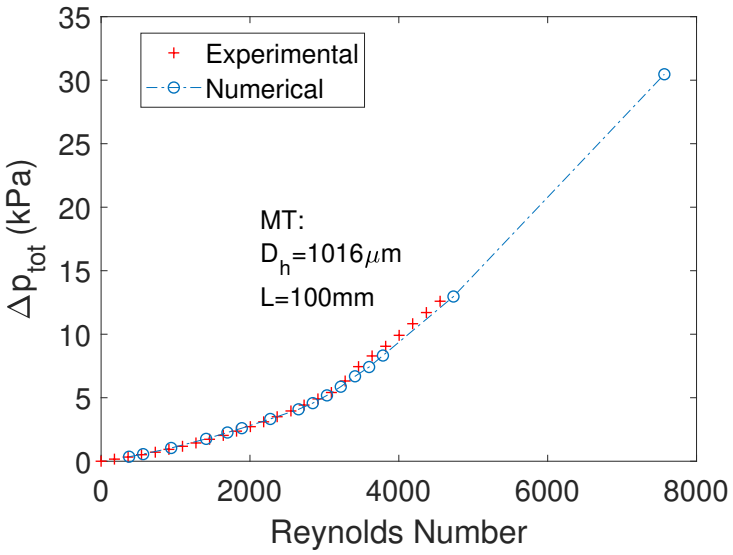

(a)

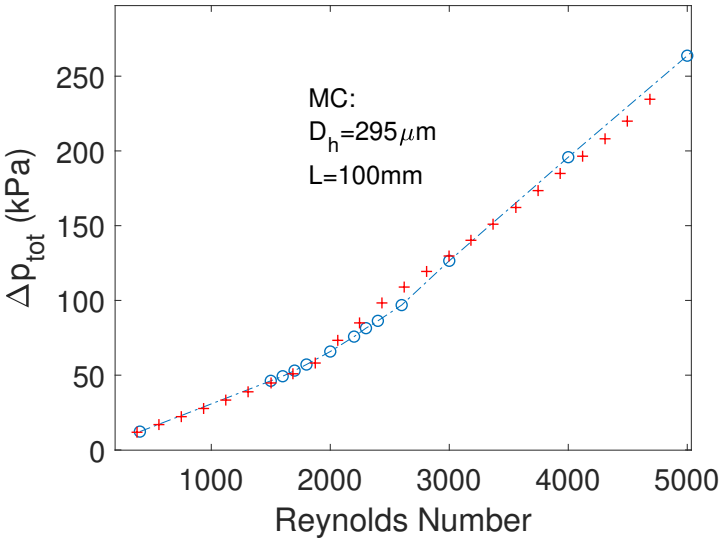

(b)

Figure 4.6: Total pressure drop comparison between experiment and numerical model for MT assembly (**a**), and MC assembly (**b**).

When the total pressure drop is compared in Fig. 4.6, both numerical and experi-

mental results showed excellent agreement in laminar and turbulent regimes with some discrepancies in the transitional flow regime. It is therefore intriguing to see that a good match between experimental and numerical total pressure drops does not yield a good agreement of f_f in the turbulent regime. Reasons of these deviations are related to data reduction methodology applied to experimental results as well as estimation of minor losses. These topics will be brought to discussion in the coming chapters. To conclude, it can be established that the trend of total numerical pressure drop in laminar, transitional, as well as turbulent regimes follows the experimental results and therefore the numerical model can be considered as validated.

4.4 Summary

An introduction to the mathematical model and governing equations of the numerical model for the analysis of internal microchannel flows are presented. Detailed description of Menter's [92] $\gamma - Re_\theta$ transitional model highlighted that model constants in original form are calibrated for external flows. Applicability of the same turbulence model for the prediction of internal transitional flows is later discussed with two modified coefficient values [1]. These coefficients were further used for the validation study where two different test sections namely circular (MT) and rectangular (MC) are employed. Comparison of experimentally evaluated friction factor to the numerical results showed that although frictional characteristics are in excellent agreement in laminar regime, this agreement deteriorates in transitional and fully turbulent regimes. However, when total pressure drop is compared between experiments and simulations, there exists an excellent agreement in laminar, transitional as well as fully turbulent regimes. This hints towards possible shortcomings/limitations of the data reduction method to deduce friction factor. Numerical model on the other hand is considered validated and will be used in the following chapters to highlight the reasons of disagreement between experimental and theoretical frictional characteristics.

Chapter 5

Fluid Flow and Heat Transfer in Microtubes

5.1 Introduction

In conventional heat exchangers, fluid is transported through circular cross sectional pipes (tubes) in order to exchange sensible heat from one fluid to the other. Because of their widespread use in conventional heat exchanging systems, it becomes a natural choice to explore their potential use even in micro heat exchanging systems. Frictional and heat transfer characteristics of circular microtubes are therefore investigated from the very earlier studies carried out in this domain e.g. Choi [6], Wang & Peng [96] and Peng et al. [39] to name a few. These researchers put forth contradictory results to an established theory for conventional sized tubes and therefore later studies critically analyzed flow characteristics inside microtubes. This effort has led to clarify the earlier ambiguities and from the literature of the recent decade, it can be established that flow characteristics inside microtubes follow conventional macro laws if there are no important scaling effects [44] present.

5.2 Adiabatic Friction Factor

In microchannels when the working fluid is a gas, an important scaling effect is compressibility which is usually not of concern in conventional tubes. A relatively higher pressure drop is needed to force the gas flow through microtubes compared to conventional pipes and therefore this can cause very high fluid velocities. This phenomenon can be ignored in the case of liquids flowing through micro dimensional pipes but is significant in the case of gas flows. Experimental studies that employ gas as working fluid inside microtubes are relatively scarce in the literature. Those studies which utilize gas flows estimate either lower [52] or higher [25] f_f in turbulent regimes. In order to revisit the fundamentals of gas flows through microtubes, pressure drop experiments are performed for microtubes with four different hydraulic diameters ranging from 133 μm to 1016 μm. Commercial stainless steel MTs as explained in Chapter 3 are cut into desired lengths using a sharp cutter to not cause any shape distortion at the outlet of MT. The average dimensions of the used MTs are tabulated in Table 5.1. Experimental methodology as explained earlier is adopted and adiabatic friction factor

Table 5.1: Dimensions of the MTs experimentally tested

Tube	D_h (μm)	L (mm)	L/D_h	$\epsilon/D_h(\%)$
MT1	133	100	751	2.25
MT2	254	400	1574	1.18
MT3	750	300	460	0.4
MT4	1016	400	363	0.3

is calculated for all the MTs tested. As MT outlet is open to the atmosphere without outlet manifold attached to the MT, an atmospheric pressure is assumed therefore at the MT outlet. Deduced results for MT1 and MT2 are shown in Figure 5.1 while for MT3 and MT4 in Figure 5.2. In the laminar regime f_f is compared to the well known Poiseuille's law given by Equation 4.18 while in turbulent regime it is compared against Blasius law (Equation 4.20). It can be seen that experimental laminar friction factor ($Re \leq$ 1000) for all the cases considered shows a good agreement with the conventio-

nal law within the experimental uncertainity. This comparison deteriorates for higher *Re*. For the two smaller tubes f_f in early turbulent regime is significantly higher than Blasius law and these findings are consistent with the previous studies [44, 2, 25].

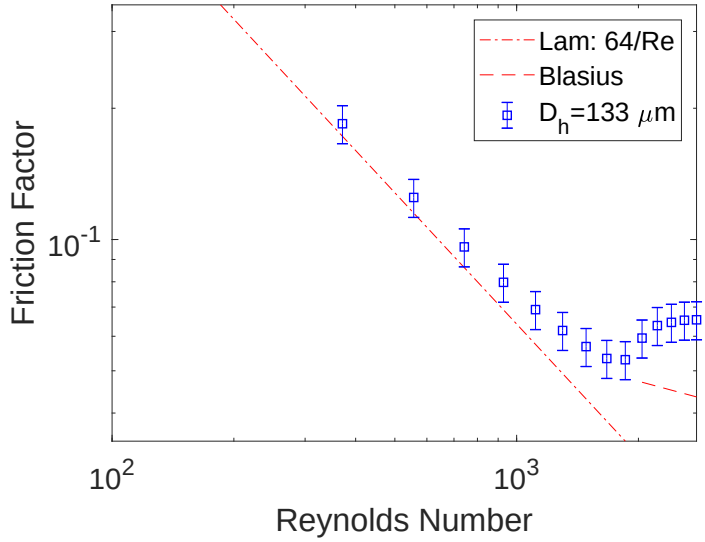

(a)

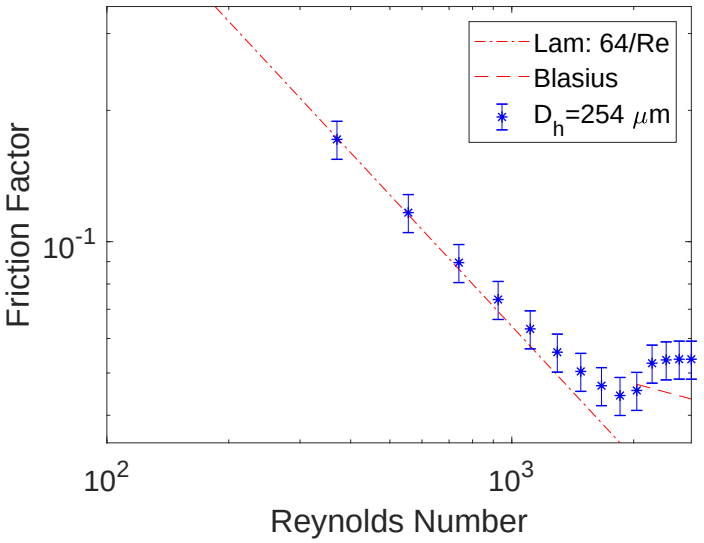

(b)

Figure 5.1: Average friction factor f_f for MT1 (**a**), and MT2 (**b**).

For relatively bigger MTs i.e. MT3 and MT4, f_f values are also higher than Blaisus in early turbulent regime, however are within experimental uncertainty. Moreover for MT3 (D_h =750 μm) f_f is slightly higher than conventional laws even for the lower laminar regime. This discrepancy will be detailed out later using a validated numerical

model.

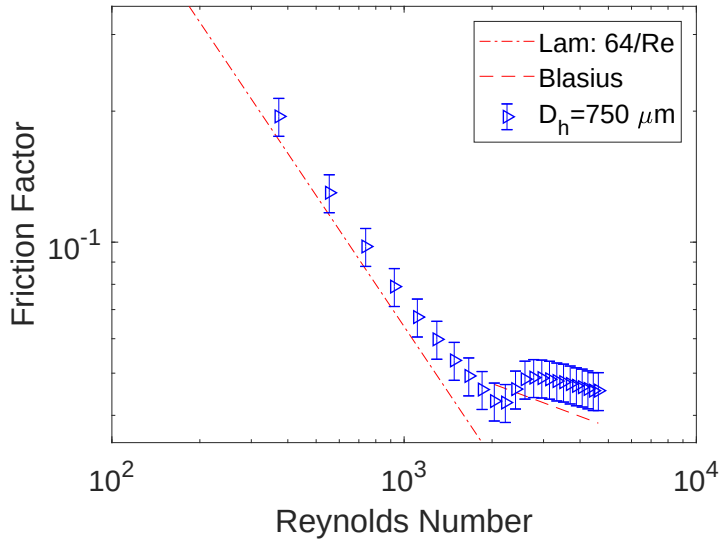

(a)

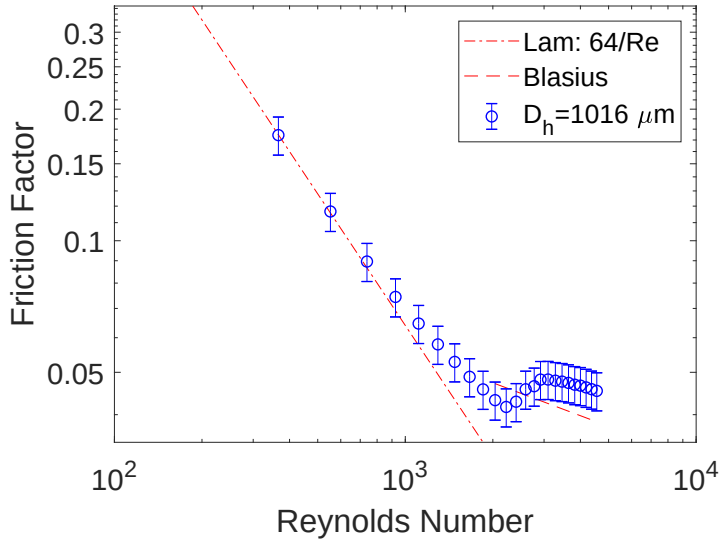

(b)

Figure 5.2: Average friction factor f_f for MT3 (**a**), and MT4 (**b**).

Comparison of all four MTs is given in Figure 5.3. As evidenced earlier, in turbulent regime f_f deviates the most for the smallest D_h (133 μm) followed by MT2. Whereas the turbulent f_f values for other two MTs (MT1 and MT2) are nearly coinciding to each other. Such comparison may lead to the conclusion that average f_f in turbulent regime is higher for MTs and this increase becomes more pronounced with a decrease in D_h below 300 μm as evidenced in MT1 and MT2.

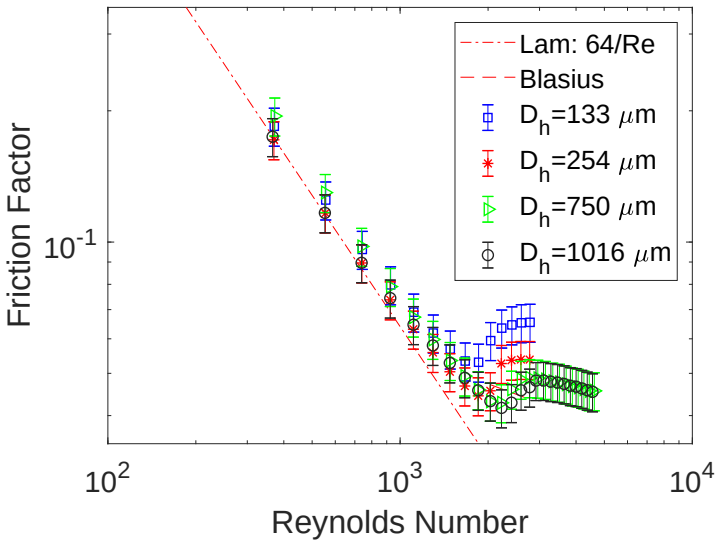

Figure 5.3: Comparison of f_f for all experimented MTs.

It is worth mentioning at this point that while performing the data reduction for the above experimented MTs, there have been certain assumptions that might have caused a relatively earlier departure of laminar f_f away from conventional laminar theory as well as a higher f_f in the turbulent regime. These assumptions are:

- Atmospheric pressure at MT outlet
- No minor losses at the inlet manifold as well as at the outlet

Therefore these assumptions will be critically examined using a numerical model in the following section.

5.2.1 Effect of Minor Losses

Improper modeling of the minor losses may result in a perceived higher pressure drop in the MT which ultimately would cause an increase in f_f evaluation. This aspect has been addressed by numerous earlier studies ([3, 97, 98]) of the last decade in order to achieve consistent laminar results with the conventional theory. As highlighted in Chapter 3 minor losses can be estimated by employing Equation 3.7 which needs the

knowledge of minor loss coefficients ($K_{in/out}$). An obvious choice for these coefficients is to assume a value recommended in general fluid mechanics text [90, 99]. The current experimental assembly uses a pipe reducer to change from a bigger tube diameter to the external diameter of MTs tested ($1.5mm$). The internal shape of this reducer causes a sudden change in the area from a bigger diameter to the internal diameter of the MT. Such sudden contraction in conventional macro flows would cause a pressure loss such that $K_{in} = 0.5 - 0.8$. Whereas for an outlet where flow experiences a sudden expansion to a comparatively very large area such as a room, a loss coefficient K_{out} may assume a value between $1 - 1.5$. The effect of different values of minor loss coefficients on the experimental friction factor for MT4 is shown in Figure 5.4.

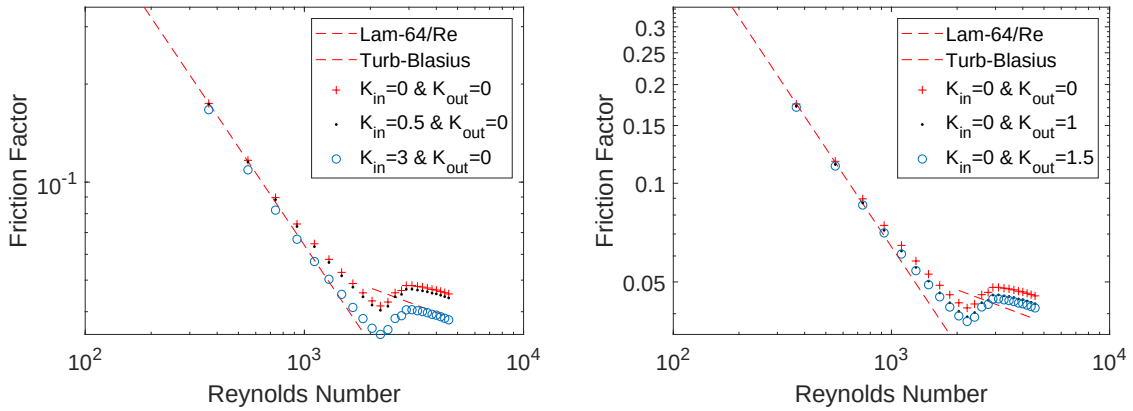

(a) (b)

Figure 5.4: Effect of minor loss coefficient for the evaluation of f_f for MT4 by different K_{in}(**a**), and K_{out} (**b**).

It can be seen from Figure 5.4a and Figure 5.4b that the introduction of loss coefficients makes f_f more compliant to conventional laws both in laminar as well as turbulent regimes. But in the case of MTs, which values are to choose and what depicts the reality is still an open question that can not be ascertained with experimental pressure drop data. It seems that K_{in} of 3 forces the experimental data to follow the conventional laws better but is such a high value of loss coefficient justified? Therefore an experimentalist can use multitudes of combinations for these coefficients in order to select one that provides better agreement between experimental f_f and conventional macroscopic laws.

On the other hand, similar values of loss coefficients for MT1 do not cause a significant change compared to the case where both loss coefficients are assumed to be zero as shown in Figure 5.5.

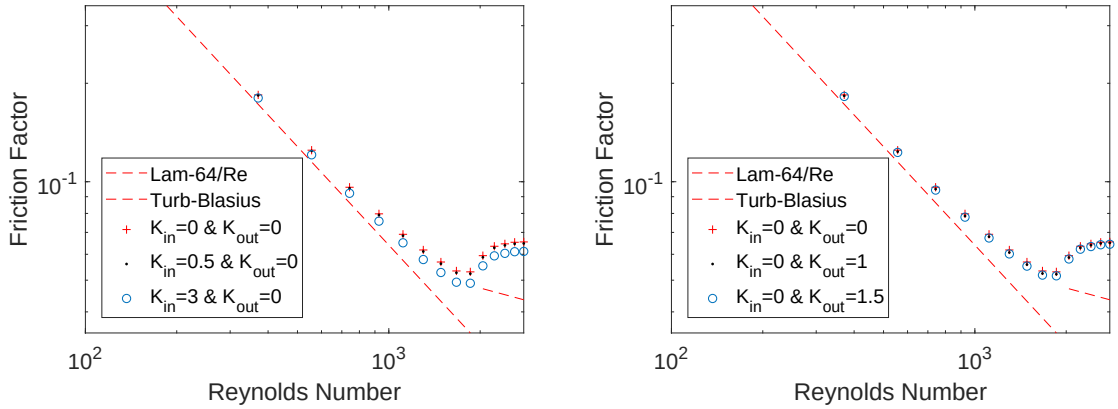

Figure 5.5: Effect of minor loss coefficient for the evaluation of f_f for MT1 by different K_{in}(**a**), and K_{out} (**b**).

This is due to the fact that pressure drop for the same Re in the case of smaller D_h MTs is significantly higher than the bigger ones and therefore minor losses represent a small share in the total pressure drop. To compare their relative shares in total pressure drop, minor losses at the inlet and outlet by assuming values of loss coefficients equal to $K_{in} = 3$ and $K_{out} = 1.5$ for both MT1 and MT4 are plotted in Figure 5.6. In both cases, after an initial spike, inlet minor losses stabilize at a constant value which is around 4% for the MT1 whereas it reaches as high as 20% for MT4. Due to this relative weight, friction factor values are more sensitive to the values assumed by loss coefficients in the case of bigger MT4 compared to MT1.

It has been demonstrated that general values of minor loss coefficients available in the literature might not be suitable to compressible gas flows inside MTs. Different values of these coefficients may affect the experimental pressure drop data such that for some specific values of $K_{in/out}$, f_f follows the macro laws closely. Therefore knowledge of these coefficients by a numerical model may serve as an aid in the experimental data reduction in order to clarify the ambiguity of f_f compliance to established macro laws.

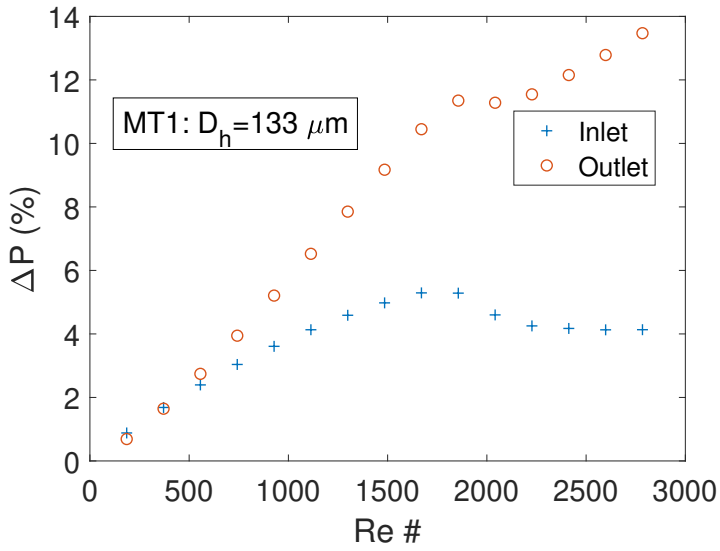

(a)

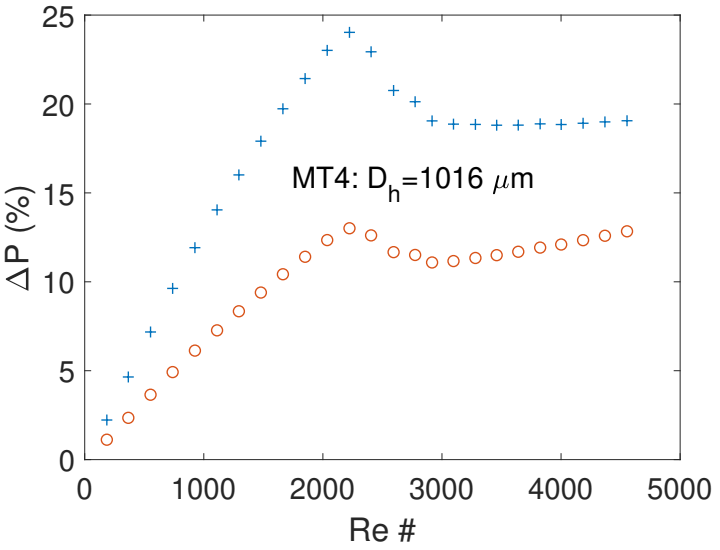

(b)

Figure 5.6: Relative share of minor pressure losses by assuming $K_{in} = 3$ and $K_{out} = 1.5$ in the case of MT1 (**a**), and MT4 (**b**).

As it has been seen that minor losses become more pertinent in MTs with bigger D_h as compared to smaller D_h, therefore numerical analysis is performed for D_h of 750 μm and 1016 μm. In order to see any possible effect of L/D_h ratio onto these minor losses, two different values of L/D_h are simulated for each tube. Dimensions of the simulated MTs are given in Table 5.2.

Numerical simulations are performed according to the methodology outlined in Chapter

Table 5.2: Dimensions of the MTs simulated for the calculation of numerical minor loss coefficient.

Tube	D_h (μm)	L (mm)	L/D_h
MT3A	750	100	133
MT3	750	300	400
MT3C	750	500	667
MT4A	1016	100	98
MT4	1016	400	394

4 by varying the inlet Re from 200 to 5000. As done previously, numerical model is validated against experimental pressure drop data of the MTs with same dimensions as tabulated in Table 5.2 and the comparison is shown in Figure 5.7 for MT3A and MT4. Similar match has also been achieved for other cases however, are not presented here for the sake of brevity.

Comparison of K_{in} for all the simulated MTs is shown in Figure 5.8. It is highest at the lowest Re and decreases steeply in the lower laminar regime. It attains a quasi saturation in turbulent regime for both D_h simulated with MT3 (all lengths) achieving a value close to 1 whereas K_{in} for MT4 (all lengths) settles down around 1.4. Both D_h show that values suggested by the literature ($K_{in} = 0.4 - 0.8$) seriously underestimate the minor losses in the lower laminar regime. It can also be noticed that there is not much difference in the K_{in} values for different L/D_h ratios for the same D_h.

K_{out} on the other hand stays close to zero for the range of Re simulated in this study and therefore shows that gas undergoes a complete expansion without suffering from a pressure loss equals to the dynamic pressure ($K_{out} = 1$) as suggested by the literature. Comparison of K_{out} for MT3A and MT4 as a representation is shown in Figure 5.9.

A variable value of K_{in} with Re for each D_h can be represented by a power law using numerically evaluated values earlier as shown in Figure 5.8. Such a definition can then be used to aid in experimental data reduction instead of assuming a constant recommended value which generally is validated for incompressible macro flows. When numerically evaluated inlet loss coefficient is used for experimental data reduction, an

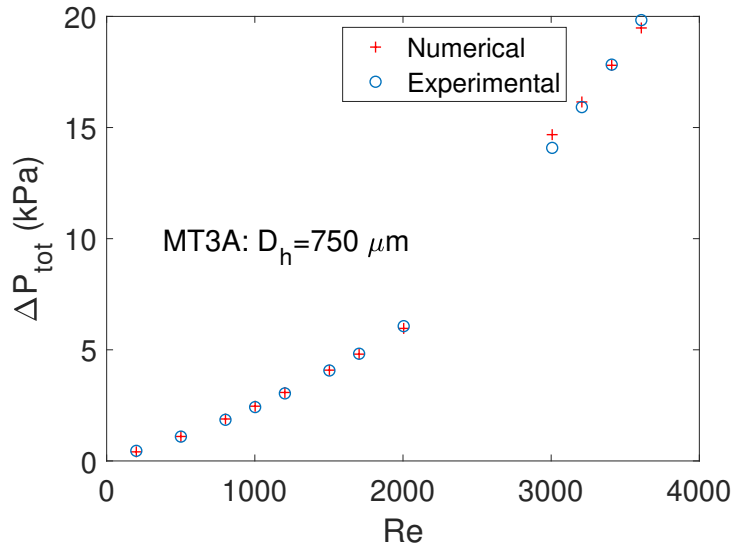

(a)

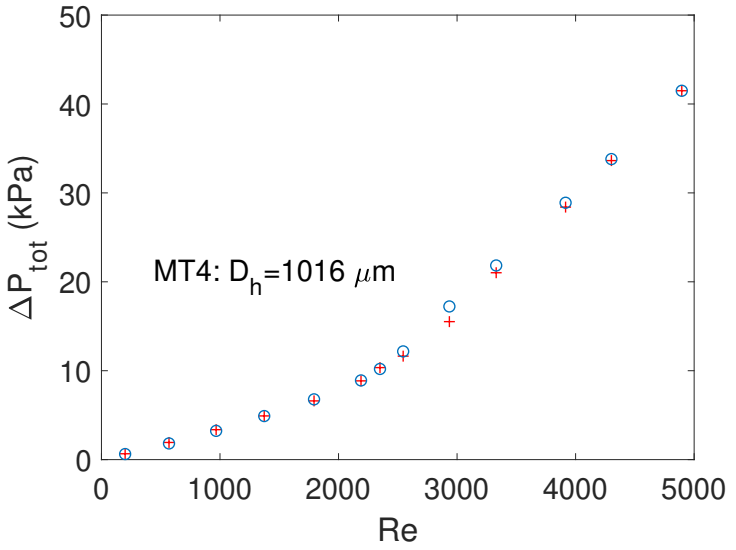

(b)

Figure 5.7: Comparison of experimental and numerical total pressure drop of the assembly in case of MT3A (**a**), and MT4 (**b**).

improvement in agreement between evaluated f_f and macro law can be seen for both MT5B and MT6A as shown in Figure 5.10. It is more pronounced in the MT4A which has L/D <100 whereas in the case of MT3 which has $L/D = 400$, such effect is only relevant in the early turbulent regime. For MT4A which is the same MT as presented in validation section of Chapter 4, it was shown that although there is an excellent match between pressure drop between numerical and experimental data but the evaluated

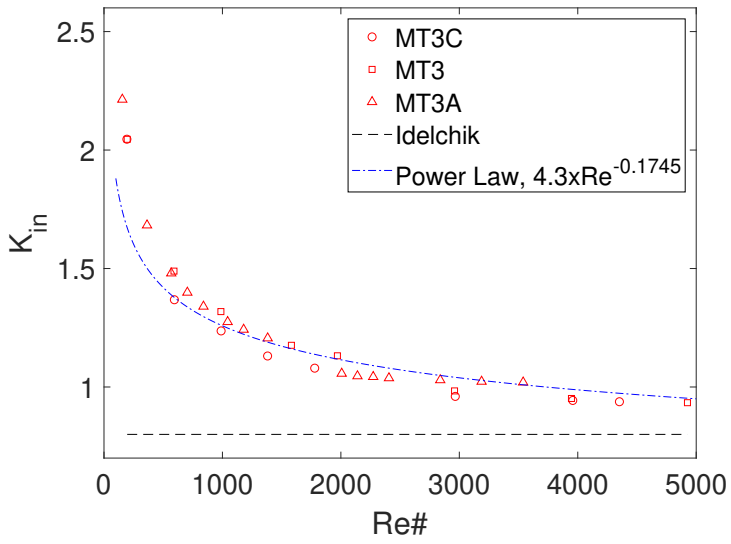

(a)

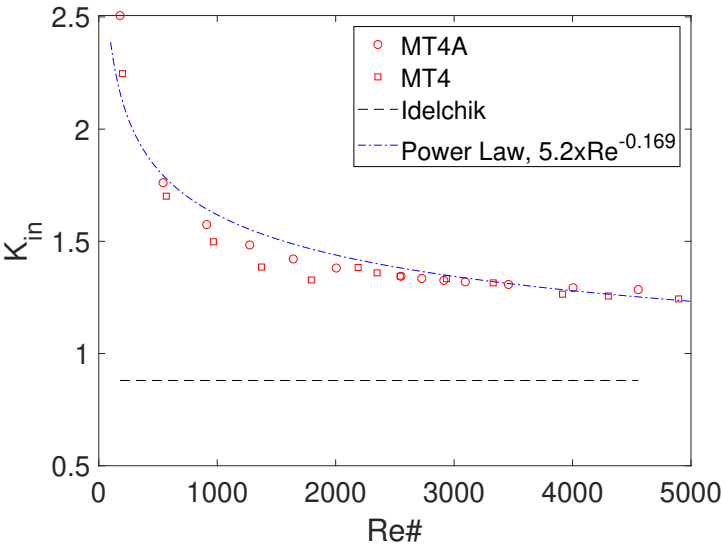

(b)

Figure 5.8: Numerically evaluated inlet minor loss coefficient (K_{in}) for MT3 series (**a**), and MT4 series (**b**).

experimental f_f was higher in the high laminar regime and transitional as well as the early turbulent regime. It has now been demonstrated how a wrong estimation of K_{in} may result in frictional characteristics that are deviant to the conventional laws or at least do not depict the reality.

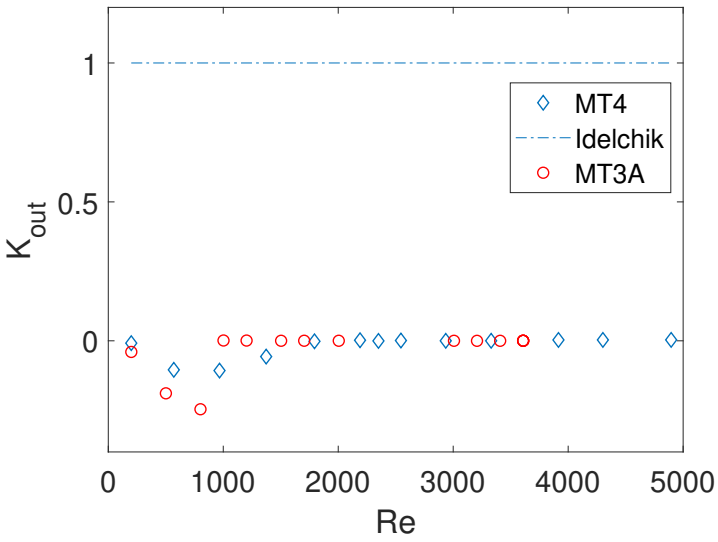

Figure 5.9: Comparison of numerically evaluated outlet loss coefficient K_{out} for MT3A and MT4.

Semi-local f_f

Numerical analysis conducted earlier has helped to elucidate that for the range of Re investigated, K_{out} stays close to zero and hence can be neglected during the experimental data reduction for the evaluation of average f_f. Moreover, it also provides an alternative means to evaluate K_{in} beforehand to aid in experimental data reduction, for the known dimensions of the MT. However, it has been seen that when compared with Blasius law experimental f_f either stayed slightly lower (MT4A) or higher (MT3) in the early turbulent regimes. Deviation of turbulent friction factor (higher or lower) than Blasius has also been reported by Morini et al. [52], Kawashima et al. [100], Yang et al. [78] and Celata et al. [22]. Since the average value of f_f is usually reported which suffers from deviation therefore, it would be interesting to perform an average from the semi-local f_f evaluated numerically. Fluid properties are extracted in the five planes (x=0L, 0.25L, 0.5L, 0.75L and L) from the numerical analysis performed earlier. Semi-local values are extracted by employing Equation 3.4 between the two consecutive planes. The comparison between numerically evaluated semi-local values and experimental average values for the two MTs of D_h =750 μm (MT3A and MT3) is shown in Figure 5.11. For the shorter MT amongst these two (MT3A), numerical as

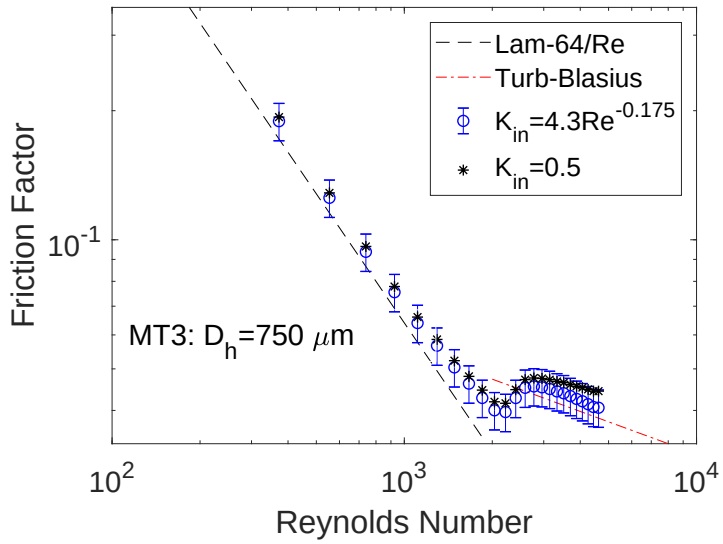

(a)

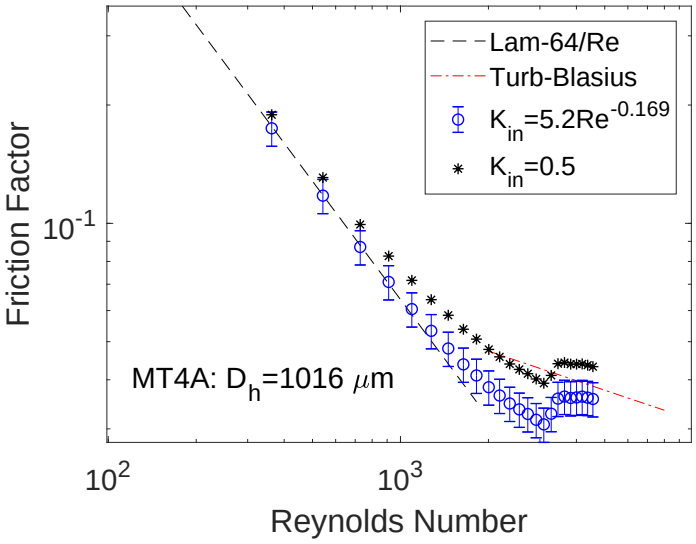

(b)

Figure 5.10: Experimental f_f comparison using numerically evaluated K_{in} for MT3 (**a**), and MT4A (**b**).

well as experimental turbulent average f_f at Re =3000 is nearly 20% higher as reported by Kawashima et al. [100] whereas it is only 4.6% higher in case of MT3 which is well within the experimental uncertainty of f_f. As expected, semi-local f_f is highest in the upstream part of the MT due to strong inlet effects for both MTs. Strictly speaking velocity profile for gas flow inside MT, due to acceleration caused by its compressible nature, never gets to a developed profile and therefore it is not possible to

define hydraulic entry length as is the case with incompressible liquid flows. However, propagating the same idea it is evident that for the MT with smaller L/D_h developing pressure loss is quite significant and hence causes a higher f_f between x/L =0-0.25. A similar analysis can be performed for the tubes having D_h =1016 μm where MT4 strictly follows the Blasius in the turbulent flow regime whereas MT with smaller L/D_h stays 7% lower than Blasius at the highest Re simulated. It is intriguing to notice that close to transitional Re, semi-local f_f stays consistently lower than average theoretical values for $x/L = 0.25 - 0.5$ as well as $x/L = 0.5 - 0.75$ whereas it follows macro laws in the last part of the MT i.e. $x/L = 0.75 - 1$. Therefore even though in the entrance region semi-local f_f is quite high, due to acute decrease in the transitional regime, evaluated average f_f stays slightly lower than Blasius which is also experienced with experimental data.

Such behavior has not been observed for any other channel and it may be pertinent to the $L/D_h \leq$100. Lower values of local f_f compared to fully developed values are also reported by Abraham et al. [1] where using currently employed $\gamma - Re_\theta$ transitional model, authors show that an intermittent nature of the flow (not fully laminar neither fully turbulent) may persist inside the tube which results in a lower value of local f_f compared to the fully developed value (given by Poiseuille's law) between $20 < x/D_h < 115$. Therefore if the length of the tube is considerably short and hydraulic diameter is big enough (100 mm and 1016 μm in our case respectively), local f_f may stay lower for most of the length of MT after an initial hike due to entrance effects. This ultimately causes the average f_f lower than the Blasius in the turbulent regime. However, if the L/D_h is reduced further, beyond a point whole length of MT suffers from the entrance effects and apparent f_f is higher than conventional laws. This is evident from all the presented results in the x/L =0-0.25 where semi-local f_f is much higher than the rest of the sections considered. For all the MTs with $L/D_h >$100, semi-local f_f in the last two sections ($x/L = 0.5-0.75$ and $x/L = 0.75-1$) strictly follows conventional laws in laminar as well as turbulent regimes whereas a high value of f_f in the entrance regions shifts the average curve such that resulting f_f when evaluated between inlet and outlet

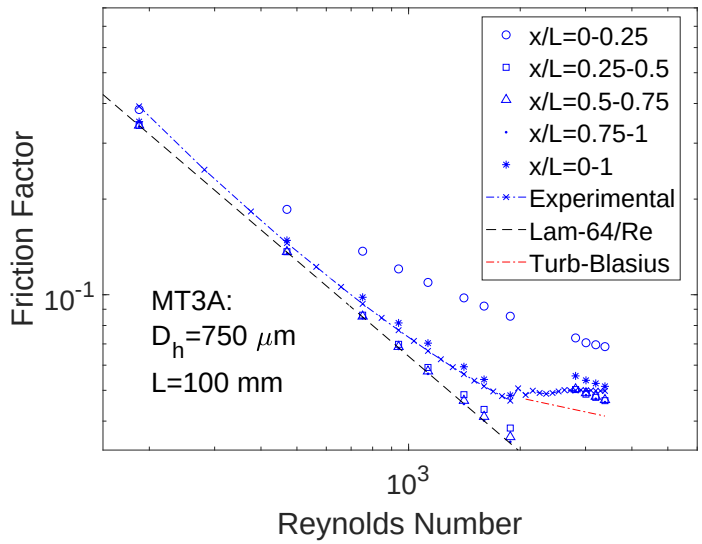

(a)

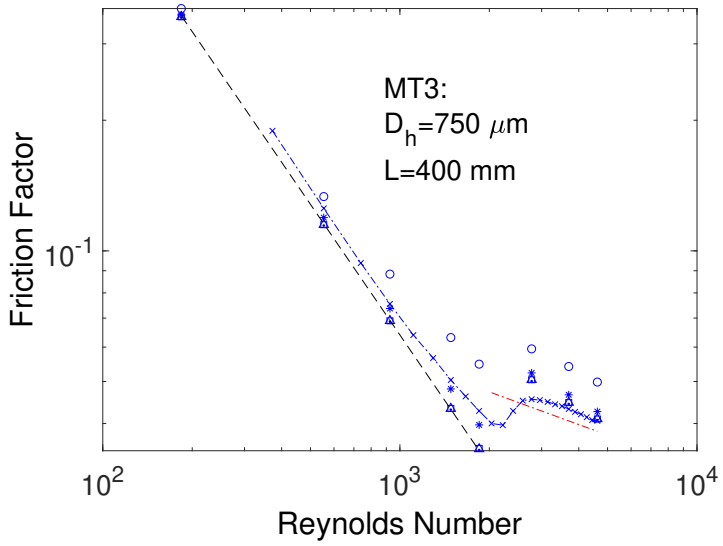

(b)

Figure 5.11: Comparison between semi-local and average f_f against experimental results for MT3A (**a**), and MT3 (**b**).

departs from the laminar theory in high laminar Re and stays higher than Blasius in turbulent regime. Similar findings were reported by Cheng et al. [101] where they recommended to use L/D_h >100 for evaluation of f_f without significant differences from conventional theory. Barlak et al. [102] also found that for MTs having a L/D_h smaller than 100, seriously affects the overall f_f where in most cases f_f values were higher than Blasius due to entrance effects. But for two MTs they were also lower as

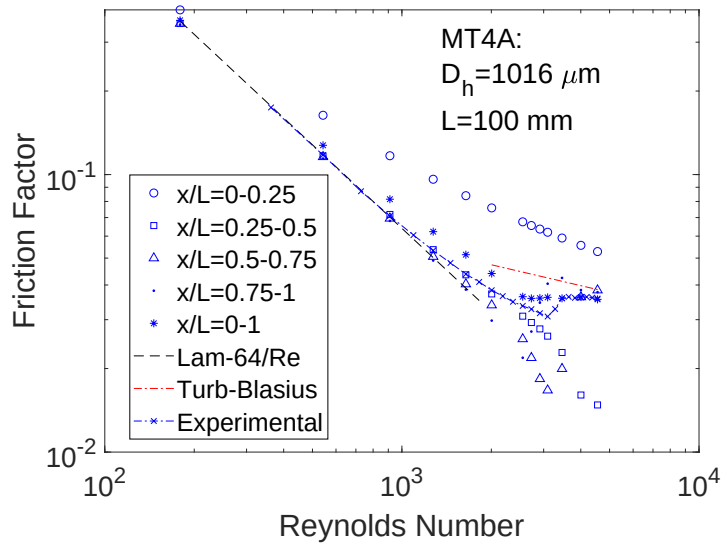

(a)

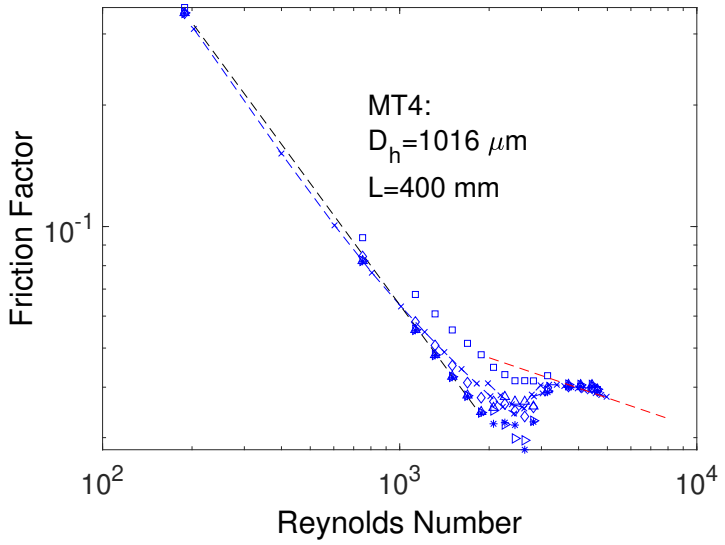

(b)

Figure 5.12: Comparison between semi-local and average f_f against experimental results for MT4A (**a**), and MT4 (**b**).

experienced in the current study. Flow characteristics of MTs with L/D_h smaller than 100 is therefore, an area that needs further investigations.

5.3 Forced Convection

Heat transfer in a fluid occurs generally by the two well known mechanisms namely convection and conduction. Heat transfer of fluid through conduction theoretically pertains to a stagnant fluid i.e. diffusion of heat within the fluid in the absence of fluid movement. Conduction occurs through the diffusion path where energized molecules transfer the energy to the molecules that possess less energy and thermal conductivity (k_f) is used to compare amongst various materials for their ability to conduct heat. Heat transfer through conduction is usually significant in solids due to highly dense arrangement of molecules whereas in fluids, molecules are far apart and hence this diffusive heat transfer takes a considerable amount of time in order to reach in steady state.

Convection, on the other hand, refers to the heat flow by means of the two sub mechanisms of advection (movement) and diffusion, occurring in parallel normal to the wall boundary and hence normal to the fluid flow direction. A dimensionless parameter that is used to evaluate the contribution of momentum diffusion with respect to the thermal diffusion for a moving fluid is known as Prandtl number (Pr) which is defined as:

$$Pr = \frac{\nu}{\alpha_{th}} = \frac{C_p \mu}{k_f} \tag{5.1}$$

where ν is kinematic viscosity, α_{th} is thermal diffusivity and C_p is the specific heat of the fluid and is a weak function of the temperature for the gases. Liquid metals normally have Pr much lower than 1 indicating that heat conduction (thermal diffusion) is more efficient than momentum diffusion whereas a lubricant oil has $Pr >> 1$ which means that that fluid diffuses momentum better than thermal energy.

Heat transfer in fluidic systems is generally enhanced by the movement of fluid close to a solid wall. Forced convection is referred to as the movement of the fluid at the expense of external input/source as opposed to the natural convection which occurs merely due to temperature gradient (buoyancy) within the fluid. When the fluids are

moving close to a solid wall, a measure of resulting heat transfer enhancement compared to a stagnant fluid is represented as a dimensionless number called as Nusselt number:

$$Nu = \frac{Advection + Diffusion}{Pure\ Conduction} = \frac{hD_h}{k_f} \tag{5.2}$$

where h is the convective heat transfer coefficient of the fluid. Nu represents the ratio of the heat transfer through convection and the pure conduction i.e. heat diffusion if the fluid had been at rest. A value of unity for Nu signifies that heat transfer through the fluid is purely conductive (diffusive only) without any advective part.

There are two main thermal boundary conditions which can be applied at the channel wall in order to study effect of forced convection on the overall heat transfer: boundary condition where a constant temperature at the channel wall is maintained (T boundary condition) or a boundary condition in which a uniform heat flux is imposed at the wall (H boundary condition). In the context of microtubes, it is quite common to heat the tube surface using Joule's heating in a laboratory environment. Such boundary condition should ideally correspond to an H boundary condition where a constant wall heat flux (q_w) is imposed along a finite heating length of the tube. As mentioned in Chapter 3, in the current work similar boundary condition is applied to study the forced convection in microtubes. For internal wall bounded flows (pipes and ducts), various empirical correlations exist to estimate the average value of Nusselt number (Nu_{av}) in all fluid regimes, from laminar to transitional and to fully turbulent. Correlations proposed by Gnielinski are used the most due to their better agreement with various experimental groups. Proposed correlations have been revisited [29] by the same author later and for circular tubes, under H boundary condition these are given as follows:

Laminar Regime ($Re \leq 2300$)

$$Nu_{lam} = {Nu_1}^3 + 0.6^{0.3} + (Nu_2 - 0.6)^3 + {Nu_3}^3 \tag{5.3}$$

where,

$Nu_1 = 4.354$

$Nu_2 = 1.953(RePrD_h/L)^{1/3}$

$Nu_3 = 0.924(Pr)^{1/3}(ReD_h/L)^{1/2}$

Turbulent Regime ($10^4 \leq Re \leq 10^6$)

$$Nu_{turb} = \frac{(0.0308/8)^4 10^4 Pr}{1 + 12.7\sqrt{0.0308/8}(Pr^{2/3} - 1)}\left[1 + (D_h/L)^{2/3}\right] \tag{5.4}$$

Transitional Regime ($2300 \leq Re \leq 10^4$)

$$Nu_{tran} = \frac{10^4 - Re}{10^4} Nu_{lam} + \frac{Re - 2300}{10^4 - 2300} Nu_{turb} \tag{5.5}$$

The results presented in this work will be compared with these correlations to validate the experimental test rig for the evaluation of heat transfer characteristics of the microflows.

5.3.1 Experimental and Numerical Analysis

Experiments are performed for a single MT having a D_h of 504 μm with a length (L) of 200 mm. Calibrated K-type thermocouples are used at five axial locations along the length of the MT. Mass flow at the inlet is varied such that inlet Re is in the range of 400 to 10000. A power of 2.3 W that translates into Wall Heat Flux of $\sim$7 kW/m^2 for the given surface area of MT, is applied at the MT wall. Frictional characteristics of the diabatic gas flows considered in this study are shown in Figure 5.13. It can be seen that f_f in the laminar regime is higher than the adiabatic theory due to increased viscosity. Wall temperature measured at various points along the length of the MT is also shown in Figure 5.13b which shows an increase in wall temperature along the length of MT. Since the walls of the experimented MT are made of steel having a high thermal conductivity, it can be said fairly accurately that it is representative of gas

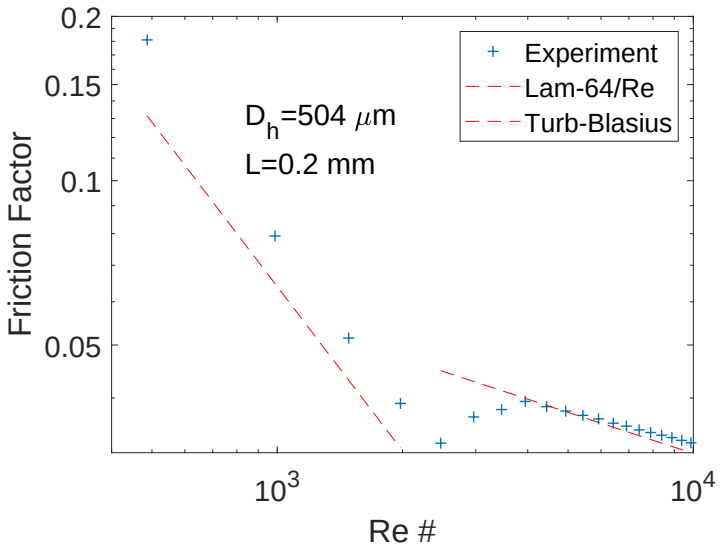

(a)

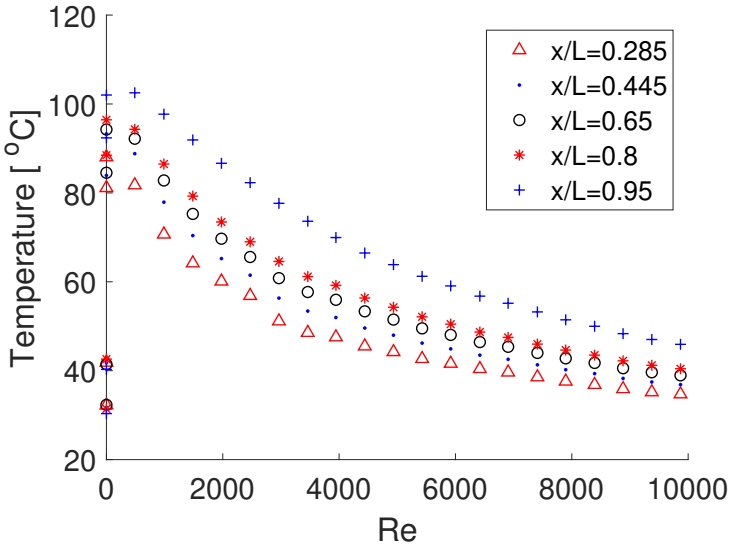

(b)

Figure 5.13: Moody chart for the diabatic flow (**a**), and wall temperature from thermocouple readings (**b**).

temperature along the inner wall of the MT. Yang [2] performed a sensitivity analysis for the gas microflows and showed that for the currently investigated MTs, given the uncertainty of the thermocouples MT wall temperature can be considered equivalent of the gas temperature along the inner wall of the MT. Experimental temperature data is further processed according to the methodology described in Chapter 3 and Nusselt number is evaluated using Equation 3.8 which is being recalled here for convenience:

$$Nu_{av} = \frac{hD_h}{k_f} = \frac{D_h q_w}{k_f(\overline{T}_w - \overline{T}_b)}$$

The resulting Nu_{av} from experimental MT is shown in Figure 5.14 which shows good agreement with aforementioned Gnielinski's correlation in the transitional regime but is significantly lower than theoretical prediction in the laminar regime.

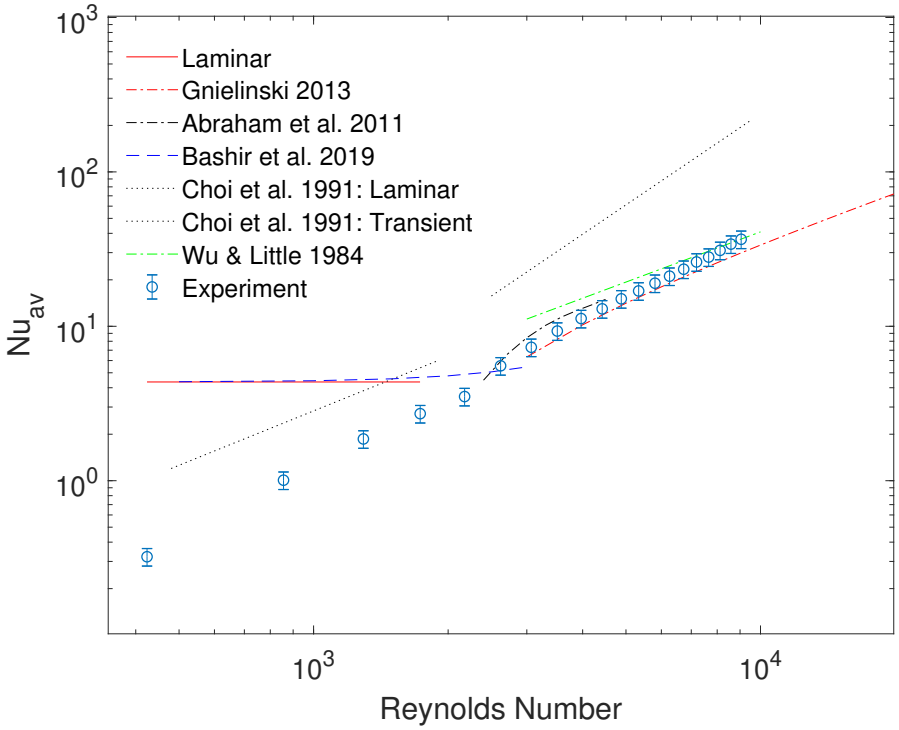

Figure 5.14: Nusselt number for experimented MT with constant wall heat flux.

For a fully developed flow inside a tube, the mean Nu_{av} in the laminar flow regime reduces to a constant value of 4.36 (Nu_1 in Equation 5.3) considering an H boundary condition. On the contrary, experimental results show a dependency on Re even in the laminar regime. The similar linear trend has also been reported in an earlier study of the air flow inside MT by Choi et al. [6] as well. For very low Re the value of Nu seems to reach less than unity hinting that there is an adverse effect on the heat transfer coefficient using forced convection which appears to be questionable. Thus to qualify whether this behavior is physical or not, local heat transfer characteristics of

the compressible gas flow must be studied. As the current experimental setup does not have pressure and temperature sensors in the entrance region therefore, it would be of interest to see if such behavior of gas flows at lower Re can also be verified using a numerical model. Numerical simulations are performed for the experimented MT using the previously described numerical MT geometry and mesh. Instead of adiabatic boundary condition at MT wall, a heat flux of 7.5 kW/m^2 is applied in this case. The rest of the boundary conditions are kept similar to that of the adiabatic numerical studies performed earlier. A comparison of numerical and experimental Nu_{av} is shown in Figure 5.15 where numerical values in the lower laminar regime are in very good agreement with the analytical value of 4.36. Moreover, there exists a good match between numerical and experimental results in the turbulent regime where both are slightly higher than Gnielinksi's correlation and rather follow the correlation presented by Wu and Little [5]. This confirms that experimental results in the lower laminar regime are misleading due to unconventional effects pertinent to the experimental setup being employed in this work and moreover these effects become less significant with higher inlet mass flow (Re) values.

In fact, if the experimental settings are critically examined one can establish the following two differences amongst experimental and numerical setups:

- the real heating length, and
- presence of significant conjugate heat transfer effects between solid walls and fluid

As mentioned earlier a uniform heat flux is applied along the total length of the MT in the numerical model. Whereas for a typical experimental campaign, heating is applied for a specific length of the MT which does not begin directly from the inlet of MT. It starts after a certain axial distance rather in order to cater for, fittings that connect MT to the piping coming from the gas supply as shown in Figure 5.16. Similarly, there is a finite length towards the downstream end of MT where heating is not applied in the experimental setup.

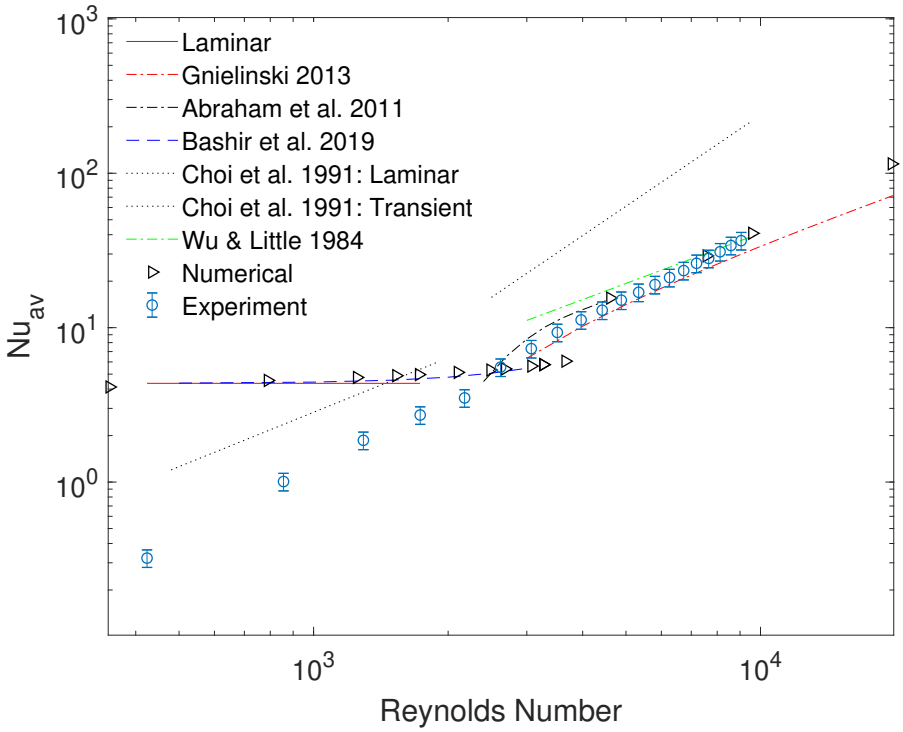

Figure 5.15: Comparison of experimental and numerical Nusselt number for experimented MT.

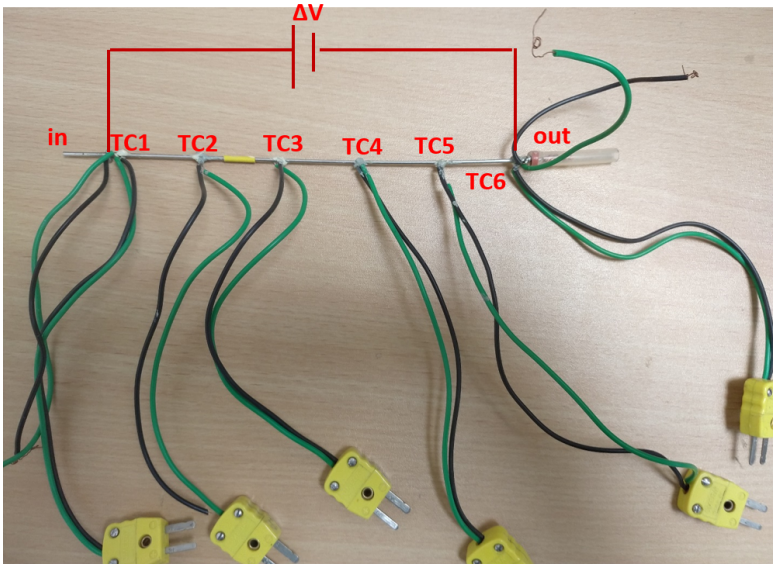

Figure 5.16: Experimented MT with attached thermocouples along the length of the wall.

In general, it is assumed that bulk temperature of the gas increases linearly along the length of the MT under H boundary condition, therefore if measurements of inlet and outlet temperatures are available, the average bulk temperature of the fluid $\overline{T}_b$ inside

MT can be estimated as:

$$\overline{T}_b = \frac{T_{in} + T_{out}}{2} \tag{5.6}$$

The linearity of fluid bulk temperature is evident from Figure 5.17 which is extracted from the numerical simulation of experimented MT. For all the cases of simulated Re the fluid temperature T_f increases linearly from inlet to the outlet of the MT for a constant heat flux at the wall. However, as soon as compressibility effects get stronger at higher values of Re, due to sudden decrease of pressure T_{wall} decreases suddenly close to the outlet of MT. As said before, in the experimental test heating of the MT is done after a finite length (∼20 mm in this case) which alters the temperature profile in the entrance region of the MT due to strong axial conduction in the solid wall of the MT. Due to high thermal conductivity wall temperature is diffused upstream the start of heating point which causes an increase in the gas temperature even in the unheated entrance region.

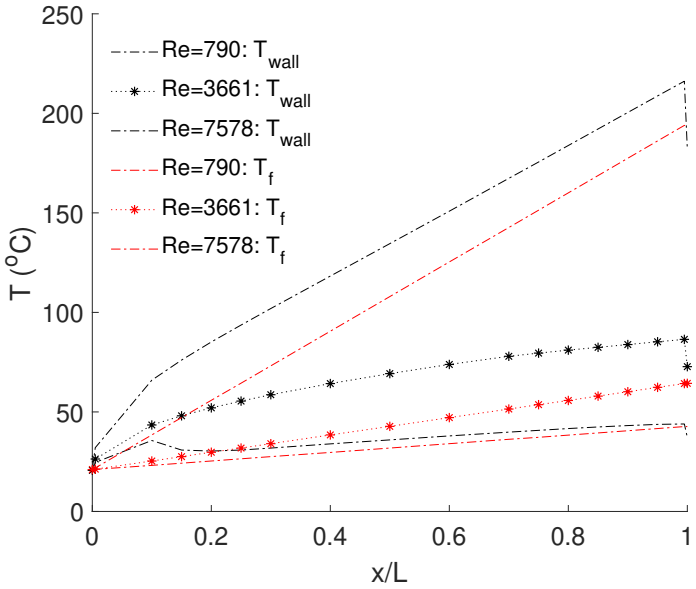

Figure 5.17: Wall temperature and local fluid bulk temperature (T_f) along the length of the MT.

Using the current experimental setup Yang et al. [2, 30] have shown that due to strong conjugate heat transfer effects present at the low Re, the gas temperature inside MT is far from being linear. They performed numerical simulation by imposing the

experimentally measured wall temperature on the MT wall. Contrary to the current numerical model they also modeled the solid wall with a respective thickness which allowed the observation of the axial wall conduction in the unheated entrance region of MT. Local fluid temperature for a MT of 750 μm as evaluated by their numerical model is shown Figure 5.18 where they showed that an estimation of linear temperature highly underestimates the net heat flux transferred to the fluid from the wall Q_f and hence results in non-physical Nu_{av} values in the laminar regime as evidenced in Figure 5.14. Axial wall conduction effects for the higher mass flows are lower and therefore linearity of the local fluid temperature is maintained enabling the correct evaluation of the experimental Nu_{av} in transitional and turbulent flow regimes. Similar conclusions have been also presented by Herwig et al. [103] showing that a linear interpolated average based on the inlet and outlet temperatures when strong axial wall conduction effects are present results in a very low experimental value of Nu_{av} in the laminar regime.

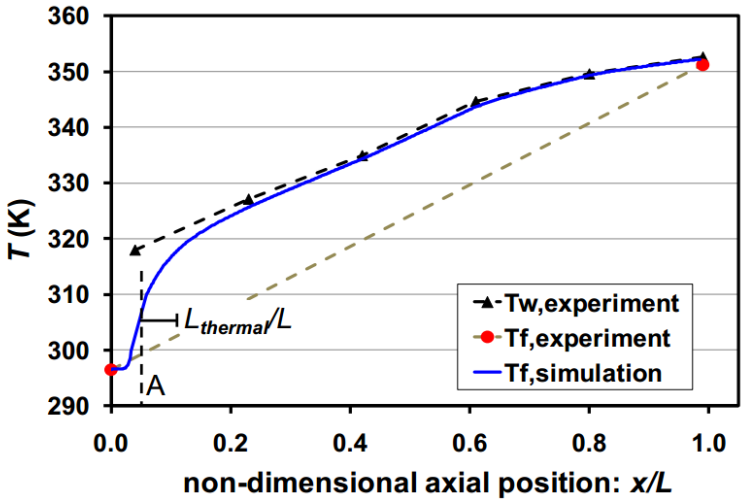

Figure 5.18: Wall temperature and local fluid bulk temperature (T_f) along the length of a MT with D_h =750 μm at an arbitrary Re in the laminar regime (reproduced from [2]).

It is important to turn the attention now to the estimation of the bulk temperature of the gas flow inside a heated MT. In the current experimental campaign, outlet temperature is measured within a small (20 mm in length) plastic pipe at the end of

the MT as shown in Figure 5.16. A small piece of metallic foam made from Nickel in inserted in the pipe 1 mm away from the MT exit and a thermocouple was directly attached with the metallic foam. A steady state temperature of the metallic foam is then considered as the outlet temperature of the fluid. Due to gas flow acceleration close to the outlet, a thermocouple placed directly close to the outlet measures a temperature that is neither static nor total and therefore it has been recommended in literature [27, 31] to measure the outlet temperature of compressible flows such that velocity is reduced allowing the gas to recover its dynamic temperature. From the standpoint of the numerical simulation, therefore using a total temperature at the outlet cross section of the MT will be closer to the experimentally measured values. To elucidate this, Nu_{av} estimated using an average of gas bulk temperature evaluated from static (T_{static}) and total temperatures (T_{total}) of inlet and outlet from the numerical simulation of MT3 is shown in Figure 5.19. It can be seen that when the total temperature of the MT outlet section is used in Equation 5.6, resulting Nu_{av} follows the experimental results because as said earlier, in the experimental readings the measured outlet temperature of the gas is more representative of the total temperature due to low velocities inside metallic foam. If the static temperature of the gas at the outlet is used instead, Nu_{av} suffers a decrease for $Re > 1000$ which is due to the considerable differences in static and total temperatures at the outlet cross section. Convective heat transfer coefficient h can be estimated by rearranging Equation 3.8 as follows:

$$h_{av} = \frac{q_f}{(T_w - T_b)} \tag{5.7}$$

As static temperature decreases along the length of the MT due to flow acceleration, using the static temperature therefore, underestimates the total flux transferred to the fluid (q_f). Moreover, it apparently increases the wall and fluid temperature difference. An underestimation of the q_f causes a decrease in the numerator of Equation 5.7 while an overestimation of the apparent wall and fluid temperature difference causes an increase in the denominator and this ultimately leads to Nu_{av} values that are

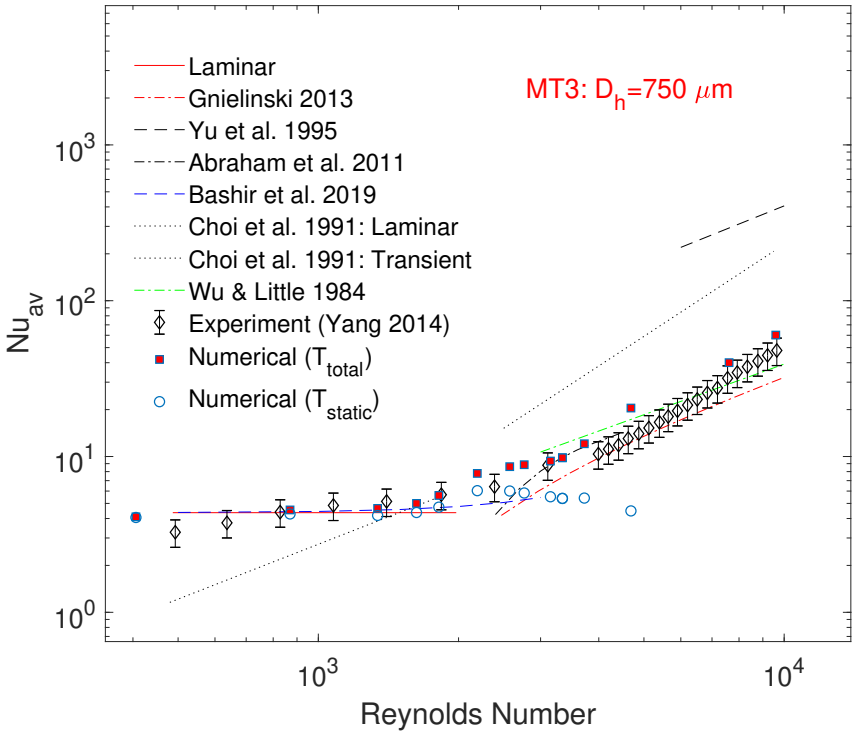

Figure 5.19: Comparison of numerical and experimental Nu_{av} for MT3.

lower than experimentally measured values. As shown in Figure 5.20a, for the current simulated case of MT3 difference between the total and static temperature at the outlet is 20% at Re of 5000 and reaches as high as 70% at Re of 10000. Using therefore, static temperature for the estimation of the bulk temperature ultimately leads to an apparent smaller Nu_{av}. In the experimental setup, inlet temperature, however, is generally measured before the heating length of the MT (in the entrance manifold in current case) and it can be seen from Figure 5.20b that there is no significant difference between static and total temperatures at the inlet and therefore either can be used while calculating the T_b of the gas flow inside MT. Thus for further evaluations of Nu_{av} from numerical results, total temperatures are utilized instead of static ones.

To better understand the heat transfer characteristics, the gas flow along the length of MT, local values assumed by Nu at 17 axial cross sections are plotted in Figure 5.21 for various Re. It shows that local Nu reduces steeply in the developing region of the MT and then settles to a lower value after x/L of 0.2. This is further evident

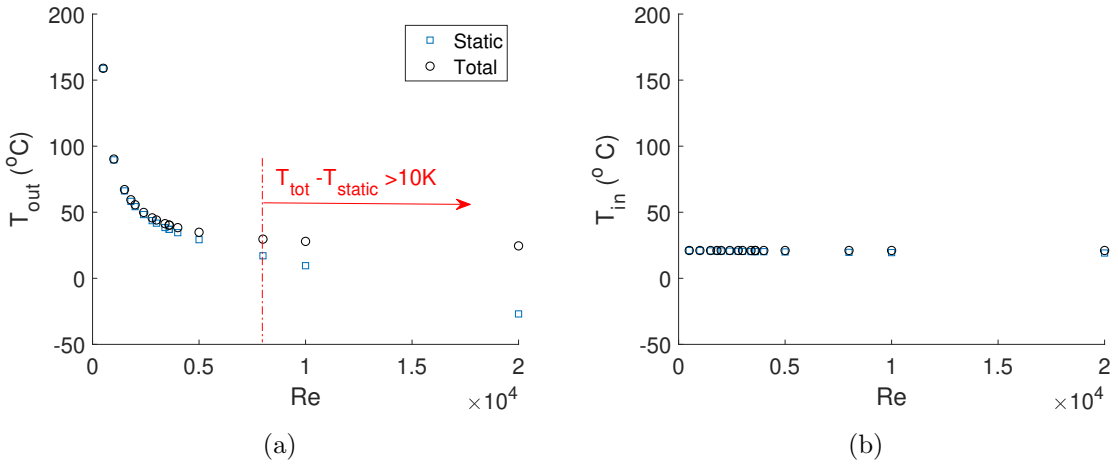

Figure 5.20: Difference between static and dynamic temperature for simulated MT at the outlet (**a**), and at the inlet (**b**).

in Figure 5.21b that for low range of Re after the developing length, Nu stabilizes close to the conventional laminar value of 4.36 for H boundary condition. As the Re increases, developing length reduces and hence the initial steep decrease moves in the upstream direction. Local Nu then increases to a maximum value and then continues to decrease further downstream.

Such behavior is in contradiction to the local Nu reported by Abraham et al. [104] for incompressible flows where after initial decrease and subsequent increase, local Nu stays constant over the entire length of the MT. This is due to the fact that liquids follow a linear decrease of pressure and hence a linear change in fluid thermal properties from MT inlet to the outlet whereas due to compressibility gas flows experience a decrease in the cross sectional static temperature as discussed earlier. This decrease in static temperature then causes a further reduction of Nu downstream. In order to calculate the local Nu reported in Figure 5.21, static averaged (mass flow based) cross sectional temperatures are used. It has already been shown that for the gas flow, the use of static temperature to calculate the Nu_{av} yields much smaller values than experimental observations in the transient and turbulent regime. This happens because not all the thermal energy gained from the wall is used by the gas to increase its temperature rather a substantial part of it is also used for velocity increase along the length of the

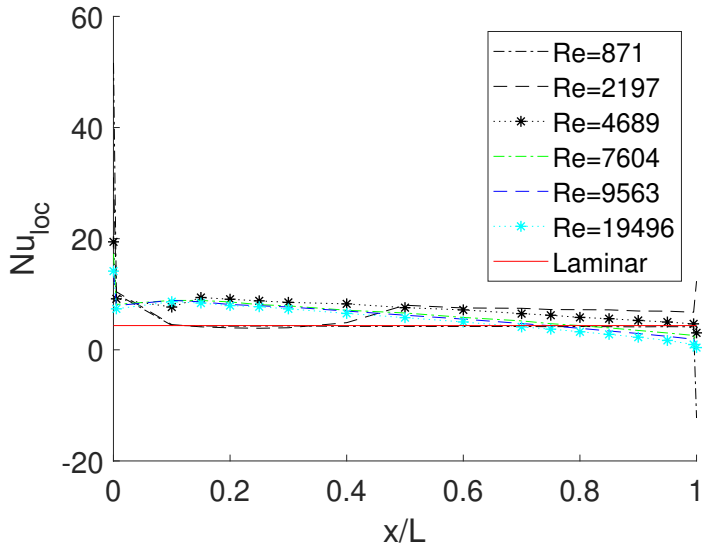

(a)

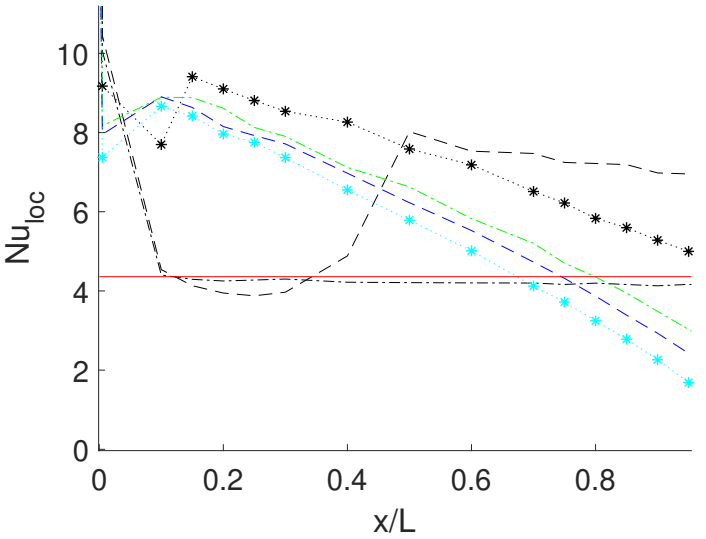

(b)

Figure 5.21: Local Nu along the length of the MT for various Re (**a**), and a zoomed view between $0.01 < x/L < 0.9$ (**b**).

MT due to the compressible nature of the gas. To cater for the thermal energy loss due to acceleration of the gas, if local Nu is recalculated using total temperature instead for cross sectional planes, local Nu then follows a more compliant behaviour compared to the trend reported by Abraham et al. [104]. This is shown in Figure 5.22. However, even in this case, it does not stabilize to a constant value and rather keeps on increasing along the length with a sharp decrease close to the outlet for $Re \leq 5000$. For values

of $Re \geq 5000$ the local Nu experiences sharp peaks and mathematically reaches to the infinity. This happens when the denominator of Equation 5.7 is approaching values equal to zero. After this singularity, Nu changes its sign and stays negative along the rest of the MT length. The vertical asymptote moves closer to the inlet when Re is increased as can be seen in Figure 5.22a.

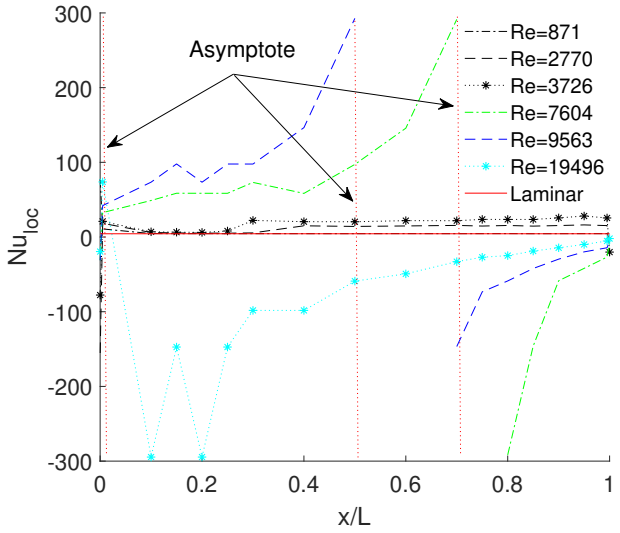

(a)

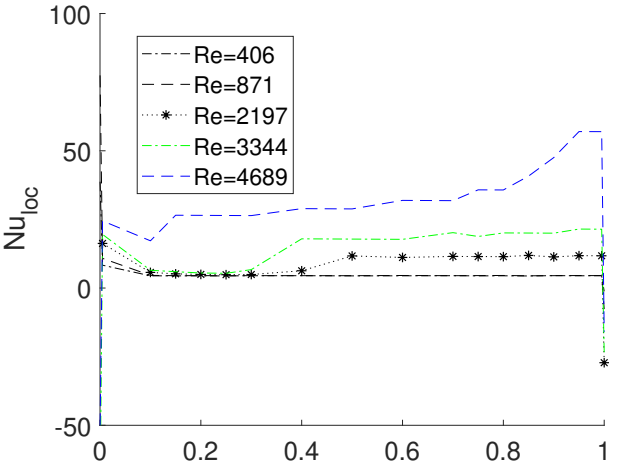

(b)

Figure 5.22: Numerical values of local Nu using total temperature at axial cross sections (**a**), and a zoomed view only until Re of 5000 (**b**).

This can further be elucidated by observing the temperature difference between wall and the fluid along the length of the MT as shown in Figure 5.23a. For Re of 871 flow

behaves as laminar and therefore temperature difference between wall and fluid bulk temperature almost stays constant throughout the length of the MT as it is expected of an incompressible flow under H boundary condition. For Re of 2197, flow is in the intermittent regime where instead of staying constant at a higher value it gradually decreases to a minimum value after half of the MT length. For higher Re cases,

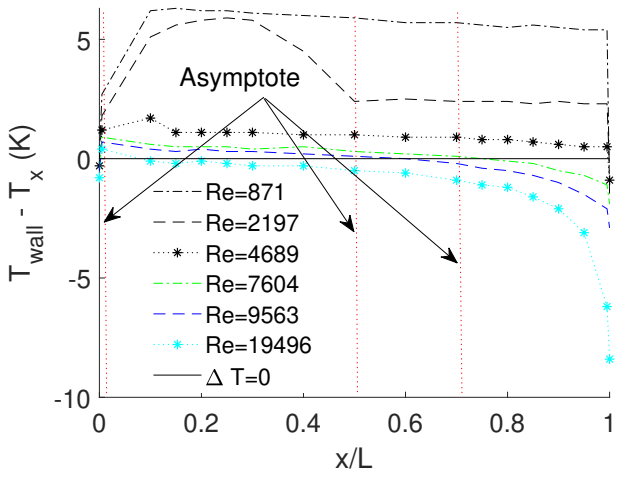

(a)

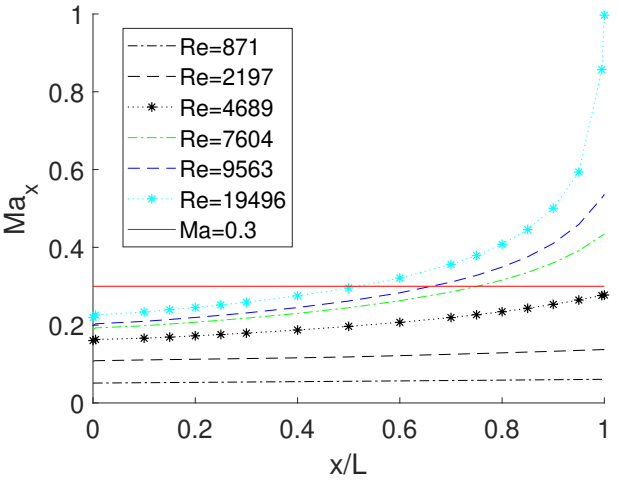

(b)

Figure 5.23: Temperature difference between wall and cross sectional averages (total) along the length of the MT (**a**), and variation of local Ma (**b**).

transition along the length is moved upstream with an increase in Re and it can be seen that temperature difference becomes negative along the length of the MT causing local Nu values to also become negative. Local Mach number (Ma_x), defined as the ratio of cross sectional mass flow averaged velocity to the cross sectional average speed

of sound, increases along the length with a sudden increase close to the outlet of the MT as shown in Figure 5.23b. When $0.2 < Ma_x < 0.3$, the temperature difference between wall and fluid reverses the sign resulting in a negative Nu. It is important to note that Nu has conventionally been defined for the flows without significant compressibility for which fluid local static temperature stays close to the total temperature and therefore in order to calculate the difference of wall temperature and the fluid bulk temperature, static temperatures of the fluid are used which always result in the positive values of Nu. It has already been explained that for gases a considerable amount of energy transferred from the wall is used also to accelerate, and therefore neglecting the kinetic energy of the gas results in very small local Nu as evidenced in Figure 5.21b. Although local values are showing such singularities, it has been seen in Figure 5.19 that except for $Re = 20000$ if the average bulk temperature is estimated as the average of inlet and outlet total temperatures, Nu_{av} still results in a positive value. However for $Re = 20000$ since the Nu_{loc} is negative throughout the length, Nu_{av} also comes out to be less than zero and therefore is not included in Figure 5.19.

It has been seen that numerical results using total temperature are also in a very good agreement with the experimental results of both MTs presented in this section up to Re of 10000. Evaluated numerical and experimental Nu_{av} although follow the trend of Gnielinski correlation but are slightly higher in the turbulent regime. As it is known that compressibility of the gas is enhanced with the reduction of D_h, therefore it would be of interest to carry out a numerical parametric study to investigate any effects of enhanced compressibility on the Nu_{av} which is the subject of the next section.

5.3.2 Numerical Parametric Analysis

From the above combined experimental and numerical approach, it has been established that Nu_{av} for the investigated MTs follows the conventional laws in the laminar regime while in the turbulent regime numerical as well as experimental results are slightly higher than Gnielinski. It has been shown that using conventional experimental settings

where thermocouples could only be mounted at the MT wall and temperature of gas can only be measured at the entrance and exit from the MT, experimental Nu_{av} in the laminar regime may yield lower values than 4.36 due to strong axial wall conduction of the MT which is not accounted for during experimental data reduction. In order to see the effect of D_h on the evaluated Nu_{av}, numerical analysis is further conducted on 5 MTs for D_h ranging between 133 μm to 750 μm. For all the MTs a constant length of 100 mm is simulated. Re is varied in the range of 500 to 20000 to cover the laminar, transitional and fully turbulent regimes and as for the previous analyses $\gamma - Re_\theta$ transitional turbulence model is used. A constant wall heat flux is applied at MT wall for the complete length of the MT after the initial reducer (see Figure 4.2). Details of the simulated MTs are summarized in Table 5.3. To calculate the Nu_{av}

Table 5.3: Dimensions of the MTs simulated for the evaluation of numerial Nu_{av}.

Tube	D_h (μm)	L (mm)	L/D_h	$q_{wall}(kW/m^2)$
MT3A	750	100	133	6
MT5	504	100	198	7.5
MT6	254	100	394	7.5
MT7	170	100	588	7.5
MT8	133	100	752	12

from numerical simulations flow properties were extracted at the 17 cross sectional planes as was done previously along the axial length of the MT. Flow properties from all these cross sections were averaged and Equation 3.8 is utilized for the calculation of the Nu_{av}. As it has been evidenced in the Figure 5.22 that local variation of Nu in a compressible gas flow is different than incompressible flows which is pertinent to flow compressibility, it would be of interest to study compressibility effect on the Nu_{av}. Although it has been observed in the previous section that for $D_h \geq$504 μm laminar as well as transitional Nu_{av} is quite in accordance with Gnielinski's correlations however, the reduction of D_h usually enhances the compressibility effects and therefore unlike incompressible flows, a variation of Nu_{av} may be expected with a decrease in D_h of MTs in the turbulent regime. For the thermal input considered in this study most of the MTs at very high Re (>10000) experienced a significant decrease of wall temperature

close to the outlet which resulted in a negative Nu_{av}. Only positive values of the Nu_{av} evaluated in all simulated cases are presented. Semi-local Nu (Nu_{SL}) was evaluated between x/L of 0-0.25, 0.25-0.5, 0.5-0.75 and 0.75-1, as it has been done for the f_f earlier. Qualitatively similar results have been obtained for all the MTs and therefore results of Nu_{SL} for MT3A and MT8 are reported in Figure 5.24. Total temperature of

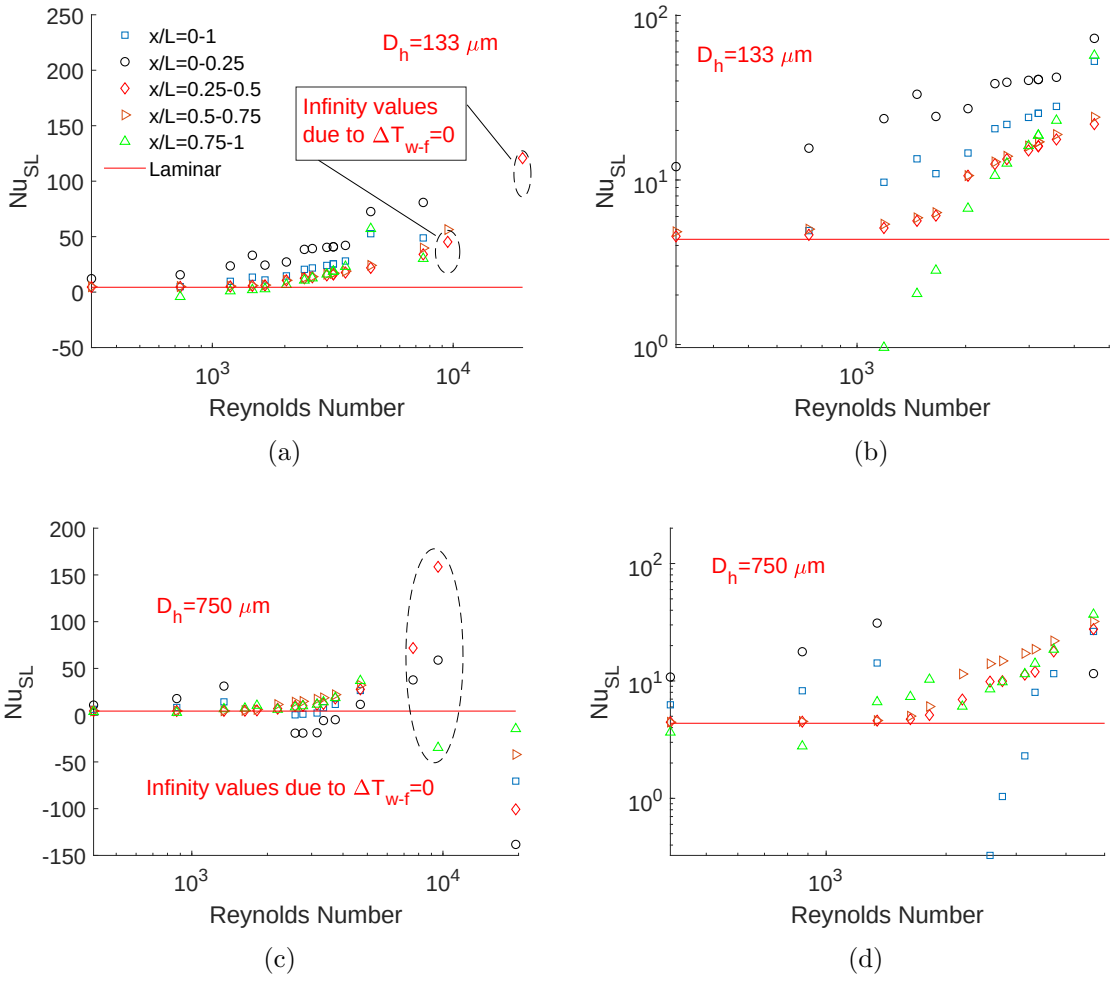

Figure 5.24: Numerical values of the semi-local Nu for MT8 (**a**), and MT3A (**c**), (**b**) and (**d**) are zoomed regions for MT8 and MT3A respectively.

the gas at the cross sectional planes was used in order to define local Nu and average of all the planes in the respective length (e.g. first 4 planes that are in x/L =0-0.25) is further used to define semi local values. It can be seen that at lower Re Nu_{SL} in the region of x/L =0.25-0.75 is equal to the macroscale laminar value of 4.36 whereas it is significantly higher in x/L=0-0.25 due to developing thermal length and entrance effects. A respective average for the whole heating length which is equals to length of

the channel L in this case (x/L =0-1) is also calculated by an arithmetic average from the semi-local values. In both D_h cases presented here, for $Re >$ 7000-8000 Nu_{SL} along the cross section approaches to the infinity due to very small temperature difference between the wall and total cross sectional temperature (ΔT_{w-f}) as explained earlier. Ultimately this ΔT_{w-f} becomes negative giving values of Nu_{av} (x/L=0-1) lower than zero which again is not physical. Since local values experience singularities therefore it would not be of practical use to evaluate Nu_{av} from semi local values to be compared with the experimental results. As explained earlier, these singularities are inherent to the definition of Nu_{av} which does not cater for total temperature of the fluid and rather is established on the basis of static temperature. Instead of arithmetic average of semi local values, an alternate way to define Nu_{av} is to extract its local variation (Nu_x) along the length as follows:

$$Nu_x = \frac{q_x D_h}{K_{fx}(T_{w,x} - T_{stag,x})} \tag{5.8}$$

where $T_{stag,x}$ denotes the stagnation temperature of the fluid at a certain cross section 'x' along the length of the MT. And then evaluating the integral average (Nu_{int}) over the whole length as:

$$Nu_{int} = \frac{1}{L}\int_0^L Nu_x dx \tag{5.9}$$

In an ideal steady state system, heat transferred evaluated from the wall side should equate to the heat gain by the gas. Therefore during the experimental data reduction heat flux from the wall to the fluid is calculated using Equation 3.9 utilizing temperature difference of the fluid between inlet and outlet of the MT. From Figure 5.25 it can be seen that heat flux from both fluid and wall side is quite close for simulated MTs. The maximum difference for the case of MT5 is 1% in the lower Re regime whereas it is 2.2% for MT7 for the highest Re simulated.

Convective heat transfer coefficient h evaluated using both heat fluxes for the MT7 is shown in Figure 5.26a. Values are quite close to each other by using both fluid and

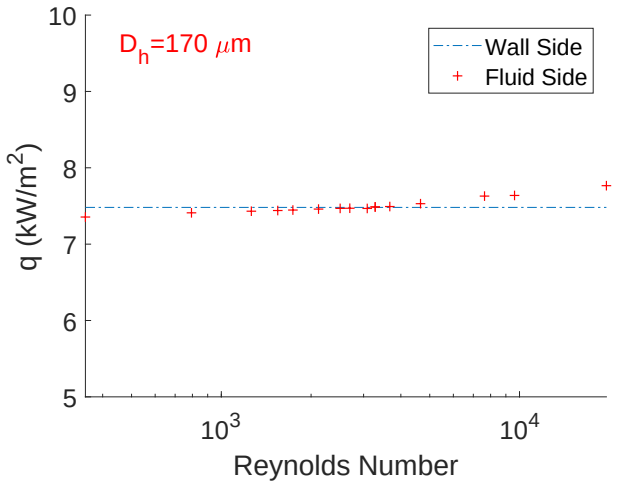

(a)

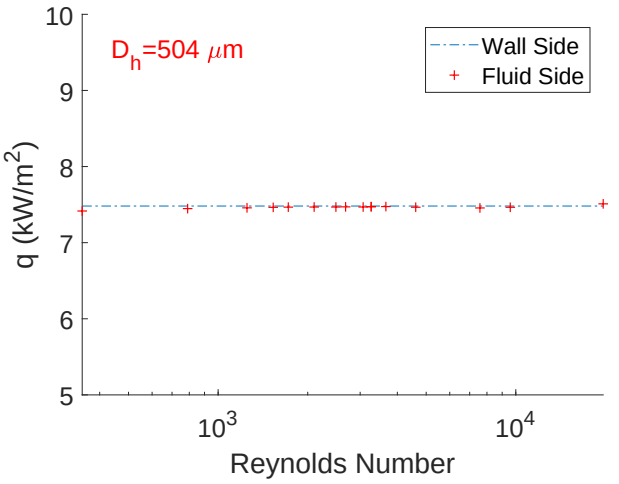

(b)

Figure 5.25: Comparison of heat flux from the wall side and fluid side for MT7 (**a**), and MT5 (**b**).

wall sides however as ΔT_{w-f} approaches to zero, a spike in the h can be noted from both methods and finally it becomes negative afterwards for higher Re. It can also be seen in Figure 5.26b that there is no significant difference in the values of ΔT_{w-f} if evaluated using different definitions of the bulk temperature. This is due to the fact that in numerical simulation, T_b increases linearly therefore integral as well as arithmetic average result in similar values.

Consequently a comparison using integral average (Equation 5.9) and the average using semi local values for the two MTs is shown in Figure 5.27. It can be seen that for

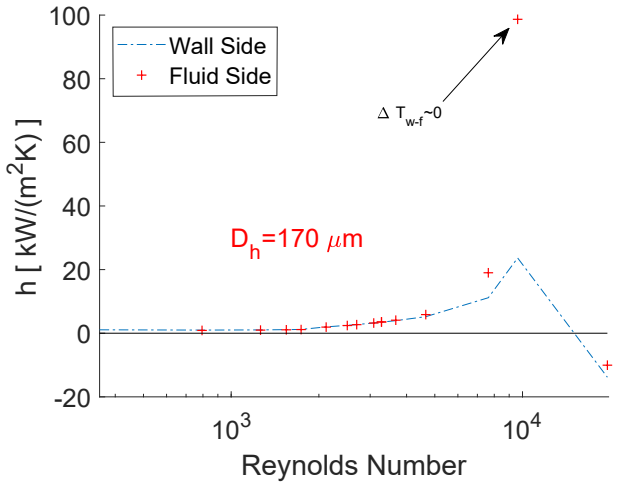

(a)

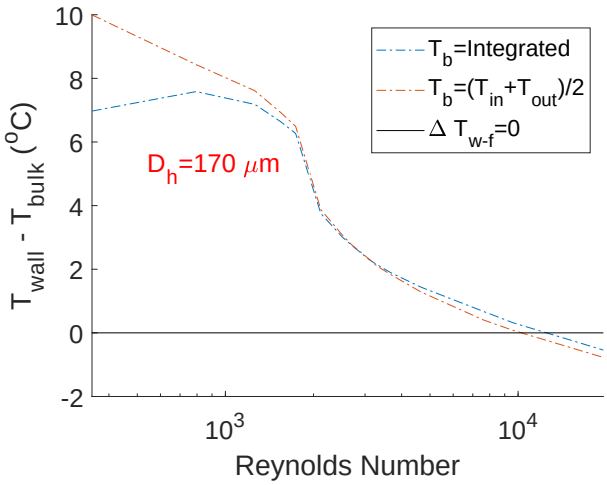

(b)

Figure 5.26: Numerical values of h for MT7 (**a**), and the difference between wall temperature and bulk fluid total temperature (**b**).

the case of MT7, a sharp peak that was seen in Figure 5.26a causes similar effect in integrated value of Nu_{av} after that it goes lower than zero as was the case with h. Local average for both MTs is significantly higher than integrated values in the transitional regime. This is generally due to the very high values of Nu in the entrance region (x/L=0-0.25) as evidenced in Figure 5.24 for the cases of MT3A and MT8.

In order to compare current numerical results with the experimental results of Yang et al. [30, 31, 2] integrated values of Nu_{av} from the numerical data are extracted and are compared for all the D_h in Figure 5.28.

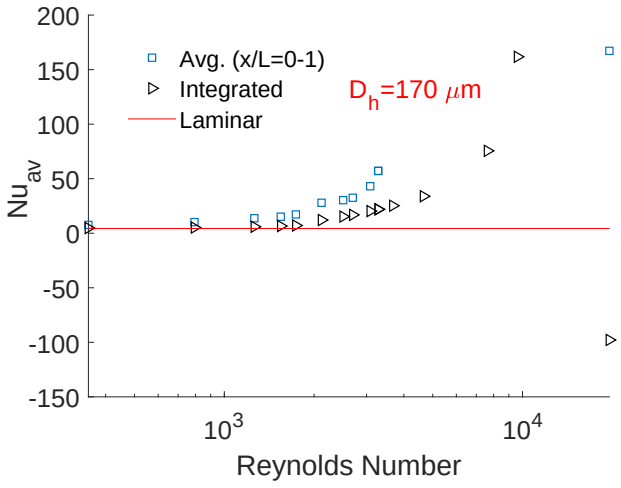

(a)

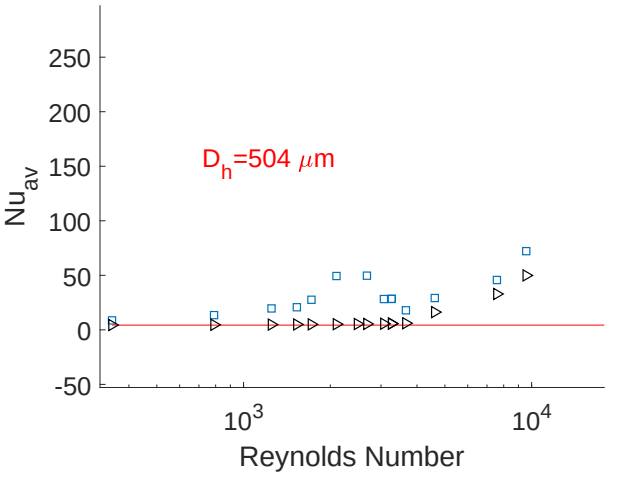

(b)

Figure 5.27: Semi local Nusselt number (Nu_{SL}) for MT7 (**a**), and MT5 (**b**).

For all the simulated MTs Nu_{av} is generally higher than Gnielinski's correlation in the earlier transitional and turbulent regimes. Nu_{av} for both MT3A and MT5 are almost 40% higher than Gnielinski at Re of 10000. A similar trend has been shown previously by Yang et al.[2, 31]. With a decrease in $D_h(\leq 254)$ μm however, transitional as well as fully turbulent Nu_{av} is significantly higher than Gnielinski. For the two smallest D_h MTs (MT7 and MT8), Nu_{av} is slightly lower than the correlation proposed by Choi et al. [6] in transitional flow regime, however, follows a different slope in the fully turbulent flow regime. Nonetheless Nu_{av} evaluated for MT7 is consistently lower than experimentally measured values by Yang et al. [31] for MT of $D_h = 170$ μm with

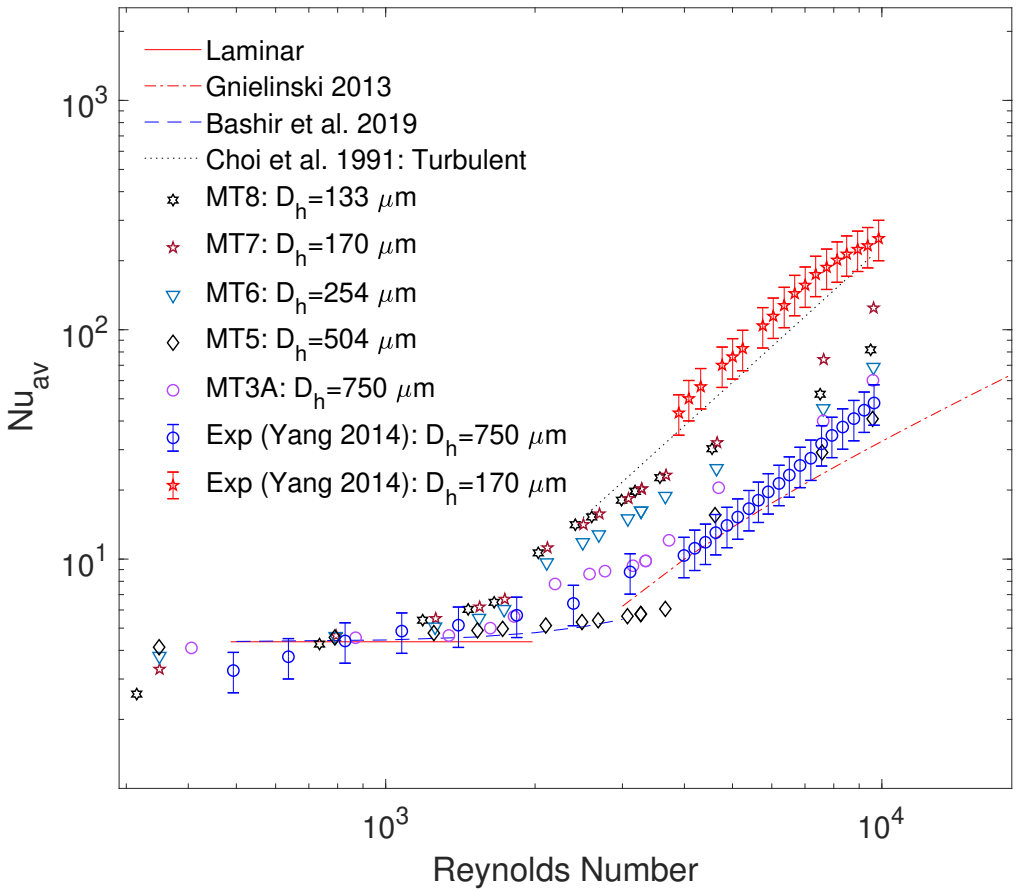

Figure 5.28: Numerical Nu_{av} for the simulated MTs.

the heat flux of 7.5 kW/m^2 (identical geometry and boundary conditions). In general, it has been observed that with a decrease in D_h, Nu_{av} for the gas flow increases in the transitional and early turbulent regimes whereas the difference minimizes for higher values of Re. Moreover Nu_{av} in laminar as well as transitional flow regime for both MTs with $D_h \leq 254\mu$m is almost identical. In the current numerical analysis, H thermal boundary condition has been imposed and significantly higher results of Nu_{av} than Gnielinski are found out in the transitional and turbulent regimes. For incompressible flows Nu_{av} for both H and T boundary conditions is identical and therefore it is recommended as future work to conduct the above performed parametric analysis using T boundary condition in order to put in evidence the differences with respect to H boundary condition, if any.

5.4 Summary

Fluid flow and heat transfer inside circular MTs is studied using both experimental and numerical techniques. Pressure drop experiments are performed for MTs having a D_h between 133-1016 μm. Results show that average f_f between inlet and outlet for MTs is in agreement with Poiseuille's law in the laminar regime whereas a discrepancy is observed between turbulent f_f in the range of D_h tested. In the early turbulent regime, experimental data reduction yields a higher f_f than Blasius law. A sensitivity analysis on the role of minor losses in the experimental evaluation of f_f is then carried out using numerical analysis. Numerical study reveals that conventional coefficients available in the literature that are generally validated for incompressible macroflows, are not suitable to micro gas flows. Significantly higher values of loss coefficients are observed and a curve fit on these results is used in the experimental data reduction. This showed that for the relatively bigger D_h MTs, minor pressure losses have a considerable effect on the evaluation of average f_f. Using numerically derived minor loss coefficients, experimental results were in agreement with the Blasius law in the turbulent regime. Minor losses, however, do not have much effect on the evaluation of f_f in smaller D_h and therefore can be ignored. Semi-local f_f are also evaluated using numerical simulations which showed that semi-local f_f in the entrance region is significantly higher than the rest of the MT length. Semi-local f_f in the last part of the MT length showed better compliance with Poiseuille's law than developing regions. For MT having L/D smaller than 100, a slight delay in laminar to turbulent transition is observed both numerically and experimentally. It is also observed that for this specific MT, f_f in the turbulent regime stayed lower than Blasius which was also observed using numerical studies.

Convective heat transfer in 504 μm MT is also studied experimentally. The purpose of this study is to validate the experimental test rig and instrumentation for the heat transfer analysis of gas microflows. Significantly lower values of Nu_{av} are observed experimentally in the laminar regime and the reasons for this have been explained. For the currently employed experimental setup, strong axial wall conduction at the lower

Re affects the linearity of the bulk fluid temperature increase along the length of the MT and therefore Nu_{av} values are considerably lower (unphysical) in the laminar regime. An H boundary condition on the numerical replica of experimented MT is then applied and a close agreement between numerically estimated Nu_{av} and the conventional value in the laminar regime is found out. Moreover, a good match between experimental and numerical results is also observed in transitional and turbulent regimes. Whereas for fully turbulent flow, Nu_{av} is 40% higher than Gnielinksi's correlation. To further see the effect of D_h on the average Nu_{av} for the gas flows, a numerical parametric study is undertaken where D_h of the MT is varied from 133 μm to 750 μm. It has been shown that utilizing the static temperature of the gas, Nu_{av} is significantly lower than experimental and conventional trends as a significant portion of the gas thermal energy is used for the gas acceleration along the length of the MT. Nu_{av} evaluated using total temperature from the numerical model instead follows the experimental trend. However, it has been seen that when the local Mach number is in the range of $0.2< Ma_x <0.3$, singularities in the Nu_{av} are encountered because of the negative temperature difference between the wall and the gas total bulk temperature. It has been explained that such singularities are pertinent to the definition of Nu therefore further investigations in this regard for the high speed gas flows are recommended. The parametric analysis showed a general increase in Nu_{av} with a decrease in D_h and for all the simulated MTs having $D_h \leq 254$ μm, Nu_{av} has significantly been higher in the transitional and turbulent regimes when compared to conventional Gnielinski's correlation. Therefore new correlations for the highly compressible gas flows usually experienced in micro sized geometries should be sought after.

Chapter 6

Fluid Flow through Microchannels

6.1 Introduction

It has been well established with the experimental as well as numerical studies of the recent decade that frictional characteristics of the microflows in the laminar regime follow the conventional Poiseuille's law in the absence of scaling effects. When it comes to the gas flows that are compressible in nature, the laminar friction factor has shown the dependence on the average Mach number of the flow [27] which is not straightforward to deduce from usual experimental settings. As already evidenced in the validation section of Ch. 4 the friction factor of gas flows deduced from experiments deviates from that of the numerical one in the turbulent regime. To better understand the limitations of the used data reduction methodologies, in this chapter a validated numerical model (Ch.4) for MC is utilized to highlight the possible reasons of disagreements between experimental and numerical friction factor.

6.2 Adiabatic Friction Factor

For an incompressible fluid, if the channel walls are adiabatic, temperature along the length of MC does not change. This does not hold true for high speed gas flows where a decrease in gas temperature is expected as it flows along the length of MC due to acceleration. However, frictional characteristics of MC gas flows have been presented under isothermal flow assumption in the past [27, 49]. This practice prevailed mainly because of the limited possibility to experimentally monitor gas temperature as it flows along the MC. Kawashima and Asako [32] recently showed that for adiabatic walls, the temperature of the gas can be found by using energy balance between the inlet and any cross section downstream. They presented Eq. 3.5 which needs cross sectional average pressure to estimate the average temperature of that cross section. By comparing the solution of this equation to the numerical simulations they showed that there is good agreement between the two approaches. Luckily, measuring the pressure of a cross section along the length of MC is relatively easier and therefore the decrease in temperature of the gas can be estimated using Eq. 3.5. For this reason following the works of Hong et. al [27, 33], 5 pressure ports are realized in the MC assembly of the current work as shown in Fig. 6.1. Having pressure taps along the length of the MC can provide invaluable experimental insight of gas temperature as it flows through the MC which finally allows calculating semi local friction factor ($\tilde{f}_f$) in different parts of the MC. However, if the goal is to seek a single average value of friction factor between inlet and outlet then a pressure port at the outlet of MC will be required in order to correctly estimate the gas temperature right at the outlet. In the absence of such measurement, a convenient practice has been to assume atmospheric pressure at the outlet of MC. This essentially means that while deducing experimental results it is assumed that gas flow undergoes a full expansion inside MC. In a conventional experimental pressure drop analysis, inlet and outlet flow characteristics (p, T, u, ρ) of a MC need to be defined with maximum possible care for an accurate estimation of friction factor of MC. As discussed in data reduction section of Ch. 3 that for

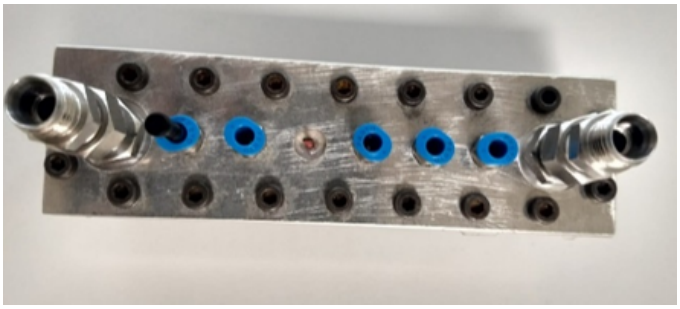

(a)

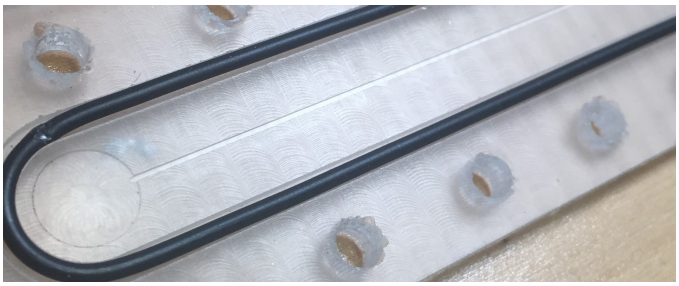

(b)

Figure 6.1: Experimental assembly for MC pressure drop testing with local pressure ports (**a**), and a view of PMMA chip having milled MC(**b**).

most of experimental campaigns pressure and temperature are measured before and after the MC in respective manifolds which necessitates to estimate the minor losses associated to these manifolds using Eq. (3.7). As evidenced in case of MTs (Ch. 5) conventional values of these loss coefficients from the standard textbook are not valid for gas microflows and hence minor losses can be defined using a validated numerical model. Data reduction methodology where numerical inlet minor loss coefficients are used along with the temperature estimation at MC outlet using Equation (3.5), is referred to as M1 in the subsequent text of the chapter. An alternative methodology (M2), is to estimate MC inlet flow properties by assuming isentropic flow between the manifold and MC inlet. This automatically caters for a reduction in MC inlet pressure and hence the use of K_{in} is no more required. Flow properties at the MC inlet using isentropic flow assumption are determined as follows (see Fig. 3.10):

- An initial estimate of the gas velocity at MC inlet is made as in M1 (i.e., using

the measured mass flow rate and density of the gas at the inlet of assembly).

$$u_{in} = \frac{\dot{m}}{\rho_1 A} \tag{6.1}$$

- Using the measured temperature of the gas in the manifold (T_1), an estimate of the gas temperature at MC inlet is then performed:

$$T_{in} = T_1 - \frac{{u_{in}}^2}{2C_p} \tag{6.2}$$

- Pressure at the inlet is then estimated using isentropic pressure ratio which can be represented as:

$$p_{in} = \frac{p_1}{\left(1 + \frac{{u_{in}}^2}{2C_p T_{in}}\right)^{\frac{\gamma}{\gamma-1}}} \tag{6.3}$$

- This is followed by the inlet density calculation using gas equation:

$$\rho_{in} = \frac{p_{in}}{RT_{in}} \tag{6.4}$$

- Finally, velocity at the inlet of MC is updated with previously calculated density at MC inlet.

$$u_{in} = \frac{\dot{m}}{\rho_{in} A} \tag{6.5}$$

- Above mentioned steps are iteratively repeated unless the difference between estimated MC inlet velocity in the first step becomes almost equals to updated MC inlet velocity calculated at the last step.

Main differences between the two experimental data reduction methods (M1 and M2) described before are summarized in Table 6.1. Experimental results for average friction factor are deduced by using both M1 and M2 approaches for a MC with $D_h = 295\ \mu m$ and $\alpha = 0.7$. These results are then compared with numerical predictions of the same MC to put in evidence discrepancies among experiment and theory. This comparison is

finally used to establish the most accurate data reduction procedure for the estimation of average friction factor for MC/MT in presence of compressible gases.

Table 6.1: Data Reduction Methods Used in Current Study for MCs.

Location	M1	M2
Inlet	- Numerical minor loss coefficient to estimate entrance manifold pressure drop - $T_{in} = T_1$ (see Figure 3.10)	- Isentropic expansion between entrance manifold (1) and MC inlet (in)
Outlet	- Fully expanded flow ($p_{out} = p_{atm}$) - T_{out} estimated using Equation (3.5)	

6.2.1 Numerical Calculation of Minor Loss Coefficients

Three MC dimensions are simulated in the current study as tabulated in Table 6.2. MC1 is used to replicate the channel tested experimentally and gain insight of flow physics by comparing with experiments. Whereas other two (MC2 & MC3) along with M1 are used to discuss the role of MC geometry on the evaluation of loss coefficients.

Table 6.2: Channel geometry used for simulations.

Channel	w (m)	h (m)	D_h (m)	α
MC1	360	250	∼295	0.7
MC2	1020	112.7	∼203	0.11
MC3	550	110	∼184	0.2

Steady state simulations using $\gamma - Re_\theta$ transitional turbulence model are performed using the boundary conditions tabulated in Table 6.3. To estimate friction factor and minor loss coefficients, five different cross-sectional planes are defined at x/L of 0.005, 0.25, 0.5, 0.75 and 0.98, respectively. In addition, two planes defined at x/L of 0.0005 and 0.9995 are treated as the inlet and outlet of MC, respectively. Results from these planes are further post processed in MATLAB to deduce required flow quantities. Numerical friction factors are then evaluated simply by using Equation (3.4).

The minor loss associated with the inlet from numerical results is calculated using

Table 6.3: Boundary Conditions.

Boundary	**Value**
Inlet	- mass flow rate: experimental or from Equation (3.3) - Turbulence Intensity, TI = 5% - Temperature T_{in} = 23 °C
Walls	- No slip - Adiabatic
Outlet	Pressure outlet, Relative p = 0 Pa

Equation (3.7) between the inlet of assembly and MC inlet and therefore includes 90° bend loss due to orthogonal flow direction change at the manifold inlet (see Figure 4.4). Results of K_{in} and K_{out} for the three MCs are compared in Figure 6.2. K_{in} decreases steeply in laminar and early turbulent flow regimes, whereas it becomes almost a constant in high turbulent flow regime as shown in Figure 6.2a. At the lower Re, MC assembly pressure drop in experimental campaign is also usually lower and hence assuming a smaller and/or constant K_{in} would certainly cause f_f to be higher than macro theory. For the smallest α simulated, K_{in} is as high as 5.19 which is significantly higher than values available in general fluid mechanics text [90]. For a rectangular MC, K_{in} is a function of α and D_h simultaneously and hence it must be evaluated numerically in advance to help in experimental data reduction. K_{out} on the other hand stays close to zero in laminar and early turbulent flow regime and shoots rapidly in higher turbulent flow regimes as seen in Figure 6.2b. From the investigated MC assembly, it is evident that K_{out} is highest for the smallest D_h simulated for high turbulent flow regime and decreases with an increase of D_h. Numerical results show that K_{out} for compressible flows, can also go higher than its limiting value of 1 as calculated using the following theoretical relation:

$$K_{out,th} = \left(1 - \frac{A}{A_{man}}\right)^2 \tag{6.6}$$

where A_{man} denotes the cross-sectional area of outlet manifold.

A MC assembly similar to that considered in the present work has been tested by Mirmanto [105]. The author used a conventional value of 1.2 as a loss coefficient for

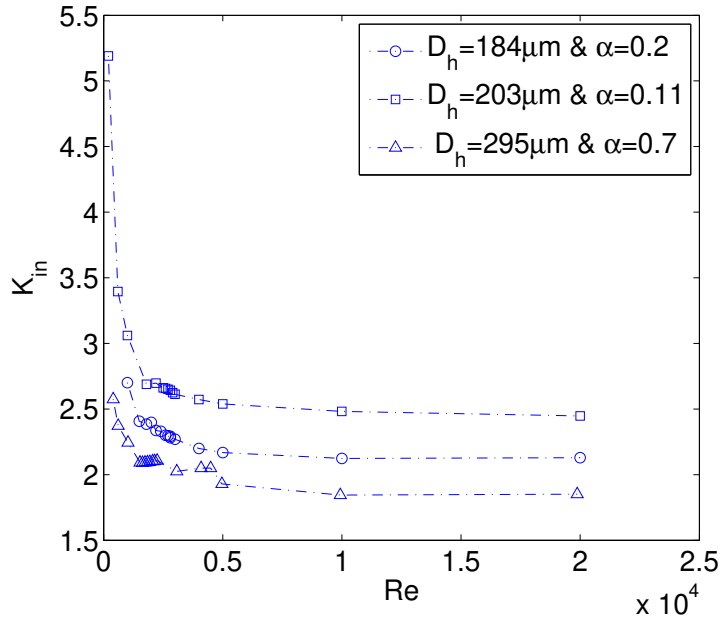

(a)

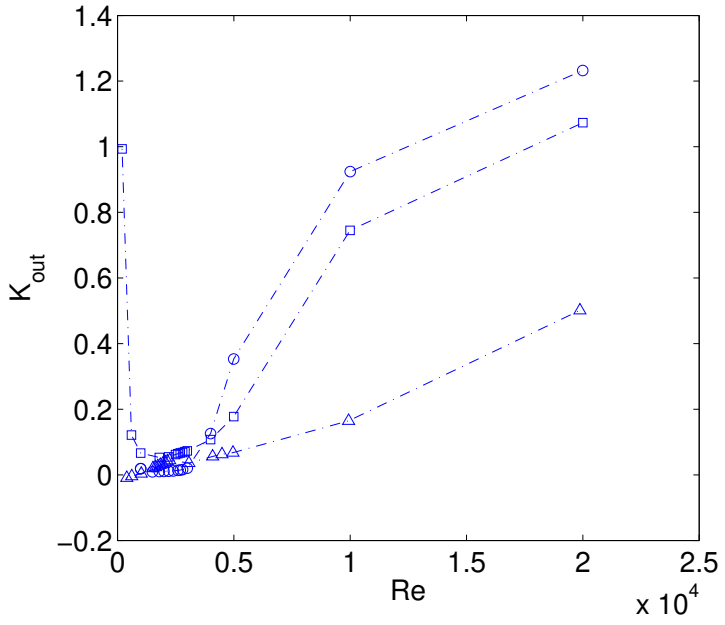

(b)

Figure 6.2: Numerical minor loss coefficients: K_{in} (**a**), and K_{out} (**b**).

90° bend which is not observed in the present numerical results. A similar assembly has also been investigated numerically by Sahar et al. [106] where inlet losses in laminar incompressible flow increased for increasing D_h for a constant value of aspect ratio α. The three MCs modeled in this section (see Table 6.2) demonstrated that minor loss coefficients are dependent on assembly as well as MC geometry and in all cases are

not equal to general values used in literature for macro flows and hence a numerical model is required for an accurate estimation friction factors especially in laminar flow regime. This is due to the fact that minor losses carry a significant portion of the total pressure drop in the laminar flow regime but as the Re is increased, the contribution of minor losses diminishes, and they do not have a significant effect on the calculation of f_f in turbulent flow regime.

6.2.2 Experimental Average Friction Factor

Pressure-drop experiments are performed for MC1 using nitrogen gas as a working fluid. Results in terms of f_f in laminar flow regime are compared with Shah & London correlation (Equation (4.19)) for rectangular channels while Blasius law (Equation (4.20)) in turbulent flow regime is used for comparison. Laminar f_f is also compared with the correlation of Hong et al. [15] that caters for an increase in laminar f_f due to compressibility. Numerically obtained values of K_{in} are used in data reduction M1. When the outlet is open to the atmosphere, a convenient practice is to estimate the experimental f_f by assuming a fully expanded flow at the MC outlet. This assumption essentially makes K_{out} to be zero and is quite realistic in the laminar and early turbulent flow regimes as shown numerically in Figure 6.2b. Therefore, due to the lack of MC outlet pressure measurement in the current experimental campaign, $K_{out} = 0$ is used in further data reduction. Limitations to this assumption will be discussed later in the text.

The previous section already put in evidence that minor losses differ for different MC geometries. Therefore, for an accurate evaluation of inlet minor losses a curve fit on the numerical results is used to extract the variation of K_{in} with Re. This is used to model the inlet minor loss to calculate f_f with data reduction M1. The adiabatic f_f calculated using Equation (3.4) for both methodologies M1 and M2 is shown in Figure 6.3. There is an excellent agreement between experimental and numerical f_f in the laminar flow regime where both follow the Hong et al. [15] correlation within

experimental uncertainty. Uncertainty bars are omitted in Figure 6.3 for reasons of clarity. Isothermal friction factor ($f_{f,iso}$) obtained by assuming $T_{in} = T_{out}$ and hence neglecting the last term of Equation (3.4), stays lower than Blasius law in turbulent regime. Results of numerical f_f are slightly higher than Blasius in a high turbulent regime. Experimental f_f in early turbulent flow regime is lower than Blasius law with both M1 and M2 methods and starts not only increasing again in high turbulent flow regime but with a slope that diverges from Blasius at $Re > 10{,}000$. On the contrary, the slope for numerical f_f does not diverge significantly from Blasius law in the turbulent flow regime. Since the relative roughness ($\frac{\epsilon}{D_h}$) of the tested channel is equal to 0.5%, such an increase in experimental f_f compared to Blasius law using both M1 and M2 methods can potentially be associated with the rough channel walls. To better investigate this aspect, experimentally deduced flow properties are further compared with numerical ones.

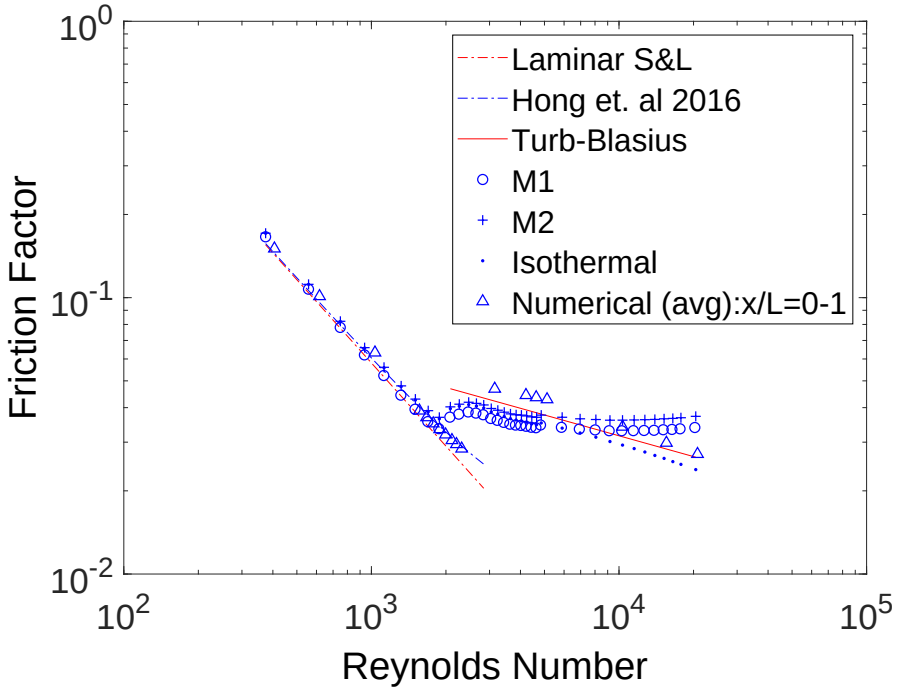

Figure 6.3: Comparison of numerical and experimental f_f using M1 and M2.

The temperature at the inlet and outlet of MC is compared in Figure 6.4a. The discrepancy in the inlet temperature for M1 method is a direct consequence of the assumption of constant density and temperature at MC inlet, both assumed equal to the measured

values at the manifold inlet. In the absolute sense, there is a maximum difference of 7K in the turbulent flow regime. Gas stays almost isothermal at low Reynolds numbers ($Re < 1000$) but as Re is increased, a relative pressure difference between the manifold inlet and MC inlet increases causing a decrease in temperature at MC inlet that is not captured in M1 method. The temperature at the outlet estimated using Equation (3.5) follows the numerical trend where the gas temperature is decreasing with increasing Re. For such an estimation, an absolute temperature difference of approximately 26K compared to 92K in case of isothermal assumption at Re of around 13,000 is observed. This difference furthers as Re is increased. On the other hand, when the MC inlet conditions are defined using M2 method, inlet expansion and hence temperature decrease from the entrance manifold to MC inlet is correctly modeled as shown in Figure 6.4a. This result suggests using M2 method for correctly predicting the MC inlet flow properties without using an additional K_{in}. Outlet flow properties, however, differ from the numerical values for both M1 and M2 methods. It is worth mentioning that outlet pressure is assumed to be atmospheric as outlined in Table 6.1 ($K_{out} = 0$) for both methods to estimate outlet temperature. Numerical value assumed by the Mach number at the MC outlet is shown in Figure 6.4b where it keeps on increasing with Re and finally gets to an almost constant value after Re =10,000. At this point, flow starts to choke and Ma at the outlet reaches a constant value of close to 1 (i.e., in this case $M_a = 1.19$ after Re = 15,000). An explanation of the supersonic jet at the exit of constant area ducts has been presented by Lijo et al. [107]. Numerical works of Kawashima et al. [100] and Hong et al. [38] showed that Ma at the outlet can go higher than its maximum limit of 1(Fanno flow). This happens due to the shear thinning of the boundary layer close to the outlet of MC/MT that serves as de-Laval nozzle for the incoming high subsonic jet of gas flow. Flow choking at the outlet is not captured by experimental data reduction methodologies M1 and M2 and therefore Ma keeps on increasing with Re in both methods. This result disagrees with what is seen in numerical results. At the maximum Re values, outlet Ma reaches as high as 2.46 for isothermal treatment of gas while it reduces to 1.88 in cases of M1 and

M2 methods. These very high values of Ma signify that both methods lack the flow physics at the outlet. This is due to the wrong estimation of outlet jet temperature using Equation (3.5) at very high Re as can be seen in Figure 6.4a. Experimental data shows flow choking at the inlet where Ma become constant for $Re > 6000$. A constant temperature and Ma ensure a constant velocity at MC inlet which explains the reason for a constant value of inlet loss coefficient in the turbulent flow regime after an initial decrease in laminar and early the turbulent flow regime, as observed in Figure 6.2a. However, it is evident that flow choking at inlet starts much earlier than the outlet and numerical results of MC inlet temperature are lower than assumed in M1. Effect of flow choking on the calculation of average f_f is discussed in the next section.

6.2.3 Flow Choking and under Expansion at Outlet

Usually, in fluid mechanics texts, flow choking is defined as the flow condition in which working fluid at the outlet of a pipe attains a sonic velocity and therefore mass flow rate cannot be increased any further. However, as shown by the current experiments and by the work of Hong et al. [38], the mass flow rate for a compressible working fluid keeps on increasing even when the flow is choked. Ma and hence velocity, however, attains a maximum at all cross sections of the pipe in choked gas flows. This is simply because of an increase in upstream density of the gas by increasing upstream pressure causes mass flow rate to increase even if velocity is choked downstream. Definition of flow choking shall be given therefore by highlighting the presence of a maximum in Ma (velocity) rather than in mass flow rate for compressible flows. Variation of numerical outlet Ma with ratio of MC outlet pressure and atmospheric pressure is shown in Figure 6.5a for all three simulated MCs. It can be seen that as soon as the outlet Ma starts to choke, MC outlet pressure starts increasing higher than atmospheric pressure which means that the flow at MC outlet becomes underexpanded. The measure of underexpansion is not much pronounced during the experimental tests on MC1 where flow choking begins around $Re = 9934$. On the contrary, flow choking is observed

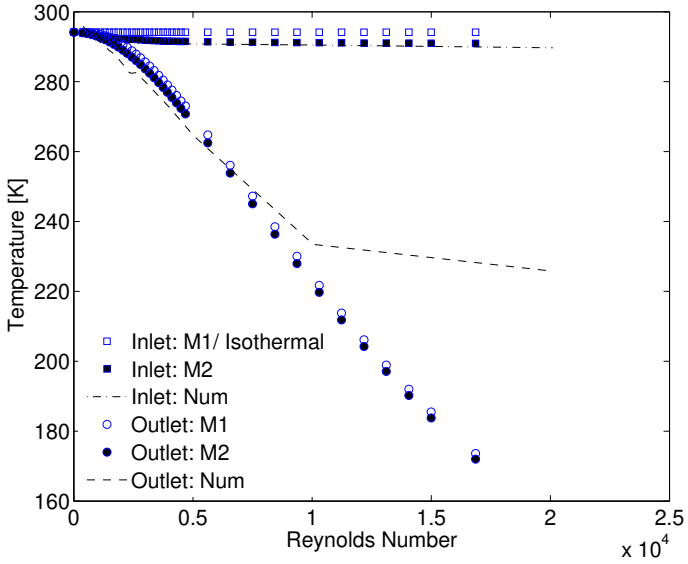

(a)

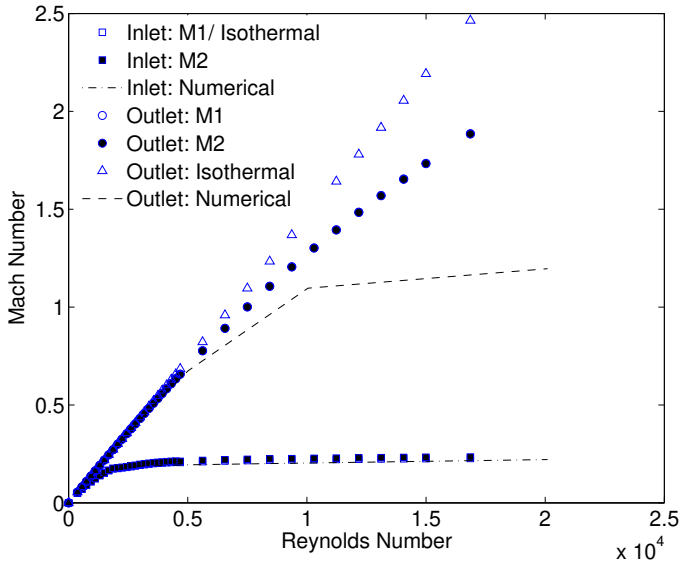

(b)

Figure 6.4: Comparison of flow properties using M1 & M2: local temperature (**a**), and Mach number (**b**).

earlier in MC2 and MC3 in correspondence of $Re = 5000$ and $Re = 3999$ respectively. After these Re, outlet pressure shoots above the atmospheric pressure and the flow cannot be considered as fully expanded as assumed in both M1 and M2 methods. As a result, a sudden increase in outlet numerical K_{out} after flow starts to choke can be noted in Figure 6.5b. As discussed earlier, for the M1 method a single value of the outlet loss coefficient is therefore not enough, especially for MCs with smaller hydraulic

diameter where flow choking can start even in the laminar flow regime.

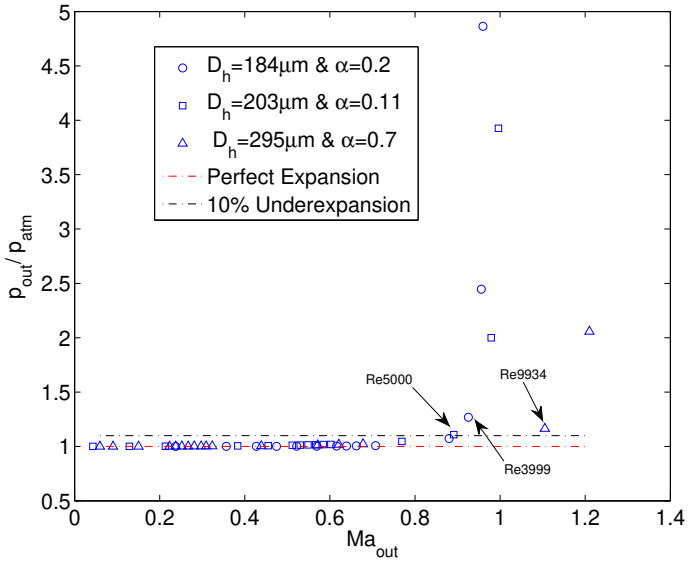

(a)

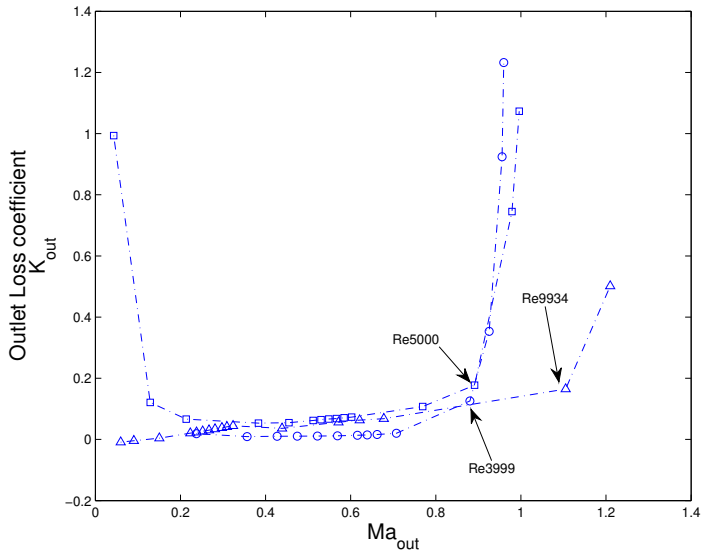

(b)

Figure 6.5: flow choking and underexpansion for simulated MCs: back pressure (**a**), and K_{out} (**b**).

From an experimental point of view, it is difficult to measure static pressure exactly at the MC outlet and therefore an assumption of fully expanded flow serves the purpose. However, as evidenced in all three simulated cases, this holds true for unchoked gas flows only. Moreover, the measure of underexpansion becomes stronger with smaller dimensions of the channel and hence should be of concern for deducing friction factors

using Equation (3.4) in any experimental campaign. As Equation (3.5) requires cross-sectional average pressure to estimate the average temperature of that cross section, full expanded flow assumption therefore always overestimates the decrease in outlet temperature in choked gas flows. This, in turn, causes an artificial increase in the calculation of friction factor in the choked flow regime from experimental pressure-drop data. Therefore experimental f_f shows a deviation from Blasius law in Figure 6.3 while numerical results agree with Blasius.

Flow choking that was observed in numerical data can experimentally be established only using local flow properties. For an adiabatic flow in a duct, fluid temperature and density at a specific cross section can be estimated using only a static pressure measurement. Thus, local pressure measurement will result in a better understanding of choked compressible flow along the length of MC. A comparison of local measured static pressure with numerical results is shown in Figure 6.6a for MC1 and a zoomed portion of laminar to early turbulent flow regime is shown in Figure 6.6b. Numerically estimated values are generally in good agreement with experimental local pressure values in laminar and early turbulent regimes. In a highly turbulent flow regime ($Re >$ 10,000) prescribed boundary conditions result in an overall lower pressure drop than what is experimentally observed. However, such difference is not too significant and therefore numerical model can be used as a priori tool to have first estimation of pressure drop and local flow physics (especially flow choking).

Numerical local temperature is also in good agreement with the estimated cross-sectional temperature obtained by using Equation (3.5) as can be seen in Figure 6.7a. Experimental flow choking of the gas flow is also evident in Figure 6.7b where numerical and experimentally deduced Ma are in excellent agreement. It is therefore, not erroneous to assume that numerical flow choking at the outlet where Ma goes higher than 1 (as in the case of MC1), would also be encountered in experiments. It is interesting to note that all through the data reduction for the results presented in this section, no numerical input has been considered as a priori and MC inlet properties

are calculated by considering an isentropic expansion between the entrance manifold and MC inlet.

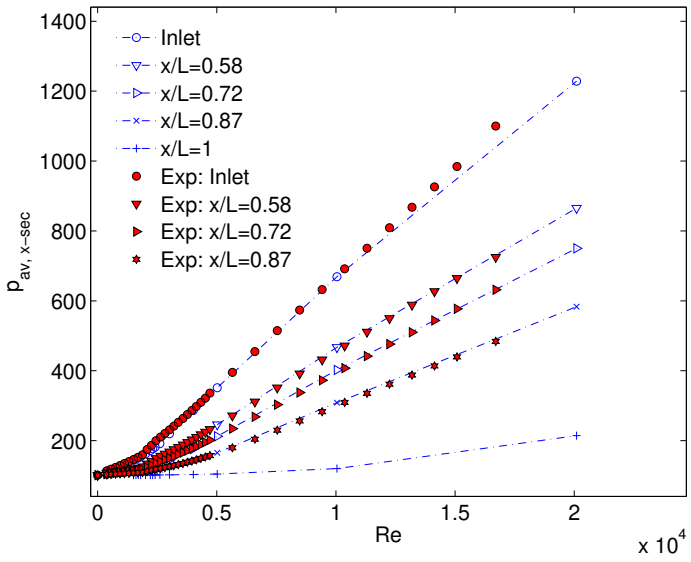

(a)

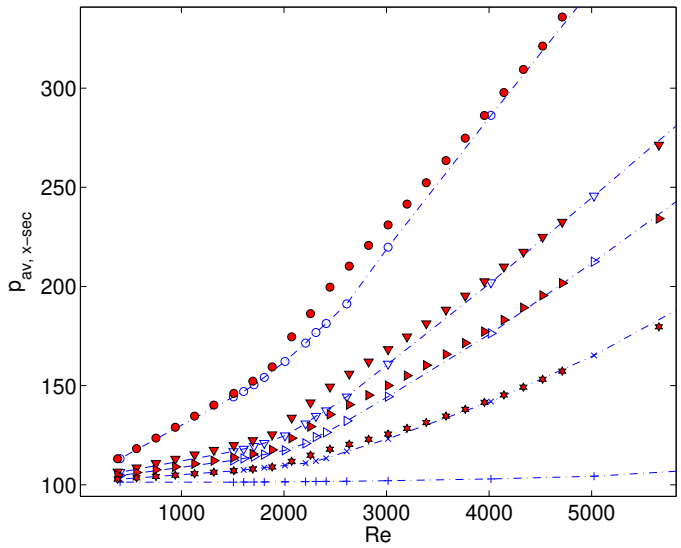

(b)

Figure 6.6: Comparison of measured and numerical static pressure inside MC1 (**a**), and zoomed low *Re* region (**b**).

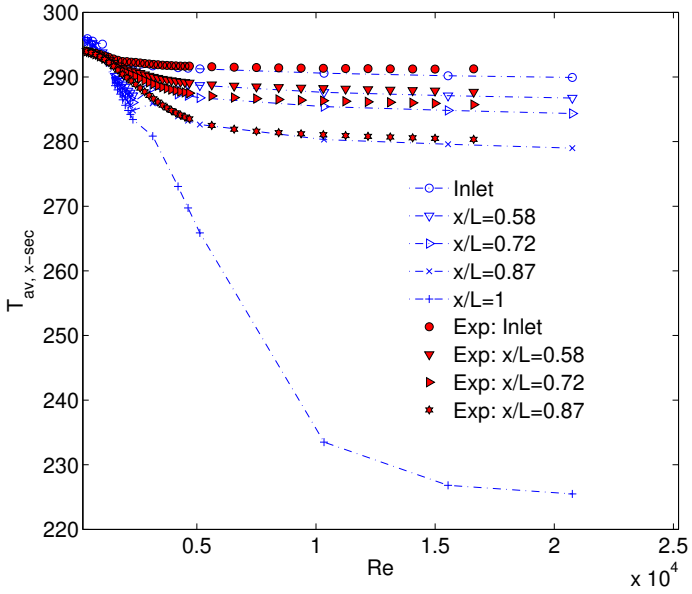

(a)

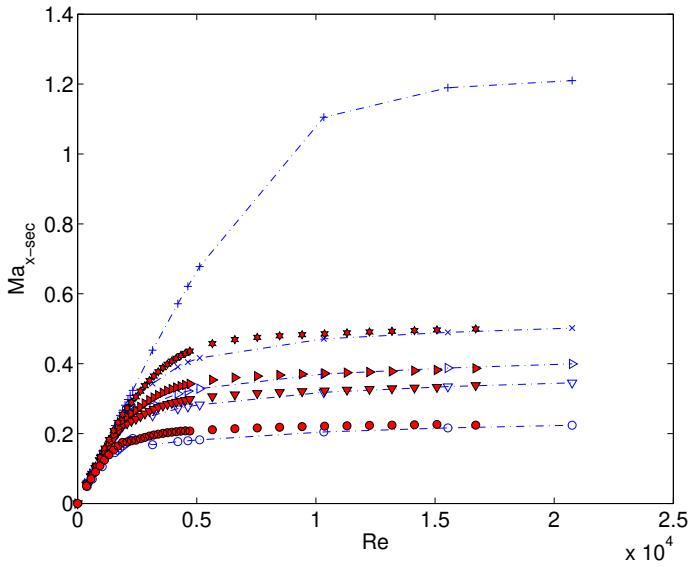

(b)

Figure 6.7: Comparison of measured and numerical static T (**a**), and Ma (**b**) inside MC1.

6.2.4 Estimation of Gas Bulk Temperature

Another interesting observation from Figure 6.3 is that in choked flow regime, isother-

mal treatment of gas results in $f_{f,iso}$ that although is lower than Blasius law but follows its slope. The same is true for semi-local $\tilde{f}_f$ between last two pressure taps at $x/L = 0.72$–0.87 which again follows the slope but stays slightly higher than Blasius law. On the contrary f_f, using both M1 and M2 methods shows a false increase when the flow chokes. This again points towards the possibility of the wrong estimation of average gas temperature assumed in M1 and M2 methods. Because such a rapid increase in the slope of f_f is not observed when the difference in gas temperature is relatively small as is the case for semi-local values (see Figure 6.9a) or when it is zero (for isothermal gas treatment). In fact, if the numerical static temperature is analyzed along the length of MC as shown in Figure 6.8a, it can be established that even for the highest simulated Re, the temperature almost stays isothermal along most of the length of the MC with a sudden decrease towards the end of MC. Therefore, to calculate average f_f between inlet and outlet, an equal weighted average of measured inlet temperature and estimated at the outlet using Equation (3.5) would underpredict the real average gas temperature. Average temperature of the gas between two pressure ports 'a' and 'b' along the length of MC can be defined by:

$$T_{av} = c_1 T_a + c_2 T_b \tag{6.7}$$

The effect of values of c_1 and c_2 on temperature average between inlet and outlet of MC and hence evaluation of f_f is shown in Figure 6.8b. It is evident that friction factor is more in agreement with Blasius law if the average is obtained with $c_1 > c_2$. Therefore, in absence of measured outlet pressure it is appropriate to estimate the average temperature by assuming a higher weight of the inlet temperature with respect to the outlet temperature (Equation (3.5)), obtained by considering the fully expanded flow assumption.

For a case where pressure taps are located close to each other such that there is no significant temperature change from one tap to the other, average temperature in between

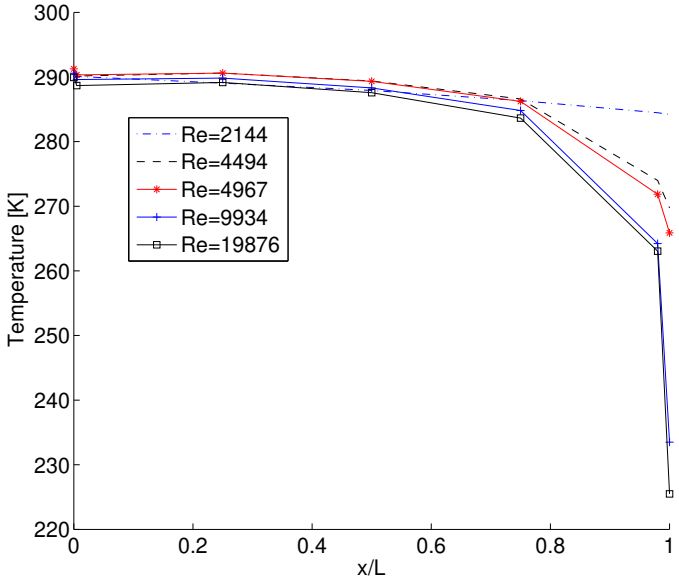

(a)

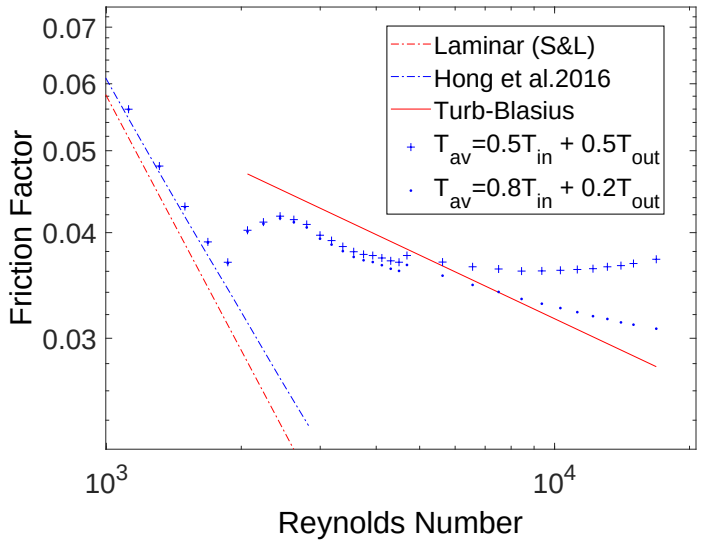

(b)

Figure 6.8: Numerical Temperature decrease along the length of MC1 at various Re (**a**), and Effect of T_{av} on calculation of experimental f_f (**b**).

can be approximated well with an equal weighted average ($c_1 = c_2 = 0.5$) and therefore semi-local $\tilde{f}_f$ follows Blasius law even in the choked turbulent flow regime. However, if the distance between these ports is large (this is the case with inlet and outlet of MC) an integral average of temperature between these ports should be considered. A detailed derivation of the average friction factor equation using such temperature

average is given in [108] and therefore it is skipped in this text. The calculation of average friction factor for Fanno flow (adiabatic walls) between two pressure ports a and b can be obtained as follows:

$$f_{f,av} = \frac{D_h}{x_b - x_a}\left[\left(-2\ln\frac{p_a}{p_b} + 2\ln\frac{T_a}{T_b}\right) - \left(\frac{1}{\dot{G}^2 R\left(T_{in} + \frac{{u_{in}}^2}{2c_p}\right)}\right)\right. \\ \left.\times\left(\frac{{p_b}^2 - {p_a}^2}{2} + \frac{B^2}{2}\ln\frac{p_b + \sqrt{p_b^2 + B^2}}{p_a + \sqrt{p_a^2 + B^2}} + \frac{1}{2}\left(p_b\sqrt{p_b^2 + B^2} - p_a\sqrt{p_a^2 + B^2}\right)\right)\right] \tag{6.8}$$

where $B^2 = 4\psi \times \frac{\dot{G}^2 R^2}{2c_p} \times \left(T_{in} + \frac{u_{in}^2}{2c_p}\right)$ and ψ, kinetic energy recovery coefficient, is taken as 2 for laminar and 1 for turbulent flow.

Semi-local $\tilde{f}_f$ curves between $x/L = 0.58 - 0.72$ and $x/L = 0.72 - 0.87$ are shown in Figure 6.9a for MC1 experiments. Average f_f between the inlet and outlet using Equations (3.4) and (6.8) is also plotted for comparison. There is an excellent agreement between $f_{f,av}$ calculated using Equation (6.8) and Blasius law even in choked turbulent flow regime. This is due to the fact that an integral average of the temperature is used instead of an equal weighted average between the inlet and outlet of MC. Whereas average friction factor calculated using Equation (3.4) suffers a deviation from Blasius law only due to erroneous estimation of the bulk fluid temperature between the inlet and outlet of MC. It is reminded to the reader that in Figure 6.9a, MC outlet pressure is still assumed to be the atmospheric as was done with M1 and M2 methods to evaluate $f_{f,av}$. However, as Equation (6.8) does not require for an explicit approximation of T_{av} between inlet and outlet of MC, resulting $f_{f,av}$ values are therefore in a better agreement with Blasius law. To emphasize it further, results of average friction factor by Equations (3.4) and (6.8) with numerical estimated pressure (num. p_{out}) instead of atmospheric pressure at outlet, are also shown in Figure 6.9b. A significant improvement in the slope of turbulent f_f calculated using Equation (3.4) can be seen when numerical outlet pressure is used due to better estimation of outlet temperature. Results however, are still higher than values calculated using Equation (6.8) because an equal weighted T_{av} between inlet and outlet ($c1 = c2 = 0.5$) is assumed.

On the contrary, $f_{f,av}$ with numerical outlet pressure calculated using Equation (6.8) is in closer agreement with Blasius law mainly due to better estimation of average temperature of gas. Therefore Equation (6.8) is recommended for calculating average experimental f_f between two pressure ports for adiabatic MCs. Equation (3.4) should be considered as an approximation of Equation (6.8) for two closely placed pressure taps, where temperature change between these taps can be well represented with an equal weighted average of respective temperatures, as is the case for semi-local friction factor calculations. An experimental/numerical campaign to analyze the applicability of Equation (6.8) on MCs of smaller D_h with even higher degree of flow choking is therefore recommended to complete this analysis.

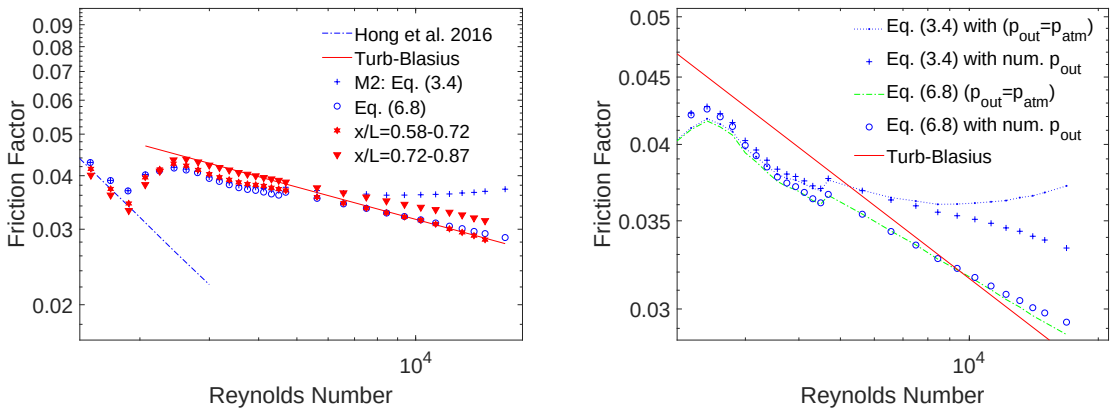

(a) (b)

Figure 6.9: Comparison of f_f calculation by using: M2, Equation (6.8) and semi-local values (**a**), Equations (3.4) and (6.8) with different outlet pressure treatment (**b**).

To summarize the results and discussion of current work following recommendations are being made:

- In the laminar flow regime, due to their significant relative contribution towards pressure drop, minor losses can only be estimated using validated numerical results for compressible gas microflows. To avoid numerical input while deducing experimental friction factor results, the M2 method can be used to correctly model pressure and temperature at the inlet of MC.

- In choked turbulent regime, MC outlet pressure should be measured to better estimate the cross-sectional average temperature using Equation (3.5). For an experimental campaign where it is not possible, adiabatic friction factor with an assumption of perfect expansion ($p_{out} = p_{atm}$) should be evaluated using Equation (6.8).

6.3 Summary

To understand the characteristics of high speed gas flows inside MCs, a combined experimental and numerical approach is followed in this chapter. Two experimental data reduction methodologies that are prevailing in the literature of gas microflows are compared. It has been shown that values of minor loss at the inlet manifold for employed experimental assembly do not match with the conventional loss coefficients available in the literature and hence it is recommended to calculate these through validated numerical models of the fluid flow. Such numerical evaluation of minor losses can then be coupled within experimental data reduction to calculate the correct friction factor in the laminar regime. It has been further shown that the assumption of atmospheric pressure at the outlet of MC always over predicts the total pressure drop in the MC. This assumption also leads to an acute underestimation of the average gas temperature at the outlet of MC which causes an apparent increase in the average friction factor, especially in the choked turbulent regime. It has been shown that estimation of gas bulk temperature from experimental data has a strong influence on the friction factor evaluation in the turbulent regime and equal weighted average between inlet and outlet results in a strong disagreement between numerical and experimental average friction factors. Such equal weighted average, on the other hand, is suitable if the distance between the pressure ports is not significantly large as in between the inlet and outlet of MC. Therefore semi-local friction factor ($\tilde{f}_f$) always follows the Blasius law in the choked flow regime as well. In order to avoid such false increase in highly

turbulent regime, a new relation (Equation 6.8) is presented for the correct evaluation of the friction factor in turbulent flow regime taking into account an integral average of the gas temperature between inlet and outlet of MC as the gas bulk temperature (T_{av} in Equation (3.4)). Experimental results using this equation better follow the Blasius law and numerical results even in the choked flow regime. Hence use of this equation is recommended for the future experimental analysis of gas flows inside MCs.

Chapter 7

Laminar to Turbulent Flow Transition in Microchannels

7.1 Introduction

Knowledge of turbulent transition in rectangular microchannels (MCs) is of prime importance as such geometries are being extensively employed in MC heat sinks and MC heat exchangers. Flow transition and consequent turbulent flow are of benefit for increased mixing and heat transfer in microsystems. Laminar to turbulent flow transition even in conventional sized channels is still an open field of investigation. Based on original experiments of Reynolds [45], the transition in pipe flow occurs around Re_c of 2000 for a rough entrance. Underlying processes that trigger such flow transition with an increase in speed for pipe flows are still not clear. Therefore this chapter attempts to investigate laminar to turbulent flow transition in adiabatic MCs. In the first experimental campaign flow transition in MCs with different aspect ratio ($\alpha = \frac{h}{w}$) is studied. The effect of inlet manifold geometry on the onset of flow transition is also studied experimentally. Both of the studies are coupled with numerical analyses in order to quantify the sensitivity of $\gamma - Re_\theta$ transitional turbulence model predictions of transition onset compared to experimental results.

7.2 Effect of Inlet Manifold Shape

Experimental analysis has been conducted in order to evaluate the influence of different entrance shapes on laminar to turbulent transition of gas flows inside adiabatic MCs. In current experimental campaign, four types of entrances are considered in order to establish if the different perturbations that they introduce have relevant effects on critical Reynolds number (Re_c) or the way in which the flow transition process happens. The four shapes are: sudden contraction inlet (SC), V-shape contraction inlet (VS), rounded entrance (RE) and Bellmouth contraction inlet (BM). To this end, four MCs are micromilled in PMMA using the methodology outlined in Chapter 3. Characteristic dimensions of the fabricated MCs are tabulated in Table 7.1. An attempt has been

Table 7.1: Channels geometry used for experiments.

Channel	h **(μm)**	w **(μm)**	L **(mm)**	α	D_h **(μm)**
SC	235	490	54	0.48	317
VS	245	505	54	0.485	330
RE	235	495	54	0.475	318.5
BM	180	452.5	54	0.398	256.7

made to keep the aspect ratio and hydraulic diameter almost similar for all MCs, however in the case of MC with BM inlet, α and D_h show an almost 18% deviation compared to the average of other 3 MCs. This is due to the fact that first 3 channels are machined together and BM shaped MC was milled separately in order to see the effect of such shape on transitional onset. Numerical simulation of these channels are also performed to compare the findings in both fields of investigations. PMMA chips containing the four investigated MCs with different inlet shapes are shown in Figure 7.1. While conducting numerical simulations, care has been taken to account for all the geometrical features of the experimental set-up as shown in Figure 7.2. The computational domain comprised of the micro channel, two manifolds, and the two inlet/outlet reducers. Inlet reducer connects the test section assembly to the piping from the volume flow meter whereas outlet reducer vents the gas exiting from MC to the atmosphere.

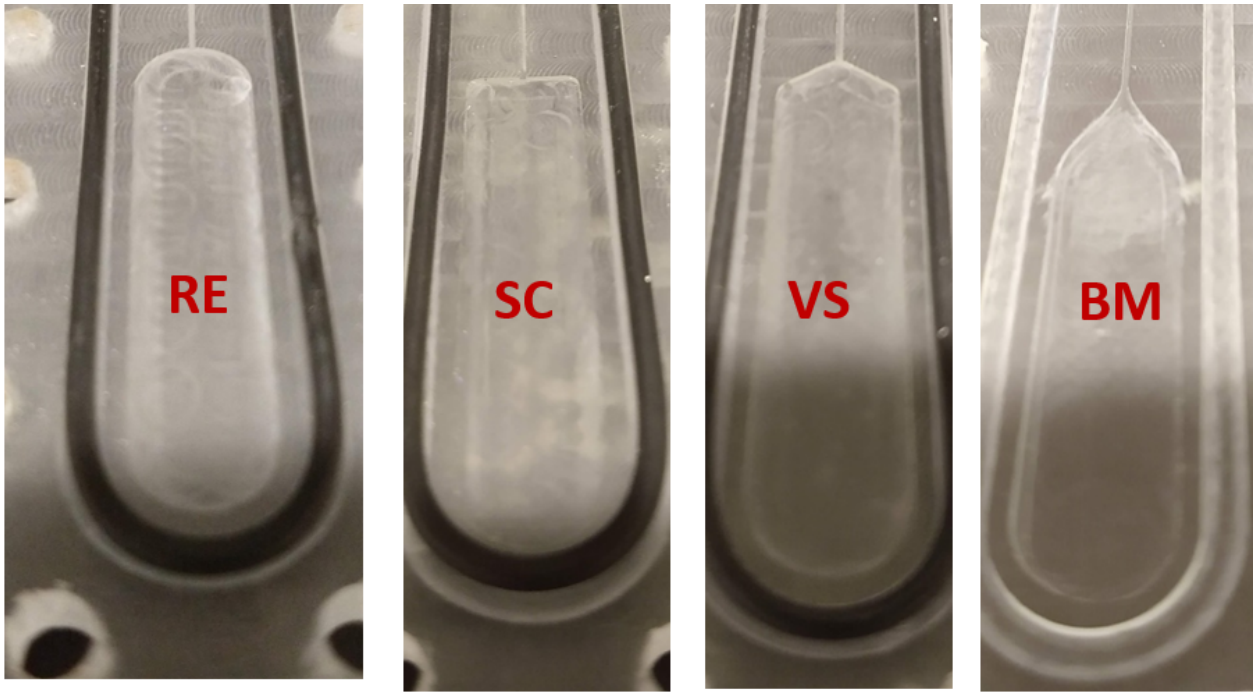

Figure 7.1: Fabricated MCs with different inlet shapes.

The mesh used in current simulations is similar to the one described in chapter 4 for MC used for the validation study. The only difference is that in the current case due to smaller channel length (54 mm compared to 100 mm) number of elements along the channel length are reduced to almost half of the validation simulation reported earlier. This allowed an increase in the number of divisions in both manifolds which have a longer length in current investigations compared to the validation case. In the current set of simulations, importance has been given to the joining part of the manifold and MC therefore in this zone mesh is significantly refined. For the number of divisions in the channel height and width and in the manifold height, a strategy similar to the one described in the validation study has been adopted. For all MCs 35 divisions on the height and 45 on the width are used in order to have y-plus smaller than one at least in the intermittent regime and an expansion ratio smaller than 1.1 in every case.

The first channel that has been tested is with the SC inlet. As for the other channels the analyzed range of Reynolds number is from approximately Re 400 to 16000. This limitation is due to the maximum volume flow rate that can be imposed by the largest flow controller that yields a maximum value of $Re = 16000$ with the current

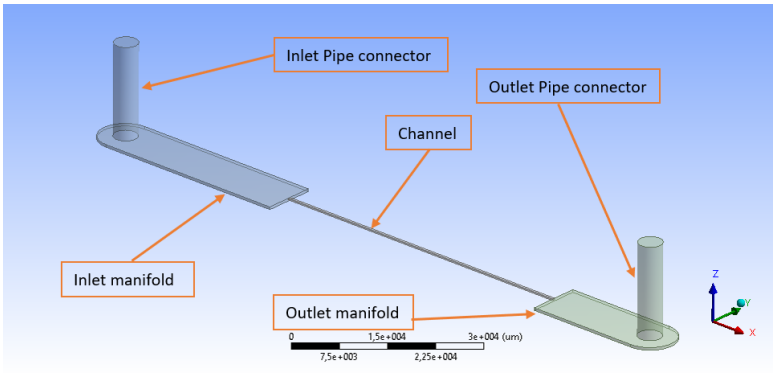

(a)

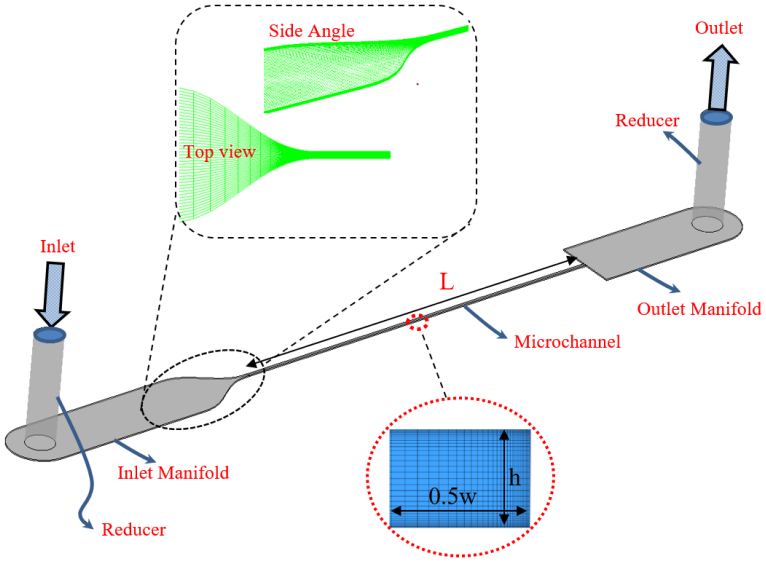

(b)

Figure 7.2: Geometric model used for numerical analysis: MC with sudden contraction (SC) (**a**), and bellmouth (BM) (**b**).

MC dimensions. In Figure 7.3 the Moody diagram for MC with SC inlet is reported. Reported values represent the average friction factor between the inlet and outlet of the MC. Experimental f_f is obtained using newly proposed Equation (6.8) and numerical results are evaluated using Equation (3.4) due to availability of inlet and outlet flow characteristics from numerical analysis. The agreement between numerical and

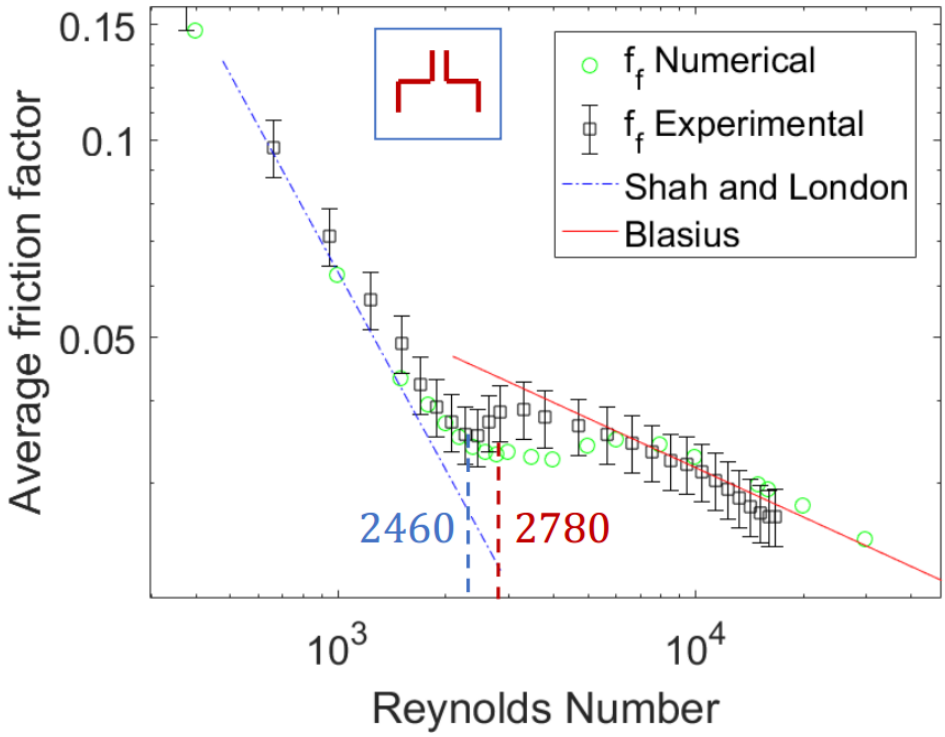

Figure 7.3: Friction factor for SC inlet.

experimental data is excellent in both laminar and turbulent regimes where the relative error is always under the 10%. However in transition interval the difference between the two values are greater, and as it can be seen in Table 7.2 it reaches the maximum at Re of 3500.

Table 7.2: Error between experimental and numerical f_f for SC channel

Reynolds Number	400	1000	2000	2400	3000	3500	5000	10000	15000
Relative error	0.080	0.106	0.028	0.043	0.152	0.166	0.063	0.038	0.091

Both numerical and experimental values are in good agreement with conventional theory for laminar (Shah & London: Equation (4.19)), and turbulent regime (Blasius:

Equation (4.20)). A similar trend is confirmed also by the second channel that has been tested, the RE one. In this sample, as in the previous one the results show a very

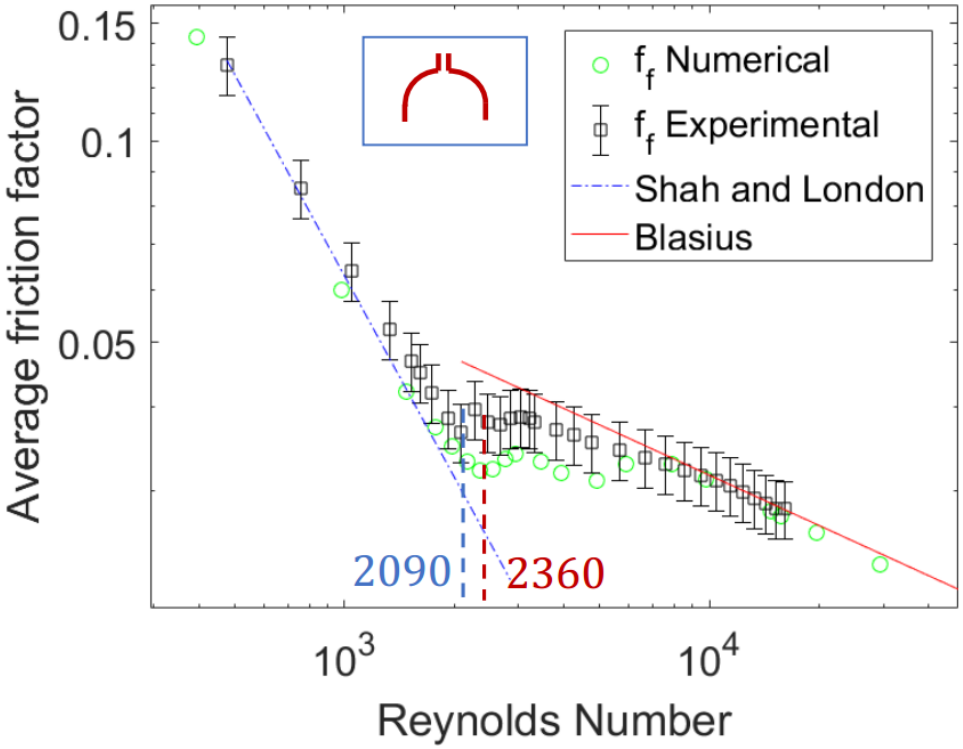

Figure 7.4: Friction factor for RE inlet.

good agreement with conventional theory, however in this case the discrepancies between numerical and experimental friction factor are slightly bigger in the transitional regimes. The maximum relative error reaches to 20% in the transitional regime as can be seen in Table 7.2.

Similar trend is exhibited by the last one of the three MCs fabricated contemporane-

Table 7.3: Error between experimental and numerical f_f for RE channel

Reynolds Number	500	1000	2000	2400	3000	3500	5000	10000	15000
Relative error	0.016	0.136	0.086	0.198	0.137	0.140	0.126	0.007	0.017

ously, that is the V-shape inlet. As in the other two cases the range of analyzed number goes from 400 to 16000, and similar mass flows have been specified as inlet boundary condition for the numerical simulation. However during the experimental testing $\dot{m}$ values are not exactly the same as of numerical simulations but are in the same range.

For this reason in order to compare the results of experimental f_f with the one obtained from the simulations, linear interpolation between experimental results is performed and data is compared in Table 7.2. As shown in Figure 7.5 that although the values

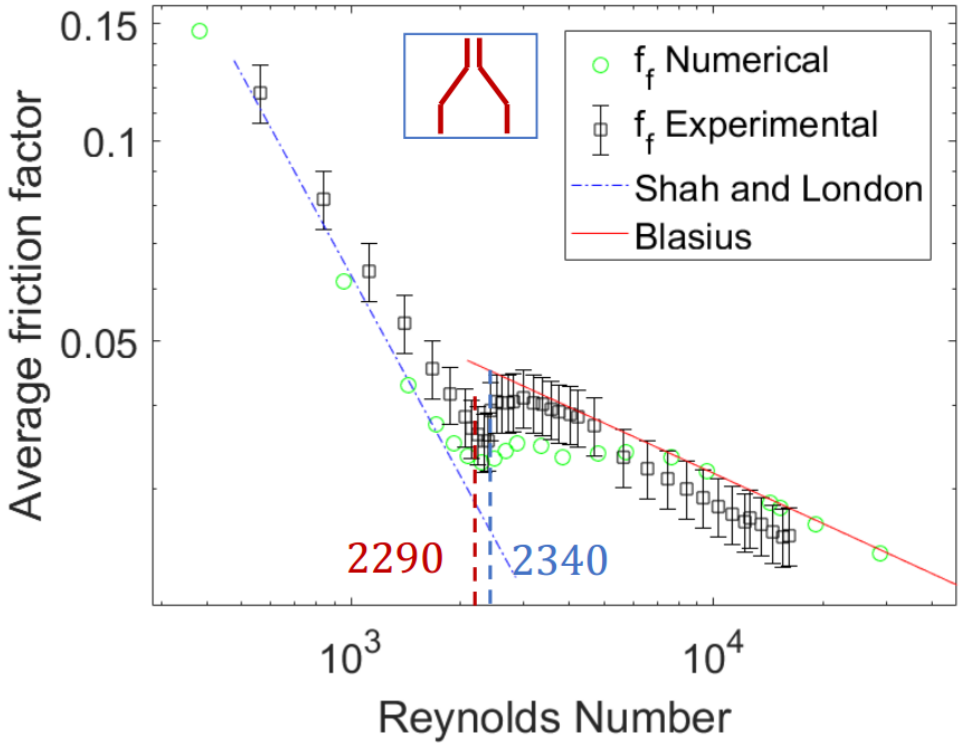

Figure 7.5: Friction factor for V-shape inlet.

Table 7.4: Error between experimental and numerical f_f for V-shape inlet channel

Reynolds Number	1000	1500	2000	2400	3000	3500	5000	10000	16000
Relative error	0.053	0.029	0.083	0.173	0.089	0.132	0.121	0.130	0.087

of f_f in the turbulent regime are parallel to Blasius correlation but are all almost 13% smaller than conventional theory. This deviation is due to an imperfect calibration of the high pressure sensing element, in fact, the shift from the Blasius curve starts from the Re at which the membrane was changed. Since the main focus of this study is in transitional regime Re and not the fully developed turbulent regime, experiments were not repeated to improve fully turbulent results and experimental Re_{cr} of 2290 is extracted from the results whereas simulation predicts it to be 2340.

The last inlet configurations analyzed is the Bellmouth. This shape results in a smoot-

her cross sectional change from the manifold to MC inlet and therefore induces fewer perturbations in the flow. This is the reason why both Ghajar et al. [109, 110] and Dirker et al. [111] found that transition was delayed in the channels with this inlet configuration compared to similar channel but with different entry shape. The design allows the flow to undergo a gradual change in section and it has the time to develop a parabolic profile. By using $\gamma - Re_\theta$ transitional turbulence model, Minkowycz et. al [95] also showed that if the parabolic profile is maintained at the channel inlet with a turbulence intensity of 1%, an abrupt flow transition from the laminar to turbulent happens at the very high Re. More recently Moruz et. al [112] have shown the similar results where they observed a Re_{cr} of ~3800 with air flow within a conventional sized channel having an α of 0.05. Numerical results also exhibit the delayed flow transition

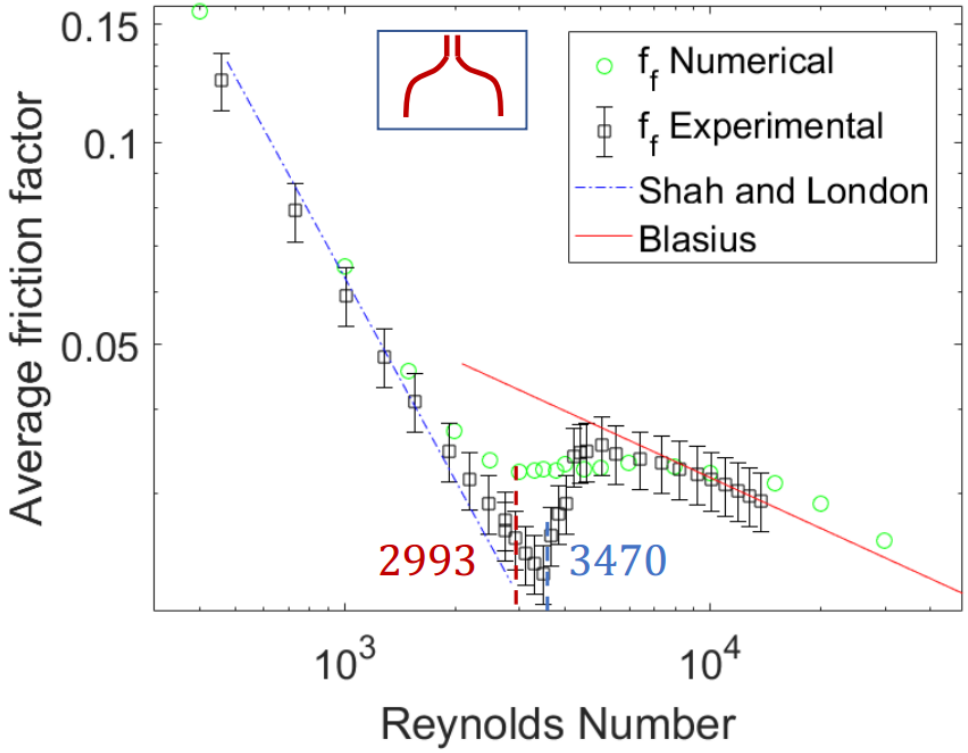

Figure 7.6: Friction factor for BM inlet.

in the case of BM compared to other cases, however it is incapable of capturing the abrupt transition observed in experimental results and rather follows the usual smooth transition pattern. This is the reason why the errors in the intermittent regime are

Table 7.5: Error between experimental and numerical f_f for BM inlet channel

Reynolds Number	1000	1500	2000	2500	3000	3500	5000	10000	13000
Relative error	0.085	0.068	0.091	0.143	0.223	0.289	0.079	0.023	0.060

close to the 30%. The experimental f_f, follows Shah and London correlation (Equation (4.19)) much longer and present a Re_c higher than 3400. Simulation on the contrary starts the detachment from laminar correlation earlier and the f_f remains almost constant during the whole intermittent regime.

In order to highlight the difference in f_f and Re_c amongst various inlet configurations a comparison of experimental f_f is given in Figure 7.7. It can be clearly seen that the BM inlet shows the most delayed transition compared to all the other three MCs. This behaviour is similar to what has been experimented by Tam et al. [110] where the smoother inlet was able to maintain the laminar state longer than other configurations by causing lower turbulent perturbations at MC inlet. The other three MCs instead, do

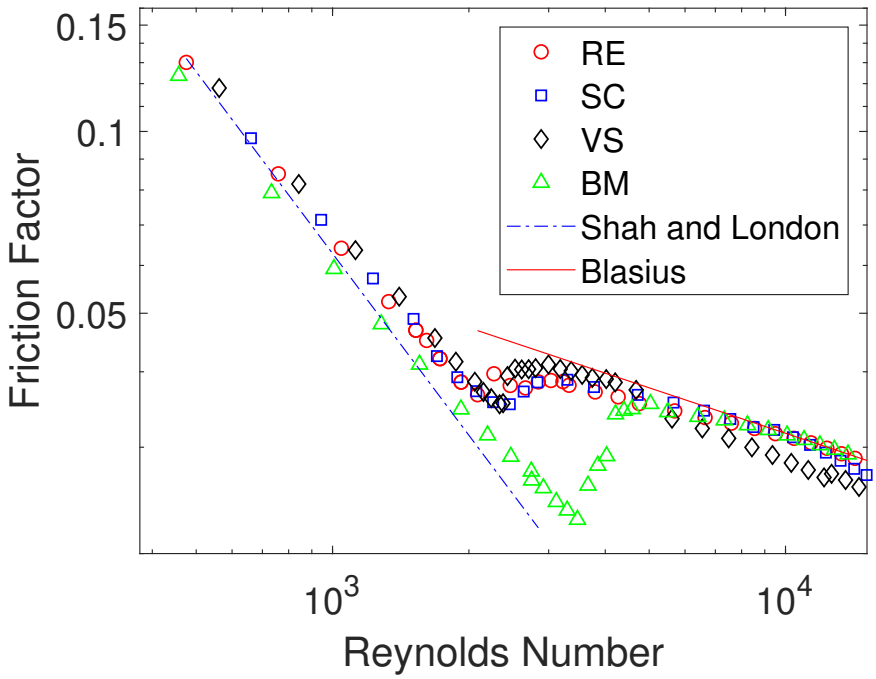

Figure 7.7: Experimental friction factor comparison among the 4 inlet configurations.

not show such big difference in Re_c, and to better capture the initiation of laminar to

turbulent transition, a magnified picture of intermittent Reynolds number is presented. Thanks to Figure 7.8 the difference in Re_{cr} amongst the SC, RE and VS channels can be appreciated. Results of current experimental and numerical study in terms of Re_{cr}

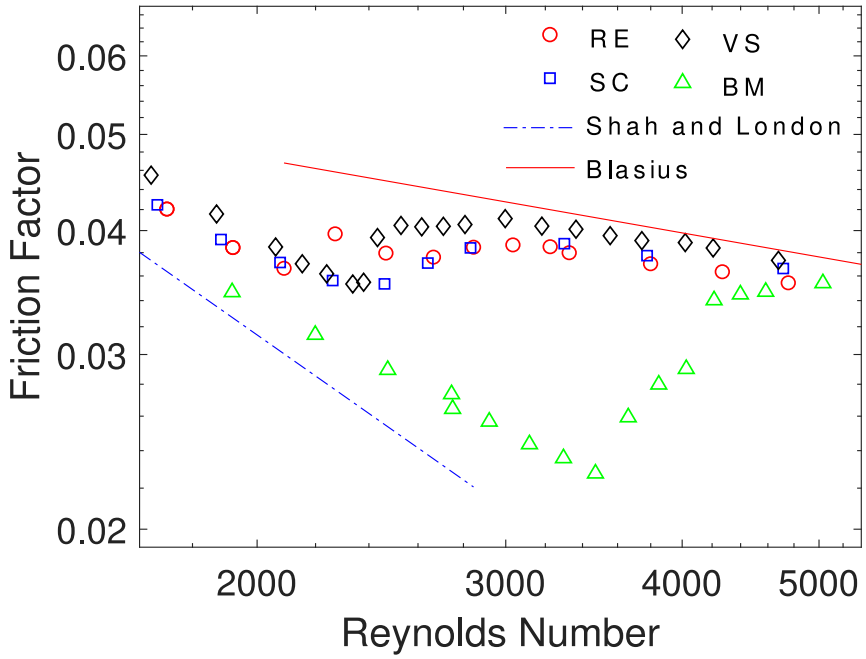

Figure 7.8: Magnified view of [1500 − 4000] Reynolds interval for experimental friction friction factor

are reported in Table 7.2. These values should be considered as indicative numbers as only a discrete set of mass flows within intermittent regime are employed in both experimental testing and numerical simulations.

Table 7.6: Numerical and experimental Critical Reynolds number

Channel	Exp. Re_c	Num. Re_c	Tam [110]	Dirker [111]	Moruz [112]
RE	2090/2660	2360	-	-	-
V-shape	2340	2290	-	-	-
SC	2460	2780	3100	2000	3600
BM	3470	2993	5100	1800	3800

Experimental results show that MC with RE inlet seems to show two relative minimum

points of friction factor in the Moody Chart before becoming fully turbulent. Similar behavior is confirmed by simulation results, even though the Reynolds number at which the minimum is observed in numerical f_f is much higher than the experimental one. Similar experimental results are also reported by Dirker et. al for bell mouth inlet of $D_h = 1.05mm$ MC where they also observed two sudden changes of friction factor before transitioning to fully turbulent flow.

In order to establish the amplitude of transitional regime in terms of Re (ΔRe_{LT}), the difference in Re between the onset of transition (Re_c) and when the flow reaches the fully turbulent condition i.e. slope of f_f parallel to Blasius law (Re_t), is used for all the four investigated inlet shapes and comparison is reported in Table 7.2. From both experimental and numerical results, it can be seen that the length of the transitional regime is also higher for BM. This is followed by RE and SC. There exists a discrepancy between numerical and experimental results of VS where experimental results show somewhat abrupt transition and numerical results show a smooth transition to fully turbulent flow. It is acknowledged that in order to have a better definition of

Table 7.7: Numerical and experimental Re_t

Channel	Exp. Re_t	Exp. ΔRe	Num. Re_t	Num. ΔRe
RE	6644	4554	6881	4521
V-shape	4020	1680	6697	4407
SC	5660	3200	5956	3176
BM	9157	5687	9973	6980

this intermittently transitional flow regime, one should have a finer sampling strategy in terms of $\dot{m}$ analyzed, both for experimental tests and numerical simulations. An experimental campaign with more $\dot{m}$ in such range is relatively straightforward and takes a few minutes whereas each numerical iteration takes considerable computational resources. High number of nodes and four additional transport equations used to model the turbulence in $\gamma - Re_\theta$ model, increase the solution time of numerical model which lasts for approximately six hours on 8 computational cores. Moreover, the initial

aim to undertake this study was to quantify the variations in Re_{cr} by changing inlet manifold shapes, therefore a finite number of $\dot{m}$ points are simulated in transitional as well as fully turbulent regime.

7.3 Effect of Aspect Ratio

7.3.1 Experimental Analysis

Experimental analysis has been performed for 6 MCs with different aspect ratio ranging from 0.25 to 1.04. D_h of the manufactured MCs ranges from 220 μm to 523 μm. As it has been done in the previous section, Re_{cr} is determined from the friction factor curve. It is individuated as a Re when f_f curve reaches its first minimum. Local pressure measurements using pressure ports (see Figure 6.1) are taken in order to establish flow transition using the semi local friction factor ($\tilde{f}_f$). This will help to establish if the transitional behavior shows a variation along the length of the MC using different pressure ports. Values of average friction factor (f_f) are calculated using Equation (6.8) whereas values of local $\tilde{f}_f$ are evaluated using Equation (3.4) applied between the last two pressure ports. Dimensions of the fabricated MCs are shown in Table 7.8.

Table 7.8: Dimensions of the MCs manufactured to study effect of aspect ratio on flow transition

Channel	h (μm)	w (μm)	L (mm)	α	D_h (μm)	ϵ (μm)	$\epsilon/D_h(\%)$
MC1	515.5	536	100	1.04	523.8	0.778	0.148
MC2	566.5	349	100	0.62	431.3	1.15	0.267
MC3	559	330	100	0.59	414.7	0.845	0.203
MC4	553.5	140	100	0.25	220.7	0.904	0.409
MC5	441	314	100	0.71	366.8	0.904	0.246
MC6	364	315	100	0.865	337.1	1.05	0.312

Experimental results of f_f for all six channels tested are shown in Figures 7.9-7.11. As evidenced before, laminar f_f is in agreement with the correlation proposed by Hong et

al. [15] in high laminar regime, especially for smaller D_h MCs. For MC1 turbulent f_f both local and average are lower than Blasius law (Eq. 4.20). Similarly for other MCs, average f_f might be slightly lower than Blasius but local $\tilde{f}_f$ follows it in all the cases. It can also be observed by the experimental results that although average and local f_f are quantitatively different for transitional regime Re but flow transition occurs at the same Re_{cr} for both cases. Thus Re_{cr} can be extracted from any of the curves (average or semi-local f_f). A comparison of friction factor between last two pressure ports for

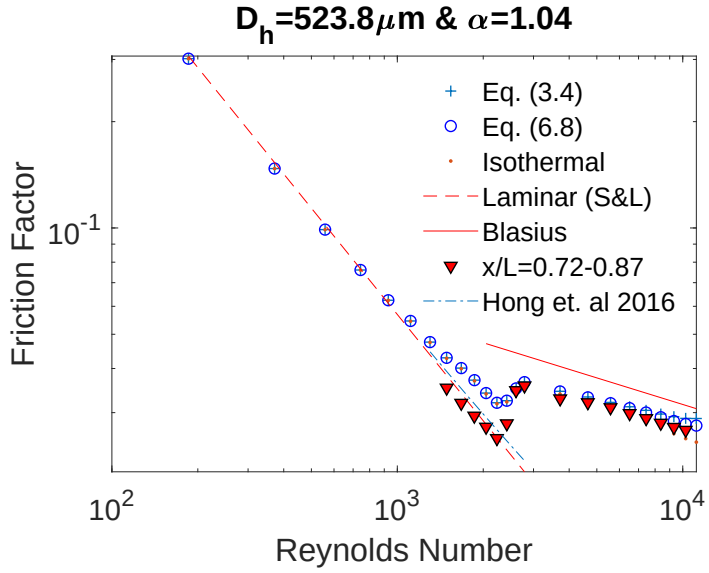

(a)

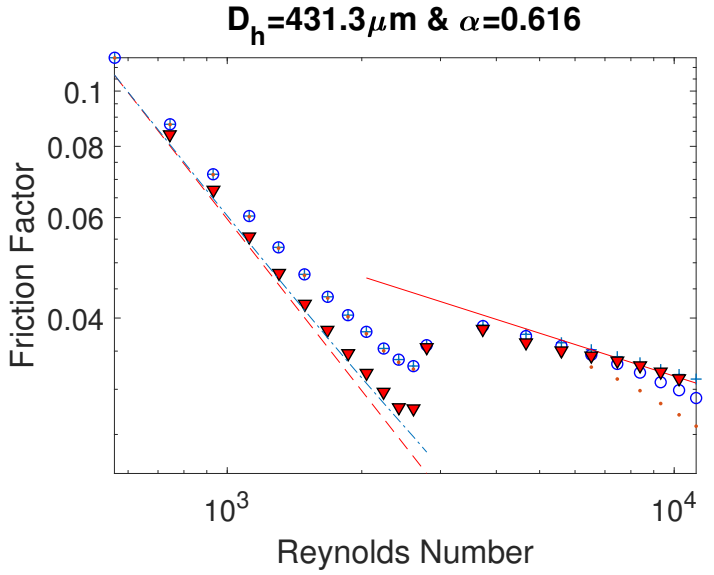

(b)

Figure 7.9: Average and local friction factor for MC1 (**a**), and MC2 (**b**).

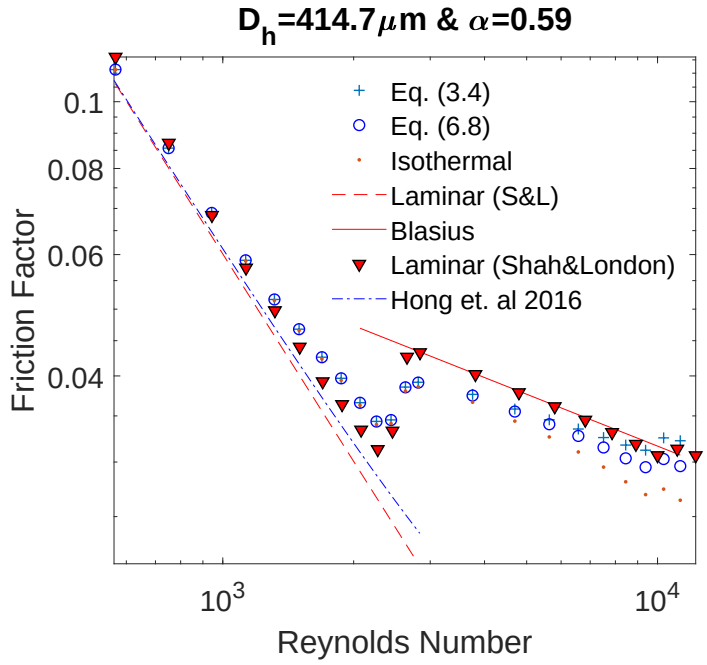

(a)

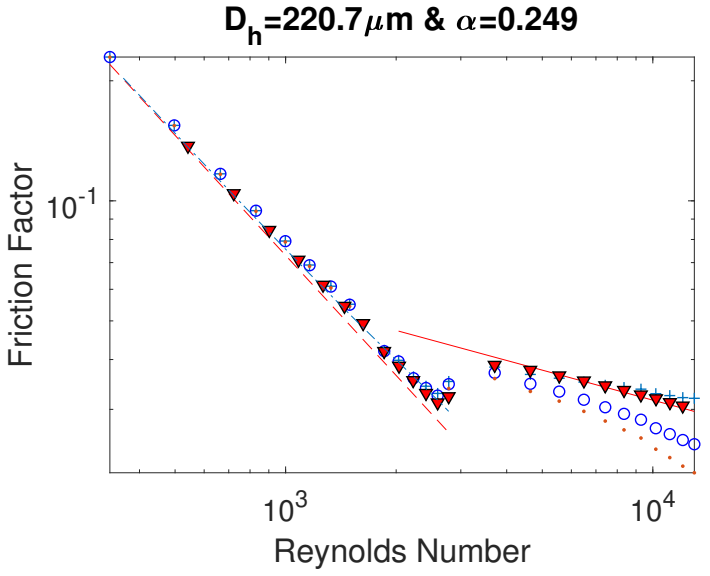

(b)

Figure 7.10: Average and local friction factor for MC3 (**a**), and MC4 (**b**).

all the experimented MCs is shown in Figure 7.12. From above analysis, flow transition happens in all the experimented channels when Re is in the range of 1863-2772 which is a classical range mentioned in textbooks for laminar to turbulent flow transition. As experiments were performed at the discrete set of Re therefore Re_{cr} is provided as a range in Table 7.9. Flow transition ought to happen in between the minimum point in the f_f curve and the successive point in experimental results. Transition is delayed

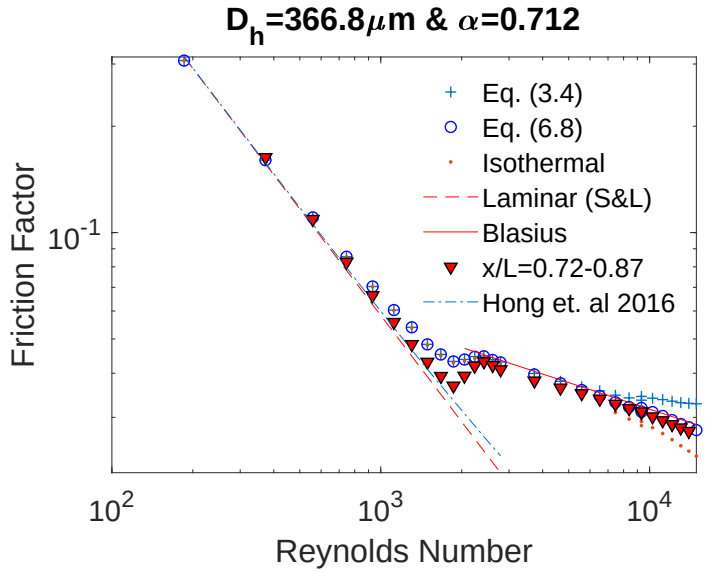

(a)

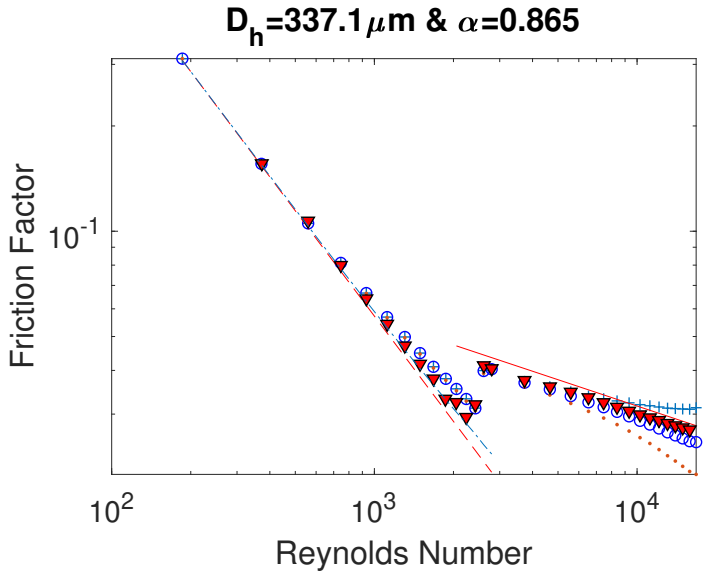

(b)

Figure 7.11: Average and local friction factor for MC5 (**a**), and MC6 (**b**).

the most in the channel with smallest α i.e. MC4. For channels MC5 and MC0, since α is almost similar, Re_{cr} is also in the same range. These channels have the smallest Re_{cr} amongst all the channels experimented. Last two channels in Table 7.9 are again showing an almost constant range of transitional Re. On close observation, no clear trend can be withdrawn from the current experimental data as to how aspect ratio of rectangular MCs affects the Re_{cr}. However ignoring MC3 shows that Re_{cr} is highest for smallest α and then decreases with an increase in α until α is $\sim$0.7. After this point

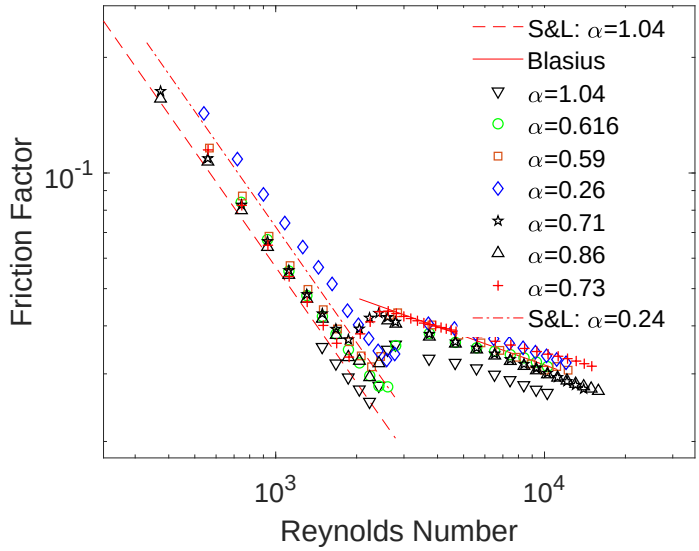

(a)

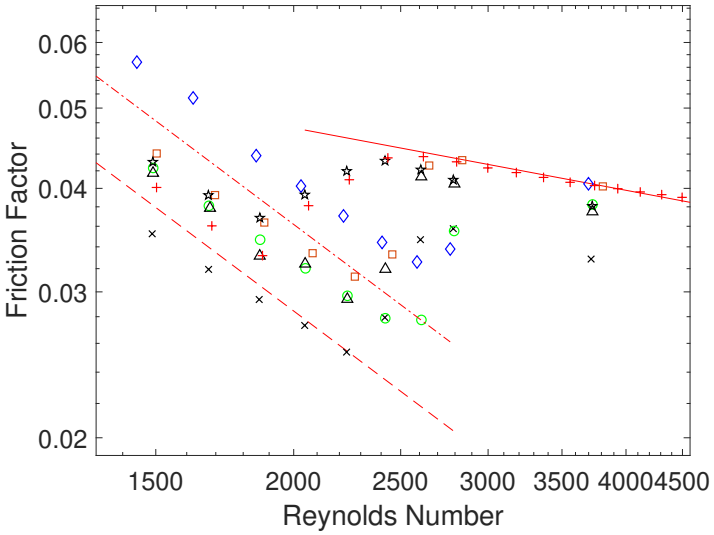

(b)

Figure 7.12: Comparison of f_f for all the tested MCs (**a**), and a zoomed region for Re between 1500 and 4500 (**b**).

Re_{cr} increases again and becomes almost constant.

While manufacturing these MCs, it was aimed to vary the α but due to the choice of same milling blade D_h also consequently varies from one MC to the other. This might be the reason that current experimental results do not show a strict dependence on the α of the MC. Therefore in order to see the dependence of Re_{cr} on α and D_h separately, a numerical parametric study is performed in the next section.

Table 7.9: Re_c for all experimented MCs.

Channel	D_h **(**μ**m)**	α	Re_{cr}
MC4	220.7	0.25	2586-2772
MC3	414.7	0.59	2272-2456
MC2	431.3	0.62	2420-2610
MC5	366.8	0.71	1863-2046
MC0	295	0.73	1873-2062
MC6	337.1	0.86	2236-2421
MC1	523.8	1.04	2233-2420

7.3.2 Numerical Parametric Analysis

The validity of the $\gamma - Re_\theta$ transitional turbulence model for the prediction of Re_{cr} has been demonstrated earlier in this chapter where numerical predictions were in close agreement with experimentally observed Re_{cr} for different shapes of inlet manifolds. Therefore the same model is utilized in this section to perform a controlled parametric study to investigate the effects of aspect ratio on flow transition. Unlike the experimental campaign, α of the MC is varied from 0.1 - 1 by keeping a constant D_h. Three D_h values ($100\mu m,\ 300\mu m,\ 500\mu m$) are considered and for each D_h four α values ($0.1,\ 0.25,\ 0.5\ and\ 1$) are simulated.

A notable difference between the current computational domain and the one detailed out in Chapter 4 is that in order to reduce computational nodes and hence solution time, inlet manifold is not considered. Rather inlet boundary condition is specified at the MC entrance as done by Minkowycz et al.[95] and Cheng et al. [101]. Moreover, instead of designing the experimental outlet manifold, the outlet of MC is extended in the form of an expansion nozzle. The length of the nozzle is kept as $10D_h$ in all cases. This was performed to allow for any under expansion at the MC outlet which will help to ascertain flow choking at higher Re. Resulting computational domain is shown in Figure 7.13.

To quantify the effects of such geometric changes compared to experimental results, simulations are performed for MC0 (used in validation study) by neglecting the inlet

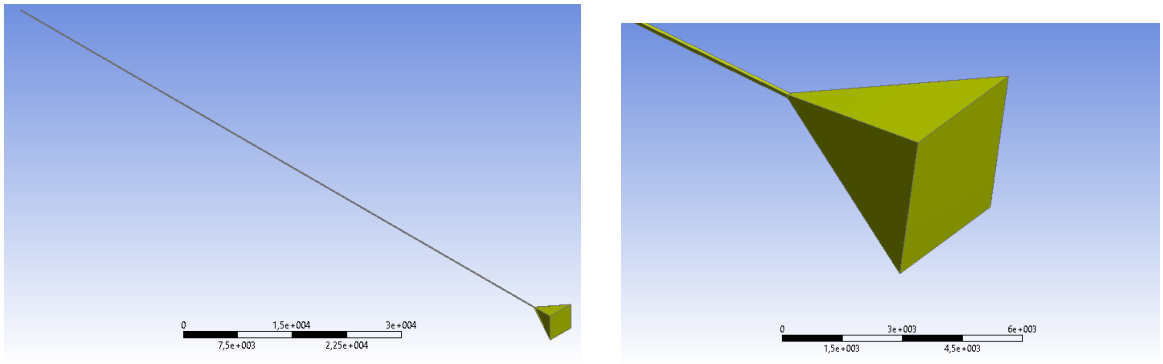

Figure 7.13: Geometry of the domain for the parametric analysis

manifold and adding a nozzle at the outlet. As shown in Figure 7.14, it affects the computational results in the transitional regime slightly but laminar and fully turbulent values match between the whole domain and by considering MC only. From Moody

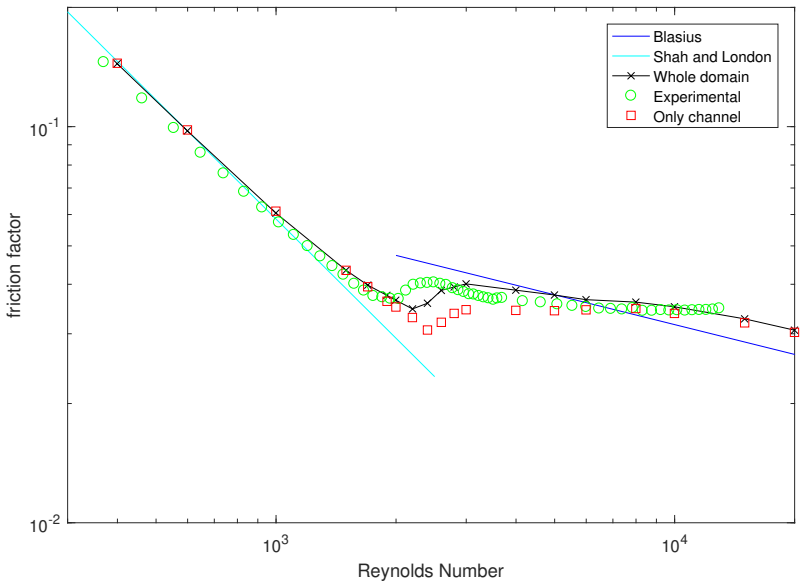

Figure 7.14: Comparison between f_f considering the whole domain and the channel only.

diagram, it can be observed that by specifying the inlet boundary condition directly at the MC inlet, Re_{cr} is slightly delayed and the fully turbulent flow is achieved at a higher Re as compared to the case of the whole domain (including inlet/outlet manifolds and piping). This signifies that although computationally inexpensive, such treatment results not only a delayed Re_{cr} but also the way transition happens in the MC and

thus the intermittent regime persists for a wider range of Re in the case where MC is considered only.

A total of 12 MCs are considered for which geometric dimensions are given in Table 7.10. Height and width of the MCs are varied for the desired aspect ratio between 0.1-1 such that D_h stayed constant. The length of the MC is kept constant in all the cases as 100 mm, which is sufficient to ensure, a ratio $\frac{L}{D_h} \geq 200$ even for the largest D_h considered.

Table 7.10: Geometric dimensions of simulated MCs

Channel	h [μm]	w [μm]	α	D_h[μm]
MC7a	55	550	0.1	100
MC7b	62.5	250	0.25	100
MC7c	75	150	0.5	100
MC7d	100	100	1	100
MC8a	165	1650	0.1	300
MC8b	187.5	750	0.25	300
MC8c	225	450	0.5	300
MC8d	300	300	1	300
MC9a	275	2750	0.1	500
MC9b	312.5	1250	0.25	500
MC9c	375	750	0.5	500
MC9d	500	500	1	500

A mesh independence study is performed for channel 8d ($D_h = 300\,\mu$m and $AR = 1$). Four meshes are generated as tabulated in Table 7.11. For each mesh three values of $\dot{m}$ corresponding to Re (1000, 2400, 10000) are simulated. In the laminar and fully turbulent flow regimes, the difference in average f_f between different mesh setups was inappreciable whereas it did change significantly in the transitional flow regime. Relative error in average f_f at $Re = 2400$ is 25% between Coarse and Medium and between Medium and Fine mesh. When compared between Fine and Very Fine, however, the relative reduces to 2.5 % only.

A similar trend can also be observed by comparing velocity profiles at the middle of

Table 7.11: Types of mesh for independence study of channel 8d

Mesh Type	Divisions in height	Division in width	Number of elements	f_f at Re 2400
Coarse	20	20	80000	0.051
Medium	30	30	180000	0.039
Fine	40	40	320000	0.0307
Very Fine	50	50	500000	0.0299

the MC along with its height. It can be seen in Figure 7.15 that velocity profiles for the last two cases are nearly identical. Therefore, considering a tradeoff between computational time and solution accuracy, a Fine grid with 320000 elements is used for further analysis. All the MCs are meshed with similar strategy by putting an emphasis on the near wall region such that $y^+ \leq 1$ and to have at least 10 number of elements in the boundary layer for all considered cases. Numerical solutions for all

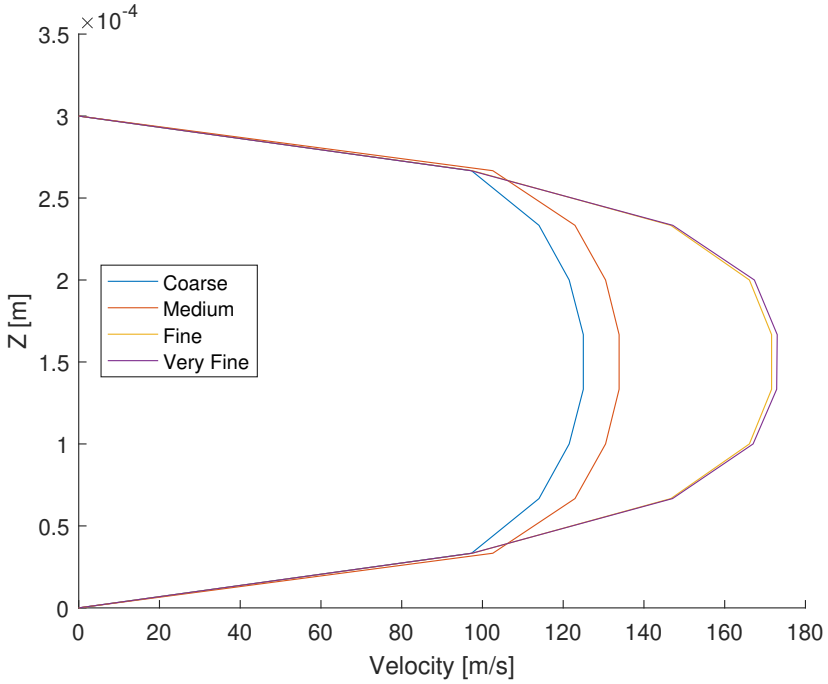

Figure 7.15: Velocity profiles for Reynolds 2400.

the channels will help to understand the laminar to turbulent flow transition from two distinct perspectives. As mentioned earlier, first it will help to study the effect of α by keeping the D_h constant which was not the case in experimental results presented in the

previous section. Secondly, considering three different D_h will also help to underscore prominent effects of D_h on the Re_{cr} if any by keeping α as constant.

Effect of aspect ratio

As specified earlier, $\dot{m}$ at the MC inlet is varied to simulate an inlet Re in the range of 400 to 20000. Curves for average f_f are compared between different α values for a constant D_h. This has been performed for all three D_h considered and the comparison for MCs with D_h of 100 μm is shown in Figures 7.16. It is quite evident that with a decrease in the α, transition of the flow from laminar to turbulent is being delayed for a constant D_h. Re_{cr} increases from 2000 to 4000 by decreasing α from 1 to 0.1. This trend is in agreement with the Li and Olson [46] and Wiber and Ehrhard [113] which noted a decrease in Re_{cr} for an increase in α for liquid flows in rectangular MCs. Both of experimental campaigns took care to test MCs of different α by keeping an almost constant D_h. Li and Olsen [46] used μPIV to ascertain flow transition and quoted that Re_{cr} decreases from 2315 to 1715 by an increase in α from 0.2 to 1. Similarly, Wibel and Ehrhard [113] using pressure drop studies observed a similar trend where Re_{cr} decreased from 2300 to 1800 by increasing α from 0.2 to 1. In a later study, Wibel and Ehrhard [47] used μPIV for the same MCs to reach a similar conclusion that flow transition occurs in the same range of 1900 - 2200. Qualitatively similar results are obtained for other two D_h values investigated in the current study and are shown in Figures 7.17 - 7.18 where Re_{cr} is in the range of 2300-4000. From results of all three D_h, it can be observed that for α of 0.1 and 0.25 laminar breakdown and transition to turbulence is much delayed that is average f_f follows the Shah and London correlation much longer. On the contrary for higher values of α deviation from laminar theory can be evidenced at a Re as small as 1500. It has been established that such deviation in the laminar regime is due to compressibility effects of the gas flows inside micro dimensional geometries [15, 27, 33]. From the numerical analysis, a qualitative as well as quantitative insight into the state of the flow inside MC that whether it is laminar,

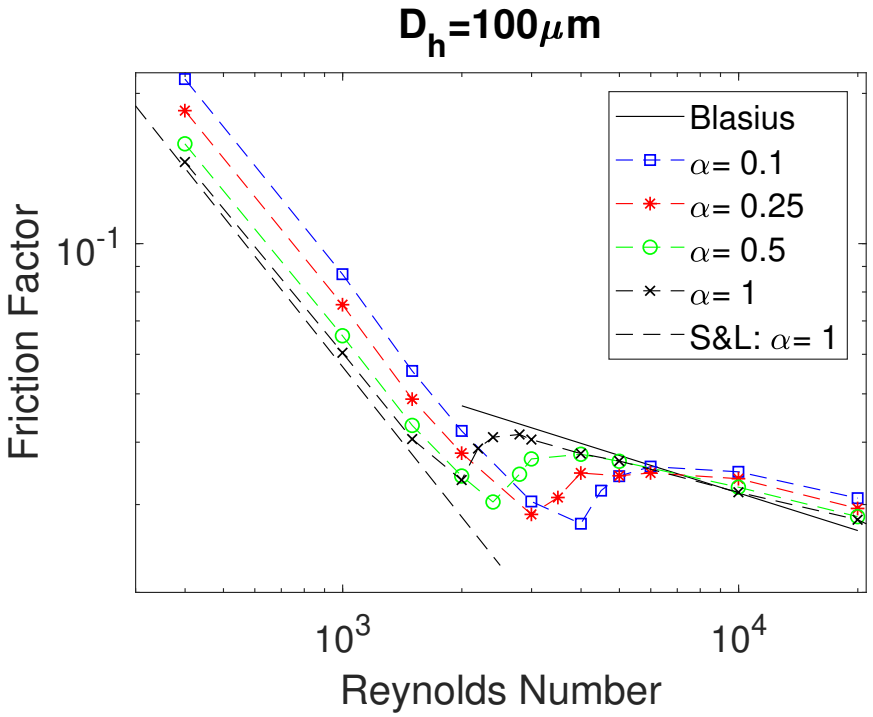

Figure 7.16: Average f_f curves for MCs with $D_h = 100\,\mu$m and different ARs (MC7).

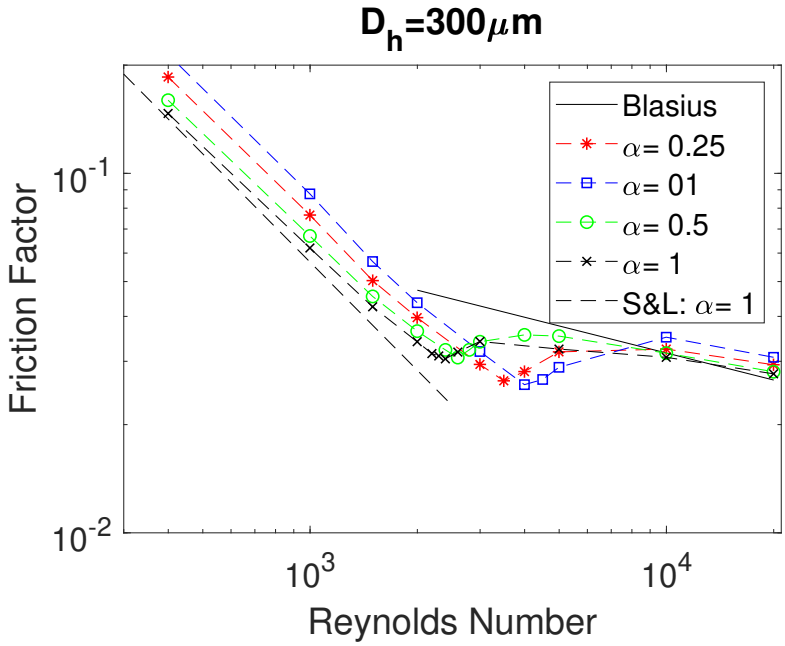

Figure 7.17: Average f_f curves for MCs with $D_h = 300\,\mu$m and different ARs (MC8).

intermittent or fully turbulent can be achieved by observing intermittency factor(γ) of the employed transitional turbulence model. As outlined in Chapter 4 that γ is a local value defined using a transport equation (Equation 4.8). To gain an overall

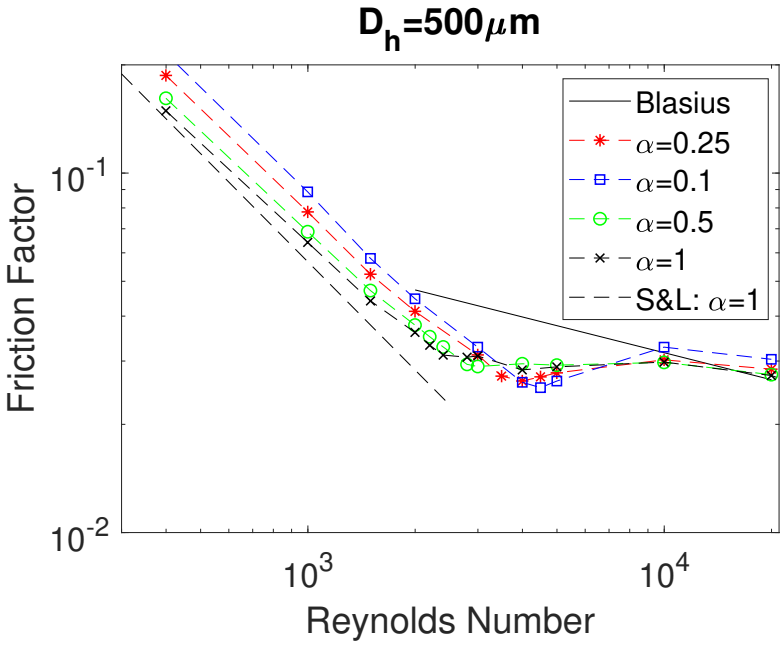

Figure 7.18: Average f_f curves for MCs with $D_h = 500\,\mu$m and different ARs (MC9).

view of the flow state, an average value over the whole computational volume can thus be defined and is plotted in Figure 7.19 for MCs with D_h of 100 μm and various α against Re. At low Re average γ values are close to zero for all the α values considered

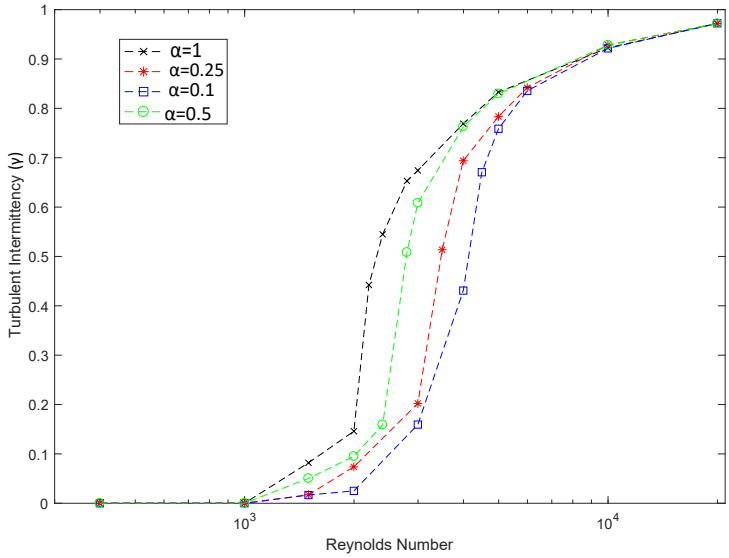

Figure 7.19: Average turbulence intermittency for MCs with $D_h = 100\,\mu$m (MC7)

which signifies predominantly laminar behavior of the fluid flow inside MC. As Re is

increased, average γ values start increasing signifying turbulent flow patterns being present in the flow and flow is in the intermittent regime whereas for very high values of Re flow exhibits its turbulent nature and consequently values assumed by γ are close to one. It is also evident from Figure 7.19 that MC with smaller α (0.1 and 0.25) persist in having smaller values of γ for a larger range of Re compared to MC with higher α (0.5 and 1). This is analogous of observing a delayed flow transition in MCs having smaller α. Similar findings for the other two D_h considered in current study are also reported in Figures 7.20 - 7.21 where qualitatively similar trends can be observed.

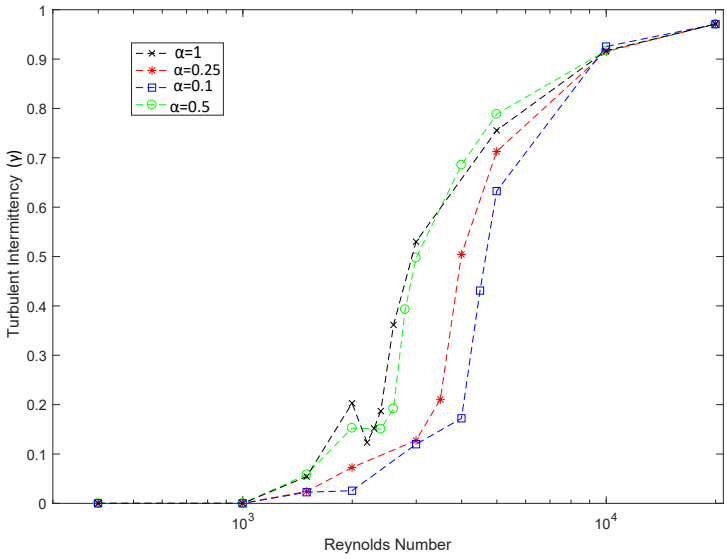

Figure 7.20: Average turbulence intermittency for Channels with $D_h = 300\,\mu$m (MC8)

As it has been mentioned before that these γ values are averaged over whole volume which also contains viscous sub-layer region. However, it is known that value of γ in this region is zero due to flow being purely laminar. It is pre determined for equation of intermittency transport (Equation 4.8) as boundary condition that γ values in the viscous sub-layer and at the channel walls are set as zero. Due to this reason, when averaged over the whole volume values of the γ are less than 1 even for fully developed turbulent flow (e.g. at $Re = 20000$). When f_f curve (Figure 7.16) is compared with γ curve (Figure 7.19), it can be seen that Re_{cr} in Moody chart corresponds to the values of Re in Figure 7.19 when averaged γ value is in between 0.2-0.3. In order to

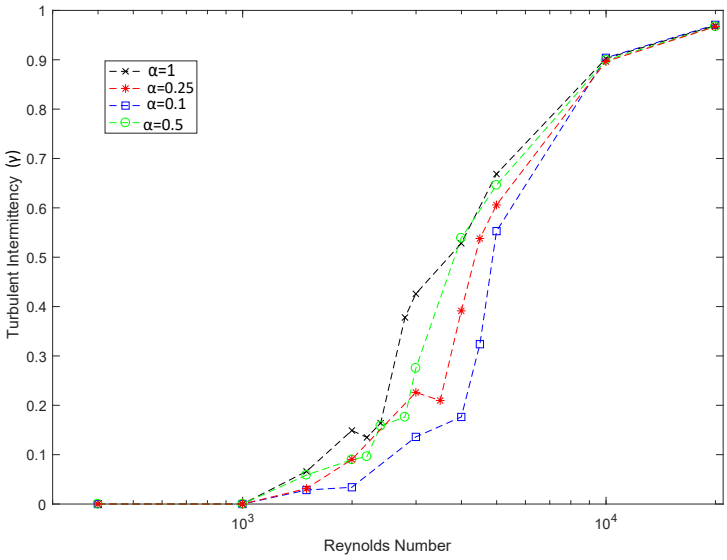

Figure 7.21: Average turbulence intermittency for Channels with $D_h = 500\,\mu$m (MC9)

see the state of the flow locally along the length of MCs, γ values are plotted along a center line of MC in Figure 7.22a. It can be seen that for Re of 1500, γ stays close to zero signifying the flow is laminar along the length of the MC. When Re is increased to 2000, γ keeps on fluctuating showing laminar behaviour in certain length and turbulent in other parts signifying the intermittently transitional flow. After an initial decrease over a very small portion of the length, from Re 2200 and onwards γ stays close to 1 for the most of the length of MC showing the turbulent state of the gas flow. To see the values for a specific cross section γ profile is also plotted at a representative cross section located at $x/L = 0.5$ of MC7d in Figure 7.22b. Similar observations as noted earlier can be made where for lower Re values assumed by γ are close to zero over the cross section but as Re increases above 2000, γ reaches unity except at the channel walls where it sharply decreases to zero due to imposed boundary condition as explained earlier.

In Figures 7.23, instead we can see profiles for the other limiting case that is AR 0.1. In this case intermittent flow is sustained until a higher Re of 4000 after which both profiles along the centre line (Figure 7.23a) as well as cross sectional (Figure 7.23b)

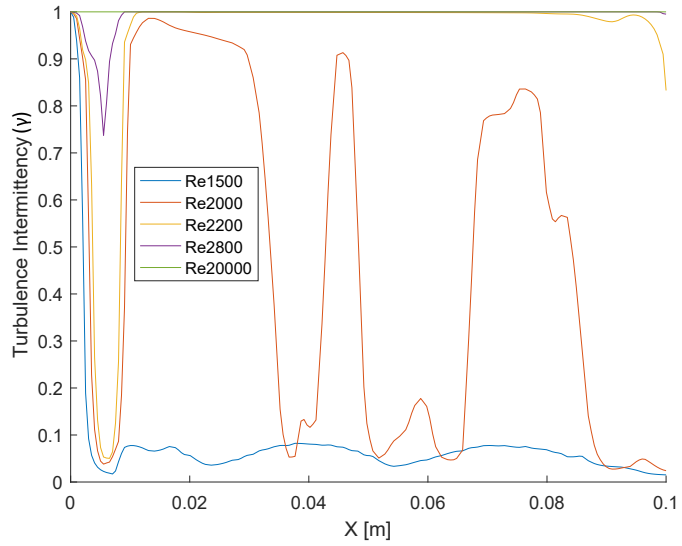

(a)

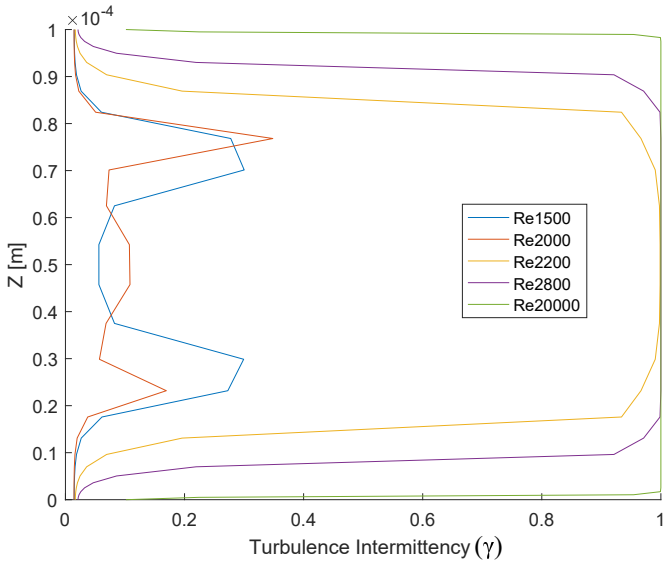

(b)

Figure 7.22: Turbulence Intermittency for MC7d $D_h = 100\mu m$ & $\alpha = 1$ along the centerline (**a**), and along vertical line at $x/L = 0.5$ (**b**).

show values of γ to be one signalling the turbulent nature of the flow. The same value for Re_{cr} of 4000 has also been extracted from Moody chart of the same MC (Figure 7.16). Considering the case for the biggest D_h of 500μm and $\alpha = 0.5$ (MC9c) variation of γ is reported in Figure 7.24. In this case it can be seen that γ profile clearly shows that intermittent flow is persisted for a longer range of Re and flow develops into fully turbulent state for Re close to 20000. Similar inference can be made from the relevant

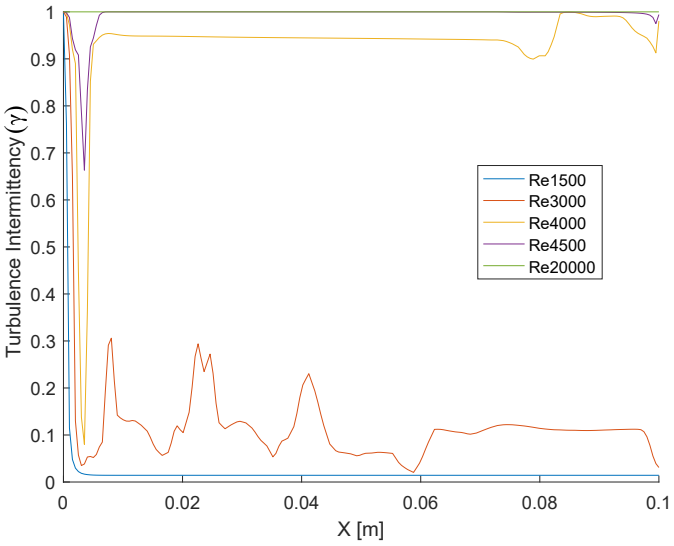

(a)

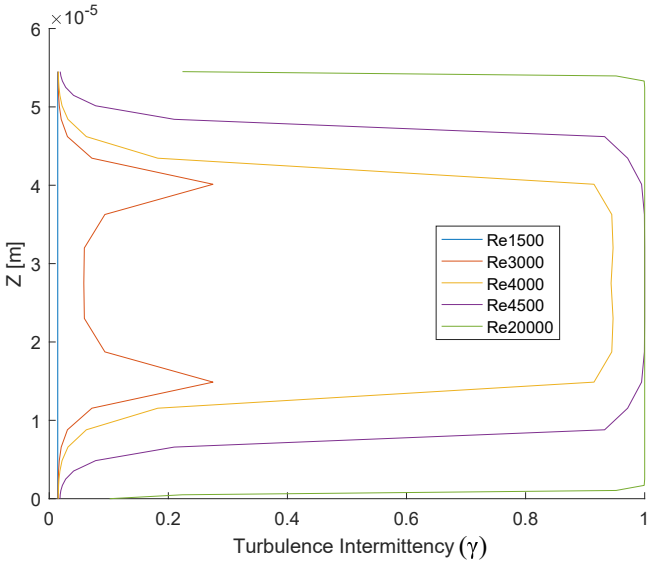

(b)

Figure 7.23: Turbulence Intermittency for MC7a $D_h = 100\mu m$ & $\alpha = 0.1$ along the centerline (**a**), and along vertical line at $x/L = 0.5$ (**b**).

curve in Figure 7.18 pertinent to MC9c where average f_f does not reach the Blasius curve until Re of 20000 signifying the larger extent of transitional flow regime. On the contrary for the smallest D_h simulated (MC7) the extent of transitional regime is smaller and relatively an abrupt transition can be noticed from Figure 7.16 where f_f becomes parallel to Blasius as early as Re of 6000, when compared to the biggest D_h simulated (MC9) shown in Figure 7.18. Qualitatively similar results are obtained for

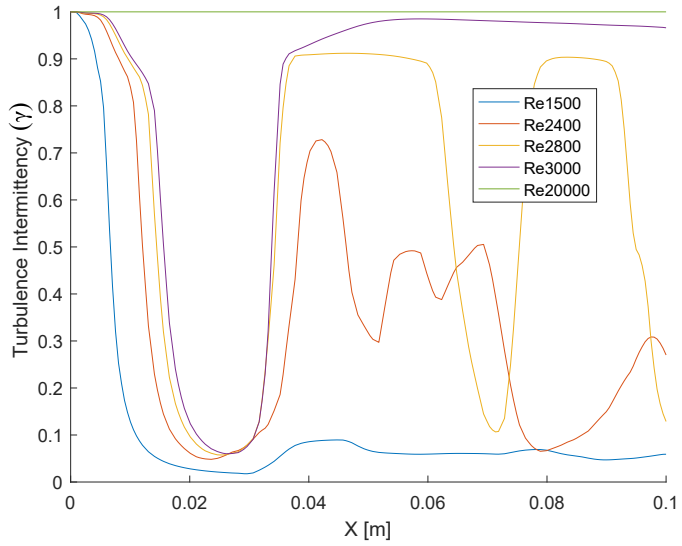

(a)

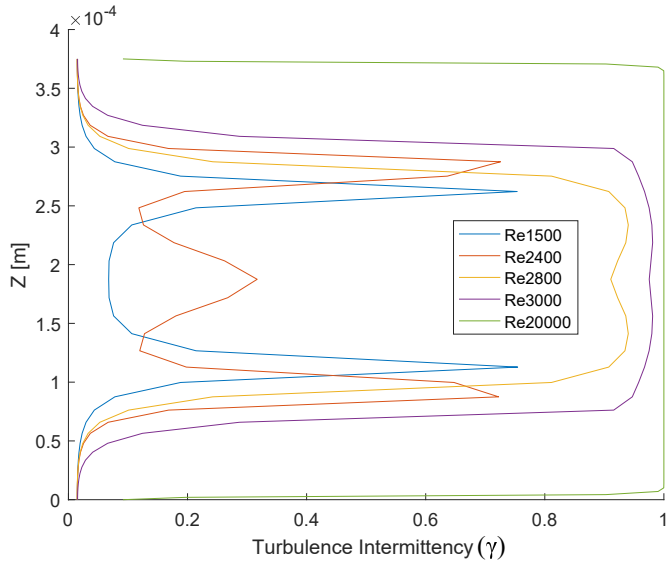

(b)

Figure 7.24: Turbulence Intermittency for MC9c $D_h = 500\mu m$ & $\alpha = 0.5$ along the centerline (**a**), and along vertical line at $x/L = 0.5$ (**b**).

all the other cases and therefore for the sake of brevity are not presented here. However analysis of f_f and γ curves from the above analysis of all the MCs considered, show a clear trend where with a decrease in α, laminar to turbulent flow transition is delayed resulting in a higher Re_{cr}. This trend is constant amongst all the three D_h investigated in the current work. Moreover the difference of Re_{cr} between α of 0.5 and 1 is not so significant whereas it increases sharply for smaller α (0.25 and 0.1) values. Similar

trend can also be seen in the experimental results reported in the previous section where all the MCs (MC2-MC6) have $\alpha > 0.5$ and therefore do not show an appreciable difference in Re_{cr} between each other whereas the MC1 which has $\alpha = 0.25$ exhibits to have the highest Re_{cr}. This shows that increase of Re_{cr} with decrease in α is not linear and to observe the difference amongst various aspect ratios and corresponding Re_{cr} all obtained results can be compared with the literature using Obot-Jones model, which will be discussed in the next section.

Effect of hydraulic diameter

Numerical data can also be analyzed to see if D_h has a significant role to play on the onset of transition and hence Re_{cr}. Variation of average f_f with Re for MCs with $\alpha = 1$ is shown in Figure 7.25a. An earlier onset of transition for the MC with the smallest D_h (100 μm) can be observed compared to the other two. There is no appreciable difference between Re_{cr} from the MCs with D_h of 300 μm and 500 μm and is around ∼2400 while it is ∼2000 for the smallest D_h of 100 μm. Moreover, there is a relatively abrupt transition in the smallest D_h MC whereas the transitional regime is quite extended for the other two MCs. Flow becomes fully turbulent (parallel to Blasius) for a Re as small as ∼3000-4000 in case of $D_h = 100$ μm whereas it stays transitional until $\sim Re = 10000$ in case of other two MCs. In order to validate such behavior from local flow properties rather than averaged between inlet and outlet, semi-local values of f_f between $x/L = 0.5 - 0.75$ are also plotted in the Figure 7.25b. It is interesting to observe that local values although show similar trend as of averaged values where MC with $D_h = 100$ μm shows an earlier transition whereas it is comparatively delayed for the other two MCs. However, MCs of all three D_h show somewhat abrupt flow transition to turbulent state and flow in all channels reaches turbulent state at the $\sim Re = 5000$ which is half of what can be estimated from the global average value. Another peculiar point is that for MCs with $D_h = 300$ μm and 500 μm local transition is delayed and abrupt whereas considering average values it is smooth and

anticipated. Such behavior, however, has not been exhibited by the MC with the smallest $D_h = 100$ μm whose Re_{cr} stayed the same in both cases of average or semi-local f_f.

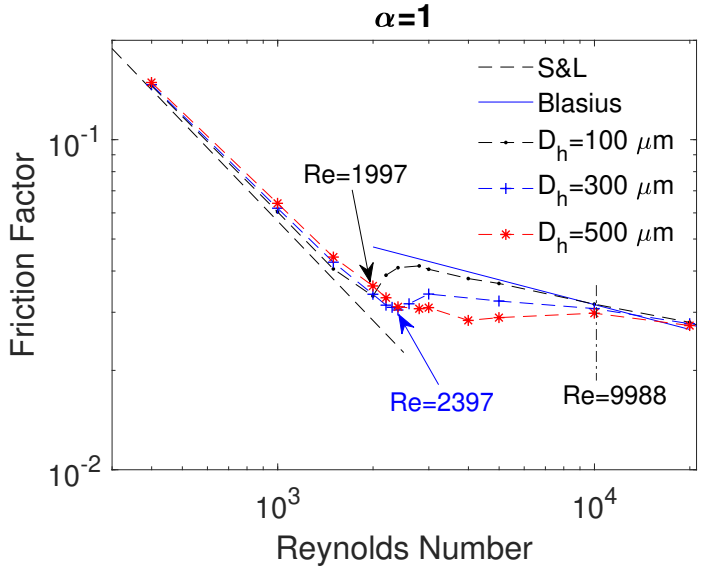

(a)

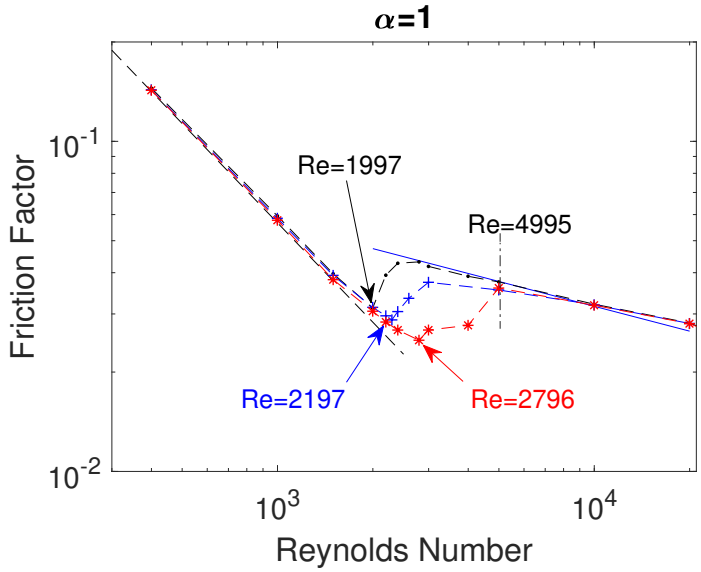

(b)

Figure 7.25: f_f curve for MCs with $\alpha = 1$: average (**a**), and semi-local ($x/L = 0.5 - 0.75$) (**b**).

For smaller values of α investigated in current work, such difference between average and semi-local f_f is not observed as shown in Figures 7.26 - 7.27. There has not been any significant influence of D_h on transitional onset as well as length of intermittent

flow regime for MCs having α smaller than unity.

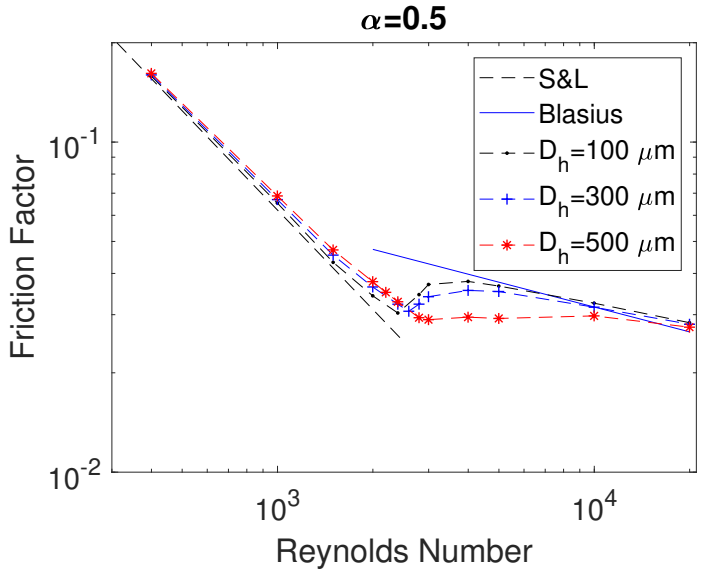

(a)

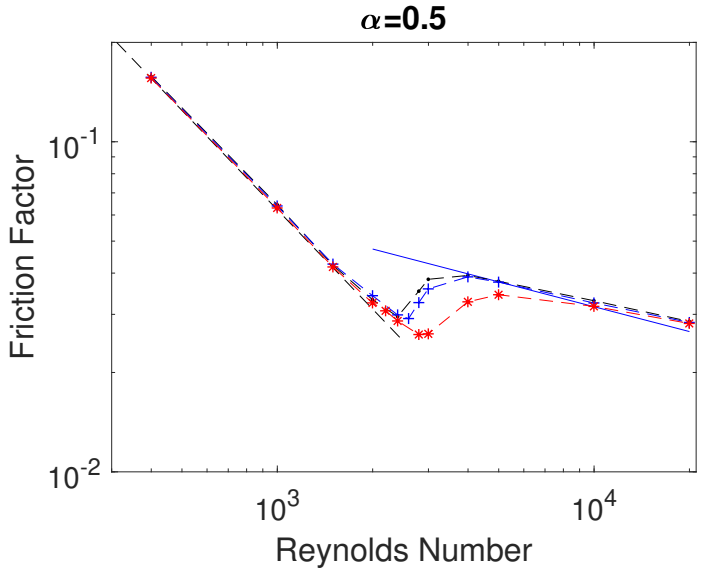

(b)

Figure 7.26: f_f curve for MCs with $\alpha = 0.5$: average (**a**), and semi-local ($x/L = 0.5 - 0.75$) (**b**).

7.3.3 Comparison with Obot-Jones Model

For noncircular ducts, Jones [114] noted that friction factor monotonically increases with an increase in α and therefore the hydraulic diameter of noncircular ducts should

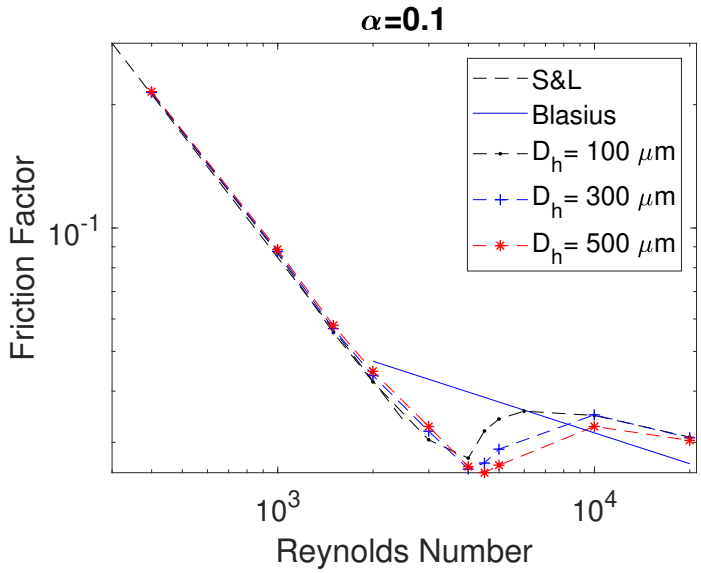

(a)

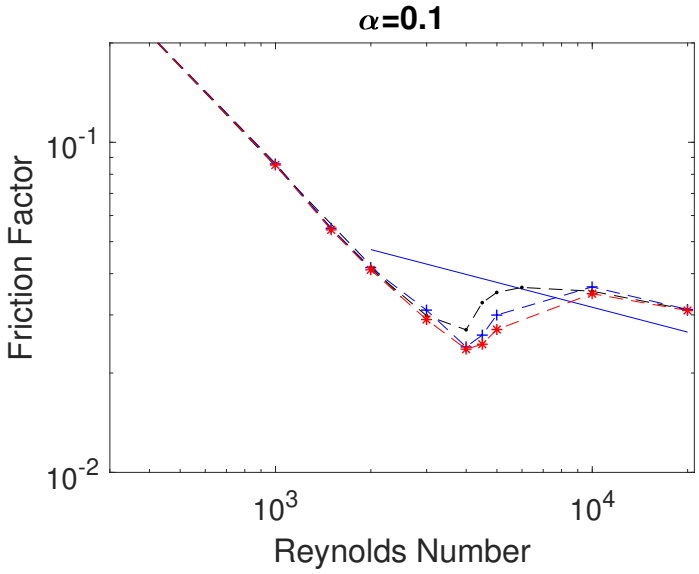

(b)

Figure 7.27: f_f curve for MCs with $\alpha = 0.1$: average (**a**), and semi-local ($x/L = 0.5 - 0.75$) (**b**).

be corrected with a geometric factor (${\phi^*}_G$) by using a laminar equivalent hydraulic diameter. Obot [115] later followed the work of Jones and concluded that Re_{cr} for a noncircular geometry ($Re_{cr,G}$) ducts can also be associated with that of circular geometry ($Re_{cr,o}$) using the geometric factor as follows:

$$Re_{cr,G} = \frac{Re_{cr,o}}{{\phi^*}_G} \tag{7.1}$$

where this geometric function can be approximated as:

$$\phi^*{}_G = \frac{64}{(fRe)_G} \tag{7.2}$$

The product of $(fRe)_G$ can be defined using Shah and London correlation (Eq. 4.19) for rectangular ducts. For conventional sized commercial circular tube with a finite roughness (ϵ), an onset of transition can be estimated as suggested by Idelchick [99]:

$$Re_{cr,o} = 1160 \left(\frac{\epsilon}{D_h}\right)^{-0.11} \tag{7.3}$$

Using these equations an estimation of Re_{cr} can be made by varying α and ϵ/D_h ratio of conventional rectangular ducts. Morini [3] has shown that most of the earlier literature on laminar to turbulent flow transition in microchannels can be represented well using this Obot-Jones model. A comparison of current experimental, numerical as well as recent literature is shown in Figure 7.28. It can be seen that indeed current experimental results follow the trendline with ϵ/D_h ratio of 0.1 % except for the two MCs with α close to 0.7 (MC0 and MC5) which follow a trendline with higher ϵ/D_h. Recently Kim [48] tested metallic chips each containing 10 parallel MCs of various α. Most of his results with one exception also follow the suggested trend of the Obot-Jones model with ϵ/D_h of almost 1%. Similarly Re_{cr} of a MC tested by Dirker [111] also follows the trend exhibited by the results of Kim [48]. Only experimental results for MCs with $\alpha \leq 0.2$ are from Hong et al. [27, 33] which were fabricated in silicon using etching resulting in a very small ϵ (2nm-60nm). If all the experimental results are compared, current ones are towards the high end suggesting a higher Re_{cr} for a given α than others. This might be peculiar to the different test assembly or the material employed to mill the MCs in this work. Except for Hong et al. [27, 33], rest all the results are presented for MCs which are mechanically milled in metals with ϵ/D_h of 0.97% for Wibel Ehrhard [113], 0.22% for Dirker et al. [111], and 0.63% - 2.3% for Kim [48]. Whereas in this work milling is performed in PMMA plastic giving ϵ/D_h is between 0.1% to 0.4% which is in general, lower than others. This

might explain a general higher Re_{cr} of current experimental work. Furthermore, it

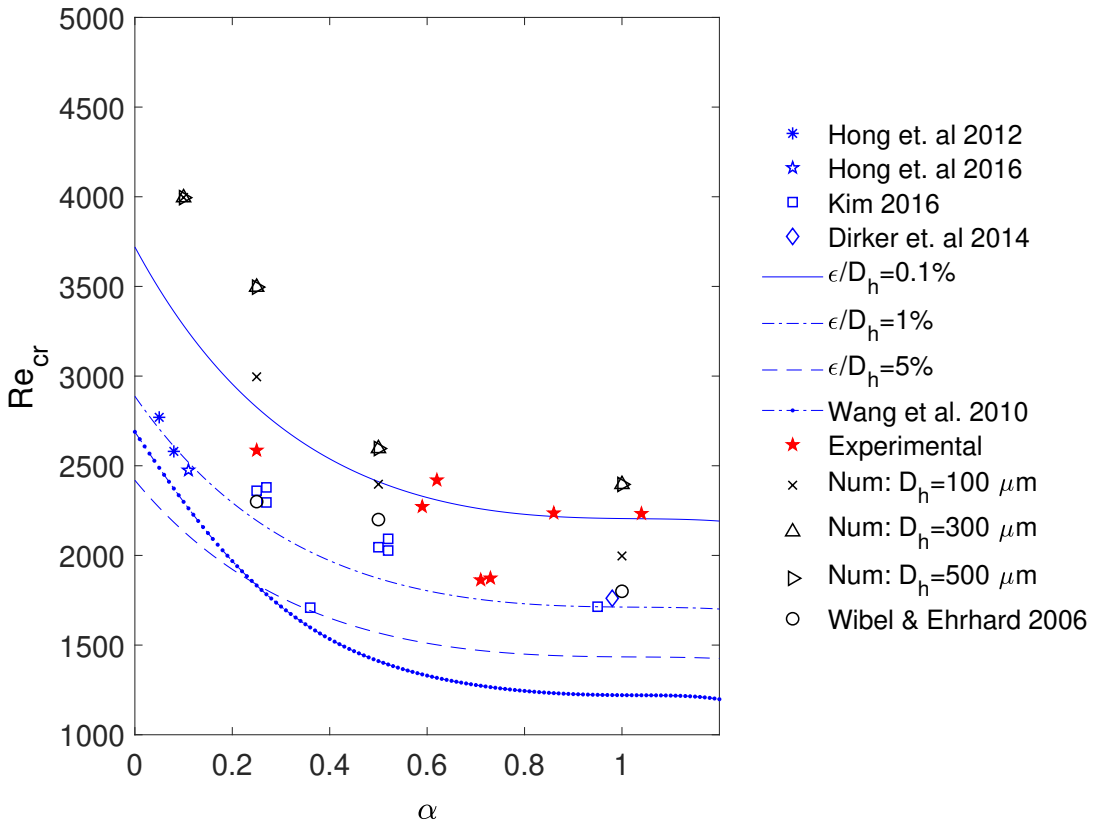

Figure 7.28: Comparison of current results of Re_{cr} and recent literature with Obot-Jones [3] model.

can be seen that considering the actual ϵ/D_h, the Obot-Jones model represents all the assimilated data only qualitatively as all the data fall between 0.1% to 1% ϵ/D_h of Obot-Jones model which is different than reported values by researchers. Numerical results presented earlier, although they follow the similar trends but predict a higher Re_{cr} than experiments for given α. This is due to the fact that only MC is modeled in the numerical model without any details of the inlet manifold. An increase in Re_{cr} has already been demonstrated for numerical results in Figure 7.14 when the inlet manifold is neglected. Moreover as noticed earlier, the difference of numerical results with different D_h is not much pronounced especially for the MCs with D_h of 300 μm and 500 μm. A recent analytical study by Wang et al. [116] presents a correlation that

relates Re_{cr} of a MC with α. This correlation is also plotted for the comparison and it shows that Re_{cr} can go as low as 1220 for $\alpha = 1$. As it can be seen that current results, as well as the recent literature results, do not follow the proposed correlation.

Combining all the results presented in Figure 7.28, it can be concluded that a clear trend there exists between α and Re_{cr} which suggests a decrease in Re_{cr} with an increase in α. Such decrease is quite prominent for lower values of α (27% from α of 0.1 to 0.5) and is insignificant for higher values of α (8% from α of 0.5 to 1). Such a small difference can well fall between the typical uncertainty of measured Re in an experimental campaign. Due to this reason, there has not been an appreciable difference in Re_{cr} for experimented MCs as 5 out of 6 had $\alpha >$ 0.5. Nonetheless, Re_{cr} for all the cases presented is higher than 1700 even for the highest α. No anomalous earlier transition is detected as being suggested by the correlation proposed by Wang et al. [116].

7.4 Summary

Laminar to turbulent flow transition in rectangular microchannels is discussed by varying different geometric parameters. At first effects of inlet manifold shape on the Re_{cr} are investigated. Experiments were performed for four different inlet manifold shapes using gas flow inside MCs. Results show that Re_{cr} is the highest with the BM inlet and is the smallest for RE inlet. A validated numerical model also showed a similar trend where BM showed the most delayed transition. A very good match between experimental and numerical results in terms of Re_{cr} prediction has been observed for all the cases considered. To see the effects of α, experiments were performed on six fabricated MCs of various α. It has been found that except for the smallest α tested (0.25), there has been no appreciable difference in Re_{cr} between the rest. Due to manufacturing constraints, MCs were manufactured in a way that not only α but also D_h was varied from one to the other. Therefore in order to distinguish between the effects of both

geometric properties (α & D_h), a numerical parametric study is carried out. Three D_h in the range of 100 μm to 500 μm are considered where for each D_h, α is varied between 0.1 - 1. Results show that the onset of transition for gas flows inside MCs is delayed by decreasing α whereas there is no pronounced effect of D_h on the Re_{cr} for the cases considered in the current parametric study. By comparing existing experimental and numerical results as well as recent literature on this subject, it has been shown that all the results qualitatively follow the Obot-Jones model. The transition seems to happen for a Re in the range of 1700-3000 for all experimental results and no anomalous earlier transition as suggested by Wang et al. [116] is observed.

Part II

Modeling and Analysis of Micro Heat Exchangers

Chapter 8

Analysis of Double Layer Gas to Gas Micro Heat Exchanger

8.1 Introduction

The discussions made in the various chapters of Part I revealed that the compressibility affects both fluid flow and heat transfer phenomena within microsystems and often causes deviations when compared to the macroscale understandings. For instance, while analyzing heat transfer characteristics inside MTs, it has been seen in Chapter 5 that conventional definition of Nu presents limitations when applied to the high speed gas flows. This compelled to the consideration of total temperature instead of static one while calculating the Nu for gas flows. Such treatment again presented a mathematical anomaly when the total temperature of the gas along the length of the channel often became higher than the wall temperature in the case of applied H boundary condition. Moreover, isolated MCs/MTs have no direct application and rather they serve as the basic building blocks for the fabrication of μHxs. Thus, it becomes vital to assess whether the lessons learnt for a single MC/MT in isolation are applicable to the understanding of thermo-fluid dynamics when a large number of parallel MCs are employed in a μHx which finds direct application in MEMS, power

and automotive industry. Considering the scope of the current work, it is specifically of interest to investigate the heat transfer from one fluid to another through a solid wall (μHx) and therefore experimental as well as numerical methods developed earlier will be expanded in Part II of the thesis to enable the fundamental investigations on double layer gas to gas μHxs.

Experimental as well as numerical studies that deal with compressible gas flows in μHxs are quite scarce in the open literature. A pioneering study that dealt with gas flows inside μHx is of Bier et al. [53], where compared to the expected laminar values, lower convective heat transfer coefficients were observed. Heat exchangers made from steel showed better performance than the one made out of copper and authors associated this decreased performance of highly conductive material μHx to the axial wall conduction. In more recent years a gas to gas multi layered μHx for both co-current and counterflow configurations is presented by Koyama et al. [74, 73]. Their experimental results showed that performance of μHx was lower than the conventional $\epsilon - NTU$ method and they proposed a model where μHx performance can be well predicted analytically by using a constant wall temperature boundary condition. As of Bier et al. [53], μHx from Koyama et al. [74, 73] were also manufactured using metallic housing i.e. steel in this case. Due to strong axial wall conduction, an assumption of constant temperature at the partition foil provided a better approximation. This is followed by very detailed experimental investigations by Yang et al. [82, 81, 2] where authors explored the performance of a double layer μHx in parallel, counter-current and cross flow configurations. They performed experiments in the range of $100 < Re < 1400$ with partition foils of different thermal conductivity and experimentally confirmed that axial wall conduction of the partition foil is detrimental to the μHx performance at lower Re whereas it did not affect the performance significantly for higher Re. Their results also showed that axial wall conduction did not affect the results of co-current flow configuration whereas if axial heat conduction is catered for while processing experimental data, μHx efficiency in counter flow and cross flow configurations can be well represented by the conventional $\epsilon - NTU$ correlations. Their heat exchanger

device that was manufactured at KIT was later studied by Gerken et al. [83] in order to analyze the heat exchanger efficiency from exergy analysis and found that μHx performance is much superior to their macro counterparts in this regards. Experimental results from the above group are by far the most comprehensive for gas flows inside μHx and due to availability of results within the MIGRATE network (MSCA ITN which the current scholar is part of), they have also been used in the validation of porous model approximation of μHx in the next chapter.

From a very brief overview of the experimental results of μHx using gas flows presented above, a need for further experimental investigations cannot be overlooked. To augment the open literature with more experimental results in the field of gas to gas μHx, the focus of this chapter is therefore to design and build a complete test bench for the experimental investigations of a prototype double layer μHx at the Microfluidics Lab of Industrial Engineering Department in University of Bologna, following the footsteps of Yang et al. [82, 81, 2, 83]. The importance of numerical simulations in gaining an insight into the local flow physics has been emphasized throughout this thesis and an attempt has been made to couple the experimental results with detailed numerical simulations where possible. Similarly, results of CHT analysis performed for μHx by varying the D_h of MCs will also be discussed in this chapter.

8.2 Experimental Analysis of a Double Layer Micro Heat Exchanger

Based on the application, micro heat exchanging devices can be subdivided into micro heat sinks and the usual plate type micro heat exchangers. In order to remove a large amount of heat generated in a very small area as encountered in a MEMS chip, usually a single or double layer micro heat sink can be utilized where the main goal is to efficiently remove the heat from the solid and at the same time avoiding any hotspots. On the

other hand, μHx represents an analogy of macro scale plate type heat exchangers in the micro dimensional realm where the aim is to exchange heat between two moving fluids. A recuperator of a micro gas turbine engine or a low grade rankine cycle are few examples where gas to gas micro μHxs are utilized. A computational design study of one such compact heat exchanger for a micro combined heat and power cycle is presented by Joseph et al. [117] for air as a working fluid. Due to very high operating temperatures (>1000K) encountered in their specific application of flue gas coming after flameless combustion, μHx was fabricated using a metallic alloy. They showed that the designed μHx is capable of providing efficiency values of 85% with a penalty of pressure drop merely 10% of the atmospheric pressure. However, in most applications, the temperature of hot gas is well within the range of what the modern day engineering plastics can handle without suffering from any material degradation. In the context of this work, PMMA is used as the housing material for the MCs that has a thermal conductivity much smaller than a metal which will also help to minimize additional heat losses due to transverse conduction within the housing.

Schematics of the whole device along with the details of PMMA chip containing MCs is shown in Figure 8.1. Modular design of the device allows to change the Hx Chip (PMMA housing with MCs) based on the design objectives (number/size of channels, shape/size of the manifolds) under consideration.

There are 3 inlet/outlet connectors in each metallic casing that enables to change the location of inlet/outlet port for the individual layer. Different combinations of inlet and outlet ports can be chosen to experimentally observe any possible effect of the flow maldistribution in collecting and dividing manifolds. There are 3 holes of 250 μm in each of the dividing and collecting manifolds to read the fluid pressure just before the inlet of the MCs. Two additional holes of 1 mm in diameter are made inside each manifold to incorporate two T-type calibrated thermocouples. This will allow to experimentally ascertain the static temperatures of gas inside the manifolds for each layer. A total number of 51 MCs were micromilled in the PMMA sheet having a

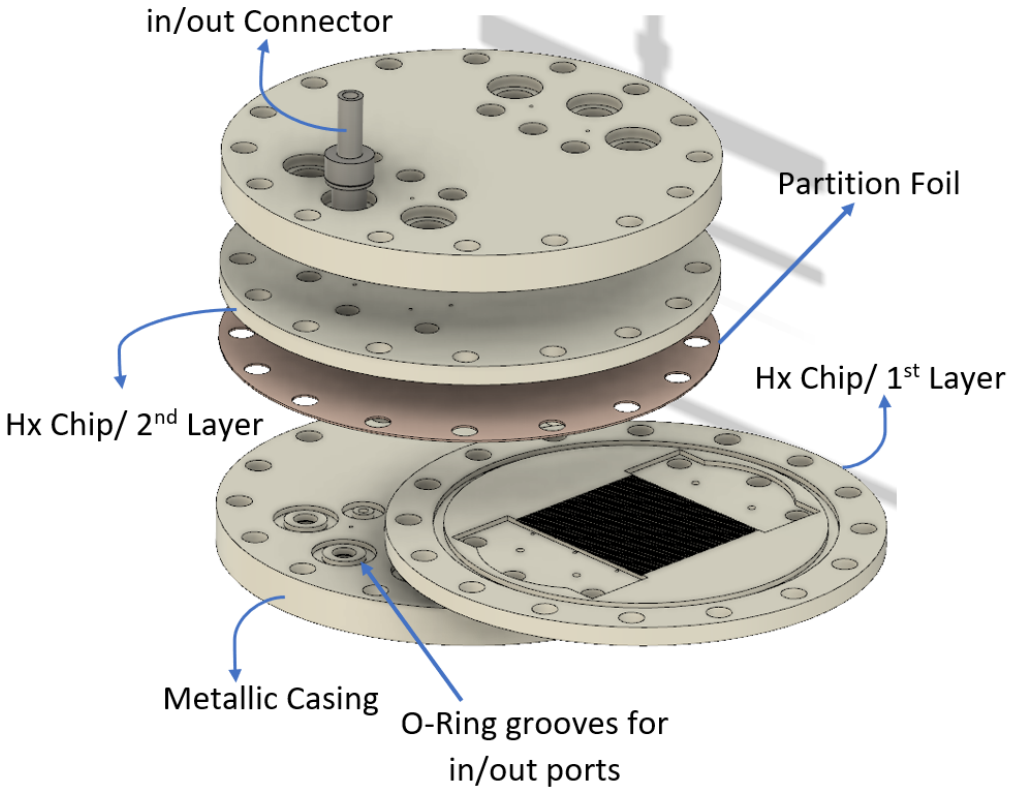

(a)

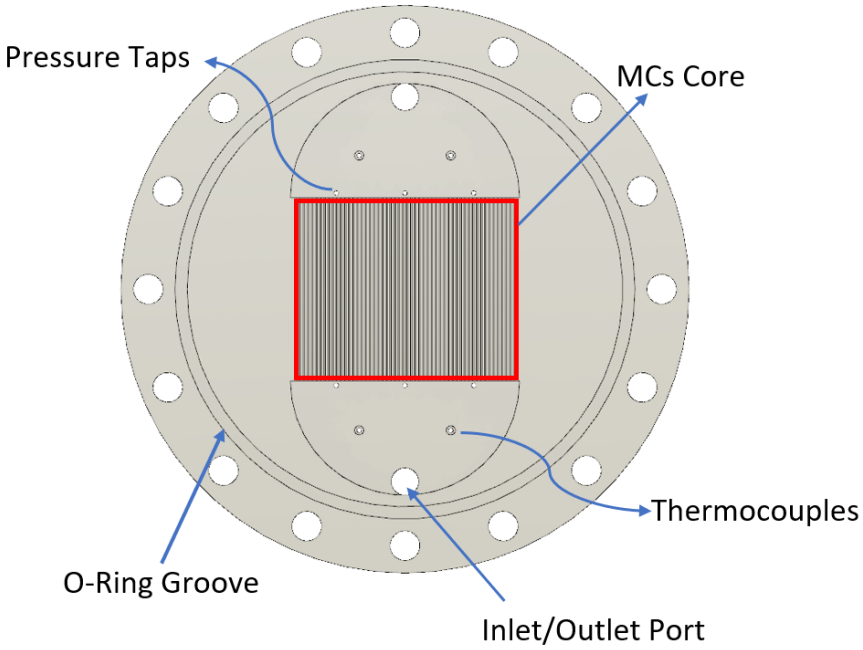

(b)

Figure 8.1: Schematics for the designed μHx assembly (**a**), and a typical single layer with single and central in/out ports (**b**).

thickness of 5 mm following a similar methodology presented earlier for the fabrication of rectangular MCs. Two layers are separated by a partition foil (PF) in between and finally, the assembly is made seal tight thanks to the O-rings and 16 peripheral M8 bolts. A separation foil made of stainless steel with 500 μm thickness is used for the current experimental campaign.

A new test bench as shown in Figure 8.2 is also developed where two flow controllers (Bronkhorst El-Flow Series, 5-200 l_n/min) are mounted in parallel for measuring hot (FC_h) and cold (FC_c) volume flow rates. Based on the desired mass flow rate from each flow controller, N_2 gas flow from the source (overhead tank) gets splitted into two streams. After passing through the FC_c, cold gas enters into the μHx at the room tem-

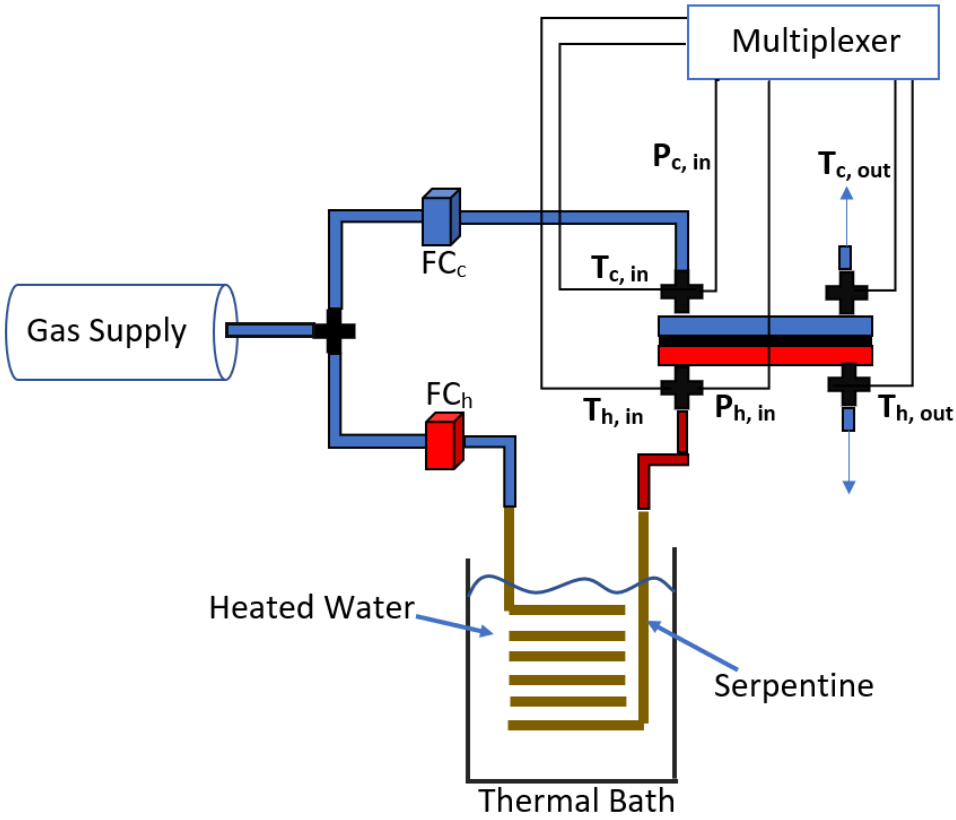

Figure 8.2: Schematics for the experimental test bench for μHx

perature whereas gas that passes through the other controller (FC_h) is forced to pass through a copper serpentine. To heat the incoming gas, this serpentine is placed inside a water thermal bath whose temperature is controlled to the desired value. Using the water thermal bath limits the maximum temperature of the hot side gas to be lower

than the boiling temperature of the water (100^oC), however for the current experimental investigations gas inlet temperature of 70-80^oC is deemed sufficient. Moreover, for each mass flow data acquisition is performed only when no significant variation of the inlet temperature for hot gas is observed for continuous 5 mins. Although the design of μHx assembly allows having three pressure taps inside each manifold, however single reading only from the central pressure port out of the three shown in the Figure 8.1b is used in the current experimental campaign. This is because the aim of the current work has not been to understand the flow maldistribution in detail where all three readings may provide an indication to the extent of maldistribution rather the aim has been to establish the heat exchanger thermal efficiency and therefore only one pressure reading is considered as sufficient. Nonetheless, to measure the overall pressure drop of the μHx, pressure measurements are also taken before the entrance of respective inlet manifolds denoted as $P_{h,in}$ and $P_{c,in}$ in Figure 8.2. In addition to the temperature measurements at the inlets ($T_{h,in}$, $T_{c,in}$) and outlets of the assembly ($T_{h,out}$, $T_{c,out}$), thermocouples are also glued with adhesive inside the manifolds for measuring the respective temperatures. While adding the adhesive care has been taken not to cover the thermocouple junction which may result in wrong temperature measurement. As for the single MC studies, pressure from all the taps is read using a solenoid switch assembly that allows to measure the pressures from 7 ports using only one pressure sensor. Validyne DP15 is therefore used to measure pressure differentials from the pressure ports. After initial experimental runs, a suitable membrane to measure the experimental pressure drop is selected with a FS of 42 kPa which has a measurement uncertainty of $\pm$0.25%.

Fabricated layer of the μHx with the central inlet and outlet ports along with the complete assembly is shown in Figure 8.3. The average dimensions as well as material properties for the fabricated μHx layers is shown in Table 8.1. In a typical experimental campaign the whole device is covered with insulation foam having a very low thermal conductivity to limit the heat losses to the surroundings. Experimental test rig with mounted μHx device is shown in Figure 8.4.

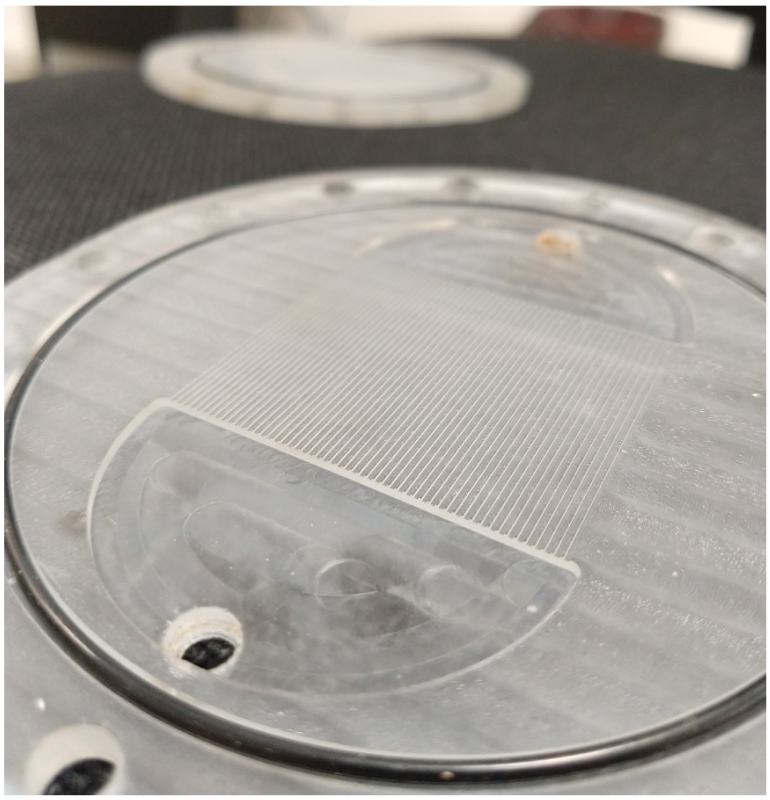

(a)

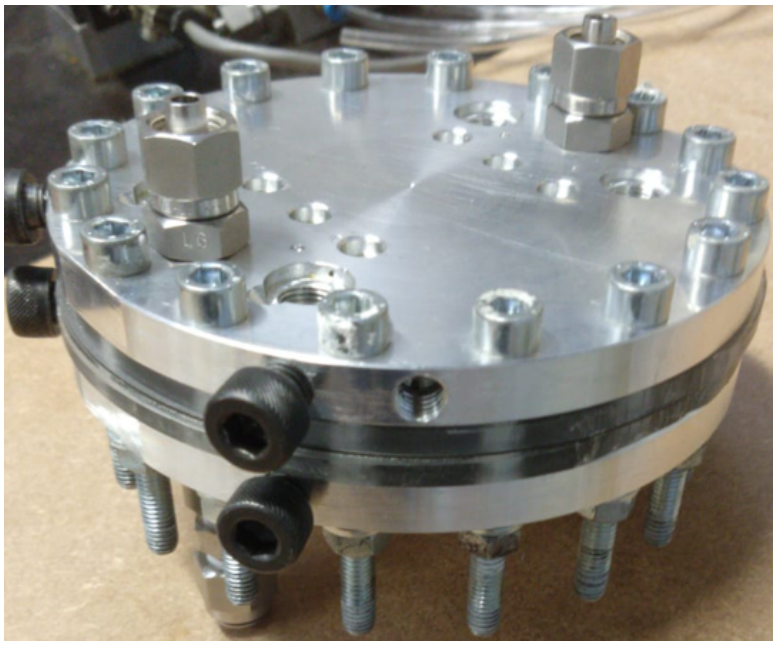

(b)

Figure 8.3: A zoomed view of a single layer of experimented μHx with multiple parallel channels (**a**), complete μHx assembly (**b**).

Table 8.1: Dimensions and properties of μHx geometry.

Parameter	**Symbol (units)**	**Value**
MC width	w (μm)	650
MC height	h (μm)	340
MC Length	L (μm)	40
Hydraulic Diameter	D_h (μm)	446
Wall Thickness	t_w (μm)	300
MC housing (PMMA) conductivity	k_{MC} $(W/m/K)$	0.25
Partition Foil (Stainless Steel) thickness	δ (μm)	500
Partition Foil conductivity	k_{PF} $(W/m/K)$	15

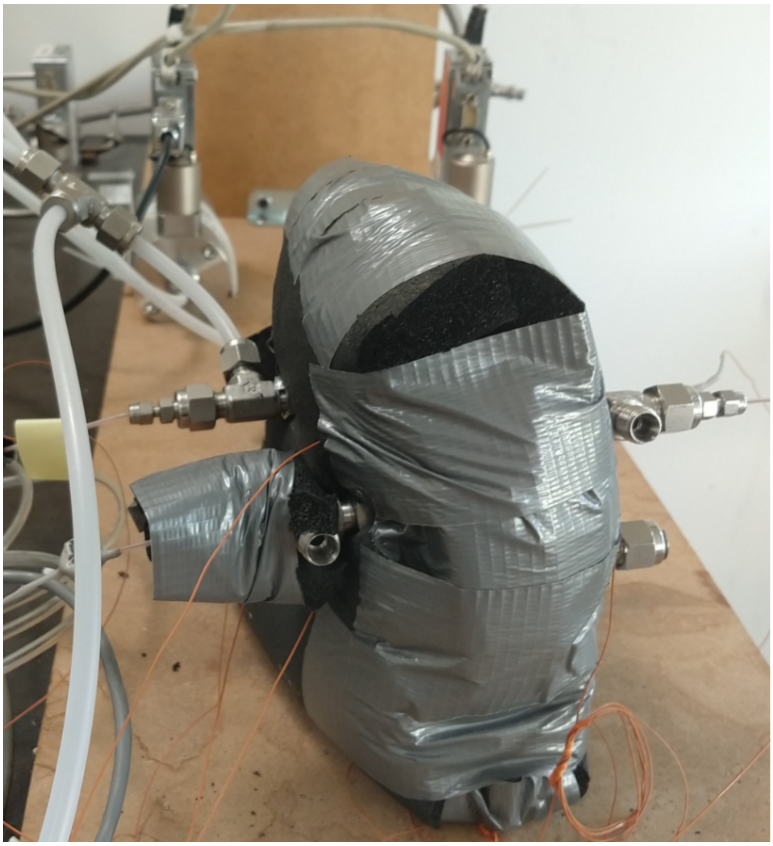

Figure 8.4: Insulated device while an experimental run in parallel flow configuration.

8.2.1 Data Reduction

Dimensions of the MCs are approximated using an inverted microscope and D_h is calculated using Equation 3.2. Based on the desired inlet Re for each of the hot and cold layers, mass flow is calculated using Equation 3.3 which is further allowed to pass through the respective layer by means of computer steered flow controllers (FC_h & FC_c). Heat transfer rate ($\dot{Q}$) on hot (h) and cold (c) side can be defined by using respective flow quantities as:

$$\dot{Q} = \dot{m} C_p \Delta T \tag{8.1}$$

The designed μHx is tested under two flow configurations namely co-current (or parallel flow) and counter current (or simply counter flow). Logarithmic mean temperature differences (LMTD) for both flow configurations are then evaluated as follows:

Parallel flow:

$$\Delta T_{LMTD,cc} = \frac{(T_{h,in} - T_{c,in}) - (T_{h,out} - T_{c,out})}{\ln\left(\frac{T_{h,in} - T_{c,in}}{T_{h,out} - T_{c,out}}\right)} \tag{8.2}$$

Counter flow:

$$\Delta T_{LMTD,cf} = \frac{(T_{h,out} - T_{c,in}) - (T_{h,in} - T_{c,out})}{\ln\left(\frac{T_{h,out} - T_{c,in}}{T_{h,in} - T_{c,out}}\right)} \tag{8.3}$$

Overall heat transfer coefficient is calculated by:

$$U = \frac{\dot{Q}_{av}}{A \Delta T_{LMTD}} \tag{8.4}$$

where $\dot{Q}_{av} = \frac{\dot{Q}_c + \dot{Q}_h}{2}$. Volumetric heat exchange power that provides a measure of amount of heat exchange per unit volume of the heat exchange fluid is defined as:

$$q_v = \frac{\dot{Q}}{n \times whL} \tag{8.5}$$

where n is the number of channels. Heat exchanger effectiveness of the complete μHx, defined as the ratio of actual heat transfer rate and maximum potential heat transfer

rate available, can be calculated using:

$$\varepsilon = \frac{Q_{av}}{(\dot{m}C_p)_{min}(T_{h,in} - T_{c,in})} \tag{8.6}$$

And finally, the number of transfer units, a parameter that signifies the number of heat units that the heat exchanger is capable of transferring from one fluid to the other across the heat transfer area A_{ht}, are determined by the following:

$$NTU = \frac{UA_{ht}}{(\dot{m}C_p)_{min}} \tag{8.7}$$

8.2.2 Parallel Flow Configuration

Experiments are performed in parallel flow configuration by attaching hot and cold gas supply lines on the same side of the μHx. Based on the maximum pressure available of the pressurized N_2 gas in the overhead tank ($\sim$6 bar) volume flow rate has been varied between 10 l_n/min to 36 l_n/min which translates into $\dot{m}$ in the range of 0.8-2.7 kg/h. The μHx is tested under a balanced mass flow condition that is by imposing the same mass flow rates from both hot and cold sides. Hot gas from the thermal bath entered in the device at 57-58 ^oC whereas cold gas at the room temperature (27 ^oC) is allowed to enter into the other layer of the μHx. Considering the inlet temperatures and corresponding viscosities of entering gas, Re from hot and cold sides vary in the ranges of 496-1620 and 524-1750, respectively. Therefore the current device is only tested in the laminar flow regime and due to limited pressure of the stored gas, turbulent flow conditions are not investigated. To ensure the leak tightness of the μHx, a total pressure drop of the device is compared from both sides under the balanced mass flow condition at room temperature. The experimental pressure drop is shown in Figure 8.5 which is equal for the complete range of investigated $\dot{m}$ signifying that both of the sides are working under the same mass flows.

Volumetric heat exchange power for the co-current case is shown in Figure 8.6a where

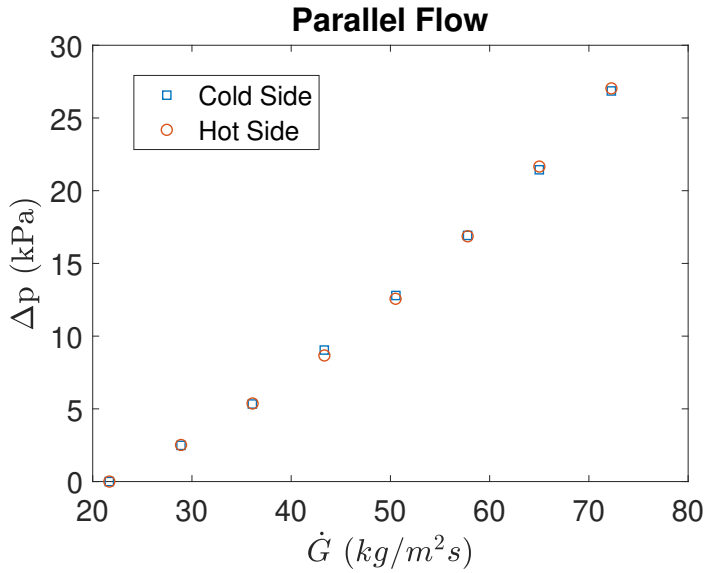

Figure 8.5: Comparison of total pressure drop of the μHx from both sides.

it reaches a maximum value of 27.5 MW/m^3. For the given fluid conditions this results in an absolute heat exchange power of 11.45 W at the highest mass flow experimented. Overall heat transfer coefficient for the total heat transfer area of all the MCs is also shown in Figure 8.6b. Current set of experiments show higher values of U compared to heat exchanger of Yang et al. [82, 81] in parallel flow configuration but show a decreasing trend at the smaller values of $\dot{G}$ which had not been seen in experiments from the aforementioned group. Nonetheless as expected, it keeps on increasing with increasing $\dot{G}$.

Heat exchanger efficiency calculated by the evaluated ΔT_{LMTD} and U for parallel flow configuration is shown in Figure 8.7. Based on the experimental values of ΔT_{LMTD}, theoretical ε for the balanced parallel flow heat exchanger can be defined as follows:

$$\varepsilon_{th,cc} = 0.5(1 - e^{-2NTU}) \tag{8.8}$$

Experimental results are therefore compared against these theoretical predictions to gauge whether conventional ε-NTU theory can be applied to micro heat exchangers. It can be seen that ε follows the theoretical predictions within experimental uncertainty and decreases with increased $\dot{G}$ (Re) almost linearly. It is further evident from Figure

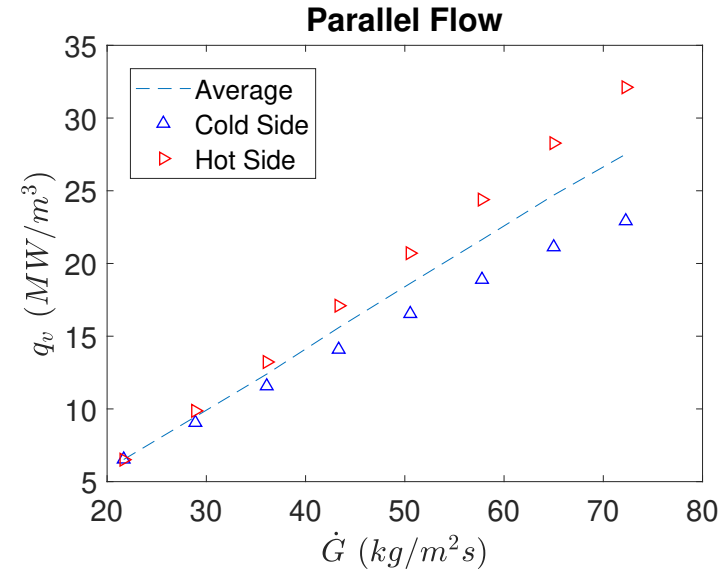

(a)

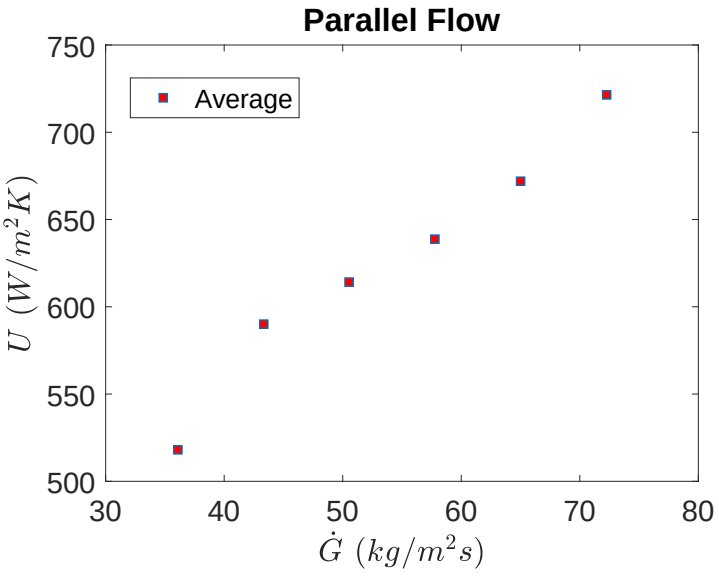

(b)

Figure 8.6: Volumetric heat exchange power for the parallel flow case (**a**), and overall heat transfer coefficient (**b**).

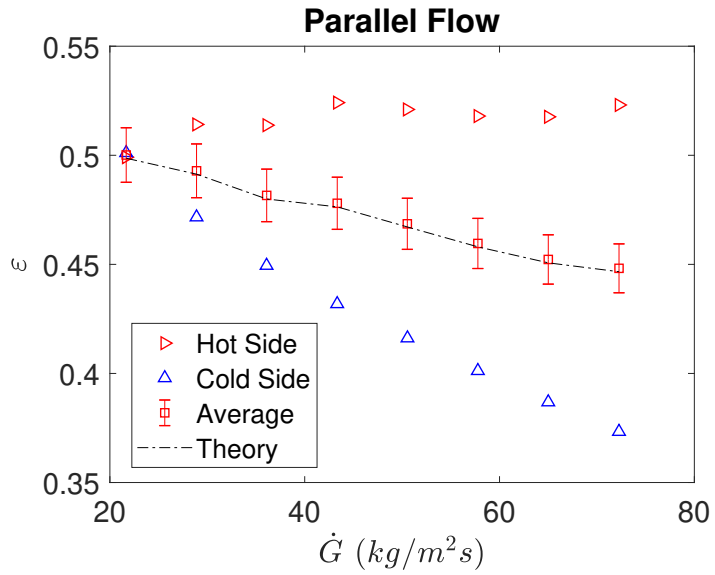

(a)

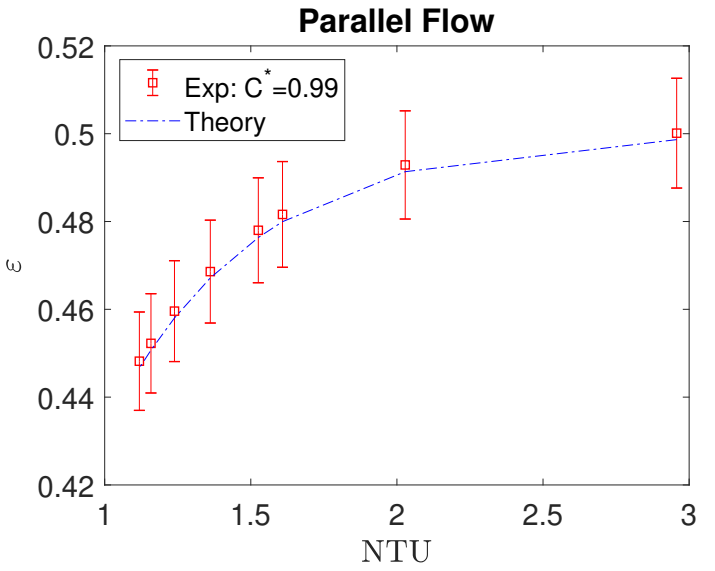

(b)

Figure 8.7: Experimental heat exchanger efficiency ε for parallel flow configuration: variation with $\dot{G}$ (**a**), and with NTU (**b**).

8.7b that experimental results follow quite well the estimation of the theoretical -NTU curve for cocurrent balanced flows.

In the above presented experimental results, it can be seen that the overall efficiency of the device deduced from the average measured heat transfer of both sides matches quite well with the theoretical prediction. However, if one is to observe hot and cold sides separately, it is evident from Figures 8.6 - 8.7 that both hot and cold sides yield different results where heat transfer and efficiency is higher on the hot side compared to the cold side. This discrepancy furthers in magnitude with increasing $\dot{G}$ of the incoming gas. This might well be associated with the losses pertinent to the convection on the external sides of the μHx (metallic covers) and radial directions due to a difference in the gas temperature and the room temperature. However, repeated experiments with more layers of insulation provided qualitatively similar results and a strong imbalance of the heat transfer rates on both sides are observed as shown in Figure 8.8.

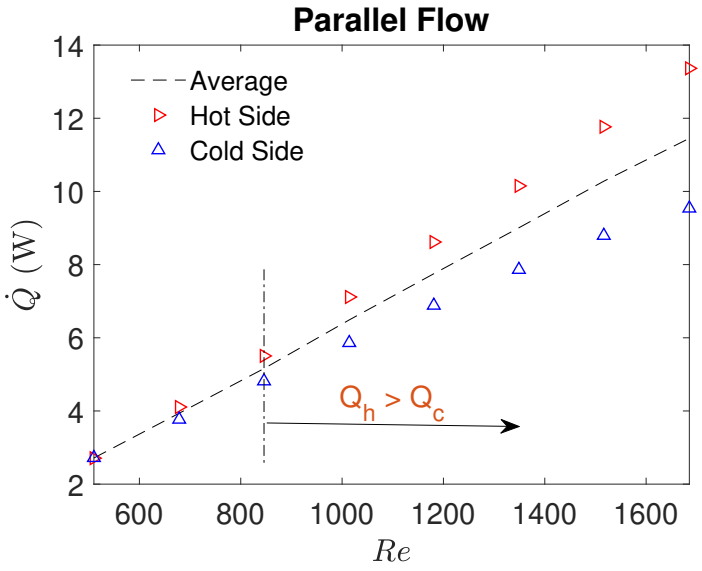

Figure 8.8: Comparison of heat transfer rates on both hot and cold sides for the experimented μHx in parallel flow configuration.

As evidenced in the values of ε in Figure 8.7, energy imbalance between hot and cold fluid gas streams starts increasing from Re >1000 onwards. In the current configuration, the relative difference between hot and cold heat transfer rate at the highest experimented Re of $\sim$ 1650, becomes more than 40%. As can be seen, the difference

continues to increase with increasing Re of the incoming gases which suggests that their might be some underlying local physics causing such differences. For the range of experimental inlet gas temperatures on both sides, it can safely be assumed that specific heat capacity of the gas at the local pressure C_p does not vary significantly and hence stays constant. Therefore in a balanced open control volume with the same gas on both sides of the μHx, which is the case under consideration, the temperature lost by the hot side should almost equate the temperature gain of the cold side. However measured temperature drops at the hot and cold fluid streams show a significant difference, especially at the higher Re as shown in Figure 8.9.

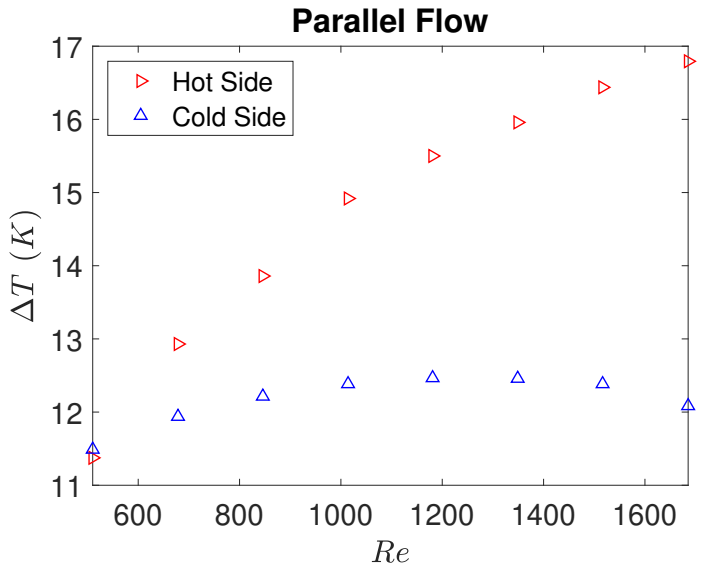

Figure 8.9: Comparison of temperature differences on both hot and cold sides for the experimented μHx in parallel flow configuration.

As leak tightness is already demonstrated earlier, a discrepancy between the temperatures from hot and cold sides can also be not associated with possible differences in mass flows due to leakage on either side. A detailed analysis to investigate the origin of such imbalance is therefore, crucial to have a correct understanding of the flow physics inside μHx.

Effect of compressibility on the heat transfer

One reason that may cause such a discrepancy in the temperature drop of both the fluid streams is related to the compressibility of the gas. It has been emphasized throughout the adiabatic and diabatic studies performed on single channels earlier, that gas flows are never hydro-dynamically as well as thermally developed because of continuous acceleration of the gas along the length of the channel under the influence of applied pressure drop. However, from the experimental and numerical analysis of adiabatic MT and MC fluid flow conducted earlier, it has been seen that the effects of compressibility are low if Ma_{av} along the length of the MC/MT is less than 0.3. If there are strong compressibility effects, there is a finite amount of gas thermal energy that will be converted to the kinetic energy of the gas on both sides of the heat exchanger. The kinetic energy of the fluid in each stream can be defined as:

$$\dot{Q}_{ke,h/c} = \frac{1}{2}\dot{m}_{h/c}\left[{u_{out}}^2 - {u_{in}}^2\right] \tag{8.9}$$

A comparison of heat power from both sides and the thermal kinetic energy loss summed from both sides' experimental results, is shown in Figure 8.10. To understand the extent of the compressibility in both fluid streams, Ma at the exit of the MCs core is also plotted in the same figure. Due to balanced flow condition in experiments, Ma at the exit from both hot and cold sides are almost equal. It can be seen that Ma at the exit is always less than 0.2 and the sum of thermal kinetic energy (represented as KE in Figure 8.10) constitutes almost 10% of Q_h at highest Re experimented. The difference between hot and cold side heat transfer however, is higher than 40% and therefore it is still not possible to completely close the balance in the experimental results.

To clarify this ambiguity further, a $3D$ conjugate heat transfer (CHT) model is setup where only MCs are modeled without a real design of collecting and distributing manifolds. However, to allow any possible underexpansion at the outlet of hot and cold MCs, computational domain is extended $15D_h$ in streamwise and $32D_h$ lateral

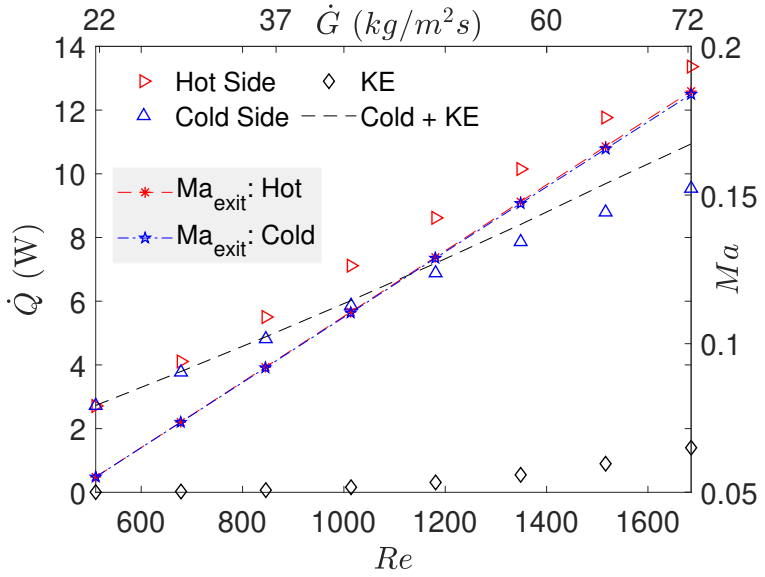

Figure 8.10: Comparison of experimental heat transfer on both sides as well as the contribution of thermal kinetic energy loss due to acceleration for the μHx in parallel flow configuration.

direction. This is why different geometric models are utilized in counter (Figure 8.11a) and cocurrent (Figure 8.11b) flow analyses.

Geometry and meshing is done using Design Modeler and ANSYS Meshing software respectively. A mesh of $40 \times 40 \times 100$ is used in the MCs. A structured mesh locally refined at the walls of the channel and manifolds is employed as shown in Figure 8.11. The mesh expansion factor is kept as 1.1. The orthogonality of mesh elements inside MC is between $0.95 - 1$ in all the simulated cases. A commercial solver CFX based on finite volume methods is used for the flow simulations. Ideal Nitrogen gas enters at the inlets of both hot and cold sides and leaves the computational domain through extreme sides of extended manifolds outlet. Laminar flow solver is used for all the cases. Higher order advection scheme available in CFX is utilized and pseudo time marching is done using a physical timestep of 0.01s. A convergence criteria of 10^{-8} for RMS residuals of governing equations is chosen while monitor points for pressure and velocity at the MC inlet and outlet are also observed during successive iterations. In case where residuals stayed higher than supplied criteria, the solution is deemed converged if monitor points did not show any variation for 200 consecutive iterations. Reference

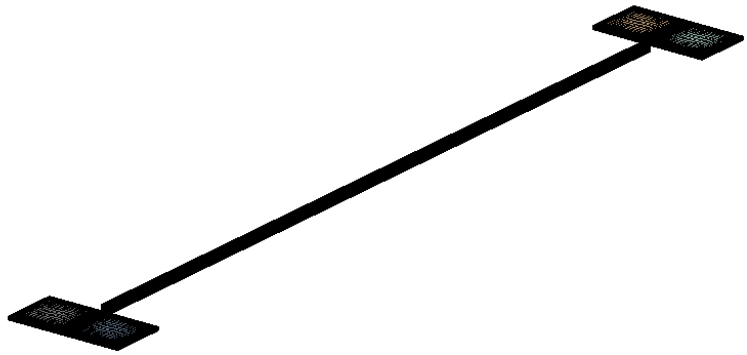

(a)

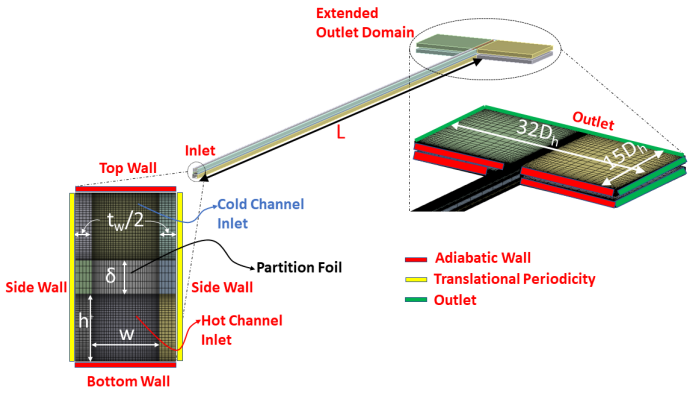

(b)

Figure 8.11: Mesh for counterflow CHT analysis (**a**), and mesh and geometric details for co current CHT analysis (**b**).

pressure of $101kPa$ was used for the simulation and all the other pressures are defined with respect to this reference value. Energy equation was activated using Total energy option available in CFX which adopts energy equation without any simplifications in governing equations solution. Kinematic viscosity dependence on gas temperature is defined using Sutherland's law. Further details of boundary conditions can be seen in Table 8.2.

Table 8.2: Boundary conditions used in the CHT Analysis.

Boundary	**Value**	
	Hot Side	**Cold Side**
Inlet	- $\dot{m}$ evaluated using Equation 3.3 for cold side	
	- $T_{h,in} = 90$ °C	- $T_{c,in} = 20$ °C
Side Walls	Translational Periodicity	
Top & Bottom Walls	Adiabatic	
Outlet	Pressure outlet, Relative p = 0 Pa	

A balanced mass flow rate at the inlets of both hot and cold fluid channels is varied such that simulated Re is between $200 - 2000$. Although the considered flow regime is laminar, flow choking for smaller hydraulic diameter MCs can be encountered [38]. As a consequence of flow choking, the pressure at the outlet of MC is higher than atmospheric pressure (far stream) and flow becomes underexpanded [118]. Therefore in order not to force the fully expanded flow at the MC outlet, the computational domain is extended downstream of the MC outlet on both hot and cold sides. This is done for both cocurrent and counter flow configurations. Pressure outlet boundary condition is then applied at the exterior walls of these extended outlet domains as shown in Figure 8.11b.

Although the above described CHT model does not include the detailed design of the distributing and collecting manifold but will help to ascertain if such temperature difference is due to the local flow physics or is a result of merely some experimental heat losses. Channel dimensions and thickness of the partition foil are chosen to replicate the experimental settings. Mass flows at the inlet are imposed based on the Equation

3.3 to simulate the desired Re at the inlet. A Re range of 200 to 2,000 is used for the CHT analysis since experimental conditions also resemble the laminar flow regime in the MCs. However, the flow might be turbulent in the manifolds due to the high characteristic dimension of the manifold as well as higher $\dot{m}$. Since in current CHT analysis manifolds are not modeled, a laminar flow solver is therefore chosen for the simulations. Inlet temperatures of the gas flows also correspond to the experimentally measured values.

Heat transfer rates from both fluid sides as evaluated by the employed CHT model are shown in Figure 8.12. As noticed in the experimental results $\dot{Q}$ from the hot and cold sides start deviating from each other with a relative difference of 11% at a $\sim Re$ of 800 where it increases to 64% at $\sim Re$ of 1900. The relative difference of $\dot{Q}$ between the hot and cold sides from the CHT model is significantly higher than experimentally measured values where it was close to 40% at the highest Re. This is due to the fact

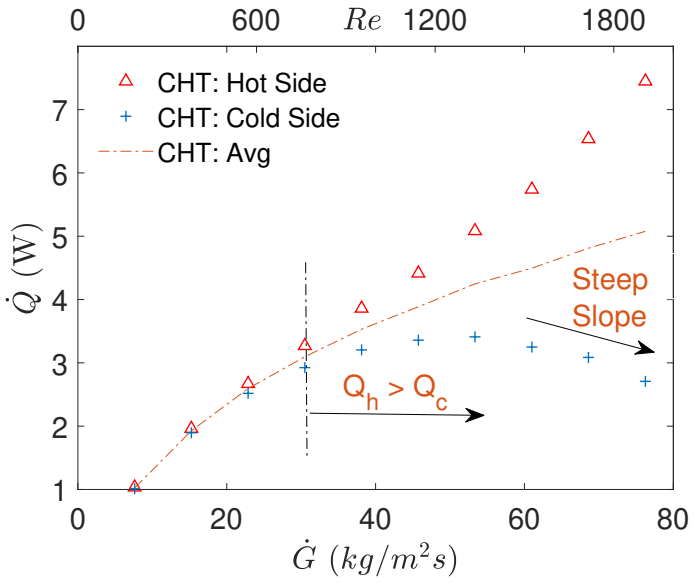

Figure 8.12: Heat transfer rates from hot and cold sides as evaluated from the CHT model of the μHx in parallel flow configuration.

that in experimental settings, there is a finite heat exchange between the two fluids in the manifold zone before entering to the MCs core which is not taken into account in CHT model. Moreover, in an experimental campaign, the temperature is not measured exactly at the inlet/outlet of MC core and rather it is measured in the vicinity of inlets

and outlets, which may provide a higher temperature at the outlet due to additional heat exchange in the outlet manifold. However, numerical CHT results are devoid of any such additional heat exchanges and therefore show a strong decrease of heat transfer rate on the cold side (conversely a strong increase on the hot side) for the higher Re cases as shown in Figure 8.12.

Inlet and outlet temperature values and therefore any deduced quantity from these, represent an average characteristic of the μHx which is often of the prime engineering interest. Inlet and outlet characteristics of the flow also make a robust way to perform the heat transfer analysis for macro scale gas flows or liquid flows as the heat loss on the hot side should be the gain on the other side. On the other hand when it comes to micro dimensions, most often these characteristics are the only dispensable tool for establishing the balance from experimental measurements. A simple 2D representation of the μHx under consideration is shown in Figure 8.13. In a steady state system, the heat flux transferred from hot fluid to the wall (q_{h-w}) should be equal to the heat flux transferred from wall to the cold fluid (q_{w-c}) on the other side. This holds true even if there are energy losses due to some underlying mechanisms such as compressibility. Therefore in order to calculate the heat flux from the hot fluid to the wall and consequently from wall to the cold fluid, numerical results of flow variables are extracted at various planes along the axial length (x) of the μHx in a CHT analysis. Since the energy equation is also solved for the solid partition foil of thickness δ, post processing of the results also provides temperature variation of the partition foil along the axial length. Heat fluxes are then evaluated as follows:

hot fluid to the wall:

$$q_{h-w} = \frac{1}{L}\int_L \left(k_{f,h} \left.\frac{\partial T_{f,h}}{\partial n}\right|_{w,x} \right) dx \tag{8.10}$$

wall to the cold fluid:

$$q_{w-c} = \frac{1}{L}\int_L \left(k_{f,c} \left.\frac{\partial T_{f,c}}{\partial n}\right|_{w,x} \right) dx \tag{8.11}$$

Considering the losses due to presence of side walls which may redistribute the heat, heat flux from hot fluid to the cold fluid (q_{h-c}) can also be defined as the average of

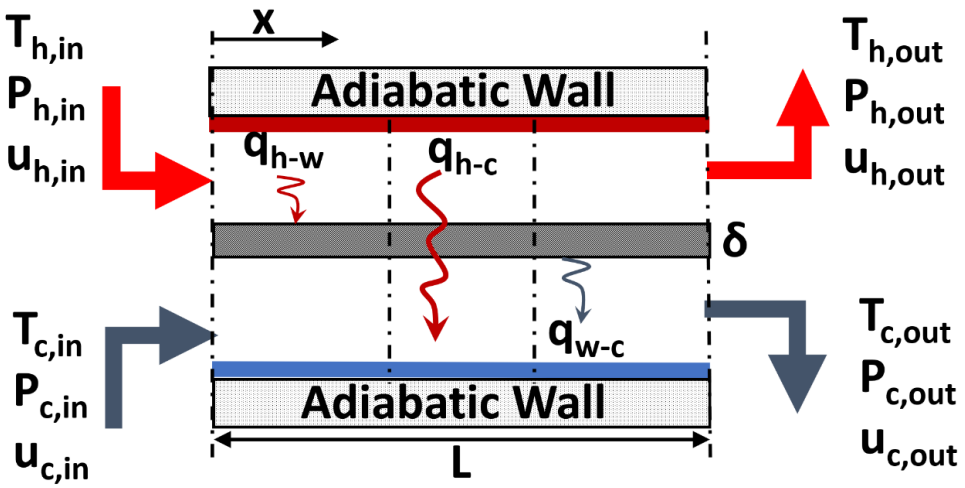

Figure 8.13: A simple schematic of the of the μHx under consideration in parallel flow configuration.

the two sides as follows:

hot fluid to the cold fluid:

$$q_{h-c} = \frac{q_{h-w} + q_{w-c}}{2} \tag{8.12}$$

Resulting integral values of the heat fluxes are shown in Figure 8.14. It can be seen that unlike the flux determined from the inlet and outlet temperatures, q_{h-w} and q_{w-c} show quite good agreement to each other. The relative error between the fluxes from both sides reduces to only 19% at the highest $\dot{m}$ simulated compared to 60% in case of heat flux determined form inlet and outlet gas flow characteristics. It is to be noted that above analysis between individual fluids and the wall is done by treating the gas uni-directional in a quasi 2D approach as shown in Figure 8.13 whereas in the 3D CHT numerical model there are also side walls of the MC which redistribute a certain amount of heat flux amongst the hot and cold fluid streams which goes unaccounted for in a 2D approach. Moreover, when a comparison of volume averaged heat flux from both hot and cold fluid streams is calculated in the post processor, it always resulted in a perfect match again emphasizing that these losses in the heat flux performed earlier are merely due to treatment of a 3D heat conduction problem as quasi 2D. Nonetheless, as it is expected of a steady state system, a very good balance can be seen between the two components (q_{h-w} and q_{w-c}) of heat transfer whereas q_{h-c} represents an average

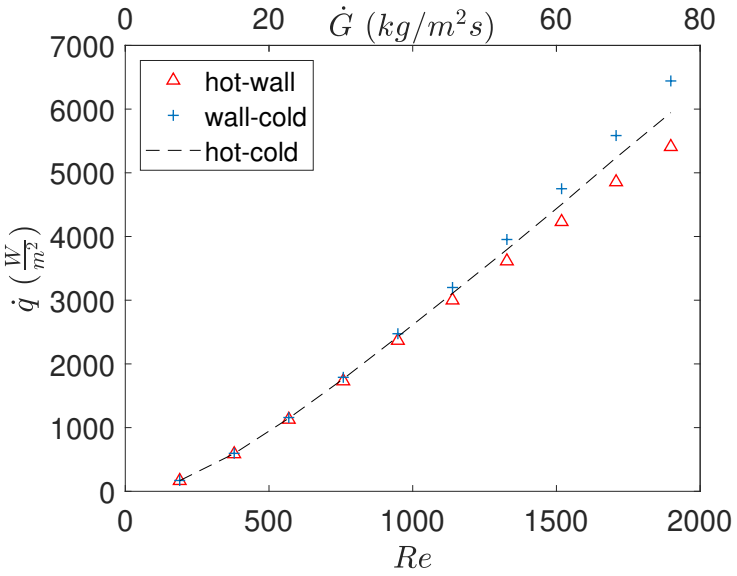

Figure 8.14: Heat flux balance as evaluated from the CHT analysis of μHx in parallel flow configuration.

between the two.

This analysis demonstrated that even though there is an excellent balance between the two fluids from an internal control volume approach, global characteristics (inlet and outlet based) still present a great disagreement between heat transfer of the two fluid streams. And as mentioned before that for a micro sized system, inlet and outlet flow variables are the only measurements available in a typical experimental campaign therefore it is essential to justify the global energy imbalance. This can be done by invoking the thermal energy loss due to increased velocity of the gas in both fluid streams and by considering the kinetic energy gain/loss, the energy balance can be rewritten as follows:

$$\dot{Q}_h = \dot{Q}_c + \dot{Q}_{ke,c} + \dot{Q}_{ke,h} + \dot{Q}_{loss} \tag{8.13}$$

where $Q_{ke,c}$ and $Q_{ke,h}$ are the heat rate into converted kinetic energy for cold and hot fluids respectively. Individual contributions of the above written balance for the CHT analysis are shown in Figure 8.15. It can be seen that if Q_{ke} (sum of KE from both sides) is catered, energy balance is in quite good agreement as observed for the experimental results when kinetic energy loss was catered for. The maximum deviation between the

heat flux from the two sides is ∼10% at the maximum simulated Re which again is in the expected range considering the presence of side walls in the computational model as discussed earlier. Mach number evaluated at the exit plane is also plotted alongside the heat flux which shows that for diabatic conditions, flow compressibility is even more pronounced and effect of thermal energy loss due to acceleration is evident at a Re as low as 800 for the current D_h which is 446μm. Corresponding Ma_{exit} when the compressibility starts becoming important in the heat balance is even less than 0.1 which is significantly lower than the established limit of 0.3 for adiabatic compressible microflows or macroflows in general. The maximum value attained by Ma at the exit is 0.19 where the discrepancy between heat transfer rates of hot and cold side, without considering KE of the gas flows and thus avoiding compressibility, reaches as high as 60%.

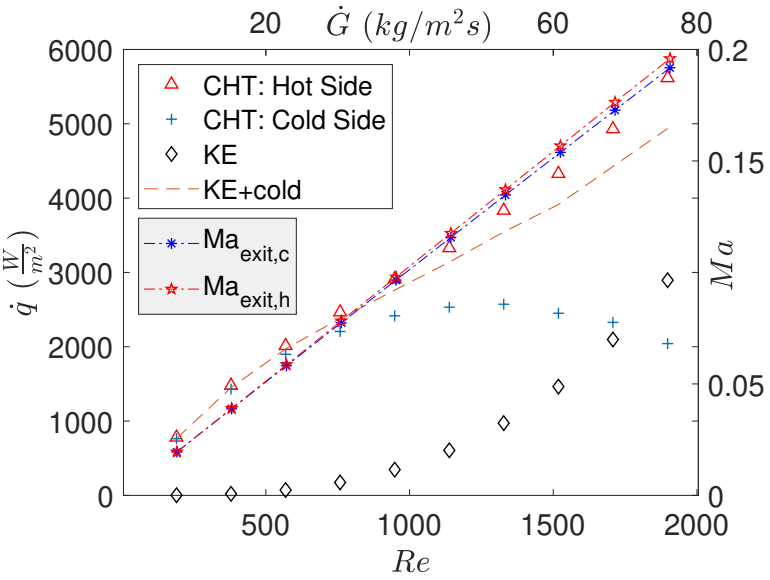

Figure 8.15: Comparison of individual components of total heat flux exchanged between the two fluids as evaluated from the CHT analysis of μHx in parallel flow configuration.

It is to be noted that an area weighted average of the Ma is used in Figure 8.15 which usually is lower than mass flow averaged values. While deducing experimental results, cross sectional velocity at the exit is calculated such that it represents an area weighted average given the measured average temperature of the exit gas from each

fluid stream. In a numerical simulation, however, one has the capability to calculate the mass flow averaged values of velocities and thus Ma which represents the reality for the compressible gas flows. A comparison of the heat flux lost due to kinetic energy using both averaging methods is shown in Figure 8.16 where it can be seen that using an area weighted average seriously undermines the total kinetic energy. Using kinetic energy calculated from area averaged velocities in the energy balance as presented in Equation 8.13 shows only a 7% improvement in closing the balance and the combined sum of $\dot{q}_c$ and $\dot{q}_{KE}$ evaluated from the area weighted average still is 53% lower than $\dot{q}_h$. Whereas values of $\dot{q}_{KE}$ evaluated using area weighted average velocities are 80% lower than the values calculated using mass flow weighted average and therefore shows no improvement in closing the energy balance. As performed in experimental data reduction, continuity equation applied at the outlet will always result in lower values of perceived Ma due to area weighted average which explains why in experimental results even after catering for the kinetic energy loss, a good balance between hot and cold fluid streams could not be achieved.

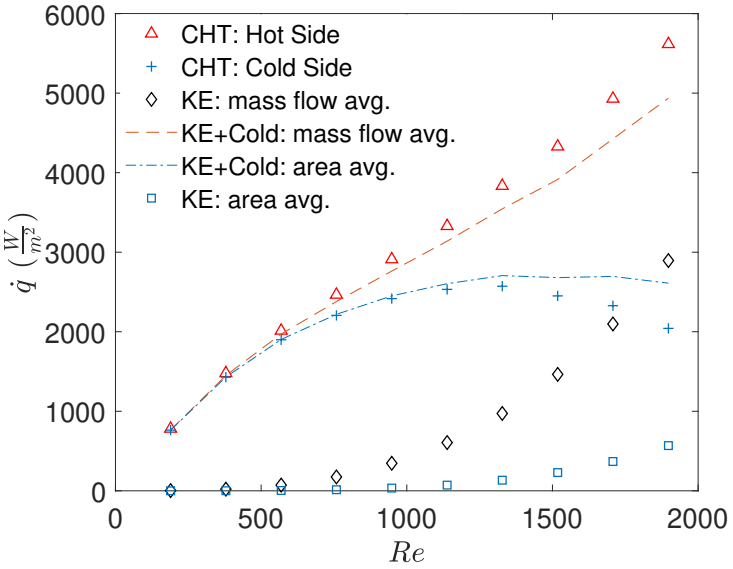

Figure 8.16: Comparison between the mass flow and area weighted averages of the kinetic energy heat flux as evaluated from the CHT analysis of μHx in parallel flow configuration.

It has been seen that by considering the kinetic energy loss from the accelerating com-

pressible fluid, the energy balance can be restored only if mass flow weighted averages are considered for flow variables. A comparison between Ma at the exit of the MC (Ma_{exit}) evaluated using mass flow or area weighted averages from the numerical results, is made in Figure 8.17. The velocity profile in channel flow is such that flow velocity is maximum at the centerline and therefore a relatively higher Ma at the centerline for the exit plane (Ma_{cl}) is also plotted for the comparison. For all cases, it can be seen that Re where energy imbalance has been observed corresponds to a much smaller Ma_{exit} as compared to the established limit of $Ma \geq 0.3$ for adiabatic macroflows. For the current set of boundary conditions taken from experimental conditions, compressibility, where energy imbalance between hot and cold sides begin to be greater than 20%, corresponds to the area weighted Ma_{exit} of as low as 0.11 and considering a pure one dimensional laminar flow this translates into a centerline value of 0.22. Therefore a conservative limit on the centerline Ma_{exit} of 0.2 is recommended while deducing the experimental results and this corresponds well in the Figure 8.10 to a Ma_{exit} of $\sim$0.1 at the Re where a considerable heat imbalance begins in the experimental results of currently investigated μHx. It is reminded again that experimentally deduced velocity and thus Ma_{exit} in the laminar regime is half of the centerline value, therefore an imbalance of the temperature drop from hot and cold sides should be expected as soon as experimental $Ma_{exit} \geq 0.1$ instead of 0.3 under diabatic conditions.

From experimental and CHT analysis undertaken, it has been made clear that compressibility effects are pertinent even at very low Ma for the investigated μHx and cause a significant imbalance of sensible heat energy between hot and cold sides. However, when it comes to evaluating the overall heat transfer coefficient of the μHx an average from both sides is usually used as it has been the case in current experimental results as well. Due to balanced flow ratios in the current experimental and numerical study, thermal kinetic energy loss on the hot and cold sides comes out to be equal. A temperature decrease due to acceleration on the hot fluid side seems to augment the overall performance of the μHx while such temperature decrease on the cold side

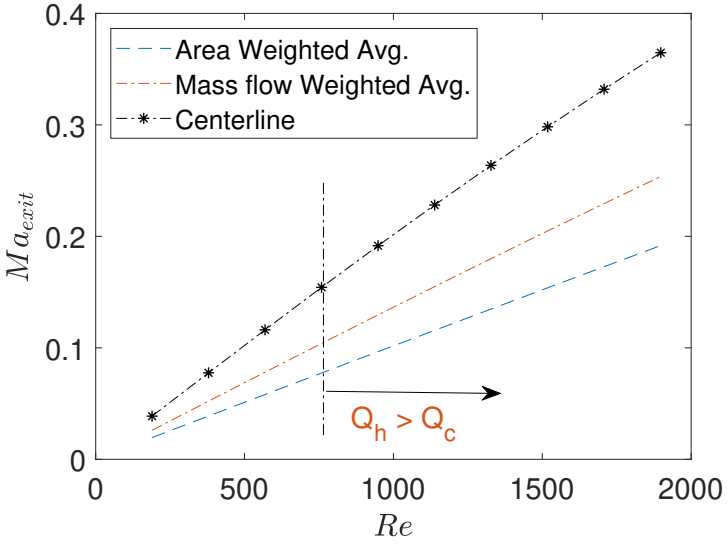

Figure 8.17: Comparison between the mass flow and area weighted averages of Ma at the exit as evaluated from the CHT analysis of μHx in parallel flow configuration.

appears to reduce it. Thus while averaging out, the performance (ε) should be the true representative of the μHx as if it were to be tested with an incompressible fluid because compressibility effects from both sides are equal which makes the efficiency gain on the hot side to be equal to efficiency loss on the cold side. Nonetheless, it is important for the designer of a gas to gas μHx to know it beforehand that if the goal is to preheat an incoming gas (as in a recuperator), the sensible heat gain of the cold fluid would be depreciated due to acceleration while it will appear to be enhanced on the hot fluid side. Whereas if the goal is to remove the heat from a solid substrate (as in a heat sink) this acceleration of the gas (decrease in gas temperature) will augment a better heat removal and thus increasing the efficiency.

Finally, a comparison between the experimental and numerically estimated thermal efficiency for parallel flow configuration is made in Figure 8.29. Although numerical results follow the decreasing trend of ε with increasing $\dot{G}$ however, are much lower when compared to experimental results. This is due to the fact that in CHT analysis, manifolds are not modeled and therefore a significant portion of the heat exchange that takes place in these manifolds is missing in the CHT analysis. From this comparison, it appears that the presence of manifolds enhances the efficiency of the currently in-

vestigated μHx in the parallel flow configuration. The presence of manifolds has also been linked to the flow maldistribution and hence decrease in the efficiency, therefore this aspect that whether the presence of manifold serves in the enhancement or attenuation of overall performance needs further investigations, however, is not pursued in the scope of current work.

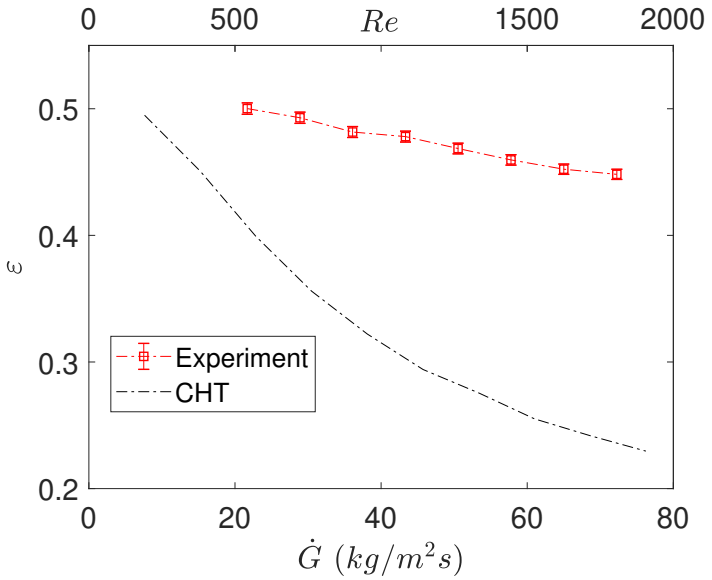

Figure 8.18: Comparison of thermal heat exchange efficiency between experimental and CHT based numerical results of μHx in parallel flow configuration.

8.2.3 Counter Flow Configuration

Fabricated μHx is also experimentally investigated in the counter flow (or counter current) configuration by connecting the gas piping such that flow travels in the opposite direction in both hot and cold sides of the μHx. As for the parallel flow case, experiments are performed in the laminar flow regime under the balanced mass flow conditions. As has been done for the parallel flow case, leak tightness is confirmed by comparing the total pressure drop from both hot and cold fluid streams under balanced mass flow conditions at room temperature. Moreover, an additional check of gas leakage with soapy water was also performed. Total pressure drop of the device is shown in Figure 8.19 which as expected is identical to the one experienced in parallel

flow arrangement (see Figure 8.5). This shows that there is no effect of the flow configuration on the pressure drop contrary to what has been reported by Gerken et al. [83]. A possible reason might be the thickness of the partition foil which in this case is 500 μm and in their case was 100 μm which might be deformed in a way that may affect the pressure drop from individual sides of the double layer μHx. The volumetric

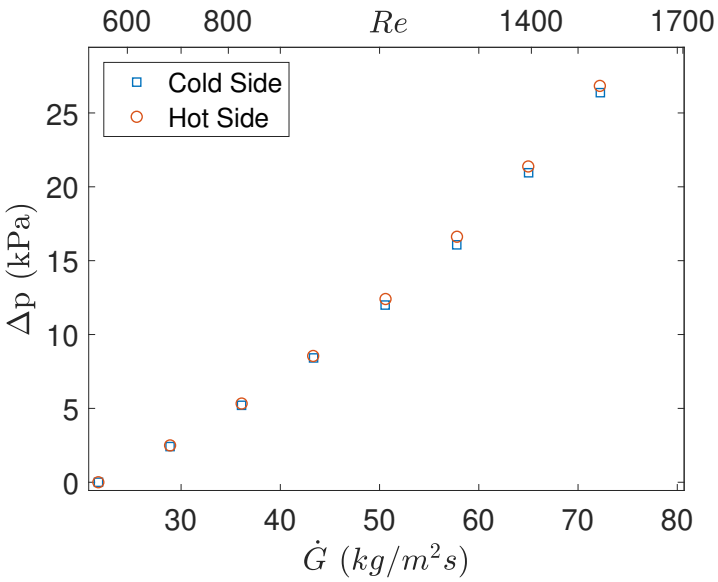

Figure 8.19: Comparison of total pressure drop of the μHx from both sides in counterflow configuration.

heat exchange rate and overall heat transfer coefficient are also plotted in Figure 8.20. As experienced for the parallel flow configuration U keeps on increasing with the increasing mass flow and the average value reaches 608 W/m^2K at the highest mass flow experimented. Similarly, q_v also shows identical values as experienced in the parallel flow arrangement.

Based on the experimental values of ΔT_{LMTD}, theoretical ε for the balanced counter flow heat exchanger can be defined as [119, 120]:

$$\varepsilon_{th,cf} = 1 - \frac{1}{1 + NTU} \tag{8.14}$$

And by considering the axial wall conduction in the partition foil, Equation 8.14 can

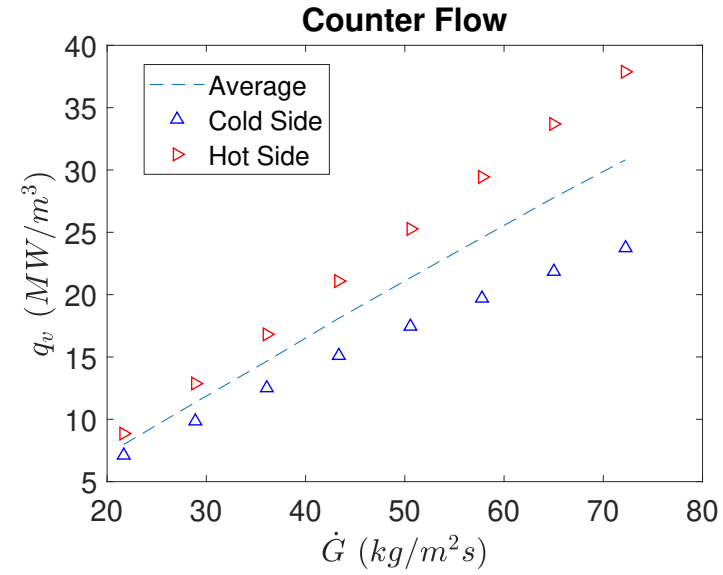

(a)

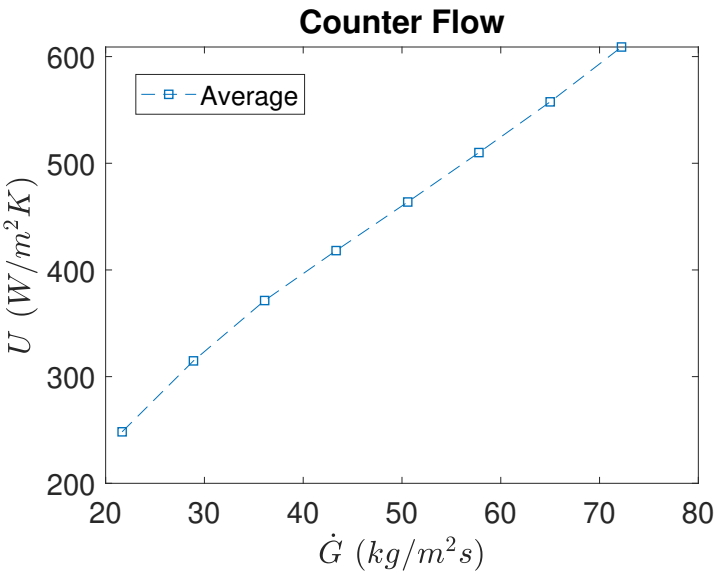

(b)

Figure 8.20: Volumetric heat exchange power for the counter flow case (**a**), and overall heat transfer coefficient (**b**).

be rewritten as:

$$\varepsilon_{\lambda,cf} = 1 - \frac{1}{1 + NTU\left(\frac{1+\lambda\phi}{1+\lambda NTU}\right)} \tag{8.15}$$

where the axial heat conduction parameter λ is the ratio of the axial conductive heat flux in the wall (q_w) to the convective heat flux of the fluid (q_f) and is defined as:

$$\lambda = \frac{q_w}{q_f} = \frac{k_w A_{ht}/L}{\dot{m}C_p} \tag{8.16}$$

in which k_w is the thermal conductivity of the wall. The parameter ϕ in Equation 8.15 is defined as:

$$\phi = \left(\frac{\lambda NTU}{1 + \lambda NTU}\right)^{1/2} \tag{8.17}$$

In Equations 8.14 - 8.17, the value of NTU needs to be the one which is calculated without the consideration of the axial wall conduction. In an experimental campaign however, measured temperatures and hence deduced values from these measurements would always have the effect of axial wall conduction and therefore if one is to compare the experimentally evaluated NTU in Equation 8.15, it will yield wrong theoretical estimations. A novel methodology to estimate the theoretical efficiency from experimental results of NTU has been presented by Yang [2] where following equation is solved for the solution of theoretical NTU based on the experimentally evaluated NTU' (having wall conduction effects):

$$\phi.^3 + \lambda\phi.^2 - NTU' = 0 \tag{8.18}$$

Heat exchanger efficiency calculated by the evaluated ΔT_{LMTD} and U for counter flow configuration is shown in Figure 8.21. Theoretical efficiency without axial wall conduction, based on the NTU from Equation 8.18 is also plotted for comparison. Axial wall conduction in the partition foil is usually detrimental to the heat exchanger efficiency in counter flow configuration as experienced in the experiments of Yang et al. [82, 81]. In current results however, both of the theoretical values are quite close and therefore it can be concluded that axial wall conduction does not affect much the μHx efficiency for the stainless steel separation foil. Yang et al. [82, 81] also obtained

the similar results with stainless steel partition foil with 100 μm thickness. Values of the λ assumed for current configuration of experimental campaign are in the range of 0.05–005 which is not significant to influence the average effectiveness of the μHx. It

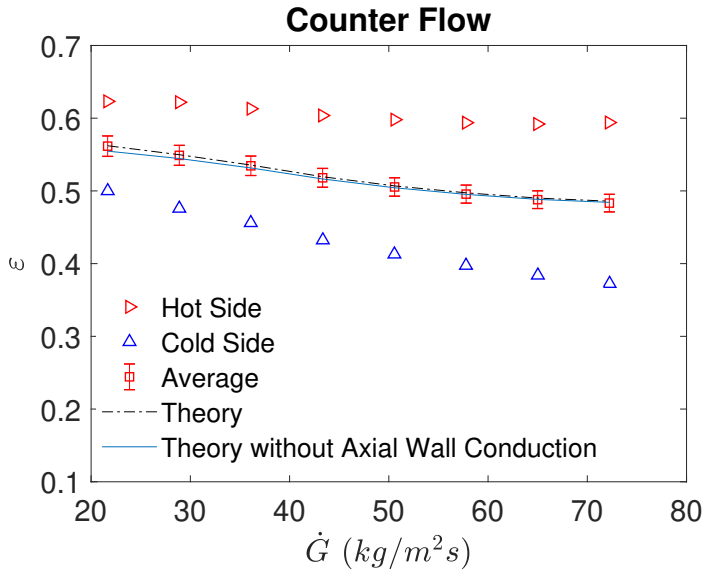

(a)

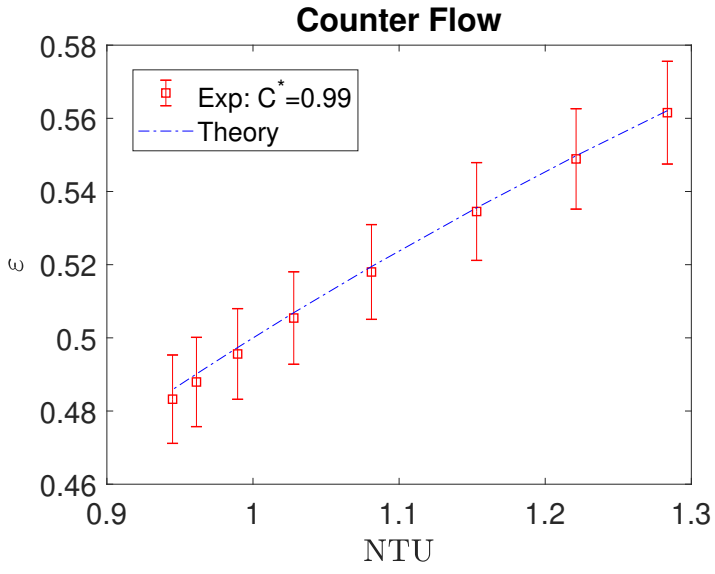

(b)

Figure 8.21: Experimental heat exchanger efficiency ε for counter flow configuration: variation with $\dot{G}$ (**a**), and with NTU (**b**).

is also evident by observation of Figure 8.21b that for a balanced case, counter flow μHx follows the conventional ε-NTU theory within experimental uncertainty. It can be seen from Figure 8.21a that even in the case of the counter flow configuration, both

sides of the μHx demonstrate an imbalance of energy and hence of the temperature. Therefore a CHT analysis is also performed for the counter current configuration using the earlier utilized model. The contribution of thermal energy due to gain in kinetic energy is also evident for currently investigated configuration at almost similar values of $\dot{G}$ and Re as shown in Figure 8.22. Qualitatively as well as quantitatively similar analogies can be withdrawn from the experimental and numerical results of counter flow configuration as were explained for the parallel flow configuration. Inclusion of kinetic energy in the balance reduces the difference between the two sides from 60% to 12%, as it was the case for parallel flow configuration. This shows that independent of the configuration, gas flow accelerates with similar Ma from both sides and compressibility starts affecting the energy balance at the same Re >800 for the experimental μHx.

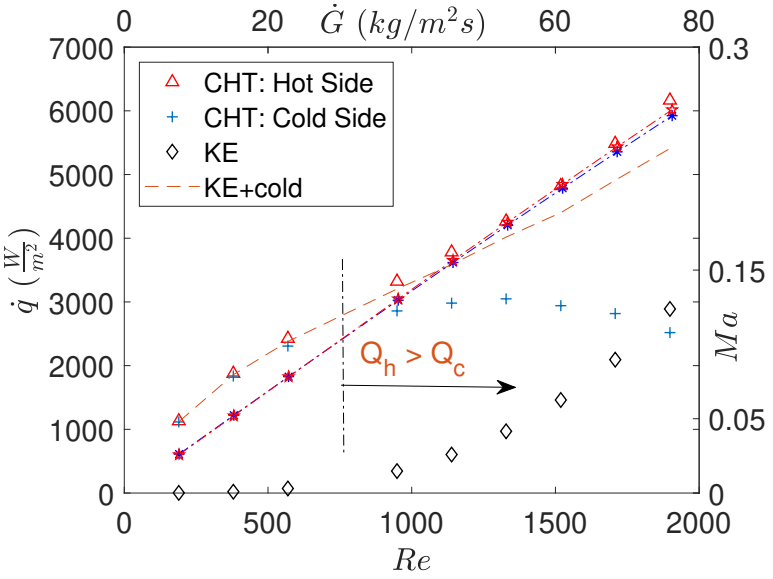

Figure 8.22: Comparison of individual components of total heat flux exchanged between the two fluids as evaluated from the CHT analysis of μHx in counter flow configuration.

Finally, the thermal efficiency of the μHx in the counter flow configuration is shown in Figure 8.23. To compare both configurations experimentally as well as numerically, ε evaluated from the respective analysis is also plotted in the same figure. From experimental and numerical results it can be established that counter current configuration results in a higher ε for the given inlet mass flow under balanced flow conditions. The

difference between the two is highest at the lower values of Re and it diminishes towards the higher end of the $\dot{m}$ tested. Efficiencies evaluated from CHT analysis are much lower compared to experimental results and this has been attributed to the presence of finite heat exchange between the fluids in the distributing and collecting manifolds. As experimental temperatures are measured in the vicinity of the inlet/outlet ports, an exact estimation of the temperature drop in the MC core only could not be performed and therefore no direct comparison with the numerical model can be made where manifolds are not modeled. It is therefore recommended to setup an experimental campaign where temperature sensors are placed right before and after MC core as was the case with the device tested by Yang et al. [82, 81], and Gerken et al. [83]. Conversely, a complete set of CFD model where manifolds are included should be used in order to quantify the heat exchange happening in the manifolds.

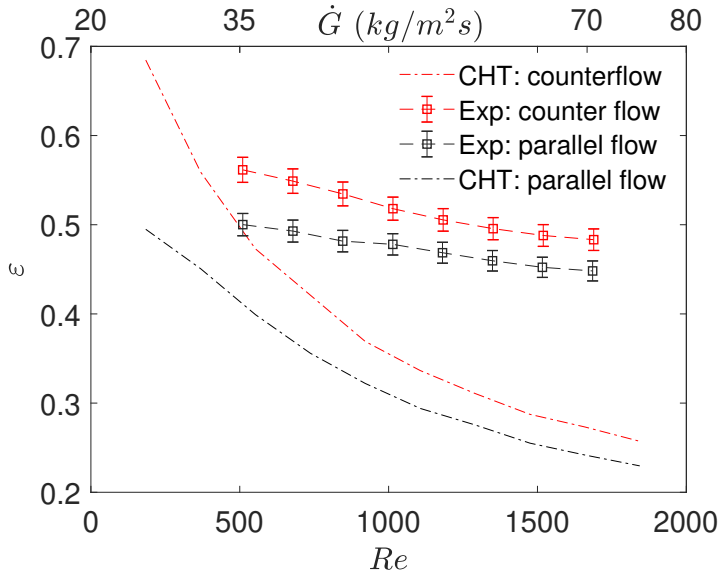

Figure 8.23: Comparison of experimental and numerical ε between parallel and counter flow configurations for experimental μHx.

It is reminded to the reader at this point that CHT model employed for the investigation of flow behavior inside MCs has been previously used during the validation study performed for the device of Yang [2] in Section 9.5. Later complete porous model analysis of the single layer for that particular μHx showed that there is a significant pressure drop and hence expansion in the manifolds and if one is to consider the

ε of the complete device, it would result in a higher value than what is reported only for MC core. Similarly for the currently experimented μHx, ε for the complete device including manifolds is higher which results in a superior performance than CHT (MC core only). Moreover, it has been clarified that the heat transfer rates on the hot and cold sides for a gas to gas μHx are different due to compressibility which becomes relevant when the experimentally evaluated Ma_{exit} $\geq$0.1. For the balanced flow conditions, thermal energy loss due to flow acceleration is equal on both sides and as mentioned earlier, overall ε of the complete μHx should not be affected. For this reason, thermal analysis carried out earlier using the average of hot and cold sides matched perfectly well with conventional ε-NTU theory which in general is validated for the macro scale incompressible flows.

8.2.4 Unbalanced Flows

When the mass flows are not balanced however, compressibility should cause a deviation between the actual and conventional ε-NTU method due to unequal thermal kinetic energy loss on either side. Results of experimental investigation for the unbalanced mass flows carried out in the parallel flow μHx are shown in Figure 8.24. As soon as the heat capacity ratio moves further from 1, ε starts showing deviation from the conventional ε-NTU method. In general, if $\dot{m}_h > \dot{m}_c$ then compressibility effects are stronger in the hot fluid side causing relatively bigger temperature drop due to conversion in thermal kinetic energy than the cold side. This shifts the average ε towards the hot side (higher values) and this can be seen from the results of two experimented cases where values of $\dot{m}_c/\dot{m}_h$ are 0.5 and 0.75. It is further clear by closely observing ε for $\dot{m}_c/\dot{m}_h$ of 0.75 that since $\dot{m}_h$ is only 25% higher than $\dot{m}_c$, the increase of ε above the theoretical line is stronger for smaller values of NTU (which means higher value of Re), again highlighting that a simple average is biased towards hotter side of the μHx at the higher Re due to compressibility. Whereas when $\dot{m}_c/\dot{m}_h$ =0.5 then the hotter side is compressible throughout the investigated domain compared to

slow moving cold fluid and therefore all the results from this case are higher above the theoretical predictions. For an incompressible flow, an unbalanced flow condition where $\dot{m}_h$ is half of the $\dot{m}_c$ and the one where $\dot{m}_c$ is half of the $\dot{m}_h$ should strictly yield the same heat exchanger efficiency but for compressible gas to gas μHx, this is not the case as shown by the data points of experiment where $\dot{m}_h/\dot{m}_c$ =0.5. In this case, since the

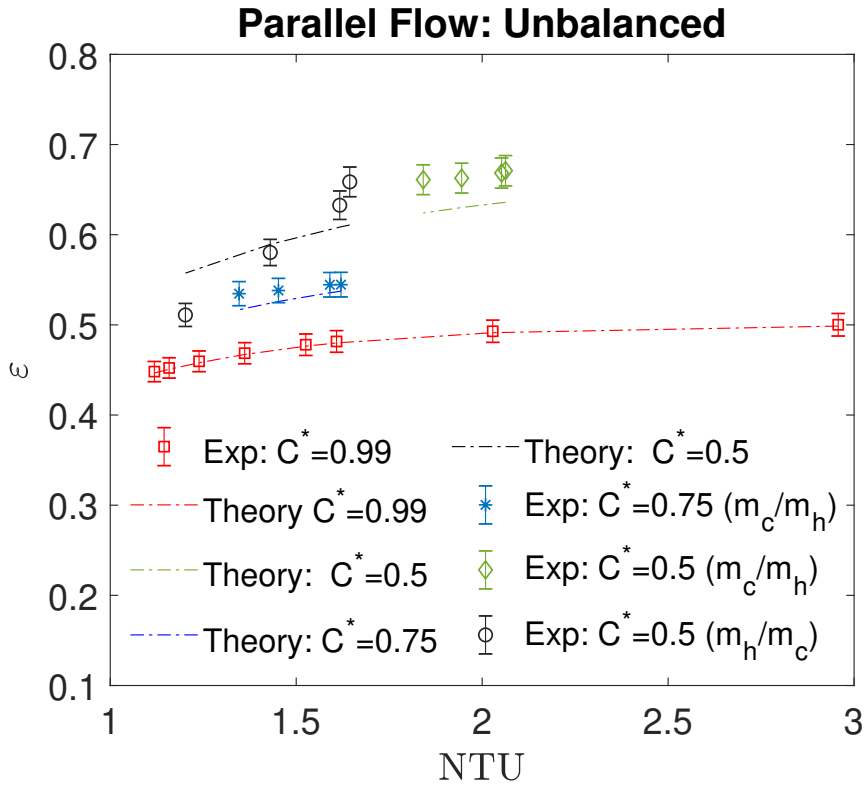

Figure 8.24: Comparison of experimental ε for unbalanced mass flow conditions in parallel configuration.

cold fluid is the fast moving fluid with higher thermal energy loss due to acceleration, this shifts the average value of ε lower than the theoretical curve at smaller NTU values (higher Re). The highest ε achieved using current experimental results is with the case where $\dot{m}_h$ is twice as fast as $\dot{m}_c$. In general, if the cold fluid is characterized by higher Ma than the hot fluid side, this results in an overall attenuation of the ε. And if Ma of the hot fluid is higher than cold fluid, it increases the average ε of the double layer gas to gas μHx.

8.3 Numerical Analysis

An increased Nu in the case of MTs with $D_h \leq 250$ μm was observed from the experimental and numerical results presented in Chapter 5. Reducing the dimensions of the MTs/MCs carrying the fluid results in an increased convective heat coefficient and similarly an increased overall heat transfer coefficient is usually observed in μHxs which motivates the engineers to investigate this promising technology further. To see if reducing D_h affects the thermal efficiency of the double layer μHx, CHT model is further exploited in both configurations. To match the experimental conditions, only laminar flow solver was used earlier in this chapter whereas for current analysis $\gamma - Re_\theta$ transitional turbulence model is used and Re is varied from 200 to 10,000. This allows to observe the thermal efficiency of a double layer μHx not only in laminar regime but also in transitional and fully turbulent regimes. Geometric characteristics of the different μHxs used in this parametric analysis are presented in Table 8.3. In order to decouple the effect of α on the thermal performance of μHx, it is kept constant as 1 for all the geometries considered. Moreover, separation foil thickness δ is also kept constant with the thermal conductivity as mentioned in Table 8.1. Boundary conditions are kept same as mentioned in the Table 8.2.

Table 8.3: Geometric details of double layer μHxs used for numerical simulations.

μHx	w (μm)	h (μm)	D_h (μm)	δ (μm)	t_w(μm)
μHx1	100	100	100	100	100
μHx2	200	200	200	100	100
μHx3	300	300	300	100	150
μHx4	500	500	500	100	300

Heat flux for μHx3 on both hot and cold sides with the respective shares of the kinetic energy of the flow are presented in Figure 8.25, in a parallel flow configuration. Due to different fluid viscosities on the hot and cold side there is a slight variation of the Re on each side and therefore an average Re is used in the rest of the discussion. It is evident that contribution of the kinetic energy starts becoming relevant at $Re > 800$ as

noticed for the tested μHx. Also in this case the corresponding Ma at the exit is close to 0.15 which as discussed earlier is slightly higher (1.3 times in the laminar regime) than the area weighted average. Therefore even in this case a limit of Ma_{exit} $\geq$0.1 is observed where the energy imbalance is evidenced.

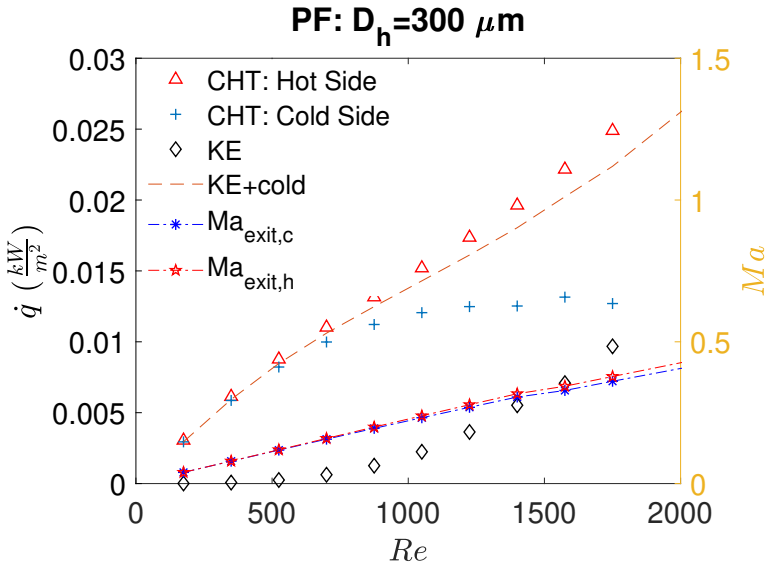

(a)

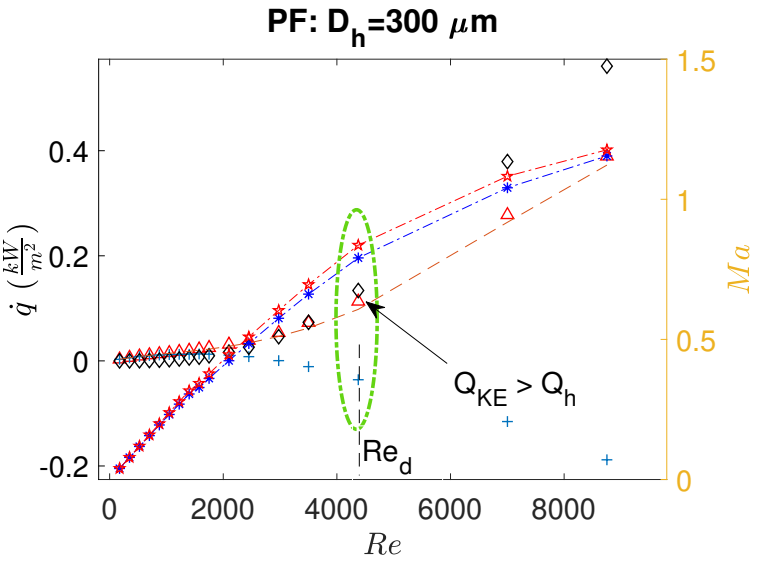

(b)

Figure 8.25: Heat flux balance for μHx3 (D_h =300μm) in the laminar regime (**a**), and for all the range of simulated Re (**b**), for parallel flow (PF) configuration.

The contributions of the individual components of energy balance (Equation 8.13) for μHx3 for the whole range of Re simulated including transitional and turbulent

is also shown in Figure 8.25b. The kinetic energy gain (thermal loss) becomes quite significant for Re >2000 so much so that it supersedes the total energy lost at the hot side. Corresponding Re is labeled as Re_d as shown in the figure. At maximum simulated $\dot{m}$ (Re), the combined sum of kinetic energies from both hot and cold sides becomes 50% higher than the heat energy loss of the hot fluid. By observing the Ma_{exit} it can be seen that it is moving towards stagnation close to a value of ∼1.17 but has not become fully constant as it has been observed for the adiabatic choked flows in MCs (see Chapter 6). Results from the μHx with the smallest D_h are also shown in Figure 8.26. In this case, Ma_{exit} of 0.1 is achieved at Re <500 and therefore energy imbalance can be seen even for smaller Re due to strong compressibility caused by the smaller dimensions. As expected because of higher Ma_{exit}, Re where the combined sum of the kinetic energy of the gas is higher than heat loss from the hot side, is lower when compared to the case of μHx3. Flow choking is also observed for Re >4000 where Ma_{exit} gets stagnant at the value of 1.34. It is again reminded to the reader that for compressible gas flows $Ma_{exit} > 1$ has been numerically and experimentally experienced ([118, 121, 107, 122]) due to boundary layer thickness close to the exit wall that serves as a De-laval nozzle for the sonic flow which ultimately becomes supersonic at the MC outlet.

Mach numbers at the outlet cross section for all the μHxs for the range of simulated Re in parallel flow configuration are shown in Figure 8.27. Flow choking (constant Ma_{exit}) is only observed for the smallest D_h of 100 μm. Whereas μHx2 and μHx3 are achieving a near choking state (Ma_{exit} almost becoming constant). The biggest D_h of 500 μm however is still less than 1 and is expected to choke way further at very high Re and for the current range of Re it shows a linear increase.

μHx efficiencies for the two presented cases earlier is also plotted in Figure 8.28. It can be seen that there exists a strong imbalance also in the μHx efficiencies if calculated from hot and cold sides individually. Due to balance flow conditions (almost similar kinetic energies) values of ε from both sides appears symmetric where averaged values

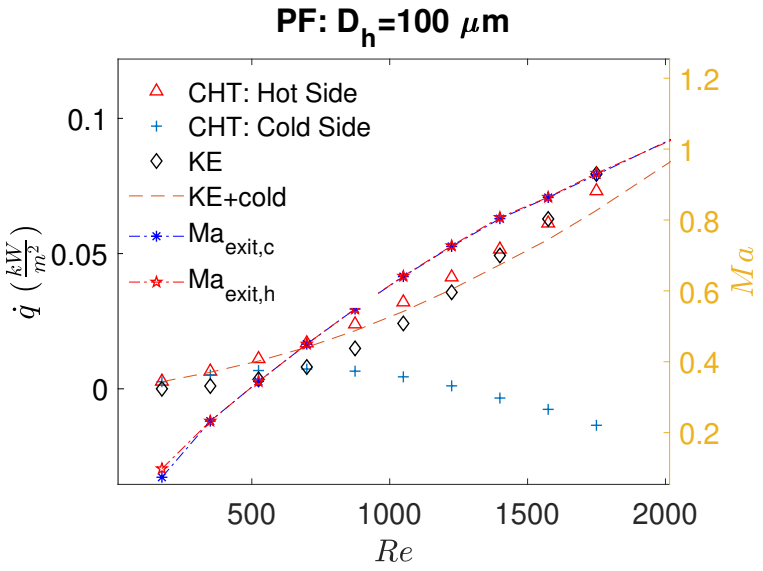

(a)

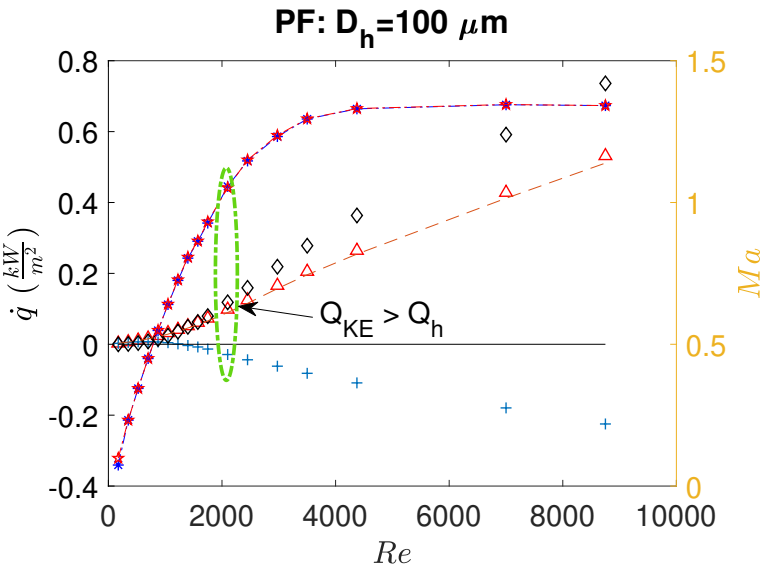

(b)

Figure 8.26: Heat flux balance for μHx1 (D_h =100μm) in the laminar regime (**a**), and for all the range of simulated Re (**b**), for parallel flow (PF) configuration.

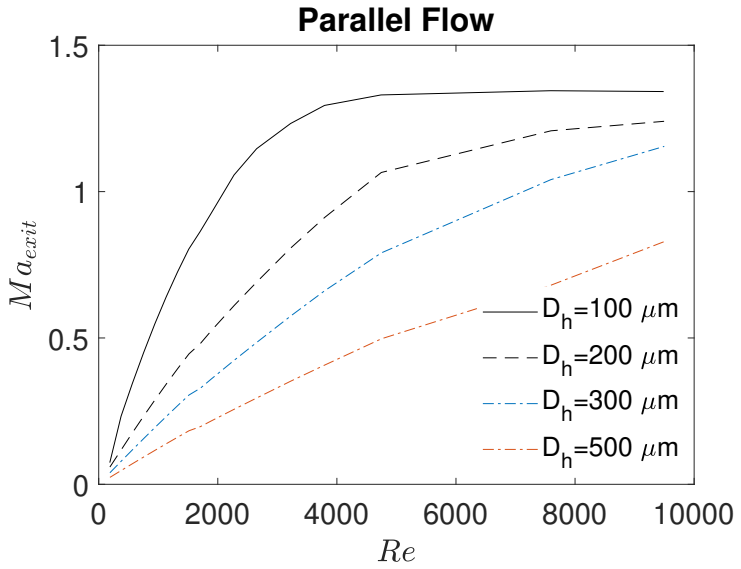

Figure 8.27: Comparison of outlet Ma for all the μHxs simulated in parallel flow configuration.

stay in the middle. It is further evident from Figure 8.28b that in the choked flow regime due to achievement of a constant Ma_{exit}, ε becomes constant whereas it decreases in the laminar flow regime.

Average values of ε for all the simulated μHxs in parallel flow configuration are compared in Figure 8.29. All the μHxs have higher ε at very low Re which decreases steeply with an increase in Re. As observed for the MTs, for a given Re μHx with the smallest D_h has the highest efficiency. In general a decrease in efficiency is observed with an increase in D_h. With the increase of Re the ε reaches its minimum at a Re_d where combined sum of the kinetic energy from both sides becomes greater than the heat energy loss from the hot side. At this point, temperature of the cold gas at the outlet is already lower than the inlet temperature ($T_{c,in} > T_{c,out}$) causing $\dot{q}_c$ to become negative. After this stage an increase in the average ε is observed which again is due to the mathematical nuances related to the definition of the ε. A generic definition of the heat exchanger efficiency is:

$$\varepsilon = \frac{Q_{fluid}}{Q_{max}} = \frac{Q_{fluid}}{(\dot{m}C_p)_{min}\Delta T_{max}} \tag{8.19}$$

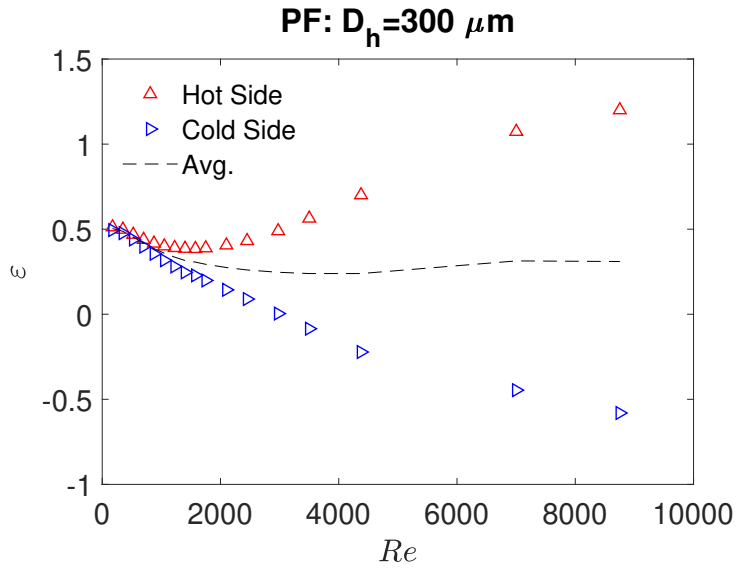

(a)

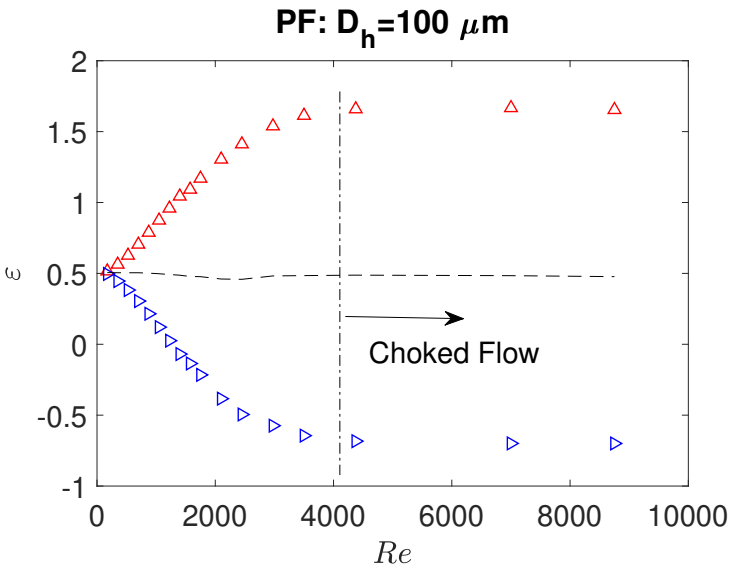

(b)

Figure 8.28: Heat exchanger efficiency in parallel flow configuration for μHx3 (**a**), and μHx1 (**b**).

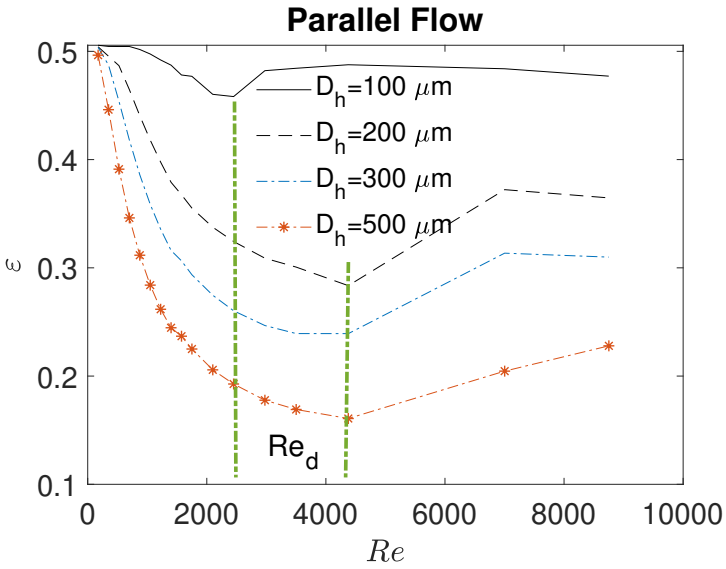

Figure 8.29: Comparison of average ε for all the μHxs simulated in parallel flow configuration.

In an incompressible heat exchanging system, it is assumed that $T_{c,in}$ represents the minimum temperature of the system and therefore maximum possible heat exchange that may happen in the system is such that $\Delta T_{max} = T_{h,in} - T_{c,in}$. However for a gas flow with strong compressibility effects, when the $T_{c,out}$ is smaller than the inlet value the maximum possible energy of the system becomes higher than the one represented with $T_{h,in} - T_{c,in}$ as in this case the minimum temperature of the whole system is $T_{c,out}$ rather than Tc_{in}. Cross sectional averages of the static temperatures in both hot and cold streams for representative case of μHx3 are shown in Figure 8.30 where for $Re \geq$4000 temperature of the cold gas at the outlet is smaller than inlet hence explaining negative values of ε from cold side as observed in Figure 8.28. Hence the denominator of the Equation 8.19 is underestimated for the cases where $T_{c,out} > T_{c,in}$ therefore causing an apparent increase of the efficiency.

If this definition is corrected for such that where $T_{c,out} < T_{c,in}$ satisfied, $\Delta T_{max} = T_{h,in} - T_{c,out}$ is utilized for the calculations (which is possible in numerical data), for the given inlet temperatures of the simulated μHx a unique Re_d of $\sim$4375 is achieved where all the curves show their minimum. The comparison of Figures 8.29 & 8.31 shows that there is no drastic improvement of the average ε at higher Re is expected

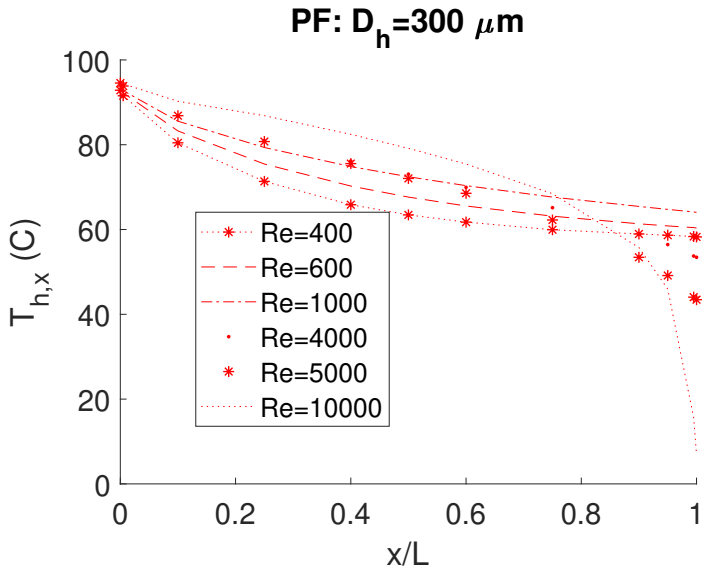

(a)

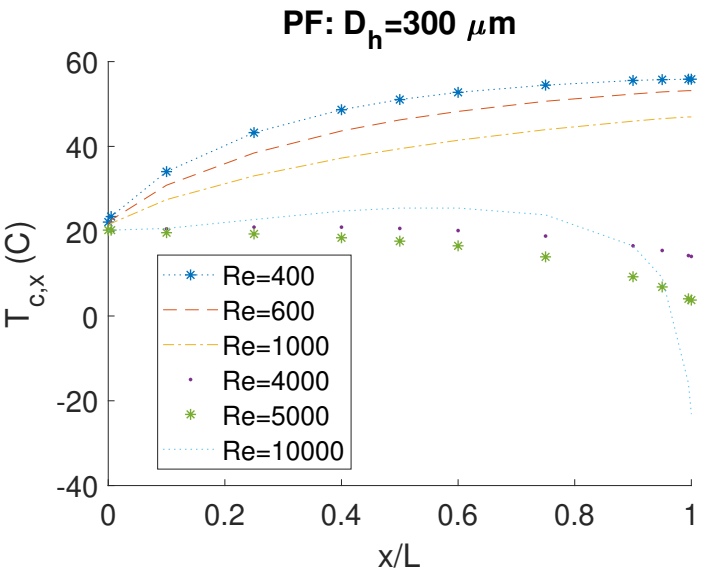

(b)

Figure 8.30: Cross sectional average static temperatures in the axial direction for μHx3 in parallel configuration: hot side (**a**), and cold side (**b**).

whereas a general trend of the decrease in ε with a decrease in D_h in the laminar regime is observed again. Using the modified definition of ε however, is not practical from theoretical point of view as a before hand information of the outlet temperature or indication as to when $T_{c,out}$ will become smaller than $T_{c,in}$.

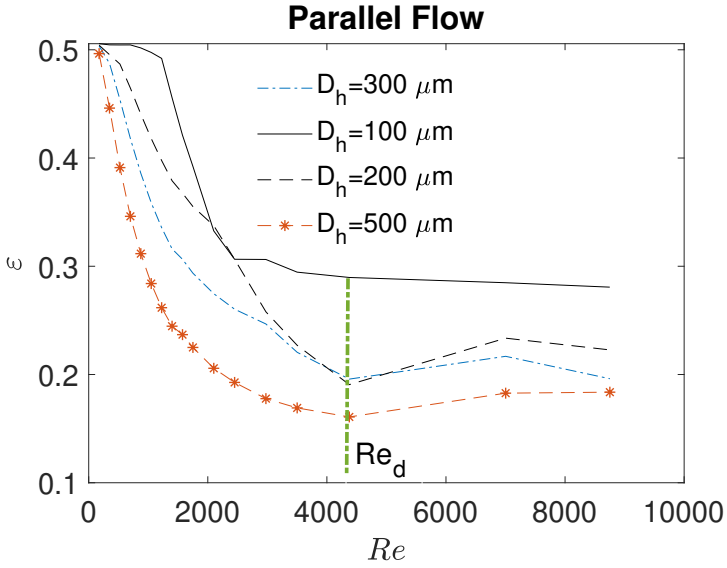

Figure 8.31: Comparison of average ε when correct values of ΔT_{max} are taken for all simulated μHx in parallel flow configuration.

Similar analysis has also been performed for all the μHxs in counter flow configuration and the comparison of ε with the change in D_h is shown in Figure 8.32a. Counter flow configuration in general shows superior behaviour compared to parallel flow as it has been evidenced from the experimental results. The efficiency of the MC core decreases suddenly in the laminar regime as experienced for the parallel flow configuration as well. For transitional and turbulent Re, there is not much variation in the performance with increasing Re where all are operating with ε <0.3 except for D_h =100 μm which has ε of 0.35. At highest Re simulated, μHx with the smallest D_h (μHx1) is haveing 94% higher efficiency than μHx with the biggest D_h (μHx4) whereas in the laminar regime it is more than 118% higher. The comparison of Ma_{exit} between the two flow configurations is also shown in Figure 8.32b where almost identical values are achieved for both configurations under balanced mass flow conditions. For a given inlet average Re under balanced flow conditions Ma_{exit} is slightly higher in counter flow configuration during the transitional

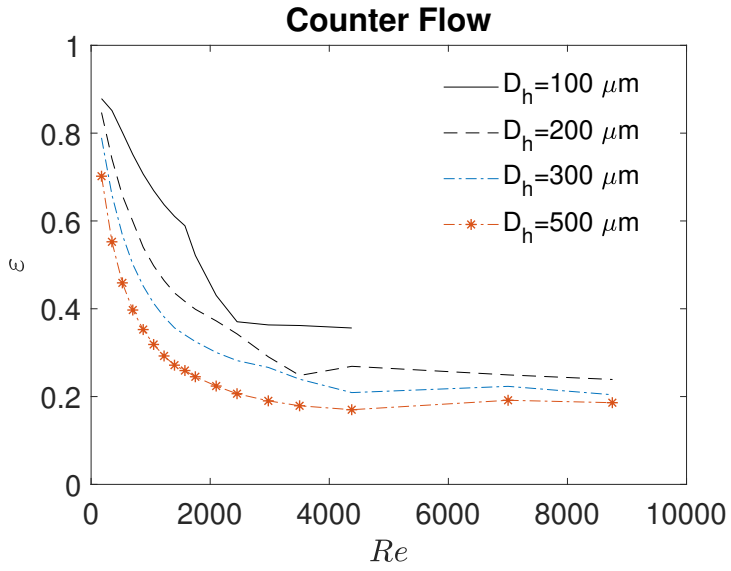

(a)

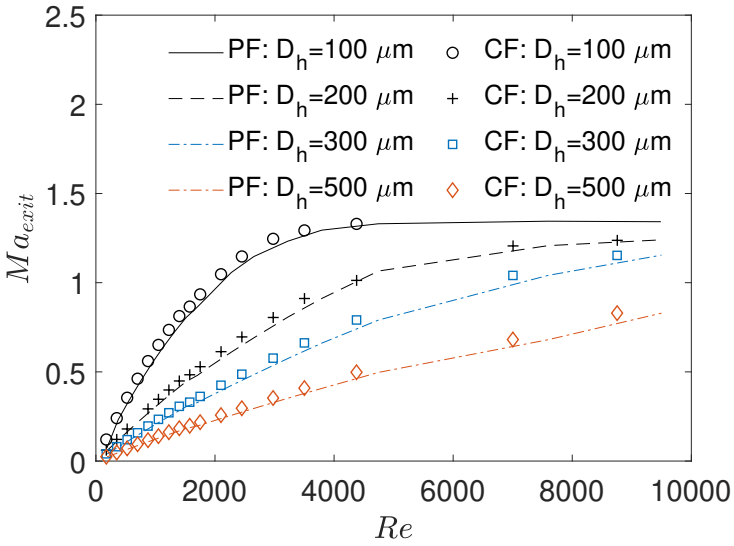

(b)

Figure 8.32: Heat exchanger efficiency in counter flow configuration for all μHxs (**a**), and comparison between Ma_{exit} between the two flow configurations (**b**).

and turbulent regimes however it is almost identical in the laminar regime for μHx3 and μHx4. On the contrary with the reduction in D_h, resulting values of Ma_{exit} are marginally higher in case of counter flow configuration during the laminar regime but almost identical to the parallel flow in the turbulent regimes.

The aforementioned analysis has provided a great insight into fluid physics of the compressible gas flows inside a double layer μHxs where the lessons learnt can also be extended to a multilayered μHx. It has been seen that unlike incompressible flows, there exists a huge imbalance between hot and cold sides of the μHx due to flow acceleration. Such discrepancy is further amplified as one reduces D_h of the MCs core and after a certain critical inlet $\dot{m}$ (or Re) heat gain on the cold side becomes negative i.e. there is no sensible heat gain or rise in static temperature of the cold fluid and rather cold fluid experiences cooling which is contrary to the engineering usage of a heat exchanger although it could be a potential benefit in heat sink application as mentioned earlier. Therefore for heat exchanger applications with the balanced flow a region where ε from the cold side (ε_c) is positive should be of relevance. On the other hand, under balanced flow condition, hot fluid side of the heat exchanger will always yield exceptional efficiencies as the initial objective of decreasing the gas temperature (cooling) from inlet to the outlet is not only fulfilled by the heat exchange from the cold fluid but also due to additional temperature drop thanks to the expansion (compressibility) close to the outlet of the MC core. But such additional cooling of the hot gas is again at the expense of the pressure drop hence for an engineering application of μHx it is essential to have a knowledge of the degree of energy imbalance between hot and cold fluids that can be afforded without compromising the initial objective of heat exchange. Figure 8.33 provides one such illustration where the ratio of thermal efficiencies from hot and cold fluids is plotted only where there is some degree of sensible heating on the cold side.

It is to be noted again that even for a balanced flow condition, Re from cold and hot sides may differ depending on the inlet temperatures and corresponding fluid viscosities

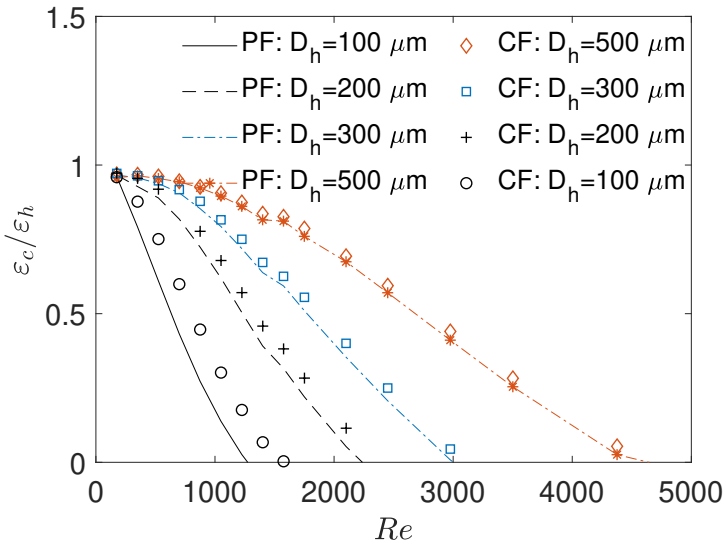

Figure 8.33: Chart for positive values for the ratio of $\varepsilon_c/\varepsilon_h$ for both flow configurations studied where CF and PF stand for counter and parallel flow configurations.

therefore in Figure 8.33 an average value of the Re is utilized. As it has been seen that for a given Re, Ma_{exit} is higher for the smaller D_h which signifies a greater imbalance of thermal energy from the two sides, conversely it can be observed by Figure 8.33 that $\varepsilon_c/\varepsilon_h$ is higher for bigger D_h for a given Re. This essentially means that in order to operate in a condition such that hot fluid transfers at least 50% of thermal energy to the cold fluid, higher inlet $\dot{m}$ can be utilized with bigger D_h μHxs.

8.4 Summary

A combined experimental and numerical approach is used in this chapter to investigate the thermal performance of double layer μHxs. An experimental test rig is realized and a prototype double layer μHx is fabricated. The modular design of the prototype device is pursued as this allows to experiment by changing the design parameters of each layer as well as the separation foil in between. In the context of this Ph.D. thesis, only a single partition foil made of Stainless steel is used with MCs core (hot and cold layers) made from PMMA. A total of 51 MCs are micromilled in parallel along with the combining and dividing manifolds, to form a single layer of the μHx under

consideration. Dimensions of the MCs are such that D_h of each MC comes out to be ∼446 μm with a constant length of 40 mm. The prototype μHx is tested in both parallel and counter flow configurations under balanced flow conditions. An imbalance of heat energy from the hot and cold side has been found out during experimental campaigns even with the proper insulation from the surroundings. To investigate if such an imbalance is due to experimental setup or there is some underlying physics that may cause this behavior, a numerical CHT model previously used in Chapter 9, is utilized in parallel. CHT analysis provided invaluable insights on the role of compressibility towards the thermal performance of the MCs core. It has been found out that due to additional acceleration (compressible nature), gas flows on either side experience an additional temperature drop that results in a significant difference in terms of temperature differences on both sides. For the experimented dimensions, CHT model showed that for Re >800, the effect of compressibility can not be ignored while making a thermal balance of the device. The corresponding Ma at the outlet where such effects become significant is found out to be 0.1 which is significantly less than the conventional limit of $Ma \geq$0.3 for adiabatic flows. In order to completely close the energy balance between the two sides of the μHx it is essential to cater the additional kinetic energy increase inside each layer and if this energy is accounted for, the total energy content (thermal and kinetic) showed an adequate balance between both sides. A similar approach was used to account for the kinetic energy gain in experimental results where at the highest Re tested, the discrepancy was still found out to be almost 40% between the two sides. Comparison has further revealed that in the experimental data reduction, utilization of continuity equation at the outlet cross section corresponds to area weighted averages of the axial gas velocities which are 1.33 times lower than the massflow averaged values and therefore using experimentally evaluated velocities underestimates the kinetic energy of the gases in both fluid streams.

Average values of experimental thermal efficiency for the prototype μHx in both flow configurations showed a good agreement with the conventional ε-NTU theory only because there exists an equal magnitude of kinetic energy in both fluid streams which gets

cancelled out while performing the arithmetic average. Using experimental runs with unbalanced flow conditions in the parallel flow configuration, yielded a disagreement with the conventional theory because of the difference in kinetic energy terms between hot and cold fluid streams. In general for $\dot{m}_h > \dot{m}_c$ the average is biased towards the hot side because the hot side contains higher thermal energy compared to slow moving cold fluid and this resulted in an apparent increase in the μHx average efficiency above the conventional theory. And for the case when $\dot{m}_c > \dot{m}_h$ efficiency depreciated at lower NTU values (higher Re) because, the cold side in this case, possesses higher kinetic energy compared to the hot side and therefore average is biased towards the cold side.

An increase in the Nu had been observed with the decrease in D_h while analyzing the forced convection in the MTs. This motivated to exploit the CHT model further in order to investigate the effect of decreasing D_h on the average thermal efficiency of double layer μHx. To this end, D_h of μHxs is varied from 500 μm to 100 μm with a constant α of 1. Flow analysis has been conducted in both parallel and counterflow configurations for an extended range of Re covering laminar, transitional and turbulent flow regimes. As expected the performance of the μHx for all the D_h depreciates steeply with increasing inlet Re. However, for a given Re the performance of a μHx with smaller D_h is superior as compared to the bigger one. This has been observed in both counter and parallel flow configurations. The validity of the proposed limit for an experimentally measurable Ma_{exit} is again validated by these set of simulations where all the D_h showed considerable energy imbalances between hot and cold fluid streams and therefore a threshold value for Ma_{exit} of 0.1 is recommended after which the effects of compressibility (energy imbalance) can not be ignored in an experimental campaign. This means that if experimentally deduced $Ma_{exit} > 0.1$, an imbalance between the temperature drop of hot side and gain of the cold side, should come as no surprise which had been the case for the author while performing experiments. It has been further clarified that although μHxs with gas flows under balanced conditions follow the conventional theory but depending on the initial objective, the designer should

know beforehand the extent of energy imbalance for the given $\dot{m}$ and D_h. For this reason, the ratio of $\varepsilon_c/\varepsilon_h$ for all the D_h considered in both parallel and counter flow configurations is presented which may provide an initial estimate as to how much of the imbalance should be expected.

Chapter 9

Porous Medium Modeling for Gas to Gas Micro Heat Exchangers

9.1 Introduction

The previous chapter has detailed the effects of compressibility on the thermal performance of the double layer gas to gas μHx. In order to explain the experimental results, a numerical model (CHT) was utilized which essentially comprised of the hot and cold fluid channels with periodicity on the side walls, hence reducing the computational domain considerably. Moreover, CHT presented an ideal case where it was assumed that the presence of manifolds does not influence the thermal performance of the μHx and therefore manifolds were not modeled. Thus, CHT model also does not cater for any possible mass flow maldistribution that is inevitable in a typical μHx due to distributing and collecting manifolds. Moreover, as it has been highlighted in Chapter 8 (see Fig. 8.23) that the presence of manifold increases the overall thermal performance of the μHx compared to only MC core. Considering the above, in order to correctly estimate the thermal performance of the μHx, it is essential to include manifolds as well as the number of parallel microchannels for computational analysis. On the other hand, a typical μHx having hundred of parallel MCs along with the

manifolds poses a huge computational burden. Therefore, it is of acute importance to provide the design engineers with the computationally efficient numerical tools without considerable compromise on hydro-thermal performance prediction for μHxs. In this chapter, one such methodology which is based on the CFD and porous media modeling (Darcy-Forchheimer law) is presented. To validate the proposed numerical methodology, experimental results of a double layer μHx with 133 parallel microchannels and triangular manifolds, available from the open literature [2, 82, 81, 83] are used. It is to be noted that the number of MCs in the chosen μHx is more than double than the μHx tested in Chapter 8. This will allow to validate the proposed methodology with a higher degree of maldistribution when compared to the μHx analyzed in the last chapter. In the following sections, the theoretical background and a mathematical model for the modified Darcy law to estimate the pressure drop in the porous medium will be presented. The developed methodology will then be validated using experimental results of a double layer μHx available in the open literature.

9.2 Background

Darcy law in its fundamental form represents an empirical relation for the pressure drop of an incompressible fluid passing through a bed of spheres. For a fluid flow in a pore space, it can be written as:

$$\frac{-\Delta p}{L} = \frac{\mu \dot{G}}{\alpha \rho} \tag{9.1}$$

where $\frac{1}{\alpha}$ is viscous coefficient representing porous medium permeability. Δp denotes the pressure drop of a fluid with density ρ and dynamic viscosity μ along the total flow length L. $\dot{G}$ denotes mass flow rate ($\dot{m}$) per unit area A ($\dot{G} = \dot{m}/A$). However, Darcy's law is limited to very low velocities such that Re is less than unity. To cater for increasing speeds or Reynolds number, Forchheimer correction is introduced to accommodate for the non linear increase in pressure drop with increasing velocity. An

extended Darcy-Forchheimer (hereafter referred to as simply Darcy) law for a porous media can then be rewritten as follows:

$$\frac{-\Delta p}{L} = \frac{\mu \dot{G}}{\alpha \rho} + \frac{\Gamma \dot{G}^2}{2\rho} \tag{9.2}$$

where Γ is an inertial coefficient of Darcy's law. Calculation of viscous ($\frac{1}{\alpha}$) and inertial (Γ) coefficients, is usually done using experimental results and therefore various empirical relations exist for different porous media geometries. One such empirical model is the Ergun equation which is originally developed for flow over a bed of spheres. From the proposed Ergun equation, viscous and inertial coefficients of a porous media modeled as the bed of spheres, are as follows:

$$\frac{1}{\alpha} = \frac{150(1-\kappa)^2}{\kappa^2 {D_p}^2}; \Gamma = \frac{3.5(1-\kappa)}{\kappa^2 D_p} \tag{9.3}$$

where κ is the fractional void volume and D_p is the effective particle diameter of the porous medium [123]. Hellstrom et al. [124] compared the pressure drop of porous medium with the bed of spheres using CFD with Ergun equation and found that pressure drop can be predicted with Ergun suggested coefficients until a moderate Re' of 20 that is based on D_p and is defined as:

$$Re' = \frac{\rho D_p \dot{G}}{\mu(1-\kappa)} \tag{9.4}$$

After this limit, CFD results with a laminar flow solver underestimated the pressure drop. In a further study [124] implemented a turbulent solver for higher Re' and found out that modeling turbulence becomes important for flows in porous media where Re' is greater than 100. By using a turbulent flow solver, their CFD results were close to the Ergun equation at higher Re'. Inertial and viscous coefficients for prediction of pressure drop in metallic foams also utilize similar formulations to that of Equation 9.2 where inertial and viscous coefficients vary from one experimental setup to another. Similarly, porous media approximation can also be extended to multiple parallel mi-

crochannels (MCs) in heat sinks. An analytical model was first developed by [125, 126] where they modeled the MCs as porous media and compared modeling results with experimental results of [127] as well as with [128]. Results showed that the developed model can be used for thermal performance and optimization of MC heat sinks. The same model has been studied by Liu and Garimella [129] and improved by Lim et al. [130]. Porous media based analytical models tend to solve a three equations model for fluid flow and heat transfer through MC heat sinks using simplified momentum and energy equations. A common trait of all the studies conducted for MC heat sinks is the use of an incompressible fluid. Moreover, a porous approximation model for a complete conjugate heat transfer analysis between hot and cold compressible fluids along with the separation wall has not been presented yet up to the best of authors' knowledge.

Micro heat exchanger studies where gas is used as a working medium on both hot and cold sides are scarce in the literature. As pressure and temperature variations in gas microflows bring significant density variations, results of heat transfer in gas to gas micro heat exchangers (μHx) can present anomalous trends when compared to conventional sized heat exchangers or liquid heat exchangers. The number of parallel channels in a μHx may vary from tens to hundreds. The fluid is distributed and collected from these MCs using manifolds whose areas can be much larger than MC area. A complete CFD conjugate model would therefore, require millions of computational elements in order to capture the hydraulic and thermal behavior of such a device. Although manifolds do not take an active role in heat transfer compared to heat exchange at MC core of a μHx, their presence does affect the flow maldistribution. This information can be crucial in order to avoid hot spots in heat sinks and heat exchangers. Fundamental experimental studies for the analysis of manifold design on maldistribution have been performed in the past [70, 80], however, those experimental settings can not be extended to study flow distribution amongst each MC of a μHx due to manufacturing and limited number of sensors constraints. This essentially necessitates researchers to investigate design performance using computational methods such as CFD. Zhuo et. al [84] recently conducted an optimization study of a double layer μHx using water as a

working fluid. They validated their numerical results with the experiment of the same device for Re of 50 to 600. For a fixed heat transfer core area, the number of parallel rectangular channels varied from $20 - 46$ based on simulated hydraulic diameter (D_h) of $1430\mu m$ to $670\mu m$ respectively. Heat exchanger effectiveness and pressure drop estimated using CFD matched well with the experimental results. Koyama and Asako [73] conducted experimental investigations on heat transfer and pressure drop of gas to gas μHx and showed the conventional NTU based theory for conventional sized heat exchangers overpredicts the effectiveness of counterflow μHx. Pressure drop was also quite high due to distributing and collecting manifolds. For cocurrent flow configuration [74], results were in accordance with the conventional theory, however. Yang et al. [82, 81] later conducted experiments on gas to gas double layer μHx with 133 parallel rectangular MCs. They found out that for both co and counterflow configurations, experimental results of heat exchanger effectiveness can be predicted using conventional NTU based method if proper effects of axial wall conduction are catered for in experimental data reduction. It was also shown by the experimental results that pressure drop in the designed collecting and distributing manifolds catered for more than 90% of the total pressure drop with a mere 10% in MCs. And therefore highlighted an efficient design of manifolds to reduce the overall pressure drop of such devices. To reduce the computational effort involved, such a design optimization can be executed with an efficient reduced model where MC core is modeled with porous media approximation and complete flow physics is modeled in the manifolds. This would allow to conduct manifold design optimization studies at a relatively less computational cost without losing the overall heat exchanger effectiveness and global pressure drop of the μHx.

In this work a two step methodology is proposed to conduct an optimization study on μHx with acceptable computational power. As a first step, a $3D$ conjugate heat transfer (CHT) model of gas to gas μHx as developed in Chapter 8 is used without distributing and collecting manifolds. Resulting pressure, velocity and temperature fields are utilized to calculate inertial and viscous coefficients of Darcy's porous law. A complete single layer of μHx with manifolds is then modeled with boundary con-

ditions such that MCs are modeled as a porous medium with a low resolution mesh. This is achieved by modeling the required pressure drop as a momentum source term using inertial and viscous coefficients of the porous medium. Similarly to incorporate heat transfer in MCs core, a source term derived by CHT analysis of MCs only, is also introduced. As seen by the literature review of the recent developments, though analytical studies to model heat sinks as porous media exist, no methodology to calculate porous medium coefficients for a μHx can be found in the literature. Moreover as highlighted by many researchers, these coefficients may need to be updated with fluid velocity (mass flow) in order to correctly predict the pressure and temperature difference from inlet to the outlet of MCs. For this reason, a novel methodology to calculate inertial and viscous coefficients to model μHx as a porous medium from $3D$ CHT model is adopted in the current study. Furthermore, if coefficients are extracted directly by comparing numerical results of pressure drop with Darcy's law, they would not suffice due to the strong compressibility effects of gas flow through MCs. Therefore, a modified formulation of Darcy's law is adopted where inertial and viscous coefficients are obtained by integrating original Darcy's law along the length of the MC by considering density variations. This will give an integral average of these coefficients along the length of MC by incorporating density variations due to pressure and temperature drops.

9.3 Determination of Porous Media Coefficients

Therefore, integrating Equation 9.2 in the streamwise direction 'x' of the MC

$$\int_{in}^{out} \frac{-\Delta p}{L} dx = \frac{\mu \dot{G}}{\alpha} \int_{in}^{out} \frac{dx}{\rho} + \frac{\Gamma \dot{G}^2}{2} \int_{in}^{out} \frac{dx}{\rho} \tag{9.5}$$

Combining gas law and a first order Taylor approximation of temperature change along the length of the MC, gas law can be rewritten in differential form as:

$$dp = RT\left[d\rho + \frac{\rho dx}{L}\right] \tag{9.6}$$

For a compressible fluid pressure and density can be used to define local speed of sound (a) as:

$$a = \sqrt{\frac{dp}{d\rho}} \tag{9.7}$$

Combining Equations 9.6 and 9.7 and utilizing ratio of specific heats (γ) yields following to relate dx with density of the flow:

$$dx = \frac{\gamma L}{\gamma - 1} RT \frac{d\rho}{\rho} \tag{9.8}$$

Substituting Equation 9.8 in Equation 9.5 and integrating between inlet 'in' and outlet 'out' of the MC results in:

$$\frac{-\Delta p}{L} = \mu\xi\dot{G}\left(\frac{1}{\alpha}\right) + \frac{\xi\dot{G}^2}{2}\left(\Gamma\right) \tag{9.9}$$

where $\xi = \frac{1}{\ln\left(\frac{\rho_{out}}{\rho_{in}}\right)}\left(\frac{1}{\rho_{in}} - \frac{1}{\rho_{out}}\right)$. Boundary conditions of CHT analysis are chosen such that there are no heat losses to the surroundings, therefore all the heat lost by hot fluid must be shared between partition foil (solid wall) and cold fluid. This is generally valid for incompressible fluids. Therefore porous medium coefficients can be extracted from either side of the CHT model. In this work, inertial and viscous coefficients are extracted from the channel with hot fluid. Starting from Equation 9.9, the methodology followed for the calculation of these coefficients is as follows:

1. Define 'n' number of steps between lower to maximum mass flow for which $3D$ CHT analysis is performed.

2. Continuous polynomial functions based on mass flow for density variations at the

inlet and outlet of MC (hot side of CHT), as well as total pressure drop (Δp) are developed using CHT results. These functions are evaluated at the 'n' number of mass flows defined in step 1. Similarly, a polynomial fit to MC viscosity (μ) is also used at the inlet of the MC. Care is taken to fit a polynomial of such order that R^2 is close to 1 for all available simulated data points.

3. From a CHT analysis of MCs only, all parameters in the Equation 9.9 are made available for a specific mass flow using steps 1-3, with inertial and viscous coefficients as the only two unknowns. However, if Equation 9.9 is applied to two consecutive mass flows $\dot{m}_i$ and $\dot{m}_{i+1}$, an average value of these coefficients between i and $i+1$ can be found out by solving a system of two linear equations for two unknowns.

4. Step 3 is repeated for all the mass flows defined in step 1. This gives $n-1$ average values of inertial and viscous coefficients by solving one equation for every pair of mass flows between the first and last value of mass flows defined in step 1. A simple polynomial function can be fitted afterward on these average porous medium coefficients. This will define the variation of these coefficients with the mass flow of the fluid.

5. Similarly a volumetric heat loss of hot fluid channel is calculated for all mass flows from CHT analysis using $\dot{q_v} = \frac{\dot{m}C_p\Delta T}{AL}$, where C_p is the specific heat of fluid at constant pressure, A and L represent the cross sectional area and length of the MC respectively. A polynomial fit is used onto the CHT analysis results for evaluation of resulting polynomial at all the mass flows defined in step 1. This volumetric heat loss is modeled as a source term in energy equation while solving for the porous medium approximation of MC core of μHx.

9.4 Numerical Strategy

As described earlier, two different numerical setups are used in the current work. First, a $3D$ CHT of MCs only, without distributing and collecting manifolds is performed. And using the results from CHT model, the performance of a complete heat exchanger with manifolds is analyzed subsequently.

Parameter to quantify mass flow maldistribution from Porous model results, is defined as:

$$\dot{m}_{dev} = \left(\frac{\dot{m}_i - \dot{m}_{ideal}}{\dot{m}_{ideal}} \right) \times 100 \tag{9.10}$$

where m_i denotes the mass flow through i^{th} MC out of total (N) MCs. Ideal mass flow rate ($\dot{m}_{ideal}$) can be calculated using experimental mass flow rate ($\dot{m}_{exp}$) as follows:

$$\dot{m}_{ideal} = \frac{\dot{m}_{exp}}{N} \tag{9.11}$$

For porous model of μHx, heat exchanger effectiveness to be compared with experimental results is calculated for the MC core only. This essentially means that temperature difference from the inlet of MC core to outlet of MC core is used to calculate ε. Moreover, as only one layer is computationally modeled in porous model, resulting effectiveness is calculated as follows:

$$\varepsilon_p = \frac{Q_p}{(\dot{m}C_p)_p (T_{h,in} - T_{c,in})} = \frac{\overline{T}_{MC,in} - \overline{T}_{MC,out}}{T_{h,in} - T_{c,in}} \tag{9.12}$$

where subscript 'p' denotes the porous model. $\overline{T}_{MC,in}$ & $\overline{T}_{MC,out}$ denote the mass flow weighted averages of static temperatures, at the inlet and outlet of N number of MCs, respectively.

Table 9.1: μHx geometry used for simulations.

Parameter	**Symbol (units)**	**Value**
MC width	w (μm)	200
MC height	h (μm)	200
MC Length	L (μm)	40
Hydraulic Diameter	D_h (μm)	200
Wall Thickness	t_w (μm)	100
MC housing (PMMA) conductivity	k_{MC} $(W/m/K)$	0.25
Partition Foil (Stainless Steel) thickness	δ (μm)	100
Partition Foil conductivity	k_{PF} $(W/m/K)$	15

9.4.1 Conjugate Heat Transfer (CHT) Model

In order to extract inertial and viscous coefficients for the porous medium using methodology outlined earlier, a $3D$ CHT model as outlined in Section 8.2.2.

MC geometry based on experimented μHx is utilized for both CHT as well as porous model analyses. Simulation relevant parameters are detailed in Table 9.1. To estimate the global as well as local evolution of flow variables with inlet mass flow, six different cross-sectional planes are defined at x/L of 0.005, 0.1, 0.5, 0.9, 0.95 and 0.995 respectively. In addition, two planes defined at x/L of 0.0001 and 0.9995 are treated as the inlet and outlet of MC, respectively. Results from these planes for both hot and cold fluid sides are further post processed in MATLAB to deduce required flow quantities. Thermal effectiveness is then simply evaluated using Equation 8.6.

9.4.2 Porous Model

Once the porous medium coefficients namely inertial (Γ) and viscous ($\frac{1}{\alpha}$) are determined using CHT model of a double layer μHx, next step is to setup a complete single layer porous model with inlet and outlet manifolds. A gas to gas double layer μHx that has been experimentally investigated previously by Yang et al. [82, 81] and Gerken et al. [83], is used for validation of proposed methodology. Fabricated μHx is shown in Figure 9.1 along with a zoomed view on a single layer of the device showing 133 parallel MCs

and distributing as well as collecting manifold. To enhance the structural rigidity of the partition foil, numerous circular pillars were added to the manifolds. Pressure and temperature are measured before the inlet and outlet manifolds for both hot and cold fluids. Additionally, sensors were placed inside the manifolds to evaluate the thermal and hydraulic performance of MCs core only. Further details of experimental setup and analysis can be found in [81, 83].

Similar to that of CHT of MCs only, geometry modeling and meshing for single layer of μHx is also performed in ANSYS Design Modeler and Meshing respectively. Sweep mapped meshing is used for the manifolds. As in fabricated device, the height of distributing and collecting manifolds (H_{man}) is kept equal to the height of the MC (h). A total number of 15 elements in the direction normal to the flow, are employed in the manifolds. Mesh close to the walls is locally refined with an expansion ratio of 1.1 to capture the boundary layer physics inside the manifolds as shown in Figure 9.2a. A total of 10 inflation layers with a growth rate of 1.09 are employed at the walls of circular pillars inside both manifolds. Inlet and outlet manifolds are extended $H_r = 5mm$ in the normal direction to simulate the metallic piping that is used to connect the experimented device with test rig as shown in Figure 9.1b. As the initial goal is to reduce the computational cost to simulate a thermo-hydraulic performance of a μHx, MCs though modeled individually but are meshed with sweep method using $3 \times 3 \times 40$ divisions. This results in a saving of 10 million node points compared to the case if all 133 MCs were to be meshed as in the CHT model earlier. On the contrary, to estimate better the flow maldistribution it is essential to have a higher number of grid points at the inlets of individual MCs. Therefore a small section of length $2.5D_h$ at the inlet and outlet of MCs is used as a joining zone with free mesh. This allows to have fine mesh at the inlet and outlet of MCs while a rough and coarse mesh elsewhere. This has been detailed in Figure 9.2b.

Due to bigger characteristic dimensions of the manifolds, gas flow inside the manifolds may reach turbulent Re even though it is laminar in individual MCs. Therefore $\gamma - Re_\theta$

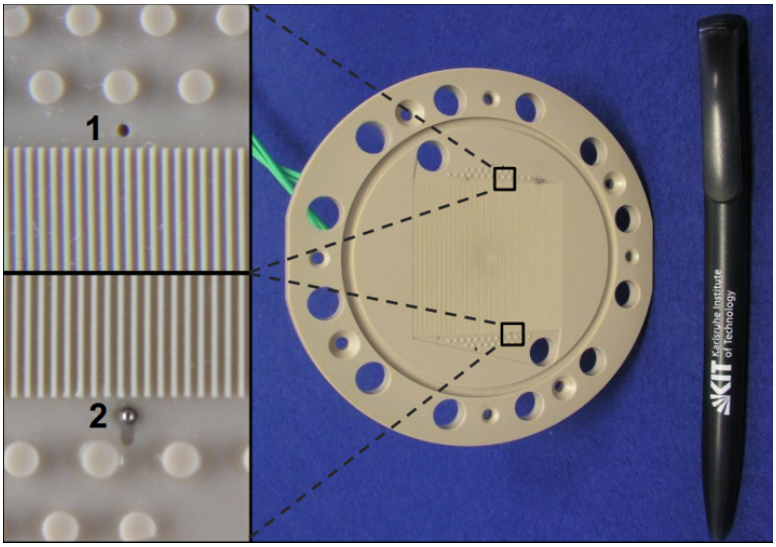

(a)

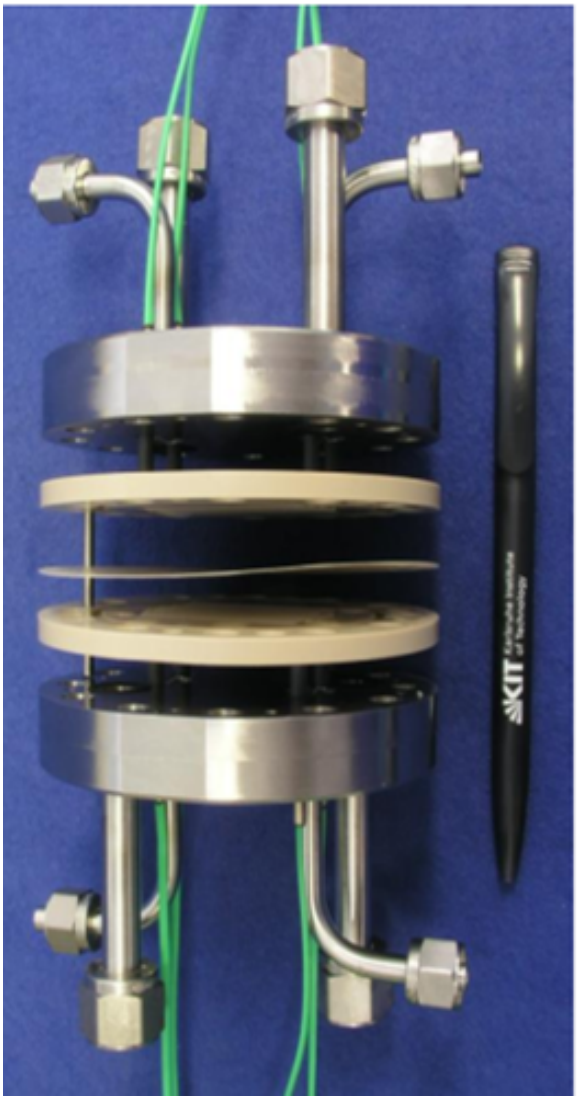

(b)

Figure 9.1: Single layer of experimented μHx (**a**), and nd complete fabricated device (**b**).

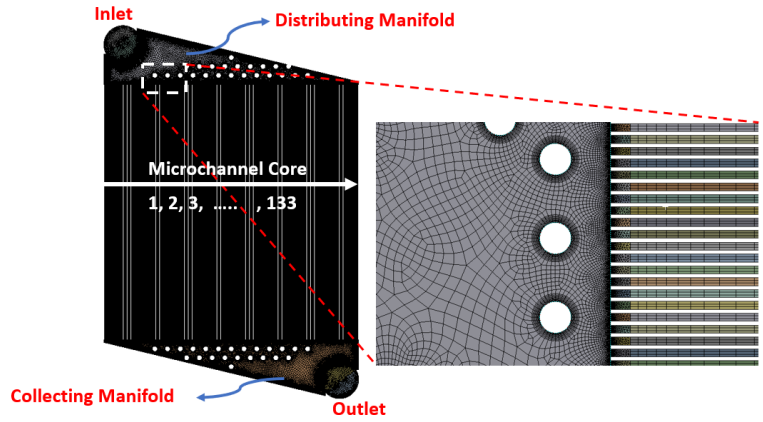

(a)

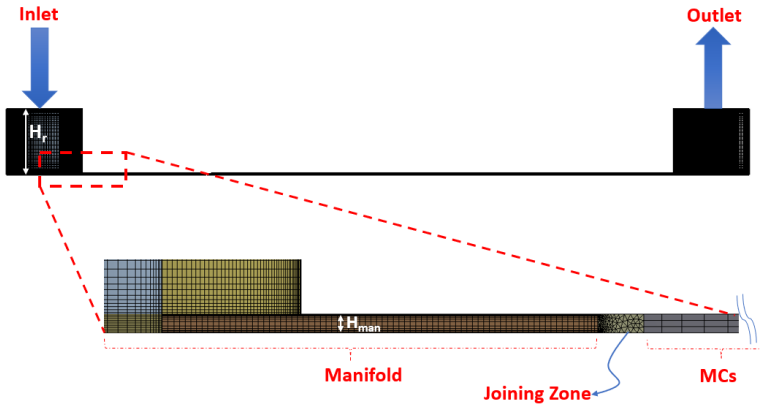

(b)

Figure 9.2: Geometry and mesh details of porous model: top view (**a**), and side view (**b**).

transition turbulence model is used as it has been proven to be able to simulate laminar, transitional and turbulent flows inside MCs [118]. Coefficients of this transitional turbulence model are modified, as recommended by Abraham et al. [1]. High turbulence numerics along with higher order convection scheme is utilized. Convergence criteria are kept the same as for the CHT model where flow variables at inlet and outlet of the porous model are monitored for minimum 500 iterations and the solution is deemed converged if monitor points did not show significant variation for 200 consecutive iterations.

Compared to MCs core, heat transfer in the manifolds is usually small and therefore for the porous model, walls of both manifolds are assumed to be adiabatic. Computational domains of both manifolds are treated as continuous fluids i.e. ideal Nitrogen case in

this case. On the contrary, MCs core is modeled as the porous medium. Polynomials for inertial and viscous coefficients derived from the CHT model are used as input to model the pressure drop. On the other hand, the temperature drop in MCs core due to the heat transfer is modeled as a source term in the energy equation of the porous domain. This volumetric heat source is evaluated as outlined in step 5 of Section 9.3. It is reminded to the reader that all through the development of porous media coefficients using CHT model, flow quantities of the MC from the hot fluid side are utilized. Therefore this resulted in a negative heat source term (sink) as the temperature of the hot fluid is decreased along the length of the MC due to the heat transfer with cold fluid and axial conduction in the wall and the fluid. The source term would be positive if MC with the cold fluid of CHT model would be utilized for the analysis. To analyze the overall thermal performance of whole μHx using porous model, net heat gain (cold side) or heat loss (hot side) can be modeled in a single layer of μHx without the need of further computational domains to model additional layers, again saving millions of computational node points. For the current case, as the comparison will be made with a double layer μHx, only one layer in the porous model would suffice the overall pressure drop and thermal performance of both layers. Furthermore, as the pressure drop in MCs core is modeled using inertial and viscous coefficients, walls of MCs in the porous model are therefore given a free slip boundary condition. This avoids modeling of any additional pressure drop due to friction inside MCs. Ideal Nitrogen gas is allowed to enter the computational domain through the inlet which is orthogonal to the MCs core. It is then distributed amongst the MCs in distributing manifold. Finally, after passing through the porous medium MCs, gas is collected in collecting manifold which vents it to the atmosphere in the orthogonal direction. Boundary conditions for porous model are summarized in Table 9.2.

Table 9.2: Boundary conditions used in the porous model for μHx.

Boundary	Value
Inlet	- $\dot{m}$ from experimental testing - $T_{h,in} = 90°C$
MCs walls	Free slip
Inertial and visocus coefficients	Determined from CHT analysis
Energy source term	Determined from CHT analysis
Manifolds walls	Adiabatic/ No slip
Outlet	Pressure outlet, Relative p = 0 Pa

9.5 Validation

9.5.1 CHT Model

CHT model with linear periodicity at side walls represents the ideal situation where there exist no maldistribution for parallel MCs. This essentially means, that all parallel MCs would have the same mass flow at their respective inlets and manifold does not play a significant role. Results for the heat transfer rate for both cocurrent and counterflow configurations are shown in Figure 9.3. For an incompressible fluid, the heat transfer rate using a numerical model on both sides should be equal. But for gases, as the gas flow experiences additional acceleration due to compressibility, heat gain on the cold side tends to differ from heat loss on the hot side. An interesting fact is that heat transfer rate on the hot side keeps on increasing with increasing mass flow. On the contrary, it keeps on decreasing on the cold side. This holds true for both cocurrent and counterflow configurations. Therefore even though there are no losses modeled to the surroundings, due to compressibility gas flows still exhibit a difference in heat transfer rate between hot and cold sides if calculated with inlet and outlet temperatures. This has already been explained in Chapter 8 while discussing the effect of the compressibility on the thermal performance of the experimented μHx.

Similar behavior can also be seen in the effectiveness where it increases with the mass flow for hot fluid and decreases for the cold fluid as shown in Figure 9.5. This is simply because gas flow accelerates at the expense of kinetic energy, therefore a part of total

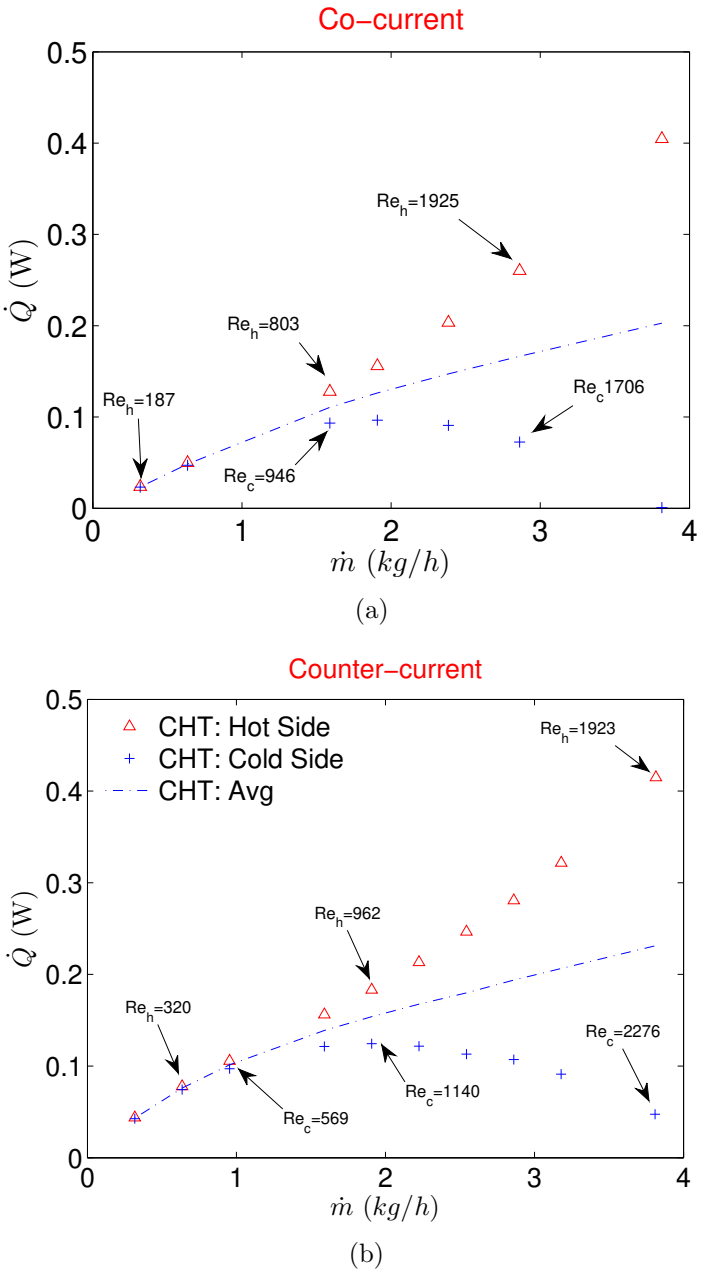

Figure 9.3: Heat transfer rate for CHT analysis when flow configuration is cocurrent (**a**), and counterflow (**b**).

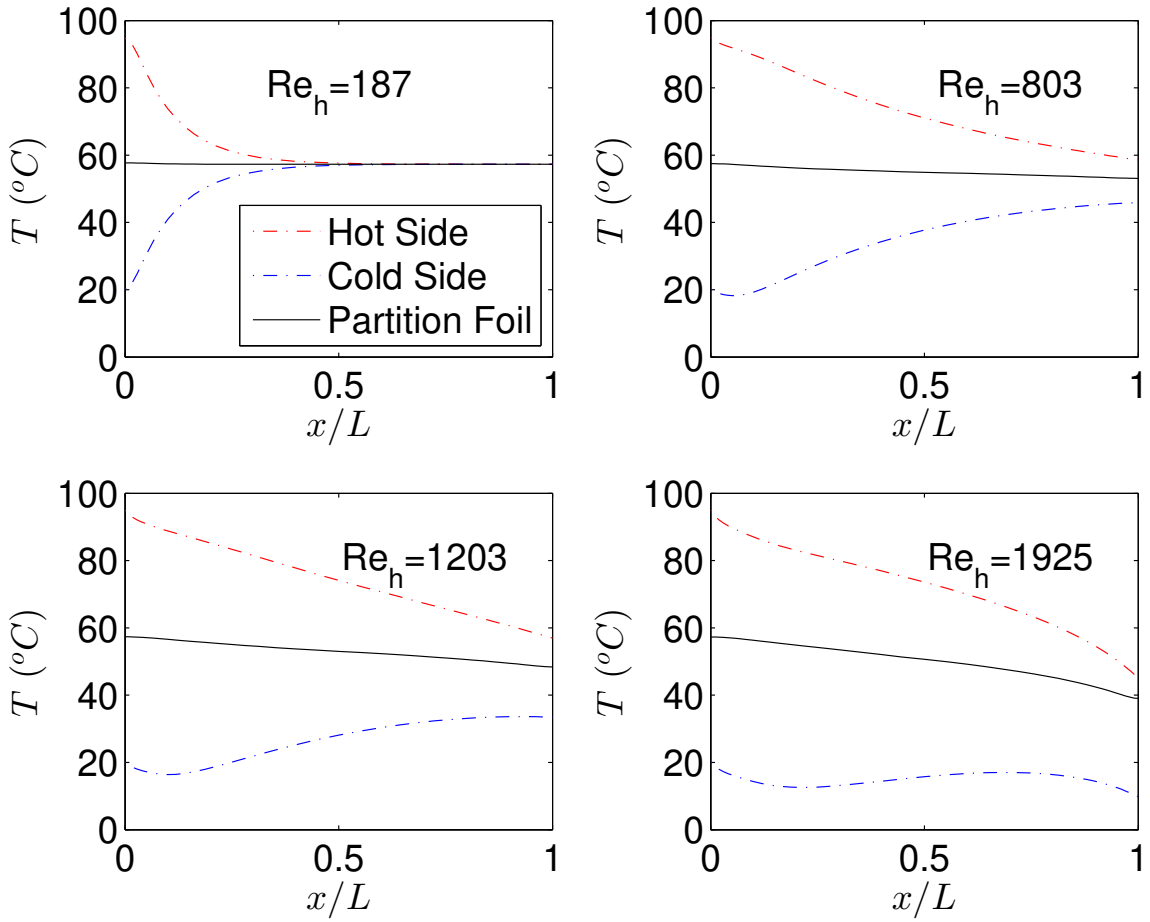

Figure 9.4: Temperature along the length of the hot and cold MCs for various Re in cocurrent flow configuration

energy is utilized for gas acceleration than to have a sensible heat transfer between the two fluids. Therefore for gas to gas μHxs, it is not recommended to operate in high mass flow regimes because at higher mass flows, gas flows experience a "self cooling" phenomenon at the expense of pressure head. This phenomenon is evident in Figure 9.4 which shows the evolution of the temperature at the centerline of both fluid streams and partition foil (solid) along the direction of the flow. For smaller mass flows (Re) temperature profiles of hot and cold streams follow the typical trend well known for incompressible fluids in cocurrent flow configuration where the temperature of hot and cold fluids are symmetric and partition foil assumes an average constant temperature of the two sides. As fluid velocities increase at the inlets of respective streams, profile symmetry deteriorates with partition foil assuming a temperature that is more influenced by the hot side than the cold fluid side. The outlet temperature of the hot fluid keeps on decreasing with an increased mass flow rate signaling a better heat transfer process. On the contrary, if one is to look at the outlet temperature of the cold fluid, it also keeps on decreasing significantly than the inlet with increasing mass flow rates. This signifies that cold fluid stream is utilizing the transferred thermal energy from the hot stream, only to increase the velocity (kinetic energy). It is well known that gas microflows, due to compressible nature accelerate at the expense of thermal energy of the fluid [72, 75, 38]. Similarly, a higher decrease of temperature and pressure very close to the outlet of the MC for the hot fluid stream is also due to the sudden expansion of the gas due to compressibility. In the result of this strong compressibility effect, gases in both fluid streams are actually utilizing respective thermal energies and converting them in kinetic energy which is deteriorating to the overall heat transfer process. Temperature decrease of the cold stream is such that static temperature at the outlet is even lower than the inlet static temperature, showing no active participation of cold fluid stream into the overall heat exchange of the device, at higher mass flow rates. This also explains the decrease of $\dot{Q}$ in Figure 9.3 on the cold side of the μHx and a continuous increase of $\dot{Q}$ on the hot side with increasing mass flow rates.

For data reduction of the most experimental investigations, an average value of $\dot{Q}$ is

used to calculate the overall heat transfer coefficient (U) to further evaluate the heat exchanger effectiveness (ε). This is done due to the practical limitation of the heat losses to the surroundings in the laboratory environment from both streams. A similar approach has been used by Yang et al. [2, 82, 81] and Koyama et al. [74, 73] for gas to gas μHxs. There are heat losses to the surroundings in a typical experimental campaign but as shown in this work, the real reason for the deviation of $\dot{Q}$ on hot and cold fluid streams in gas to gas μHx is due to the compressibility effects. However, in order to be consistent with experimental data reduction of the experimental results, numerical results of ε are also calculated with an average $\dot{Q}_{ave}$ from CHT analysis and are compared with experimental results of Yang et al. [81] in Figure 9.5. For a cocurrent configuration, a CHT analysis overestimates the average ε as compared to experimental results for all the mass flows considered in this study. Difference between the two decreases though at higher mass flow rates. On the contrary ε for counterflow configuration is underestimated by CHT analysis for the complete range of mass flows investigated. Such discrepancies between experimental results of μHx and an equivalent CHT analysis with periodic boundary conditions are expected as CHT model used in this study is devoid of flow maldistribution effects. Also, any temperature change that might occur in the manifolds due to flow deceleration caused by the presence of numerous circular pillars in distributing and collecting manifolds, is not catered for.

A further step is to evaluate the inertial and viscous coefficients of the modified Darcy's law using flow quantities evaluated in CHT analysis. For this reason, flow characteristics are extracted at various planes along the length of the hot and cold fluid MCs. These are used to form a set of linear system of equations to solve for porous medium coefficients utilizing the methodology outlined in Section 9.1. The solution of this system of equations for various mass flow rates results in data points where a polynomial with mass flow rate as a dependent variable can be fit to be given as input to the porous medium model available in ANSYS CFX®. In theory, pressure drop from the hot side and cold side should be almost similar and furthermore, it should be independent of the flow configuration. Therefore any side of the fluid stream (hot or cold) from

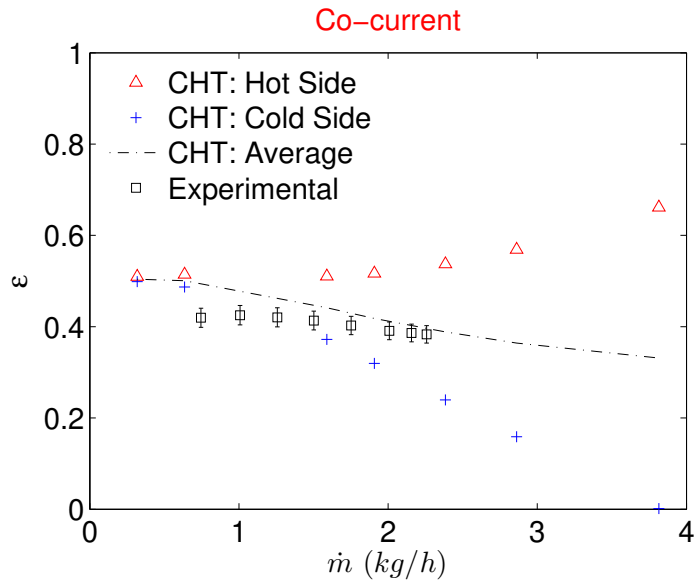

(a)

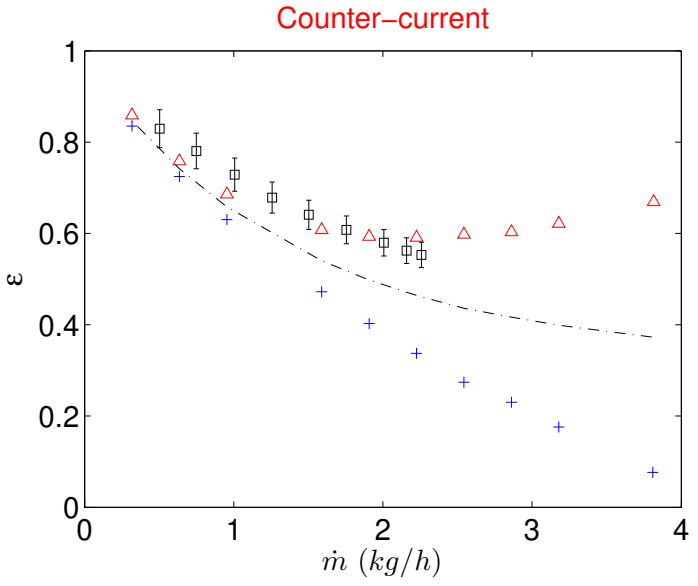

(b)

Figure 9.5: Heat exchanger effectiveness for CHT analysis when flow configuration is cocurrent (**a**), and counterflow (**b**).

CHT analysis can be used to evaluate porous medium coefficients. For the scope of this work, the hot fluid side is used to evaluate porous medium coefficients. Resulting viscous and inertial coefficients are shown in Figures 9.6 and 9.7 respectively for both cocurrent and counterflow configurations.

To model the desired temperature drop on the hot fluid side, a source term q_v is extracted from the hot fluid stream of CHT analysis. Variation of this volumetric heat source term with the mass flow rate is shown in Figure 9.8. A polynomial fit on this q_v is given as a source term to the energy equation in CFX.

9.5.2 Porous Model

The presence of manifolds introduces flow maldistribution that affects both pressure drop as well as heat exchanger effectiveness of a μHx compared to earlier performed CHT analysis. A single layer of a double layer μHx shown in Figure 9.1 is modeled in the porous model. This is due to the fact, that pressure and temperature drops of hot side from CHT analyses that are used to extract porous medium coefficients and source term respectively, already catered for heat transfer effects of both layers. Therefore modeling only one layer with these coefficients and source term should be sufficient to emulate a double layer μHx. However, it is reminded that for unbalanced flows, the effect of heat transfer rate will be different than for the balanced flow as in the current case. Therefore new source term for the temperature gain/drop has to be evaluated from the respective CHT analysis. Moreover, as porous media coefficients as well as source term are mass flow rate dependent, based upon encountered maldistribution each MC will exhibit respective pressure and temperature drop along the length.

The experimental pressure drop of the double layer μHx being considered in this study for different flow configurations has been reported by Gerken et al. [83]. Resulting pressure drop showed dependence on the flow configuration as well as the material and thickness of the partition foil employed during the experimental tests. A possible

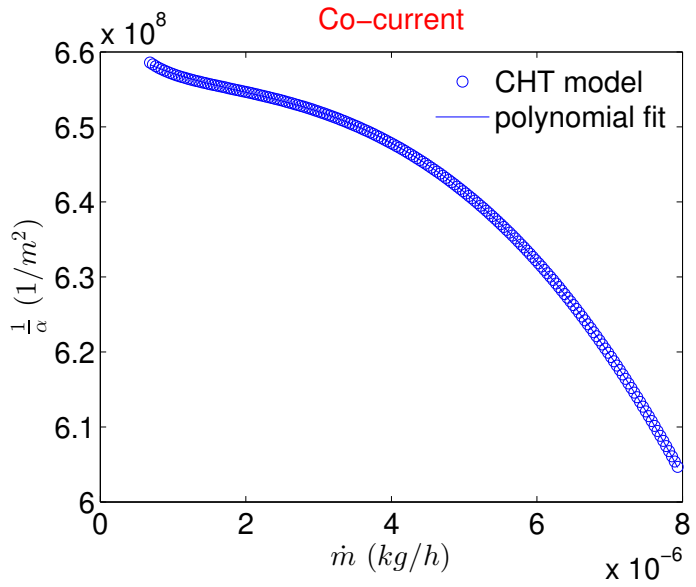

(a)

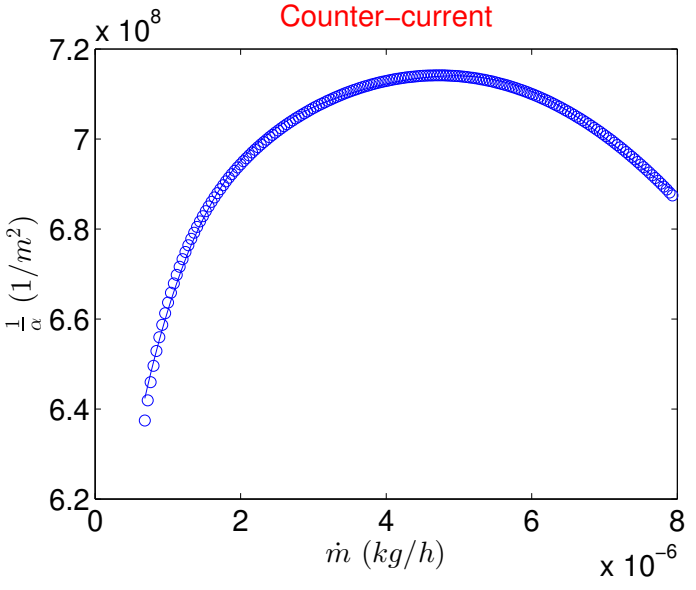

(b)

Figure 9.6: Viscous coefficient when flow configuration is cocurrent (**a**), and counterflow (**b**).

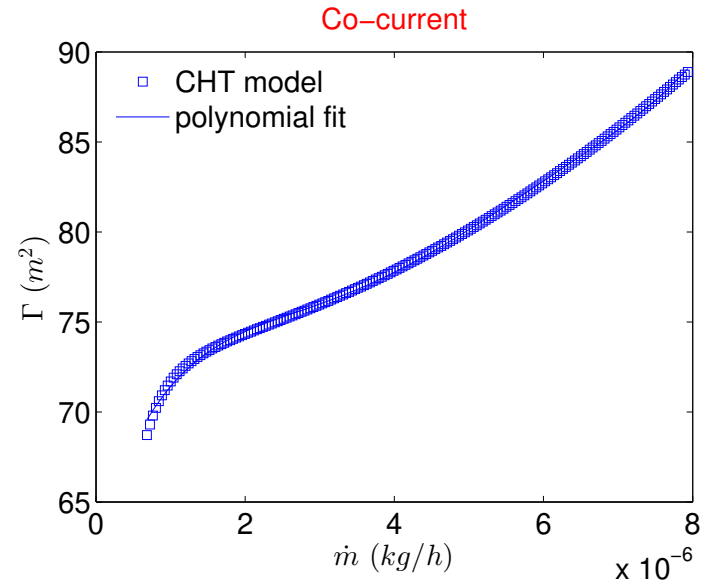

(a)

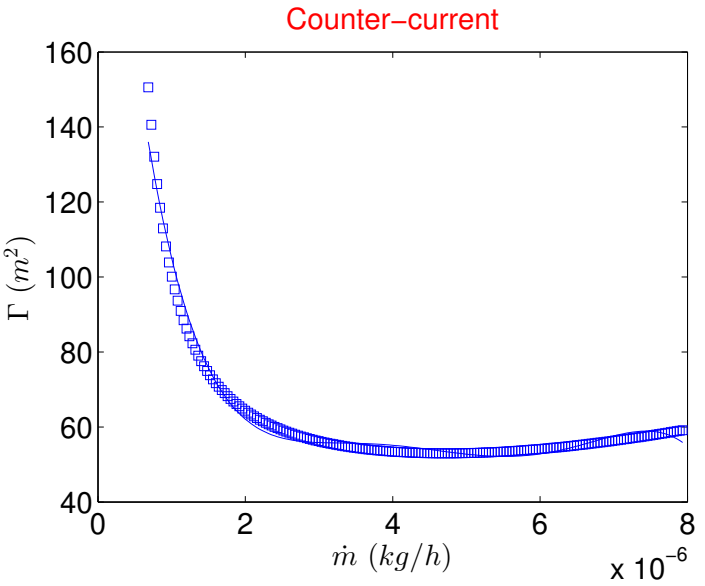

(b)

Figure 9.7: Inertial coefficient when flow configuration is cocurrent (**a**), and counterflow (**b**).

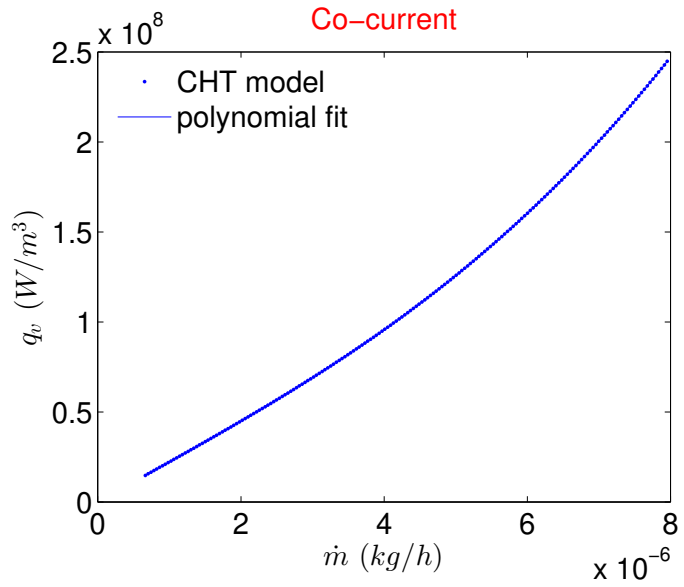

(a)

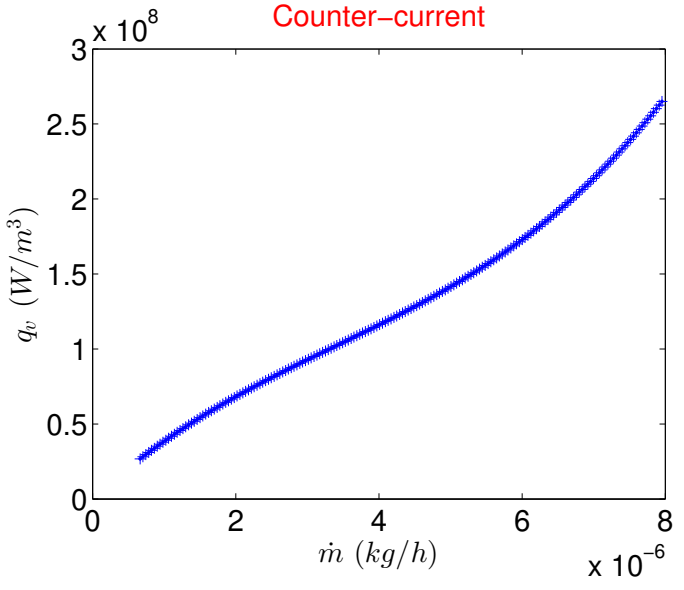

(b)

Figure 9.8: Volumetric heat source term when flow configuration is cocurrent (**a**), and counterflow (**b**).

reason for this deviation between different foil materials and thicknesses was associated with possible bending of the thin partition foils inside manifolds although a strong layer of circular pillars was placed underneath to protect against such undesired deflection of partition foil. Computational results of pressure drop from the porous model are compared with the experimental results reported for the same μHx from two different studies [81, 83]. As results differ from one separation foil material to the other, only results with stainless steel foil with a thickness of 100 μm (as utilized in the current study) are compared and are shown in Figure 9.9a. It can be seen that the total pressure drop of the device shows a good agreement between the average of two experimental investigations on the same μHx. Results are more compliant with the results of Yang et al. [81] for smaller mass flows while they match better with Gerken et al. [83] for higher mass flow rates. Pressure drops in the distributing manifold and MC core are also shown in Figure 9.9b where there exists a very good match between the current porous model and experimental results of Gerken et al. [83]. However, the pressure drop of MC core is slightly overestimated at higher mass flow rates with modeled porous medium coefficients with incorporated source term in the energy equation. This slight variation could also be due to the fact that porous medium coefficients are derived by assuming MC length of 40 mm, however, porous medium is applied to 39 mm of the length only, utilizing the rest 1 mm in the joining zone for better meshing at the inlet and outlet of MC as explained in Section 9.4.2.

Flow maldistribution is shown in Figure 9.10 for both cocurrent and counterflow configurations where MC indexing is done as outlined in Figure 9.2a. As expected, maldistribution shows a weak dependence on the flow configuration where except for the furthest MCs from the inlet, it shows similar patterns in both flow configurations. However, due to the presence of circular pillars, maldistribution does not exhibit a typical profile to be expected of triangular manifolds [117, 131]. Another reason for this could be the orthogonal direction of the inlet with reference to the channel flow whereas in most experimental as well as numerical studies, an inline flow is encountered where fluid enters parallel to the base plane of distributing manifold.

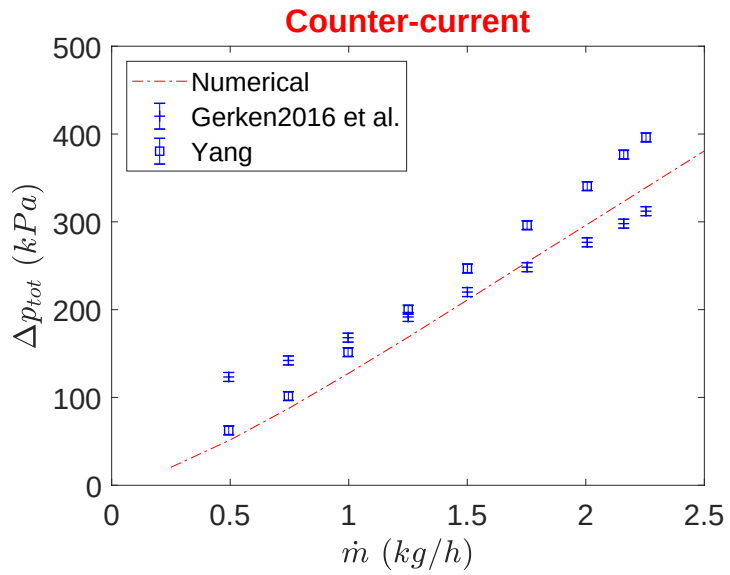

(a)

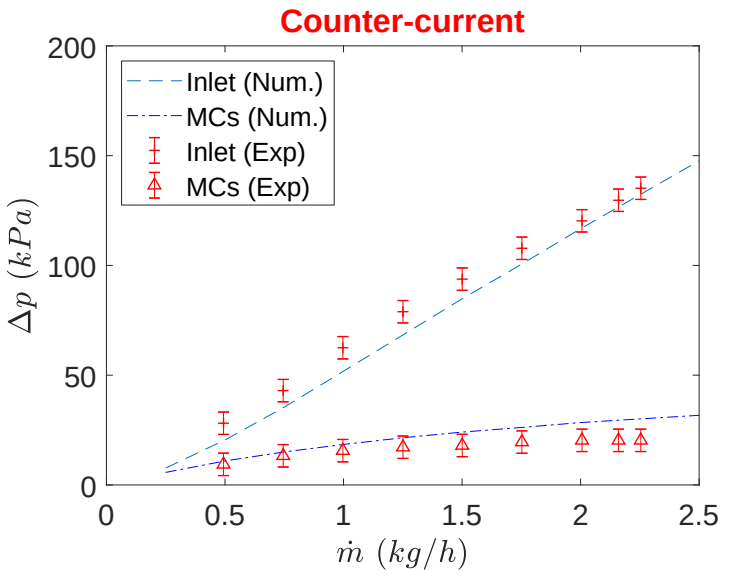

(b)

Figure 9.9: Comparison between experimental and numerical total pressure drop of μHx (**a**), and in the inlet and MCs only (**b**).

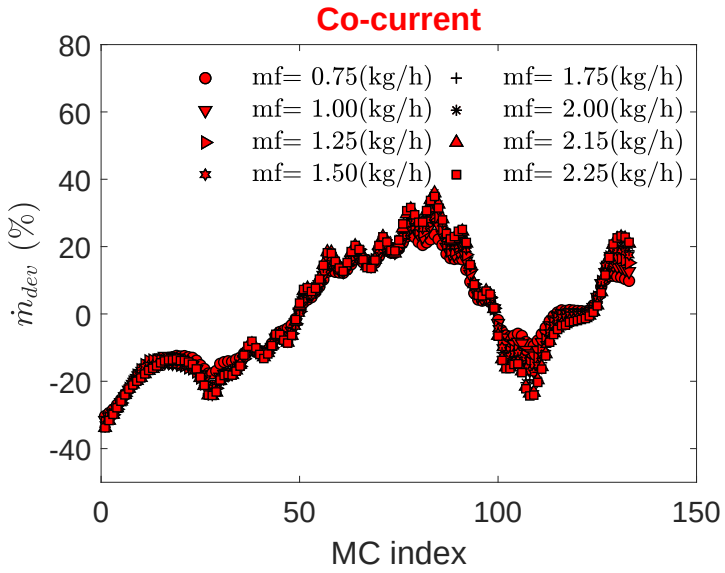

(a)

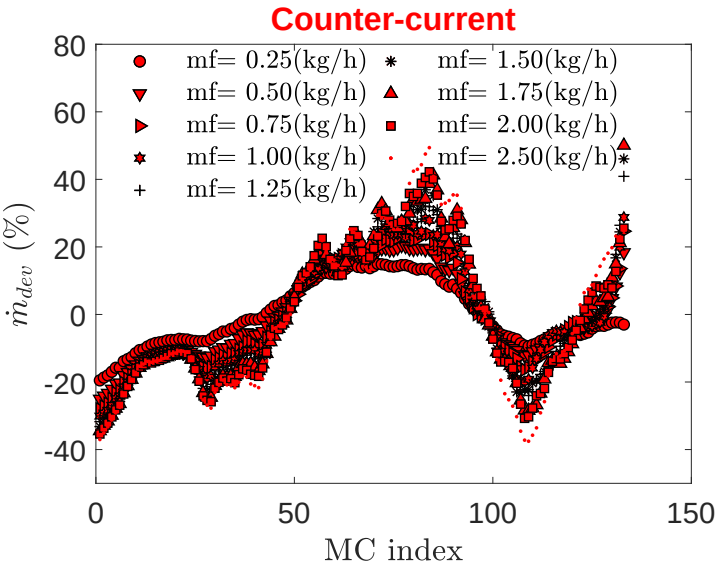

(b)

Figure 9.10: Flow maldistribution in MCs for cocurrent flow (**a**), and counterflow (**b**).

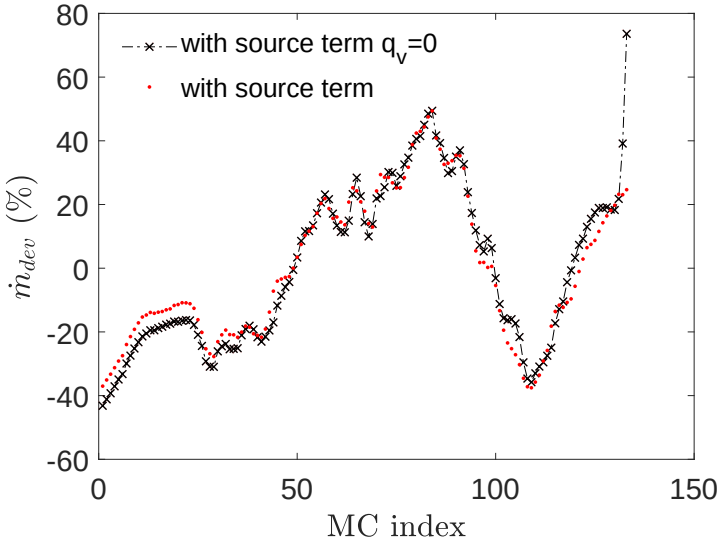

Figure 9.11: Flow maldistribution with (a) and without (b) source term q_v for counterflow configuration with $\dot{m}_f = 2.5\ kg/s$

To compare the effect of heat transfer on the flow maldistribution, counterflow porous model results are calculated at a mass flow rate of 2.5 kg/s by deactivating the energy source term and results are shown in Figure 9.11. It is evident that temperature drop does not substantially affect the maldistribution pattern in the middle core of the current manifold while it is higher on either extreme for the case when the source term is not modeled. In other words, for current configuration heat transfer helps to decrease the maldistribution in first and last MCs.

Heat exchanger effectiveness evaluated using Equation 9.12 is shown in Figure 9.12 for both flow configurations. In the experimental campaign, one pressure and two temperature sensors were placed 0.4 mm from the inlet and outlet of the MCs core to represent an average value of pressure drop and temperature drop or gain through the hot or cold side of MCs core. For a cocurrent configuration, porous model predictions match to the experimental results within the experimental uncertainty. However, for the counterflow configuration, the results of the porous model seem to underestimate the ε compared to experimental results. To investigate this discrepancy, average fluid temperatures at two planes of $0.5\ mm \times 0.5\ mm$ are used in the vicinity of the locations where experimental temperature sensors were placed. The average temperature of the

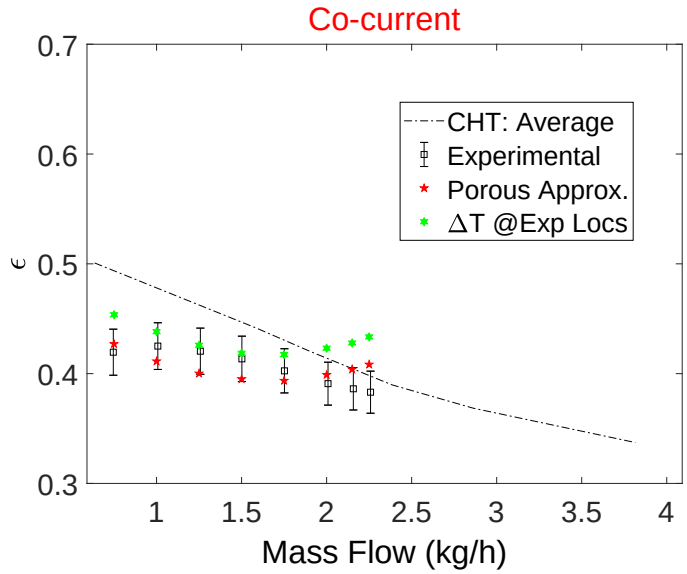

(a)

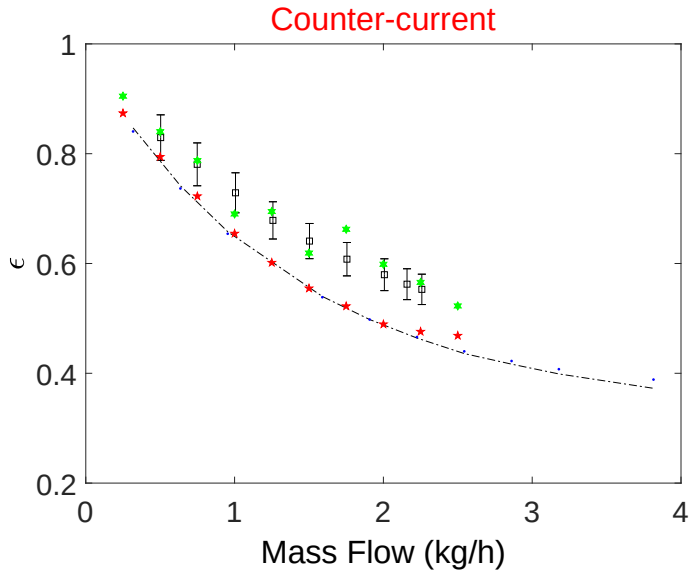

(b)

Figure 9.12: μHx effectiveness for cocurrent flow (**a**), and counterflow (**b**).

gas is then calculated using a simple equal weighted average of these two temperatures as done in the experimental campaign. Therefore, as it can be seen in Figure 9.12b when temperature estimation at the inlet and outlet of MCs core is done in a way that is close to experimental settings, it resulted in a higher temperature drop which translated into an apparent increase in ε. However when mass flow weighted averages of temperatures at inlet and outlet of MC core are considered from numerical simulations, resulting ε is slightly lower than what has been reported for experimental tests. On the other hand, a limited number of sensors are practical limitations inside micro devices therefore, averaging performed using a limited number of temperature and pressure sensors would always result in a slight discrepancy between experimental and numerical global characteristics of the μHxs. Results of ε from the porous model are also compared with the CHT analysis. It can be noted from Figure 9.12b that porous model with all the flow maldistribution results in an overall heat exchanging efficiency that is identical to that of a simple CHT model without manifolds, for the counterflow configuration. A similar conclusion was also presented by Joseph et al. [132, 117] where CHT analysis with periodic side walls for a 60 layered counterflow compact heat exchanger showed only 4 % deviation in ε compared to experimental results. This points to the fact, it is sufficient to use a CHT model to predict the thermal effectiveness of a multilayered parallel channel counterflow μHx. Pressure drop analysis of the entire device, however, cannot be performed using only CHT analysis as there is a significant pressure drop in the distributing and collecting manifolds. On the contrary, ε results for the cocurrent configuration show a dependence on the maldistribution where the porous model and experimental results are different than CHT model with CHT model overestimating the ε when compared to the porous model.

Independent of the flow configurations studied in this study, the developed porous medium based numerical model shows an excellent match with experimental results for both flow configurations. Moreover, as flow inside porous MCs is not treated as wall bounded rather a free slip boundary condition is applied, a substantial amount of computational power is saved in the process. Also, proposed porous medium model

requires only one layer of μHx, with MCs core modeled as porous medium, it eliminates the need of simulating all the layers of such microdevice where a layered structure is quite common and an effort to computationally model such device with all the layers would require a staggering computational power. Therefore the proposed model for the analysis of parallel channel μHx can prove to be a feasible option for rapid design optimization in engineering studies.

9.6 Summary

Based on the discussion conducted earlier, the following conclusions can be inferred:

1. Porous medium coefficients for parallel channel μHx can be extracted for compressible fluids by modifying the existing Darcy-Forchheimer law to incorporate for the strong density variations with increasing mass flow rates in MCs.

2. CHT analysis revealed that gas in both hot and cold fluid streams experiences a "self-cooling" phenomenon where the temperature of the gases keeps on decreasing from inlet to the outlet at higher mass flow rates (Re). Therefore for a μHx operating under balanced mass flow rates, smaller values of mass flow rates are recommended.

3. Pressure drop of the porous model is much higher compared to the CHT due to the presence of collecting and dividing manifolds. Pressure drop estimation using the porous model is in good agreement with the experimental results of the same μHx.

4. Overall heat exchanger effectiveness of a μHx in a counterflow configuration is identical to that of the CHT analysis on the range of mass flows investigated in this study. For a cocurrent configuration, however, heat exchanger effectiveness from porous model matches well with experimental results while CHT model overpredicts it.

5. Compared to the meshing strategy adopted in CHT analysis, the porous model results in saving of at least 20 million computational nodes for the double layer gas to gas μHx investigated in this study with good enough predictions of global pressure drop and heat exchanger effectiveness.

Chapter 10

Conclusions and Future Work

10.1 Conclusions

In this thesis an attempt has been made to further the current understanding of the flow behaviour and heat transfer characteristics of gas flows inside microchannels and micro heat exchangers. Flow physics and heat transfer mechanisms for microscale liquid flows have been dealt in detail in the literature but there is a limited understanding of gas heat exchanging systems at such scale. If one is to summarize the reviewed literature it becomes evident that using gas microflows a considerable attention has been paid to the frictional characteristics in the recent decade but still a handful of studies dealt with the heat transfer of compressible fluids. Moreover those that exist, deal with a limited set of boundary conditions and the findings from one is in contradiction to the others. The main achievements and conclusions that can be withdrawn from the discussions conducted in the respective chapters are presented in this chapter.

10.1.1 Validation of a Transitional Turbulence Model

It has been clear that in order to fully understand the gas flow behaviour inside micro geometries, local information of the flow physics is needed. A prime achievement of

the current work is to establish a numerical model that could be used to augment and explain the experimental results.

Laminar to turbulent flow transition is still an open field of investigation not only in microflows but also in macro scales. A numerical model in the RANS framework that is capable of predicting such laminar to turbulent transition is a relatively recent achievement that appeared in the open literature. We use and calibrate the modified version of Abraham et al. [1, 104] to predict the transitional flow behaviour of the compressible gas flow inside microchannels and microtubes, which has not been applied widely yet in the literature. Rigorous validation of the model against experimental results of gas microflows has been performed using adiabatic flow conditions and excellent agreements in the laminar and turbulent flow regimes have been observed. Prediction of the laminar to turbulent transition or so to speak critical Re has also shown an acceptable accuracy between the validated model and experimental results. This transitional turbulence model is validated for both circular and rectangular geometries. Finally, the model has been further utilized to investigate effect of aspect ratio and inlet manifold shape on the laminar to turbulent transition, which are still open questions in the microfluidic community.

10.1.2 Frictional Characteristics of Microtubes and Microchannels

Experimental investigations were conducted to better understand the frictional characteristics of the gas flows for both microtubes and microchannels. A deviation from the macro scale theory in the values of the friction factor in the laminar and turbulent regimes was noticed and using the validated numerical model it has been found out that such is due to inaccurate modeling of the minor losses which are first of all not constant with increasing Re but also are higher in the early laminar regime. An excellent agreement between experimentally deduced friction factor and the theory was

then demonstrated by considering the minor losses variation extracted from numerical results. For microtubes having smaller D_h the percent share of minor pressure losses is quite less compared to the total pressure drop and hence accurate evaluation of the minor losses is not necessary for experimental deduction of friction factor from the pressure drop. However for the smallest commercial microtube experimented, friction factor in the turbulent regime was higher than Blasius correlation which could be due to the higher relative surface roughness.

Experimental investigations of similar MT diameters from the other manufacturers is therefore recommended as the friction factor evaluated from the numerical analysis where walls are treated as smooth, follow the Blasius law. Moreover it is recommended to perform numerical simulations with different wall roughness in order to see if the trend of experimental friction factor in the turbulent flow regime can be representative of rough microtubes.

While testing the microchannels, local pressure measurements were also made which allowed to establish a better comparison with the numerical model for the local flow physics. An excellent match of the local static temperature, Mach number and fluid velocity was observed between the experimentally measured and numerical values even in the transitional flow regime. By comparing the existing experimental data reduction techniques available in the literature, the role of axial temperature drop of the gas due to strong compressibility effects of the adiabatic microchannels was clarified. It has been found out that currently available data reduction techniques need to be complemented with additional effects related with average temperature of the gas that before has been considered as the arithmetic average between inlet and outlet. A new equation in collaboration with Hong et al. [108] has been proposed in this regards which correctly takes into account the integral average of the gas temperature along the length of the MC and it has been shown that the friction factor evaluated using this equation (Equation 6.8) follows the numerical as well as theoretical Blasius law for the smooth MCs. Therefore use of this equation for the analysis of adiabatic friction factor in

microchannels is recommended, especially when the flow is choked. Flow choking has been established for the gas flows in MCs at higher values of Re and hence Ma. Locally measured pressures allowed to observe this phenomenon by showing a stagnation of local Ma and velocity of the gas.

10.1.3 Heat Transfer in Microtubes

Forced convective heat transfer for gas flows inside MTs was investigated by employing Joules heating (H boundary condition). Comparison of experimental and numerical results has shown that Nu for a high speed gas flow differs from the conventional correlations for microtubes having $D_h < 200$ μm. Moreover it is important to redefine the usual definition of the Nu such that instead of static temperature of the gas at the outlet, total temperature is used. Because for a high speed gas at the exit of the MT, kinetic energy of the gas carries more weight than thermal energy. Since for compressible flows, temperature and velocity fields can not be separated therefore different thermal boundary conditions result in different Nu. Even when the total gas temperatures of the gas at the inlet and outlet are used for the evaluation of Nu, there exists a point when total average temperature of the gas at the outlet exceeds the wall temperature which causes an anomaly in the evaluation of the Nu where it tries to reach infinity and then reverses the sign to become negative for higher Re. However this anomaly has never been reported with experimental results but it is discussed in the earlier numerical works [11, 133]. Author is of the view that Nu should always be reported based on the static inlet and outlet temperatures, because in a heat exchanging system the heat transfer between a solid wall and the fluid happens due to difference in wall temperature and the gas static temperature instead of the total temperature. Then again, with the experimental setup using a thermocouple at the outlet of the MT/MC, it is not possible to measure the static temperature of the gas and hence discrepancy between experimental and numerical results may exist until a better way of measuring the static temperature or the total temperature is employed in the literature.

10.1.4 Limitations of the Gas to Gas Heat Exchanging Systems

As it has been emphasized in the heat transfer studies of the single MT with gas flows, it has been found out that due to gas acceleration the apparent heat transfer on the hot side (thermal energy loss) of the gas to gas heating systems is different than thermal energy gain on the cold side due to increased kinetic energy of the accelerating gas flow. Therefore the usual understanding where it is assumed that heat transfer on both sides of the heat exchanger is equal does not hold true for the gas to gas micro heat exchangers as soon as the compressibility effects become dominant. In order to close the thermal energy balance between both sides, kinetic energy of both fluids must be considered else results will be misleading.

It has been found out that compressibility effects where thermal energy on the hot side and cold side of the gas to gas μHx starts to deviate correspond to a $Ma_{exit} \geq 0.1$ which is less than the usual textbook limit ($Ma > 0.3$) valid for adiabatic gas flows. Increasing the mass flow further does not substantially increase the gas temperature of the cold gas inside MC core of the μHx and hence would be redundant in the gas recuperators where the primary objective is to preheat the incoming cold gas. Therefore, such devices should be operated at low Re such that compressibility effects are not dominant.

This increase in kinetic energy at very high values of Ma_{exit} might serve as potential opportunity if the objective is to cool down a wall as is the case of heat sink for electronic chip cooling. It has been now understood that the most significant decrease of the gas static temperature happens close to the outlet of the MC core, this might cause hot spots in the chip cooling application. Therefore an unconventional heat sink design where gas is allowed to accelerate in MC core before the electronic chip might be beneficial instead of conventional design where MC core is right on top of the chip. A drawback of this design is that one has to use additional space before the real chip

to be cooled and hence might not be a feasible option where space and weight are the decisive factors for miniaturized cooling systems.

10.1.5 Thermal Performance Evaluation of the MC core using Porous Model Approximation

A relatively inexpensive computational methodology to predict the thermal performance of the MC core in a double layer gas to gas μHx is presented in this work. This methodology is an extension to the work of Joseph et al. [132, 117] where they developed similar methodology tailored to high temperature gas but incompressible gas flows. Current methodology is suitable to predict the thermal performance of the MC core in a μHx considering the any maldistribution effects due to the presence of dividing and combining manifolds. Validation of the developed methodology with the experimental results of an earlier reported μHx showed an excellent match and hence provided a framework to treat MCs as porous medium in order to further study the effects of manifolds and multiple layers.

10.2 Recommendations for Future Work

Based on the conclusions and discussions of respective Chapters, following recommendations for the future work are being made:

1. Current numerical results deviate from the experimentally reported trends of Nu from Choi et al. [6] and Yang et al. [31] for MTs with $D_h < 200$ μm at higher Re in the turbulent regime. Therefore it is recommended that heat transfer analysis in single MTs should be pursued further experimentally using MTs from a different manufacturer to see if such discrepancy is due to different tube materials or total temperature measurements of the gas at the outlet of the MT.

2. For a constant heat flux boundary condition at the wall of the MT, it has been observed that the wall temperature decreases than the total (stagnation) temperature of the gas at higher Re in the turbulent flow regime. This causes a singularity (please see the asymptote in Fig. 5.23a) in the mathematical evaluation of Nu. Therefore it would be of interest to see if a constant wall temperature boundary condition yields the similar results in the turbulent regime using developed numerical model.

3. Due to sharp decrease of static temperature (due to compressibility) close to the outlet of the MC core in a μHx, outlet manifold may be having the biggest share of heat exchange between the two fluids across the partition foil. Moreover a thick partition foil might be causing maximum heat transfer between the fluids in the inlet manifold as it achieves the average temperature of the two gases in a steady state heat exchanging system which may be causing practically no heat exchange in the MC core. This has been seen in the simulation based design of Deng et al. [86] where all the heat exchange happens in the mixing zones (manifolds) rather than MCs. Therefore prototype heat exchange device should be improved in order to have better estimation of individual contributions of manifolds and MC core in the total heat transfer rate of the μHx. This will be done by adding thermocouples inside the manifold but very close to the start of the MC core instead of current scheme where they were placed in the vicinity of entrance and exit ports.

4. Maldistribution causes the thermal efficiency of the μHx to decrease whereas current experimental results showed a positive influence of the manifolds to the average thermal efficiency. It is recommended to use the developed porous model approximation of the MC core and to model the manifolds as well as separating foil in the CFD study to see how this increased efficiency due to the manifold contribution is affected by the thickness and material of the separation foil.

Bibliography

[1] J. Abraham, E. Sparrow, and J. Tong, "Breakdown of laminar pipe flow into transitional intermittency and subsequent attainment of fully developed intermittent or turbulent flow," *Numerical Heat Transfer, Part B: Fundamentals*, vol. 54, no. 2, pp. 103–115, 2008.

[2] Y. Yang, *Experimental and Numerical Analysis of Gas Forced Convection through Microtubes and Micro Heat Exchangers*. PhD dissertation, Alma Mater Studiorum- Universita di Bologna, 2012.

[3] G. Morini, "Laminar to turbulent flow transition in microchannels," *Microscale Thermophysical Eng.*, vol. 8, pp. 15–30, 2004.

[4] W. Peiyi and W. Little, "Measurement of friction factors for the flow of gases in very fine channels used for microminiature joule-thomson refrigerators," *Cryogenics*, vol. 23, no. 5, pp. 273 – 277, 1983.

[5] P. Wu and W. Little, "Measurement of the heat transfer characteristics of gas flow in fine channel heat exchangers used for microminiature refrigerators," *Cryogenics*, vol. 24, no. 8, pp. 415 – 420, 1984.

[6] S. Choi, "Fluid flow and heat transfer in microtubes," *Micromechanical Sensors, Actuators, and Systems, ASME*, pp. 123–134, 1991.

[7] D. Yu, R. Warrington, R. Barron, and T. Ameel, "An experimental and theoretical investigation of fluid flow and heat transfer in microtubes," *ASME/JSME Thermal Engineering Conference*, vol. 1, pp. 523–530, 1995.

[8] P. Rosa, T. Karayiannis, and M. Collins, "Single-phase heat transfer in microchannels: The importance of scaling effects," *Applied Thermal Engineering*, vol. 29, no. 17, pp. 3447 – 3468, 2009.

[9] Z. Guo and X. Wu, "Compressibility effect on the gas flow and heat transfer in a microtube," *International Journal of Heat and Mass Transfer*, vol. 40, no. 13, pp. 3251 – 3254, 1997.

[10] Z. Y. Guo and X. B. Wu, "Further study on compressibility effects on the gas flow and heat transfer in a microtube," *Microscale Thermophysical Engineering*, vol. 2, no. 2, pp. 111–120, 1998.

[11] Z.-Y. Guo and Z.-X. Li, "Size effect on microscale single-phase flow and heat transfer," *International Journal of Heat and Mass Transfer*, vol. 46, no. 1, pp. 149 – 159, 2003.

[12] D. Du, *Effect of compressibility and roughness on flow and heat transfer in microtubes*. PhD dissertation, Tsinghua University- Beijing, 2000.

[13] Y. Asako, T. Pi, S. E. Turner, and M. Faghri, "Effect of compressibility on gaseous flows in micro-channels," *International Journal of Heat and Mass Transfer*, vol. 46, no. 16, pp. 3041 – 3050, 2003.

[14] M. Kohl, S. Abdel-Khalik, S. Jeter, and D. Sadowski, "An experimental investigation of microchannel flow with internal pressure measurements," *International Journal of Heat and Mass Transfer*, vol. 48, no. 8, pp. 1518 – 1533, 2005.

[15] C. Hong, Y. Asako, and J.-H. Lee, "Poiseuille number correlation for high speed micro-flows," *J. Phy. D Apll. Phy.*, vol. 41, no. 10, 2008.

[16] C. Hong and Y. Asako, "Heat transfer characteristics of gaseous flows in a microchannel and a microtube with constant wall temperature," *Numerical Heat Transfer, Part A: Applications*, vol. 52, no. 3, pp. 219–238, 2007.

[17] C. Hong and Y. Asako, "Heat transfer characteristics of gaseous flows in microtube with constant heat flux," *Applied Thermal Engineering*, vol. 28, no. 11, pp. 1375 – 1385, 2008.

[18] G. L. Morini, M. Lorenzini, and S. Salvigni, "Friction characteristics of compressible gas flows in microtubes," *Experimental Thermal and Fluid Science*, vol. 30, no. 8, pp. 733 – 744, 2006. ECI International Conference on Heat Transfer and Fluid Flow in Microscale.

[19] A. H. Shapiro, *The Dynamics and Thermodynamics of Compressible Fluid Flow*, vol. 1–2. John Wiley, 1953.

[20] G. Tang, Z. Li, Y. He, and W. Tao, "Experimental study of compressibility, roughness and rarefaction influences on microchannel flow," *International Journal of Heat and Mass Transfer*, vol. 50, no. 11, pp. 2282 – 2295, 2007.

[21] G. Celata, M. Cumo, S. McPhail, L. Tesfagabir, and G. Zummo, "Experimental study on compressible flow in microtubes," *International Journal of Heat and Fluid Flow*, vol. 28, no. 1, pp. 28 – 36, 2007.

[22] G. Celata, M. Lorenzini, and G. Morini, "Friction factor in micropipe gas flow under laminar, transition and turbulent flow regime.," *Int J Heat Fluid Flow*, vol. 30, pp. 814–822, 2009.

[23] K. Vijayalakshmi, K. Anoop, H. Patel, P. Harikrishna, T. Sundararajan, and S. K. Das, "Effects of compressibility and transition to turbulence on flow through microchannels," *International Journal of Heat and Mass Transfer*, vol. 52, no. 9, pp. 2196 – 2204, 2009.

[24] M. Lorenzini, G. L. Morini, and S. Salvigni, "Laminar, transitional and turbulent friction factors for gas flows in smooth and rough microtubes," *International Journal of Thermal Sciences*, vol. 49, no. 2, pp. 248 – 255, 2010.

[25] S. Murakami and Y. Asako, "Local Friction Factor of Compressible Laminar or Turbulent Flow in Micro-Tubes," vol. ASME 2011 9th International Conference on Nanochannels, Microchannels, and Minichannels, Volume 1 of *International Conference on Nanochannels, Microchannels, and Minichannels*, pp. 295–303, 06 2011.

[26] C. Hong, T. Yamamoto, Y. Asako, and K. Suzuki, "Heat Transfer Characteristics of Compressible Laminar Flow Through Microtubes," *Journal of Heat Transfer*, vol. 134, 1 2012. 011602.

[27] C. Hong, T. Yamada, Y. Asako, and M. Faghri, "Experimental investigation of laminar, transitional and turbulent gas flow in microchannels," *J Heat Mass Transfer*, vol. 55, pp. 4397–4403, 2012.

[28] C.-Y. Yang, C.-W. Chen, T.-Y. Lin, and S. G. Kandlikar, "Heat transfer and friction characteristics of air flow in microtubes," *Experimental Thermal and Fluid Science*, vol. 37, pp. 12 – 18, 2012.

[29] V. Gnielinski, "On heat transfer in tubes," *International Journal of Heat and Mass Transfer*, vol. 63, pp. 134 – 140, 2013.

[30] Y. Yang, H. Chalabi, M. Lorenzini, and G. L. Morini, "The effect on the Nusselt number of the nonlinear axial temperature distribution of gas flows through microtubes," *Heat Transfer Engineering*, vol. 35, no. 2, pp. 159–170, 2014.

[31] Y. Yang, C. Hong, G. L. Morini, and Y. Asako, "Experimental and numerical investigation of forced convection of subsonic gas flows in microtubes," *International Journal of Heat and Mass Transfer*, vol. 78, pp. 732 – 740, 2014.

[32] D. Kawashima and T. Asako, "Data reduction of friction factor for compressible flow in micro-channels," *International Journal of Heat and Mass Transfer*, vol. 77, pp. 257–261, 2014.

[33] C. Hong, T. Nakamura, Y. Asako, and I. Ueno, "Semi-local friction factor of turbulent gas flow through rectangular microchannels," *International Journal of Heat and Mass Transfer*, vol. 98, pp. 643–649, 2016.

[34] D. Kawashima and Y. Asako, "Measurement of quasi-local friction factor of gas flow in a micro-tube," *Proceedings of the Institution of Mechanical Engineers, Part C: Journal of Mechanical Engineering Science*, vol. 230, no. 5, pp. 782–792, 2016.

[35] C. Hong, S. Matsushita, Y. Asako, and I. Ueno, "Characteristics of Turbulent Gas Flow in Microtubes," vol. 7: Fluids and Heat Transfer, Parts A, B, C, and D of *ASME International Mechanical Engineering Congress and Exposition*, pp. 993–998, 2012.

[36] D. Kawashima, T. Yamada, C. Hong, and Y. Asako, "Mach number at outlet plane of a straight micro-tube," *Proceedings of the Institution of Mechanical Engineers, Part C: Journal of Mechanical Engineering Science*, vol. 230, no. 19, pp. 3420–3430, 2016.

[37] C. Hong, Y. Yoshida, S. Matsushita, I. Ueno, and Y. Asako, "Supersonic micro-jet of straight micro-tube exit," *Journal of Thermal Science and Technology*, vol. 10, 12 2015.

[38] C. Hong, G. Tanaka, Y. Asako, and H. Katanoda, "Flow characteristics of gaseous flow through a microtube discharged into the atmosphere," *International Journal of Heat and Mass Transfer*, vol. 121, pp. 187 – 195, 2018.

[39] X. Peng, G. Peterson, and B. Wang, "Frictional flow characteristics of water flowing through rectangular microchannels," *Experimental Heat Transfer An International Journal*, vol. 7, no. 4, pp. 249–264, 1994.

[40] T. M. Harms, M. J. Kazmierczak, and F. M. Gerner, "Developing convective heat transfer in deep rectangular microchannels," *Int J Heat and Fluid Flow*, vol. 20, no. 2, pp. 149–157, 1999.

[41] T. M. Adams, M. F. Dowling, S. Abdelkhalik, and S. M. Jeter, "Applicability of traditional turbulent single-phase forced convection correlations to non-circular microchannels," *Int J Heat and Mass Transfer*, vol. 42, no. 23, pp. 4411–4415, 1999.

[42] M. Asadi, G. Xie, and B. Sunden, "A review of heat transfer and pressure drop characteristics of single and two-phase microchannels," *Int J Heat and Mass Transfer*, vol. 79, pp. 34–53, 2014.

[43] T. Dixit and I. Ghosh, "Review of micro- and mini-channel heat sinks and heat exchangers for single phase fluids," *Renewable and Sustainable Energy Reviews*, vol. 41, pp. 1298–1311, 2015.

[44] G. L. Morini, "Single-phase convective heat transfer in microchannels: a review of experimental results," *International journal of thermal sciences*, vol. 43, no. 7, pp. 631–651, 2004.

[45] O. Reynolds, "Xxix. an experimental investigation of the circumstances which determine whether the motion of water shall be direct or sinuous, and of the law of resistance in parallel channels," *Phil Trans R Soc*, vol. 174, 1883.

[46] H. Li and M. G. Olsen, "Aspect ratio effects on turbulent and transitional flow in rectangular microchannels as measured with micropiv," *Journal of fluids engineering*, vol. 128, no. 2, pp. 305–315, 2006.

[47] W. Wibel and P. Ehrhard, "Experiments on the laminar/turbulent transition of liquid flows in rectangular microchannels," *Heat Transfer Engineering*, vol. 30, no. 1-2, pp. 1298–1311, 2009.

[48] B. Kim, "An experimental study on fully developed laminar flow and heat transfer in rectangular microchannels," *International Journal of Heat and Fluid Flow*, vol. 62, pp. 224–232, 2016.

[49] G. Morini, M. Lorenzini, S. Salvigni, and M. Spiga, "Analysis of laminar-to-turbulent transition for isothermal gas flows in microchannels," *Microfluidics and Nanofluidics*, vol. 7, no. 2, pp. 181–190, 2009.

[50] S. G. Kandlikar, D. Schmitt, A. L. Carrano, and J. B. Taylor, "Characterization of surface roughness effects on pressure drop in single-phase flow in minichannels," *Physics of Fluids*, vol. 17, no. 100606, 2005.

[51] W. Chang, G. Pu-Zhen, T. Si-chao, and X. Chao, "Effect of aspect ratio on the laminar-to-turbulent transition in rectangular channel," *Annals of Nuclear Energy*, vol. 46, pp. 90–96, 2012.

[52] G. L. Morini, M. Lorenzini, S. Colin, and S. Geoffroy, "Experimental analysis of pressure drop and laminar to turbulent transition for gas flows in smooth microtubes," *Heat Transfer Engineering*, vol. 28, no. 8-9, pp. 670–679, 2007.

[53] W. Bier, W. Keller, G. Linder, D. Seidel, K. Schubert, and H. Martin, "Gas to gas heat transfer in micro heat exchangers," *Chemical Engineering and Processing: Process Intensification*, vol. 32, no. 1, pp. 33 – 43, 1993.

[54] C. Harris, M. Despa, and K. Kelly, "Design and fabrication of a cross flow micro heat exchanger," *Journal of Microelectromechanical Systems*, vol. 9, pp. 502–508, Dec 2000.

[55] C. Harris, K. Kelly, Tao Wang, A. McCandless, and S. Motakef, "Fabrication, modeling, and testing of micro-cross-flow heat exchangers," *Journal of Microelectromechanical Systems*, vol. 11, pp. 726–735, Dec 2002.

[56] K. Schubert, J. Brandner, M. Fichtner, G. Linder, U. Schygulla, and A. Wenka, "Microstructure devices for applications in thermal and chemical process engineering," *Microscale Thermophysical Engineering*, vol. 5, no. 1, pp. 17–39, 2001.

[57] J. Brandner, E. Anurjew, L. Bohn, E. Hansjosten, T. Henning, U. Schygulla, A. Wenka, and K. Schubert, "Concepts and realization of microstructure heat exchangers for enhanced heat transfer," *Experimental Thermal and Fluid Science*, vol. 30, no. 8, pp. 801 – 809, 2006. ECI International Conference on Heat Transfer and Fluid Flow in Microscale.

[58] S. Li, H. Zhang, J. Cheng, X. Li, W. Cai, Z. Li, and F. Li, "A state-of-the-art overview on the developing trend of heat transfer enhancement by single-phase flow at micro scale," *International Journal of Heat and Mass Transfer*, vol. 143, p. 118476, 2019.

[59] I. A. Ghani, N. A. C. Sidik, and N. Kamaruzaman, "Hydrothermal performance of microchannel heat sink: The effect of channel design," *International Journal of Heat and Mass Transfer*, vol. 107, pp. 21 – 44, 2017.

[60] K. Nikitin, Y. Kato, and L. Ngo, "Printed circuit heat exchanger thermal–hydraulic performance in supercritical co2 experimental loop," *International Journal of Refrigeration*, vol. 29, no. 5, pp. 807 – 814, 2006.

[61] T. L. Ngo, Y. Kato, K. Nikitin, and N. Tsuzuki, "New printed circuit heat exchanger with s-shaped fins for hot water supplier," *Experimental Thermal and Fluid Science*, vol. 30, no. 8, pp. 811 – 819, 2006. ECI International Conference on Heat Transfer and Fluid Flow in Microscale.

[62] M. Utamura, "Thermal-Hydraulic Characteristics of Microchannel Heat Exchanger and Its Application to Solar Gas Turbines," vol. 4: Turbo Expo 2007, Parts A and B of *Turbo Expo: Power for Land, Sea, and Air*, pp. 287–294, 05 2007.

[63] N. Tsuzuki, Y. Kato, and T. Ishiduka, "High performance printed circuit heat exchanger," *Applied Thermal Engineering*, vol. 27, no. 10, pp. 1702 – 1707, 2007. Heat transfer and sustainable energy technologies.

[64] N. Tsuzuki, M. Utamura, and T. L. Ngo, "Nusselt number correlations for a microchannel heat exchanger hot water supplier with s-shaped fins," *Applied Thermal Engineering*, vol. 29, no. 16, pp. 3299 – 3308, 2009.

[65] B. Alm, U. Imke, R. Knitter, U. Schygulla, and S. Zimmermann, "Testing and simulation of ceramic micro heat exchangers," *Chemical Engineering Journal*, vol. 135, pp. S179 – S184, 2008. Microreaction Technology IMRET 9: Proceedings of the Ninth International Conference on Microreaction Technology.

[66] N. García-Hernando, A. Acosta-Iborra, U. Ruiz-Rivas, and M. Izquierdo, "Experimental investigation of fluid flow and heat transfer in a single-phase liquid flow micro-heat exchanger," *International Journal of Heat and Mass Transfer*, vol. 52, no. 23, pp. 5433 – 5446, 2009.

[67] H. Cao, G. Chen, and Q. Yuan, "Testing and design of a microchannel heat exchanger with multiple plates," *Industrial & Engineering Chemistry Research*, vol. 48, no. 9, pp. 4535–4541, 2009.

[68] H. Cao, G. Chen, and Q. Yuan, "Thermal performance of crossflow microchannel heat exchangers," *Industrial & Engineering Chemistry Research*, vol. 49, no. 13, pp. 6215–6220, 2010.

[69] T. Dang, J. tong Teng, and J. cherng Chu, "A study on the simulation and experiment of a microchannel counter-flow heat exchanger," *Applied Thermal Engineering*, vol. 30, no. 14, pp. 2163 – 2172, 2010.

[70] T. Dang and J. tong Teng, "The effects of configurations on the performance of microchannel counter-flow heat exchangers–an experimental study," *Applied Thermal Engineering*, vol. 31, no. 17, pp. 3946 – 3955, 2011. SET 2010 Special Issue.

[71] T. Dang and J.-T. Teng, "Comparisons of the heat transfer and pressure drop of the microchannel and minichannel heat exchangers," *Heat and Mass Transfer*, vol. 47, pp. 1311–1322, Oct 2011.

[72] J. Miwa, Y. Asako, C. Hong, and M. Faghri, "Performance of Gas-to-Gas Micro-Heat Exchangers," *Journal of Heat Transfer*, vol. 131, 03 2009. 051801.

[73] K. Koyama and Y. Asako, "Experimental investigation of heat transfer characteristics on a gas-togas counterflow microchannel heat exchanger," *Experimental Heat Transfer*, vol. 23, no. 2, pp. 130–143, 2010.

[74] K. Koyama and Y. Asako, "Experimental investigation of heat transfer characteristics on a gas-to-gas parallel flow microchannel heat exchanger," *The Open Transport Phenomena J.*, vol. 2, no. 3, pp. 1–8, 2010.

[75] K. Koyama, C. Hong, and Y. Asako, "Effect of partition wall on heat transfer characteristics of a gas-to-gas counterflow microchannel heat exchanger," *Heat Transfer Engineering*, vol. 33, no. 6, pp. 533–547, 2012.

[76] R. J. Kee, B. B. Almand, J. M. Blasi, B. L. Rosen, M. Hartmann, N. P. Sullivan, H. Zhu, A. R. Manerbino, S. Menzer, W. G. Coors, and J. L. Martin, "The design, fabrication, and evaluation of a ceramic counter-flow microchannel heat exchanger," *Applied Thermal Engineering*, vol. 31, no. 11, pp. 2004 – 2012, 2011.

[77] R. Nacke, B. Northcutt, and I. Mudawar, "Theory and experimental validation of cross-flow micro-channel heat exchanger module with reference to high mach aircraft gas turbine engines," *International Journal of Heat and Mass Transfer*, vol. 54, no. 5, pp. 1224 – 1235, 2011.

[78] Y. Yang, J. Brandner, and G. Morini, "Hydraulic and thermal design of a gas microchannel heat exchanger," *Journal of Physics: Conference Series*, vol. 362, 05 2012.

[79] G. Maranzana, I. Perry, and D. Maillet, "Mini- and micro-channels: influence of axial conduction in the walls," *International Journal of Heat and Mass Transfer*, vol. 47, no. 17, pp. 3993 – 4004, 2004.

[80] E. Vasquez-Alvarez, F. T. Degasperi, L. G. Morita, M. R. Gongora-Rubio, and R. Giudici, "Development of a micro-heat exchanger with stacked plates using LTCC technology," *Brazilian Journal of Chemical Engineering*, vol. 27, pp. 483 – 497, 09 2010.

[81] Y. Yang, I. Gerken, J. J. Brandner, and G. L. Morini, "Design and experimental investigation of a gas-to-gas counter-flow micro heat exchanger," *Experimental Heat Transfer*, vol. 27, no. 4, pp. 340–359, 2014.

[82] Y. Yang, G. L. Morini, and J. J. Brandner, "Experimental analysis of the influence of wall axial conduction on gas-to-gas micro heat exchanger effectiveness," *Int. J. Heat & Mass Transfer*, vol. 69, pp. 17–25, 2014.

[83] I. Gerken, J. J. Brandner, and R. Dittmeyer, "Heat transfer enhancement with gas-to-gas micro heat exchangers," *App. Thermal Eng.*, vol. 93, pp. 1410–1416, 2016.

[84] F. Zhou, W. Zhou, Q. Qiu, W. Yu, and X. Chu, "Investigation of fluid flow and heat transfer characteristics of parallel flow double-layer microchannel heat exchanger," *Applied Thermal Engineering*, vol. 137, pp. 616 – 631, 2018.

[85] F. Zhou, W. Ling, W. Zhou, Q. Qiu, and X. Chu, "Heat transfer characteristics of cu-based microchannel heat exchanger fabricated by multi-blade milling process," *International Journal of Thermal Sciences*, vol. 138, pp. 559 – 575, 2019.

[86] Y. Deng, S. Menon, Z. Lavrich, H. Wang, and C. Hagen, "Design, simulation, and testing of a novel micro-channel heat exchanger for natural gas cooling in automotive applications," *Applied Thermal Engineering*, vol. 110, pp. 327 – 334, 2017.

[87] G. Morini and J. Brandner, "The design of mini/micro heat exchangers: A world of opportunities and constraints," *International Heat Transfer Conference*, vol. 2018-August, pp. 469–486, 2018.

[88] J. Singh, A. Montesinos-Castellanos, and K. D. P. Nigam, "Process intensification for compact and micro heat exchangers through innovative technologies: A review," *Industrial & Engineering Chemistry Research*, vol. 58, no. 31, pp. 13819–13847, 2019.

[89] "Web of science. microchannel heat transfer," *Clarivate Analytics: Philadelphia, PA, USA*, 2019.

[90] B. R. Munson, T. H. Okiishi, A. P. Rothmayer, and W. W. Huebsch, *Fundamentals of fluid mechanics*. John Wiley & Sons, 2014.

[91] F. R. Menter, "Two-equation eddy-viscosity turbulence models for engineering applications," *AIAA journal*, vol. 32, no. 8, pp. 1598–1605, 1994.

[92] F. R. Menter, R. B. Langtry, S. Likki, Y. Suzen, P. Huang, and S. Völker, "A correlation-based transition model using local variables—part i: model formulation," *Journal of turbomachinery*, vol. 128, no. 3, pp. 413–422, 2006.

[93] ANSYS, "Cfx version 18.1 manual," *ANSYS, Inc., Cannosburg, PA*, 2018.

[94] F. Menter and R. Langtry, "Transition modelling for turbomachinery flows," in *Low Reynolds Number Aerodynamics and Transition*, InTech, 2012.

[95] W. Minkowycz, J. Abraham, and E. Sparrow, "Numerical simulation of laminar breakdown and subsequent intermittent and turbulent flow in parallel-plate channels: Effects of inlet velocity profile and turbulence intensity," *International Journal of Heat and Mass Transfer*, vol. 52, no. 17-18, pp. 4040–4046, 2009.

[96] B. Wang and X. Peng, "Experimental investigation on liquid forced-convection heat transfer through microchannels," *International Journal of Heat and Mass Transfer*, vol. 37, pp. 73–82, 1994.

[97] G. L. Morini, Y. Yang, H. Chalabi, and M. Lorenzini, "A critical review of the measurement techniques for the analysis of gas microflows through microchannels," *Experimental Thermal and Fluid Science*, vol. 35, no. 6, pp. 849–865, 2011.

[98] S. G. Kandlikar, S. Colin, Y. Peles, S. Garimella, R. F. Pease, J. J. Brandner, and D. B. Tuckerman, "Heat transfer in microchannels—2012 status and research needs," *J. Heat Transfer.*, vol. 135, no. 9, 2013.

[99] I. Idelchick, *Handbook of hydraulic resistance*. Hemisphere Pub. Co., 1986.

[100] D. Kawashima, T. Yamada, C. Hong, and Y. Asako, "Mach number at outlet plane of a straight micro-tube," *Proceedings of the Institution of Mechanical Engineers, Part C: Journal of Mechanical Engineering Science*, vol. 230, no. 19, pp. 3420–3430, 2016.

[101] J. Cheng, H. Li, Z. Zhu, and Z. Tao, "Numerical simulation of flow transition in a rectangular microchannel," in *ICHMT DIGITAL LIBRARY ONLINE*, Begel House Inc., 2017.

[102] S. Barlak, S. Yapıcı, and O. Sara, "Experimental investigation of pressure drop and friction factor for water flow in microtubes," *International Journal of Thermal Sciences*, vol. 50, no. 3, pp. 361 – 368, 2011. Nano, Micro and Mini Channels.

[103] H. Herwig and O. Hausner, "Critical view on "new results in micro-fluid mechanics": an example," *International Journal of Heat and Mass Transfer*, vol. 46, no. 5, pp. 935 – 937, 2003.

[104] J. Abraham, E. Sparrow, and W. Minkowycz, "Internal-flow Nusselt numbers for the low-reynolds-number end of the laminar-to-turbulent transition regime," *International Journal of Heat and Mass Transfer*, vol. 54, no. 1, pp. 584 – 588, 2011.

[105] M. Mirmanto, D. Kenning, J. Lewis, and T. Karayiannis, "Pressure drop and heat transfer characteristics for single-phase developing flow of water in rectangular

microchannels," *Journal of Physics Conference Series*, vol. 395, pp. 2085–, 11 2012.

[106] A. M. Sahar, J. Wissink, M. M. Mahmoud, T. G. Karayiannis, and M. S. A. Ishak, "Effect of hydraulic diameter and aspect ratio on single phase flow and heat transfer in a rectangular microchannel," *Applied Thermal Engineering*, vol. 115, pp. 793–814, 2017.

[107] V. Lijo, H. Kim, and T. Setoguchi, "Analysis of choked viscous flows through a constant area duct," *Proceedings of The Institution of Mechanical Engineers Part G-journal of Aerospace Engineering*, vol. 1, pp. 1–12, 11 2010.

[108] C. Hong, Y. Asako, G. L. Morini, and D. Rehman, "Data reduction of average friction factor of gas flow through adiabatic micro-channels," *International Journal of Heat and Mass Transfer*, vol. 129, pp. 427–431, 2019.

[109] A. J. Ghajar and L.-M. Tam, "Heat transfer measurements and correlations in the transition region for a circular tube with three different inlet configurations," *Experimental thermal and fluid science*, vol. 8, no. 1, pp. 79–90, 1994.

[110] L. M. Tam and A. J. Ghajar, "Effect of inlet geometry and heating on the fully developed friction factor in the transition region of a horizontal tube," *Experimental thermal and fluid science*, vol. 15, no. 1, pp. 52–64, 1997.

[111] J. Dirker, J. P. Meyer, and D. V. Garach, "Inlet flow effects in micro-channels in the laminar and transitional regimes on single-phase heat transfer coefficients and friction factors," *International Journal of Heat and Mass Transfer*, vol. 77, pp. 612–626, 2014.

[112] L. Moruz, J. Kitzhofer, D. Hess, and M. Dinulescu, "Analysis of the isothermal transition process in wide aspect ratio rectangular channels," *Experimental thermal and fluid science*, vol. 105, pp. 316–331, 2019.

[113] W. Wibel and P. Ehrhard, "Experiments on liquid pressure-drop in rectangular microchannels, subject to non-unity aspect ratio and finite roughness," in *Proc. of ICNMM2006. 19-21 Jun, Limerick Ireland*, 2006.

[114] O. Jones, "An improvement in the calculation of turbulent friction in rectangular ducts," *J. Fluids Eng.*, vol. 98, pp. 173–180, 1976.

[115] N. Obot, "Determination of incompressible flow friction in smooth circular and noncircular passages: A generalized approach including validation of the nearly century old hydraulic diameter concept," *J. Fluids Eng.*, vol. 110, pp. 431–440, 1988.

[116] C. Wang, P. Gao, S. Tan, and Z. Wang, "Forced convection heat transfer and flow characteristics in laminar to turbulent transition region in rectangular channel," *Experimental Thermal and Fluid Science*, vol. 44, pp. 490–497, 2013.

[117] J. Joseph, R. Nacereddine, M. Delanaye, J. G. Korvink, and J. J. Brandner, "Advanced numerical methodology to analyze high-temperature wire-net compact heat exchangers for a micro-combined heat and power system application," *Heat Transfer Engineering*, vol. 0, no. 0, pp. 1–13, 2019.

[118] D. Rehman, G. L. Morini, and C. Hong, "A comparison of data reduction methods for average friction factor calculation of adiabatic gas flows in microchannels," *Micromachines*, vol. 10, no. 3, p. 171, 2019.

[119] S. Kakaç, R. K. Shah, and W. T. Aung, *Handbook of single-phase convective heat transfer*. 1987.

[120] Y. A. Cengel, *Heat Transfer*, vol. 2. McGraw Hill, 2008.

[121] K. Kubo, Y. Miyazato, and K. Matsuo, "Study of choked flows through a convergent nozzle," *Journal of Thermal Science*, vol. 19, no. 3, pp. 193–197, 2010.

[122] Y. Asako, D. Kawashima, T. Yamada, and C. Hong, "Mach number on outlet plane of a straight micro-tube," in *ASME 2013 International Mechanical Engi-*

neering Congress and Exposition, pp. V07AT08A020–V07AT08A020, American Society of Mechanical Engineers, 2013.

[123] J. Hellstrom and T. Lundstrom, "Flow through porous media at moderate reynolds number," *4th International Scientific Colloquium Modelling for Material Processing*, vol. 19, no. 1-–12, pp. 129–134, June, 2006.

[124] J. Hellstrom, "Parallel computing of fluid flow through porous media," *Licentiate thesis, Luleå: Luleå tekniska universitet,*, vol. 19, no. 1-–12, pp. 129–134, 2007.

[125] S. J. Kim and D. Kim, "Forced convection in microstructures for electronic equipment cooling," *ASME J. Heat Transfer*, vol. 121, no. 1-–12, pp. 639–645, 1999.

[126] S. J. Kim, D. Kim, and D. Y. Lee, "On the local thermal equilibrium in microchannel heat sinks," *Int. J. Heat Mass Transfer*, vol. 43, no. 1-–12, pp. 1735–1748, 2000.

[127] D. Tuckerman and R. Pease, "High-performance heat sinking for vlsi," *IEEE Electron Device Lett.*, vol. 5, pp. 126–129, 1981.

[128] R. Knight, J. Goodling, and D. Hall, "Optimal thermal design of forced convection heat sinks- analytical," *ASME Journal of Electronic Packaging*, vol. 113, pp. 313–321, 1991.

[129] L. Dong and S. Garimella, "Analysis and optimization of the termal performance of microchannel heat sinks," *CTRC Research Publications*, p. Paper 59, 2005.

[130] F. Y. Lim, S. Abdullah, and I. Ahmad, "Numerical study of fluid flow and heat transfer in microchannel heat sinks using anisotropic porous media approximation," *J. of App. Sci.*, vol. 10, no. 18, pp. 2047–2057, 2010.

[131] C. Renault, S. Colin, S. Orieux, P. Cognet, and T. Tzédakis, "Optimal design of multi-channel microreactor for uniform residence time distribution," *Microsystem Technologies*, vol. 18, no. 2, pp. 209–223, 2012.

[132] J. Joseph, R. Nacereddine, M. Delanaye, A. Giraldo, M. Roubah, and J. Brandner in *Proc. of 6th Micro and Nano Flows Conf. 6-7 Sep, Atlanta USA*, Sept. 2018.

[133] M. A. Coppola, *Heat Transfer in Gaseous Microflows: Conjugate Heat Transfer, Rarefaction and Compressibility Effects*. PhD dissertation, Universita Degli Studi Di Udine, 2012.